



UNIVERSITA' DEGLI STUDI DI PADOVA

Sede Amministrativa: Università degli Studi di Padova

Dipartimento di Processi Chimici dell'Ingegneria

SCUOLA DI DOTTORATO DI RICERCA IN INGEGNERIA INDUSTRIALE

INDIRIZZO INGEGNERIA CHIMICA

XXI° CICLO

Multistructured membranes based on electro-dynamic technologies: process optimization and catalytic performances

Direttore della Scuola: Ch.mo Prof. Paolo BARIANI

Supervisore: Ch.mo Prof. Michele MODESTI

Dottoranda: Martina ROSO

SUMMARY

Riassunto.....	I
Summary.....	VII
Introduction.....	1
CHAPTER 1 Electrohydrodynamic processes: fundamentals and application	3
1.1 Electro spraying and electro spinning: history and basic principles	5
1.2 Electro spraying of nanoparticles.....	10
1.3 Process of fiber production	13
1.4 Nanofibers structure and characterization	28
1.4.1 Polymer solution parameters	28
1.4.1.1 Molecular weight and solution viscosity	28
1.4.1.2 Surface tension	32
1.4.1.3 Solution Conductivity	33
1.4.1.4 Solvent dielectric constant.....	34
1.4.2 Processing conditions.....	35
1.4.2.1 Applied voltage.....	35
1.4.2.2 Flow rate	38
1.4.2.3 Nozzle collector distance.....	38
1.4.3 Ambient parameters	39
1.4.3.1 Temperature	39
1.4.3.2 Humidity	40
1.4.3.3 Pressure and type of atmosphere.....	40
1.5 Electro spinning design.....	49
1.6 Applications	55
1.6.1 Filtration and membranes.....	55
1.6.2 Catalysis and sensors	60
1.6.3 Electrical applications.....	66
1.6.4 Composite reinforcing	68
1.6.5 Bioapplications	71
1.6.5.1 Tissue engineering scaffold	71
1.6.5.2 Wound dressing.....	78
1.6.5.3 Drug release	79
1.7 Conclusive remarks on future challenges.....	86

CHAPTER 2 Response Surface Methodology	89
2.1 Introduction.....	89
2.1.2 Response Surface Methodology and Robust Design.....	91
2.1.3 The Sequential Nature of the Response Surface Methodology.....	92
2.2 Building Empirical Models	92
2.2.1 Linear Regression Model	92
2.2.1.1 Estimation of the Parameters in Linear Regression Models.....	93
2.2.2 Hypothesis testing in multiple regression	94
2.2.2.1 Properties of the Least Squares Estimators	94
2.2.2.2 Test for Significance of Regression	95
2.2.2.3 Residual Analysis	96
2.3 Variable Selection and Model Building in Regression	97
2.3.1 Procedures for Variable Selection	98
2.3.1.1 All Possible Regression	98
2.3.1.2 Stepwise Regression Methods	98
2.4 Steps of Response Surface Methodology.....	100
CHAPTER 3 Photocatalytic oxidation.....	105
3.1 Semiconducting nanomaterials.....	105
3.2 Photocatalytic oxidation (PCO).....	106
3.3 VOCs exposure in indoor environment	108
CHAPTER 4 Materials.....	111
4.1 Macromolecular materials for electrospinning.....	111
4.2 Nanoparticles.....	112
4.2.1 Titanium dioxide nanoparticles	112
4.2.2 Magnesium Oxide nanoparticles production via aerogel technique	112
4.2.3 Dispersant agent.....	113
CHAPTER 5 Methods	115
5.1 Characterization techniques	115
5.1.1 Dynamic light scattering.....	115
5.1.2 Scanning electron microscopy.....	117
5.1.2.1 Electron-Sample Interactions	117
5.1.2.2 Fundamental Principles of Scanning Electron Microscopy (SEM)	119
5.2 Analytical techniques.....	121
5.2.1 UV spectroscopy.....	121

5.2.1.1	General principles	121
5.2.1.2	Operating conditions	122
5.2.1.3	Quantitative procedures	123
5.2.2	High Performance Liquid Chromatography (HPLC).....	123
5.2.2.1	General principles	123
5.2.2.2	Instrumentation	125
5.2.3	Gas spectroscopy-Mass spectrometry	126
CHAPTER 6	Optimization of Electrospinning parameters via RSM	131
6.1	Introduction.....	131
6.2	Case study: Polymer/solvent system.....	131
6.2.1	Screening experiments for the Polymer/solvent system	131
6.2.2	RSM for polymer-solvent system.....	137
6.2.2.1	Design Summary	137
6.2.2.2	Model adequacy checking	141
6.3	Case study: Polymer/solvent/salt system	145
6.3.1	Screening experiments for the system polymer-solvent-salt	145
6.3.2	RSM for the system polymer-solvent-salt.....	148
6.3.2.1	Design Summary	148
6.3.2.2	Model adequacy checking	151
6.3.2.3	Diagnose the Statistical Properties of the Model.....	154
6.3.2.4	Contour plot analysis	156
6.3.2.5	Propagation of Error (POE)	159
6.3.2.6	Finding Solutions of Optimum	160
CHAPTER 7	Fabrication of nanostructured membranes	163
7.1	Introduction.....	163
7.2	Electrospraying optimization.....	164
7.2.1	Sonication time effect.....	164
7.2.2	Feed rate effect	165
7.2.3	Applied voltage.....	166
7.2.4	Nanoparticles concentrations.....	167
7.2.5	Nanoparticles dispersion studies.....	168
7.2.6	Electrospraying modified set up	170
7.3	Membranes processing and characterization.....	172
7.3.1	Multistructured membranes production PSU-TiO ₂ /MgO	172

7.3.1.1 Pressure drop analysis	174
7.3.2 Multistructured membranes production PMMAcoMMA/PANcoVAc/TiO ₂	177
7.3.2.1 Multistructured membranes characterization	179
7.4 Conclusion	186
CHAPTER 8 Photocatalytic activity of multistructured membranes.....	189
8.1 Introduction.....	189
8.2 Liquid phase Photocatalytic activity	190
8.2.1 PSU/TiO ₂ /MgO membranes	190
8.2.2 PANcoVAc/PMMAcoMAA/TiO ₂ Membranes	191
8.3 Gas phase Photocatalytic activity	189
8.3.1 Experimental apparatus.....	189
8.4 Results and discussion	190
8.4.1 Case study: Trichloroethylene (TCE) photo-degradation in gas phase.....	190
8.4.2 Case study: Acetone photo-oxidation in gas phase	198
Conclusions	207
References	211

Riassunto

Le tecnologie elettrodrodinamiche entrano a far parte della macro area delle tecnologie di produzione di nanofibre e nanoparticelle. Il termine “nano” (dal Greco nan(n)os “piccolo uomo”) è nel sistema SI Sistema Internazionale delle Unità) il prefisso che denota un milionesimo (10^{-9}) dell’unità di riferimento, quindi un nanometro corrisponde a 10^{-9} metri, un nanosecondo a 10^{-9} secondi e un nanofarad a 10^{-9} farad.

Per avere il senso della nanoscala basta pensare che un capello umano ha una dimensione media di 50.000 nanometri, una cellula batterica misura qualche centinaio di nanometri e il più piccolo oggetto osservabile dall’occhio umano misura 10.000 nanometri.

Un’introduzione relativa ai processi ElettroIdroDinamici (EHD) e una revisione dello stato dell’arte della ricerca scientifica in questo campo, sarà discussa nel Capitolo 1. Sia le tecniche di electro spraying che quelle di elettrofilatura comportano l’utilizzo di un potenziale applicato al fine di generare un getto elettricamente carico. Per quanto concerne l’electro spraying, il risultato consiste nella formazione di piccole gocce o particelle in conseguenza della partizione del getto elettrificato di una soluzione a bassa viscosità. Tale processo è stato utilizzato per depositare films ultra sottili di materiali inorganici, organici e biologici al fine di generare nanoparticelle e aumentare la loro dispersione per l’ottenimento di nanomateriali. L’electrospray ha trovato riscontri commerciali nel campo della spettrometria di massa, nella verniciatura e nelle stampanti a getto d’inchiostro. Utilizzando questa tecnica è possibile vaporizzare un’ampia gamma di biomolecole in fase gas senza decomposizione e, accoppiando tale tecnica alla spettrometria di massa (ESIMS), è stato possibile identificare in tutti i laboratori del mondo numerose proteine, polimeri sintetici, ecc.

D’altra parte l’elettrofilatura è un processo che consente la produzione di fibre continue di diversi materiali con diametro nella scala nanometrica. In tal senso, anticipiamo che l’opportuna combinazione di elettrofilatura ed electro spraying potrà risultare utile per ampliare il range di applicazione di tali tecniche spaziando dalla catalisi alle applicazioni militari. Al momento non sono stati trovati in letteratura lavori relativi alla produzione di membrane combinando le tecniche di elettrofilatura e spraying.

La tecnica dell’elettrofilatura può essere vista come una variante del processo di electro spraying. La differenza sostanziale tra i due processi riguarda lo stiramento del getto a fronte della repulsione di cariche superficiali e l’evaporazione del solvente comporta dunque la formazione di fibre continue. Come verrà spiegato nei Capitoli 1, i processi EHD sono influenzati da diverse variabili e dalla potenziale interazione tra le stesse. Per questo motivo si è scelta la tecnica di Risposta delle Superfici (RSM) per sviluppare, migliorare e ottimizzare il processo. Una estesa panoramica riguardo la letteratura inerente verrà esposta nel Capitolo 2. Il settore della “metodologia di risposta

delle superfici” consiste nell’individuazione di una strategia sperimentale per esplorare una regione di spazio relativa a determinate variabili indipendenti, nella modellazione empirica statistica per lo sviluppo di un’adeguata relazione che sia in grado di esprimere la relazione tra i parametri e le variabili indipendenti e nella ricerca di metodi di ottimizzazione per trovare la configurazione delle variabili di processo che consente di ottenere una prefissata risposta.

Come suggerito nella Sezione I, i parametri che influenzano il processo di elettrofilatura sono diversi e quindi sono diverse le morfologie che si possono ottenere. Lo scopo di questo studio è stato quello di ottenere il massimo controllo sulle variabili e sui parametri che governano il processo in modo tale da avere ulteriori informazioni circa la possibile interazione tra le diverse configurazioni di parametri.

Lo stadio a monte dell’ottimizzazione di processo, ha visto la programmazione e lo sviluppo di esperimenti di screening al fine di valutare il range dei parametri, di soluzione e di processo, più adeguato, ovvero il campo di azione all’interno del quale è garantito l’ottenimento di fibre.

Inoltre grazie a tali esperimenti è possibile avere un’idea dei parametri che principalmente influenzano il processo e quindi decidere in modo adeguato i fattori da analizzare nella fase successiva di risposta delle superfici. I due sistemi in oggetto di studio sono stati:

Sistema Polimero/solvente

Sistema Polimero solvente/sale

E i risultati relative al significato delle prove di screening verrà discusso nel Capitolo 4. In seguito l’analisi di risposta delle superfici verrà condotta su entrambi i sistemi e verrà ampiamente analizzato l’effetto dei parametri considerati e delle loro eventuali interazioni.

Per il sistema polimero/solvente, è stato scelto un piano Box-Behnken all’interno della famiglia dei piani a tre livelli per fittare superfici di risposta del secondo ordine. I fattori considerati (tre livelli ciascuno) sono stati A: [Voltaggio applicato], B: [PMMACoMAA], C: [portata di alimentazione], D: [distanza tra gli elettrodi]. A seguito degli esperimenti di screening, che hanno consentito di determinare il range operativo, l’analisi di risposta delle superfici è stata condotta considerando un modello quadratico per la variabile risposta (il diametro medio delle fibre). Il risultato qui riportato deriva da un processo iterativo che ha consentito l’individuazione e l’eliminazione di “outliers”. Dall’equazione finale di modellazione è stato osservato come ci sia solo un’interazione significativa tra A: [voltaggio applicato] e B: [PMMACoMAA]. L’andamento della superficie di risposta fornisce delle indicazioni circa la relazione di scala tra i suddetti fattori rispetto alle forze su cui essi influiscono e di conseguenza sulla risposta del sistema. Per quanto concerne la concentrazione di polimero, in regime semidiluito, è possibile identificare un valore limite oltre il quale le forze viscoelastiche aumentano drasticamente e sovrastano le altre forze in gioco. Per bassi valori di B,

un aumento di voltaggio si traduce infatti in una diminuzione del diametro. Spostandosi invece al secondo livello di B, si apre una regione in cui il voltaggio non influisce sulla risposta. Questo significa che le relazioni di scala hanno un ordine diverso e il fattore B prevale su A, che non influenza più la variabile risposta. Un altro risultato interessante riguarda l'influenza della variabile D: distanza, che è risultata non significativa all'interno del range considerato.

Grazie ai risultati ottenuti dall'analisi del primo sistema, si è osservato che per qualsiasi configurazione il diametro medio ottenuto era nella scala dei micron e per questo motivo si è deciso di agire sulle proprietà di soluzione per spostarsi nel range "nano". In particolare sono state modificate tensione superficiale e conducibilità elettrica della soluzione ed un nuovo sistema polimero/solvente/sale è stato dunque analizzato valutando l'effetto di 4 fattori quali A: [voltaggio] applicato, B: [PMMACoMAA], C: [LiCl], D: [portata di alimentazione] e delle loro interazioni sulla risposta. Dal piano Box- Behnken si è passati ad un piano D-optimal e il modello quadratico è risultato il più appropriato per descrivere il sistema. Tra i parametri significativi in questo caso risultano i singoli fattori e le interazioni AC, AD, BC, CD.

In accordo alla teoria, un aumento di potenziale applicato comporta una riduzione del diametro medio delle fibre mentre un aumento di portata ha ovviamente l'effetto opposto. Tuttavia il risultato relativo all'interazione tra questi due fattori (AD) ha rivelato che a basso voltaggio, l'aumento di portata comporta una diminuzione del diametro delle fibre mentre oltre il punto di sella viene invertito l'effetto. Questo comportamento trova spiegazione se consideriamo che per ogni potenziale applicato esiste una precisa velocità di stiro con la quale il getto viene trascinato verso il collettore. Se tale velocità è inferiore alla velocità con la quale la soluzione arriva all'uscita dell'ago, si avrà un eccesso di cariche elettrostatiche e di conseguenza i fenomeni di instabilità (movimento a frusta e ramificazione del getto) e stretching del getto verranno amplificati. Il risultato finale vedrà dunque fibre di diametro inferiore.

Per quanto riguarda l'interazione [LiCl]-[potenziale] (AC), a parità di altri fattori mantenuti al livello medio, il grafico delle curve di livello mostra come un aumento di voltaggio, ad una fissata concentrazione di sale, comporti un effetto di riduzione o aumento del diametro in funzione di quest'ultima. Questo andamento è legato al fatto che nel range operativo le forze elastiche derivate dalla viscosità della soluzione e dall'evaporazione del solvente possono intervenire in determinate condizioni operative in modo tale da arrestare prematuramente il getto a diametri maggiori.

In accordo agli esperimenti di screening è emerso come la concentrazione polimerica giochi un ruolo fondamentale nel processo di elettrofilatura sovrastando l'effetto degli altri fattori. La concentrazione del polimero sembra essere indipendente dalla concentrazione di sale (BC) e si ritiene sia il principale fattore che influenza il diametro delle nanofibre.

La concentrazione di sale influenza principalmente la conducibilità della soluzione polimerica. I risultati relativi all'interazione CD ha evidenziato la presenza di una concentrazione limite di sale (0.2wt%) oltre la quale non si ottiene alcun effetto benefico in termini di riduzione dei diametri.

Lavorando al disotto di questo valore limite, un aumento di portata comporta un aumento delle instabilità elettriche con conseguente stiramento del getto e diminuzione del diametro finale.

Lo scopo principale dell'ottimizzazione di processo è quello di minimizzare la risposta (diametro medio delle fibre). Sono stati assegnati i limiti della variabile risposta (300-370 nm) e dei parametri di processo (impostati in modo da minimizzare anche questi ultimi) e la configurazione di ottimo è stata verificata in modo tale da utilizzare questi risultati per la produzione di nuove membrane nanostrutturate (Capitolo 7).

Lo scopo di questa parte del lavoro è infatti quella di creare membrane multistrato combinando opportunamente elettrofilatura ed electrospraying per ottenere strutture multifunzionali che trovano riscontro in un ampio spettro di applicazioni specialmente nel campo dei tessuti di protezione e della filtrazione (aria)

La metodologia proposta e messa a punto prevede la deposizione di nanoparticelle inorganiche e l'ottimizzazione della loro distribuzione su nanofibre polimeriche. I seguenti obiettivi tecnologici riassumono l'approccio utilizzato:

1. studio dell'electrospraying di nanoparticelle inorganiche al fine di comprendere l'effetto dei parametri di processo sulla distribuzione e uniformità dei "nanocluster" depositati;
2. messa a punto di un adeguato apparato sperimentale per l'accoppiamento dei due processi di produzione in modo da ottenere risultati controllati e riproducibili;
3. caratterizzazione delle membrane prodotte in termini di morfologia e proprietà filtranti.

È stato verificato come sia il tempo di sonicazione che la stabilità della sospensione (ottenuta mediante aggiunta di un agente disperdente) influenzino la deposizione delle nanoparticelle sul collettore. Inoltre le condizioni ottimali per la deposizione via electrospraying è stata ottenuta grazie all'opportuna modifica dell'apparecchiatura standard comunemente usata.

Quindi si è passati alla produzione delle membrane multistrato costituite da nanofibre polimeriche elettrofilate (polisulfone (PSU), poli metimetacrilato-co-acido metacrilico (PMMA-co-MAA), poliacrilonitrile-co-acetato di vinile (PAN-co-VAc)) e nanoparticelle di TiO_2 o MgO . Tali membrane sono state opportunamente caratterizzate in termini di cadute di pressione, morfologia (SEM) e analisi qualitativa e quantitativa dei loro componenti (EDAX,TGA). È stato osservato come le cadute di pressione attraverso le membrane siano funzione inversa rispetto al contenuto in nanoparticelle. Un tale andamento si può spiegare considerando il processo di deposizione delle nanoparticelle che vede una loro distribuzione sulle fibre senza formazione di grossi aggregati che

bloccano i pori tra le stesse. Di conseguenza i diversi strati di fibre risultano maggiormente distanziati e ciò si traduce in minori perdite di carico (9%-34%) del manufatto rispetto alle membrane prive di particelle.

L'enorme interesse per i problemi ambientali e la necessità di trovare nuove avanzate soluzioni per ridurre l'inquinamento, hanno fornito lo spunto per testare le performance delle membrane nanostrutturate nell'ambito della degradazione fotocatalitica eterogenea di diversi composti organici inquinanti. Poiché a temperatura e pressione ambiente i composti organici inquinanti possono essere convertiti a CO_2 ed H_2O grazie ai processi di fotocatalisi, alcuni studiosi hanno visto in questi metodi un valido strumento per affrontare il problema delle acque di scarico e della purificazione dell'aria. Il principio, ampiamente illustrato nel Capitolo 3, si basa essenzialmente sulla formazione di vacanze elettroniche grazie all'irradiazione ultravioletta e alla successiva formazione di radicali OH, per reazione con i gruppi ossidrilici esposti sulla superficie della titania. I radicali OH rivestono un ruolo chiave nel processo di ossidazione dei composti organici.

In questo panorama, le performance catalitiche delle membrane a base nanofibre/nanoparticelle sono state valutate sia in fase liquida che in fase gas (Capitolo 8). Si tratta di casi studio che presentano diverse problematiche, diversi apparati sperimentali e diversi comportamenti e quindi è stato necessario definire dei metodi per testare l'efficacia delle membrane multistrato, dal momento che non sono stati trovati in letteratura sistemi catalitici di questo tipo. In questo lavoro riportiamo i risultati preliminari ottenuti fino ad ora, nonostante siano necessari ulteriori approfondimenti per migliorare e completare lo studio.

Si è osservata l'azione catalitica delle particelle di TiO_2 e di MgO in fase liquida nei confronti di un simulante dell'iprite (CEPS) e i risultati ottenuti, se pur preliminari, dimostrano il buon potenziale di queste membrane. La percentuale di agente degradato non è molto elevata (max 11%) ed è funzione del contenuto in nanoparticelle.

Per quanto riguarda le membrane a base PMMAcoMMA-PANcoVAc- TiO_2 i test fotocatalitici in fase liquida con fenolo hanno mostrato migliori risultati se paragonati all'attività delle vernici a base TiO_2 presenti nel mercato. Tuttavia queste membrane sono state progettate per la degradazione fotocatalitica di composti organici volatili (VOCs), responsabili oltre che dei problemi ambientali, anche dell'inquinamento indoor. In tal senso infatti le membrane proposte possono svolgere una doppia funzione: da un lato l'azione filtrante ad opera del web di nanofibre (già riconosciuta in letteratura) e dall'altro l'azione chimica di degradazione ossidativa degli inquinanti. Tali aspetti le rendono infatti dei buoni candidati per l'applicazione nei settori di filtrazione civile e industriale (purificazione gas).

Trichloroethylene (TCE) and Acetone sono stati scelti come inquinanti di riferimento. Le analisi di degradazione condotte hanno permesso di verificare gli effetti di rigenerazione delle membrane e l'affinità del catalizzatore per i composti in esame. L'ossidazione del TCE procede attraverso un meccanismo complesso che vede la formazione di intermedi di reazione. Tuttavia si ottiene una conversione del 23% che aumenta con i cicli di rigenerazione a base di aria umida. La degradazione dell'acetone segue invece un meccanismo diretto di mineralizzazione a CO₂ ed H₂O e la conversione è circa del 14%. Lo studio dell'effetto della rigenerazione è stato condotto nonostante dalla letteratura sia ipotizzato un effetto negativo del vapor d'acqua che compete con l'acetone per i siti attivi del catalizzatore. Dai risultati preliminari qui esposti prevale l'effetto positivo del vapor d'acqua che migliora la reattività fornendo gruppi OH per l'inizializzazione radicalica. Infine nelle Conclusioni saranno riassunti i risultati ottenuti e le prospettive future di queste tecnologie.

Summary

Electrohydrodynamic technologies are part of this macro area of manufacturing technologies dealing with “nanoparticles” or “nanofibers”. The term “nano” (from Greek nan(n)os "dwarf, little old man") is in the SI system (Système International d'Unités,) a prefix denoting a billionth (10^{-9}) of the reference unit such as a nanometer is a 10^{-9} meter, a nanosecond is 10^{-9} second and a nanofarad correspond to 10^{-9} farad.

To get a sense of the nano scale, a human hair measures 50,000 nanometers across, a bacterial cell measures a few hundred nanometers across and the smallest things observable with the unaided human eye are 10,000 nanometers across.

An introduction to the ElectroHydroDynamic (EHD) processes and a literature review about the scientific research in this field will be discussed within Chapter 1. Both of the electrospraying and electrospinning techniques involve the use of high voltage to generate a liquid jet. As regards electrospray technique, a small droplet or particles are formed as a result of break up of electrified jet from the low viscosity solution. This process has been used to deposit ultra-thin films of inorganic, organic and biological materials, to generate nanoparticles and quantum dots, to sort them according to their sizes, and to help with dispersion and delivery of nanomaterials. Electrospray has found various commercial applications in the field of mass spectrometry, painting, and inkjet printing. By utilizing this technique, it could be achieved the vaporization of large biomolecules into gaseous phase without decomposition, which in conjunction with mass spectrometry (ESIMS) has been used in the laboratory all over the world to identify the large molar mass of proteins, synthetic polymers, etc. Besides, the electrospinning process has the ability to mass-produce continuous fibers with nanometer scale diameter of different materials. Likewise, we anticipate that combining electrospray with electrospinning technique and their understanding will solve the existing unsolved problems of application of electrospinning technique in large area of applications ranging from catalysis to defence applications. So far, no reports are available in the literature on the combination of electrospraying and electrospinning techniques and their applications.

The electrospinning technique can be accounted as a variant of electrospraying process. Differently to electrospraying, electrospinning process involves the stretching of the jet due to the electrostatic repulsion between the surface charges and the evaporation of the solvent and consequently long continuous fibers are obtained.

As it will be explained in Chapter 1, EHD processes are affected from different variables, controllable and uncontrollable and the nanoparticles or nanofibers characteristic size depends on them and on the potential interaction among factors. Because of this Response Surface

Methodology (RSM) has been chosen for developing, improving, and optimizing processes. An extensive review about the methodology will be presented in Chapter 2.

The field of response surface methodology consists of the experimental strategy for exploring the space of the process or independent variables, empirical statistical modeling to develop an appropriate approximating relationship between the yield and the process variables, and optimization methods for finding the values of the process variables that produce desirable values of the response.

As suggest in Section I, few parameters affect electrospinning process and consequently the nanofibers morphology. The purpose of this study is to obtain a maximum control over the variables and parameters that govern this process and to have a better understanding of the interaction among different structural configurations.

The early stage of the optimization process has exploited a set of screening experiments in order to evaluate the range of parameters, both solution and process parameters, within which fiber morphology is obtained. Moreover is it possible to define which parameters mainly affect the response, that is the mean fiber diameter, and then decide on the factors for the next response surface analysis. Two systems have been consecutively studied:

- Polimer/solvent system
- Polimer/solvent/salt system

and the results of screening experiments meaning will be discuss in the Chapter 4. Subsequently Response Surface analysis for both the systems has been carried out and the parameters effect and their interactions have been extensively studied.

For the Polymer/solvent system, Box-Behnken Design has been chosen within the family of efficient three-level designs for fitting second order response surfaces. The factors were A:[Voltage], B:[PMMAcoMAA], C: [flow rate] and D: [electrodes distance] moving on three levels. According to the screening experiment, which have been useful for determining the proper operating range of the single factors, the response surface analysis based on listed experiments has been performed considering a quadratic model for fitting the response. The result showed here comes from an iterative methodology which leads the identification of outliers and then their removal from the modelling.

From the final equation of surface modelling it has been observed that there is only one significant interaction between A:Voltage and B:[PMMAcoMAA]. The surface trend provides some information about the scaling relationship order of those factors with respect to the forces they act on and consequently to the response. As regards the polymer concentration, within the semidilute entangled regime, it is possible to identify a threshold value over which the viscoelastic forces

increase drastically and strongly overhang the other forces. At the low level of B, an increase of Voltage results on diameter reduction. Moving up to the second level of B, a new wide region may be detected, where voltage effect is not significant. This means that the power law dependences have such a different order, that factor B prevails on the response. If the dependence orders of the factors on the response are strongly different, is not possible to have interaction anymore. Moreover it has been pointed out that the distance doesn't affect significantly the response because within the operating range chosen, no response variability can be detected.

According to the response surface analysis performed on the previous system, it has been pointed out that the response, which is the mean fiber diameter, falls into the microscale range. In order to move to the nanoscale we decided to turn the solution properties, in particular surface tension and conductivity. Because of this the Polymer/solvent/salt system has been studied and the effect of 4 factors (A:[Voltage], B:[PMMAcoMAA], C: [LiCl], D:[flow rate]) and their interactions effect on the response (mean fiber diameter) have been evaluated.

According to the screening experiments, from a Box-Behnken design we moved to a D-optimal design for the study of the response as a function of process parameters. The Quadratic model results appropriate for representing this system. The significant model terms include the single factors and interaction AC, AD, BC, CD.

As suggest from the literature, an increase of applied voltage generally results in a reduction of the mean fiber diameter of electrospun nanofibers while the increase of flow rate has the opposite effect. For low applied voltage, an increase of flow rate (AD interaction) results on the smaller fiber diameter and this behaviour is inverted after the saddle point on the response surface. This can be explained if we consider that for every applied voltage there is a fixed dragging rate which moves the forming-fiber toward the collector. When the feed rate of polymer solution is higher, an excess of electrostatic charges will be cumulated in the solution at the tip of the needle resulting on whipping motion and jet splaying and consequently these instabilities enhance diameter reduction.

As regards [LiCl]-applied voltage interaction (AC) (other controllable variables being equal in the mean level), the contour plot in shows how an increase of voltage, at a fixed salt concentration, affects the mean diameter. If the salt concentration is below 0.2%by weight, as the applied voltage increase, the smaller fiber diameter is obtained (especially at low level of [LiCl]). Above 0.2%w the trend changes and the higher is [LiCl], the higher is the fibers diameter obtained by raising the applied voltage. This trend could be explained if we consider that out of a specific range, elastic forces arising from solution viscoelasticity or solvent evaporation may intervene under certain operating conditions to arrest the jet prematurely with larger diameter.

As suggested from the screening experiments, polymer concentration, strictly connected to the elastic forces arising from solution viscoelasticity, play a fundamental role in electrospinning process and it often hides the interactions among other factors. Polymer concentration seems to be independent from salt concentration (BC interaction) and then it represents the main factor affecting the nanofiber diameter.

Salt concentration mainly affects the conductivity of the polymer solution. Results about salt concentration- flow rate (CD) interaction it has been shown once again that salt concentration of 0.2%w represents a sort of limit beyond which no more effects can be detected on the response. If we work below this threshold value, an increase of flow rate probably induces the rapid growth of the whipping instability during electrospinning, which is responsible for massive stretching of the fluid jet and concurrent decrease in the jet diameter.

This case study needs process optimization in term of minimization of the response. Thresholds for the response are provided to get the desirability equation to work properly. The assignment of optimization parameters has been done in order to minimize every controllable variable, except the flow rate which is set to be maximized. The optimum solution has been chosen for obtaining a fiber diameter size ranging from 300nm to 370 nm and this parameters configuration will be used for moving to fabrication of novel nanostructured membranes (Chapter 7).

The aim of this part of the project is then to create multilayers nanomaterials combining electrospinning and electro spraying techniques in order to obtain a multifunctional membrane as a good candidate in a wide range of application such as for protective clothing, respirators as well as air purifiers.

The implemented method has the objective to deposit inorganic nanoparticles and optimize their distribution over polymeric nanofibers. The following technological objectives summarize the approach that has been assumed:

1. to study electro spraying of inorganic nanoparticles to have a better understanding of the process and suspension parameters effect on the nanoclusters distribution and uniformity.
2. to design a proper process equipment for coupling electrospinning and electro spraying sets up and to optimize them for controllable and reproducible processing.
3. to characterize the manufactured membranes in terms of morphology and filtration property (pressure drop).

Sonication time and suspension stability (achieved by dispersant agent addition) have been verified to affect the nanoparticles distribution over the collector. Moreover different parameters configurations have been tested and the optimized conditions for electro spraying have been found out thanks to a modification of the standard apparatus. After electro spraying optimization,

multilayers membranes based on electrospun nanofibers (Polysulfone (PSU), Poly methylmethacrylate-co-methacrylic acid (PMMA-co-MAA), Poly acrylonitrile-co-Vinylacetate (PAN-co-VAc)) and TiO₂ /MgO nanoparticles were produced and completely characterized in term of pressure drop, morphology (SEM), and qualitative-quantitative analysis of the components (EDAX. TGA). It has been noticed that the pressure drop across the multilayers membranes tends to decrease mainly as a function of the raised nanoparticles content. This behaviour can be explained since the nanoparticles pent up among the electrospun web layers are able to enhance those distances resulting in an effective decrease in pressure drop from 9% to 34% when compared to the control membrane (without nanoparticles) depending on the nanoparticles content.

Heterogeneous photocatalytic degradation of various kinds of organic pollutants using semiconductor powders as photocatalysts has been extensively studied since since the increasing environmental pollution create a pressing need for new advanced solutions. Since under room temperature and air pressure, the organic pollutants could be completely degraded into CO₂, H₂O and other mineral acids by the photocatalysis method, some scholars predicted that in the near future the photocatalysis method will become one of the most effective means in dealing with various kinds of industrial wastewater as well as air purification. The principle, extensively reviewed in Chapter 3, is based on the generation of photoholes by ultraviolet irradiation and the subsequent generation of OH radicals, caused by reactions with hydroxyl groups adsorbed to the hydrophilic titania surface. These OH radicals play a key role in the oxidation of organic compounds.

Within this outline, here we focus on photocatalytic performances of multistructured membranes based on electrospun fibers and electrosprayed nanoparticles carried out in liquid phase and in gas phase (Chapter 8). These case studies involved different problems, different experimental set up and different behaviours and they required the tweak of methods for testing the effectiveness of the multilayers membranes for this purpose, which has not been found yet in the literature. Preliminary results are reported here even if further investigation are necessary to complete this part of the work. As expected, the. TiO₂ nanoparticles as well as MgO nanoparticles act as a catalyst for chemical agent detoxification (mustard agent stimulant, CEPS) and this property make these multilayers membranes very attractive for this purpose. The percentage of detoxified stimulant is not very high (maximum 11% of the initial concentration) and is a function just of the nanoparticles amount. It means, as higher the nanoparticles concentration as higher will be the reactivity.

As regards the membranes based on PMMAcoMMA-PANcoVAc-TiO₂ the photocatalytic test in liquid phase with phenol, revealed that their degradation efficiency is much higher than the TiO₂ based paints which are commonly used. However the main application of these processed

membranes regards the photocatalytic degradation of volatile organic compounds (VOCs) which is gaining more and more interest, since the emission of these compounds contribute to environmental problems, such as tropospheric ozone formation, stratospheric ozone layer depletion and global warming. In fact the multistructured membrane would play a double function: a filtering action (admitted in literature reports) as well as a chemical action of pollutants removal and then they could be a good candidate for filtering civil (indoor pollution) and industrial application (gas stream purification). Trichloroethylene (TCE) and Acetone have been chosen as pollutants. It has been performed the degradation analysis exploring the membranes regenerating effect and the affinity of the catalyst to the chemicals. TCE oxidation proceeds throughout a complex mechanism with intermediate formation and the maximum conversion has been found to be about 23% and it increases with the regenerating cycles. As regards acetone, its degradation follows a simple mechanism of mineralization to CO_2 and H_2O and the oxidation is roughly 14%. The effect of regenerating cycles has been performed, even if the literature suggested a poisoning effect of the water vapour molecule by blocking the active sites. Experimental evidences showed that prevail the positive effect of water vapour which enhances reactivity by supplying OH groups for radical-initiated chemistry.

Conclusions will then summarize the results of this work and an outline about the future perspective of these technologies will be covered.

Introduction

Nanofiber filter media have enabled new levels of filtration and environmental clean up performances in a broad range of applications since they have proven to be a good candidate for promoting a significant increase in filter efficiency and more contaminate holding capacity. The multipurpose membranes we deal with, will exploit the filtering properties of electrospun nanofibers and the catalytic activity of inorganic nanoparticles on volatile organic compounds (VOCs) decomposition.

Electro-Dynamic processes have been rediscovered since nineties as a versatile and economic tool for manufacturing micro- and nanoscale architectures. These structures can be a good candidate in a wide range of applications such as membrane technologies, reinforced materials, textiles, catalysis, sensors and biomedical field as suggest from the literature. The main advantage of these techniques is the ability to process a vast array of inorganic, hybrid materials, and organic polymers in order to tailor the best and suitable result to the specific application you deal with. An other advantage that makes these techniques more and more promising is the ability to form various fibre assemblies. Both the electrospraying and electrospinning processes are driven by the application of a relatively high voltage applied to a fed solution with respect to a grounded substrate, a key difference being that the electrospinning jet can be essentially thought as a string of charged elements connected by a viscoelastic medium, where the chain entanglements are enough to stabilize the initial jet against break-up into droplets. Several forces play a role during electrospray, the coulombic, electric field, viscoelastic, surface tension, air drag and gravitational forces, respectively. In the conventional view, when the voltage overcomes a threshold value depending on the specific system, electrostatic charging of the fluid at the tip of a nozzle results in the formation of the well-know Taylor cone, from the apex of which a single fluid jet is ejected. The jet moves towards a ground plate acting as counter electrode and it is affected by different instabilities (Rayleigh instability, bending instability) due to electrical effects and surface charge density influence.

These techniques, for producing multistructured and multifunctional membranes, based on nanofibers and nanoparticles, represent a challenging task in the nanotechnology field applied to nanocatalysis since they could greatly improve the activity of the catalysts used in the degradation of polluting agents. Before going toward fabrication of multistructured membranes, it is necessary to optimize the process of fiber formation. At this regard Response Surface Methodology (RSM) represents a versatile tool for exploring the space of the process or independent variables, empirical statistical modeling to develop an appropriate approximating relationship between the yield and the process variables, and optimization methods for finding the values of the process variables that produce desirable values of the response.

Subsequently, the implemented method for multilayer membranes fabrication has the objective to deposit inorganic nanoparticles and optimize their distribution over polymeric nanofibers. The following technological objectives summarize the approach that has been assumed:

1. to study electrospaying of inorganic nanoparticles to have a better understanding of the process and suspension parameters effect on the nanoclusters distribution and uniformity.
2. to design a proper process equipment for coupling electrospinning and electrospaying sets up and to optimize them for controllable and reproducible processing.
3. to characterize the manufactured membranes in terms of morphology and filtration property (pressure drop).

The photocatalytic performances of the obtained membranes will be extensively studied both in liquid phase and in gas phase. These case studies involved different problems, different experimental set up and different behaviours and they required the tweak of methods for testing the effectiveness of the multilayers membranes for this purpose, which has not been found yet in the literature. In liquid phase, a mustard agent simulant and phenol degradation have been tested in batch reactor and in order to perform studies in gas phase a proper apparatus has been set up and the effect of regenerating cycles has been exploited for two different VOCs , that is Trichloroethylene (TCE) and acetone. The mechanisms of degradation will be shown and a comparison of the photocatalytic activity of TiO_2 will be presented.

CHAPTER 1 Electrohydrodynamic processes: fundamentals and application

An introduction to the ElectroHydroDynamic Atomization (EHD) processes and a literature review about the scientific research in this field will be discussed within this chapter. Both of the electrospraying and electrospinning techniques involve the use of high voltage to generate a liquid jet. As regards electrospray technique, a small droplet or particles are formed as a result of break up of electrified jet from the low viscosity solution [1]. This process has been used to deposit ultra-thin films of inorganic, organic and biological materials, to generate nanoparticles and quantum dots, to sort them according to their sizes, and to help with dispersion and delivery of nanomaterials. Electrospray has found various commercial applications in the field of mass spectrometry, painting, and inkjet printing. By utilizing this technique, it could be achieved the vaporization of large biomolecules into gaseous phase without decomposition, which in conjunction with mass spectrometry (ESIMS) has been used in the laboratory all over the world to identify the large molar mass of proteins, synthetic polymers, etc. Besides, the electrospinning process has the ability to mass-produce continuous fibers with nanometer scale diameter of different materials. Likewise, we anticipate that combining electrospray with electrospinning technique and their understanding will solve the existing unsolved problems of application of electrospinning technique in large area of applications ranging from catalysis to defence applications. So far, no reports are available in the literature on the combination of electrospraying and electrospinning techniques and their applications.

It is essential in the beginning to firstly define the macro-area where the electrohydrodynamic technologies take place. Since this manufacturing technology deals with “nanofibers” or “nanoparticles”, we begin by considering the meaning of this word. The term “nano” (from Greek nan(n)os "dwarf, little old man") is in the SI system (Systeme International d'Unites,) a prefix denoting a billionth (10^{-9}) of the reference unit such as a nanometer is a 10^{-9} meter, a nanosecond is 10^{-9} second and a nanofarad correspond to 10^{-9} farad.

To get a sense of the nano scale, a human hair measures 50,000 nanometers across, a bacterial cell measures a few hundred nanometers across and the smallest things observable with the unaided human eye are 10,000 nanometers across.

A Nanotechnology definition [2] refers to the field of science and engineering concerning materials, structures and devices wherein at least one dimension is 100 nm or less. This term has also been used more broadly to refer to techniques that design and build objects by the specification and

placement of individual atoms or molecules where at least one dimension is on a scale of nanometers.

Then when we talk about nanofibers, we deal with one dimensional nanostructures that have gained recently the interest in the research community due to their unique properties and potential applications in many areas.

The electrospinning technique can be accounted as a variant of electrospraying process. Differently to electrospraying, electrospinning process involves the stretching of the jet due to the electrostatic repulsion between the surface charges and the evaporation of the solvent and consequently long continuous fibers are obtained [3].

Even though several methods have been used for nanofibers processing, such as drawing [4], template synthesis [5,6], phase separation [7] and self-assembly [8], electrospinning provides the simplest and versatile way through which a huge variety of materials, as melt polymers and polymer solutions, can be manufactured.

The drawing is a discontinuous process similar to dry-spinning, which can make one-by-one very long single nanofibers. However it requires a material with a pronounced viscoelastic behavior to undergo strong deformation, while being cohesive enough to support the stresses developed during the pulling [4]. With template synthesis organic and metal microfibrils and microtubules with highly monodisperse dimensions, have been synthesized using the cylindrical pores of microporous membranes as geometric templates [6]. In phase separation [7] a nano-porous foam can be obtained and the mechanism implies polymer dissolution, gelation and then solvent extraction, freezing and drying. This process allows the direct fabrication of nanofiber matrix and the control of its mechanical properties, but only a few polymers can be processed.

Self- assembly [8] is a typical bottom down approach in which intermolecular forces bring the smaller units together and the shape of the macromolecular nanofiber depends on the shape of the single units.

A comparison of these processing methods [1] drives to underline that only electrospinning can be scaled up and the fibers dimension is controlled. Moreover, despite its effective cost, nanofibers can be produced continuously throughout electrospinning and then this technique seem to be the only one method that can be further developed for mass production of nanofibers from various polymers. The first following section of this chapter takes a look at theoretical constructs in electrospinning process exploring the origin of the method, the principles and the steps involved. The second section discusses the nanofibers structure and characterization as well as the parameters that can affect the process (polymer solution parameters, process parameters, ambient condition).

The third section elucidates the technology and equipment developed whereas the fourth section explores the potential applications of electrospun nanofibers. The fifth section completes the present work delving into electrospinning of different polymers which have been widely processed until now. Then a personal prospective on the oncoming work will be presented.

1.1 Electro spraying and electrospinning: history and basic principles

Looking at the grassroots of electrohydrodynamic atomization processes, it is necessary to come back to 1700s when Gray(1732) announced the discovery of electrical induction and the distinction between conductors and insulators and even in 1745 Bose [9], suggested the nature of those obscure experiments on “force of electricity” and he applied a high potential to a liquid at the end of a glass capillary tube, obtaining an aerosol spray. Afterwards, Larmor (1898) studied the excitation of dielectric liquid under the influence of an electric charge and Lord Rayleigh [10,11], dealt with the stability of an isolated charged liquid droplet of radius r_0 predicting that it becomes unstable and fission takes place when the charge Q is sufficiently high if compared to the stabilizing effect of the surface tension T . In particular Rayleigh's result was that when $Q^2 > 4\pi r_0^3 T(n+2)$ the drop becomes unstable for a displacement proportional to the Legendre function $P_n(\cos \theta)$, provided $n \geq 2$. When $Q^2 < (16\pi r_0^3 T)^{1/2}$ or the potential $V < (16\pi r_0 T)^{1/2}$, the drop is stable for all displacements, and when V first exceeds this value the drop becomes unstable only for the disturbance $P_2(\cos \theta)$ for which it becomes slightly ellipsoidal while the displacement is small [12].

Thanks to these studies, in the early 1900s the first apparatus for electrically dispersing fluids can be tracked, proposed by John F. Cooley [13] and William J. Morton (1902) [14] (Figure 1).

Subsequently, several researchers focus them studies on the distorsion and bursting of water drops. Zeleny in 1917 [15,16] studied the behaviour of low molecular weight liquids, such as ethanol and glycerol, observing the role of the surface instability in electrical discharges from charged droplets. Drops held at the end of capillary tubes and raised to a high potential were photographed. He measured the potential at which they disintegrated owing to the formation of a pointed end from which issued a narrow jet.

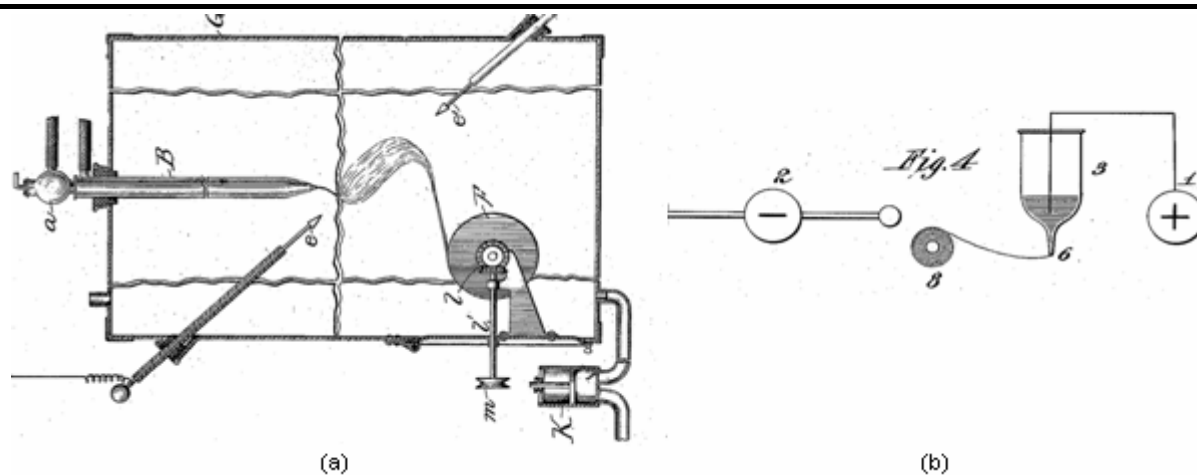


Figure 1 (a) Schematic apparatus patented by Cooley (1902) ; (b) Schematic apparatus by Morton (1902).

Wilson & Taylor [17,18] found that a similar phenomenon occurs when an uncharged soap bubble is subjected to a uniform electric field. Macky (1931) [19] and Nolan (1926) [20] showed that the same kind of disintegration occurs when a drop of water falls between parallel plates when a potential gradient is maintained between them. Zeleny [16] showed experimentally that the disintegration is due to hydrodynamical instability rather than the formation of ionic currents and he concluded, on dimensional grounds, that the criterion of instability must be of the form $V^2/r_0T = C$ where V is the potential, r_0 the radius of the drop, T surface tension and C a constant. His results were in fact well presented by taking $C = 140$ when V was expressed in electrostatic units. Nevertheless his ideas about the mechanics of the situation rest on the implicit assumption that instability occurs when the internal pressure is the same as that outside the drop [12]. Several years later Taylor shown that this assumption was false and that instability of an elongated drop would not occur unless a pressure difference existed. This author played a fundamental role because he provided guidelines in understanding fundamentals of electrospinning process.

From 1934 to 1940 Formhals [21] patented several set-ups to produce artificial threads; for instance his first patent reported the spinning of cellulose acetate solution with acetone but the technique adopted had some technical disadvantages such as the drying of the fibers which resulted in a less aggregated web structure. Then, in a subsequent work, these problems were overcome changing the distance nozzle-collector and a different set up was also proposed in order to obtain composite materials of different polymers with a multiple jet on a conveyor belt collector [22].

In 1952 Vonnegut and Neubauer [23] produced streams of highly electrified uniform droplets about 0.1 mm. in diameter applying potentials of 5–10 kV to liquids with low conductivity in small capillaries (diameter of a few tenths of millimeter). Then, thanks to this simple apparatus for electrical atomization a monodisperse aerosols having a particle radius of a micron or less has been obtained. In 1955 Drozin [24] investigated experimentally and theoretically the dispersibility of a

series of liquids at high electric potentials. It has been found out the dielectric constant affects the dispersibility of the liquid because the electrostatic pressure plays a predominant part in the process of dispersion and it is a function of dielectric constant as well as the radius of curvature of the liquid in the capillary.

Then, in 1966 Simons [25] referred a method and an apparatus for the production of patterned and textured non-woven fabrics wherein electrically-spun filaments are aggregated into bundles or clusters defining a controlled pattern of high filaments density contrasting with controlled areas of low-filament density. With his apparatus, a wide range of polymers can be processed such as cellulose esters and ethers, vinyl resins, polystyrene, polyurethanes and polycarbonate.

The influence on the process of the nature, magnitude, and placement of electric potential has been tested along with testing different values of viscosity, dielectric constant, conductivity and solvent volatility. For the first time it has been supposed that these parameters are interdependent.

In 1971 Baumgarten [26] produced fibers measuring less than 1 μ in diameter were spun by electrostatic means from dimethyl formamide (DMF) solutions of acrylic resin. High-speed photographs showed that a single fiber was drawn out from the electrically charged drop which was suspended from a metal capillary. Calculations indicated that spinning velocity probably reached and perhaps exceeded the velocity of sound in air. Electric field maps and other theoretical considerations showed that electric conductivity plays an important role in the spinning mechanism. The effects on fiber diameter and jet length of process, ambient and solution parameters were also evaluated. Results revealed a changed shape in the spinning drop as a function of the increase viscosity as well as a direct proportionality from the jet length and the fiber diameter was also noted. However, a detailed overview on the effect of those parameters on the process will be widely discuss in the next section.

In 1977 Martin et al. [27], developed an apparatus that provides a mat comprising a plurality of fibers of organic material. The mats were flexible, non-adsorbent, porous and hydrophobic. Moreover blends of polymer were electruspun using a multi-jet apparatus on metal screen collector or movable belt. The patent claimed the mat to be composed of fibers of high molecular weight thermoplastic polymer based either on a fluorinated hydrocarbon, silicone or an urea/formaldehyde. These were suggested to be used as a wound dressing as a lining for a prosthetic device.

In a detailed study in 1978 Simm et al. [28], produced a filter fleeces based on electrospun fibers that can be used as air filter. The filter action for minute dust particles is due to a considerable extent to the action of electric fields between the fibers because the residual electrostatic charge of the fibers interact with the charge or uncharge particles that consequently are retained by adhesive forces. Another important influence on filtering action is the fineness and density of the fibers. The

spinning liquids used are high polymers, such as polystyrene, cellulose esters or polycarbonate, in volatile organic solvents like methylene chloride, chloroform, carbon tetrachloride.

A couple of years later, in 1980, Fine and Tora [29], electrospun polyurethane in tetrahydrofuran that has been fed in a cup supplied of rotatory motion and cross motion. The combined actions of the centrifugal and electrostatic forces, together with the evaporation of the solvent, cause the formation of long fibers on the belt collector in front of the cup.

Instead of placing the polymer solution in a cup, Guignard (1980) [30], proposed an other apparatus, subsequently implemented in 1981. The basic setup was made up of two movable belts; one of them carried the charge molten polymer towards the grounded belt and in the meantime the formation of several jets from the surface of the exposed melt occurred; then the fibers were collected on the grounded belt.

Larrondo and Manley [31] first studied, in 1981, electrospinning from the melt obtaining continuous filaments of rapidly crystallizing polymers, such as polyethylene and polypropylene. The electrospun fibers were characterized by x-ray diffraction and mechanical testing.

The molten polymer was fed into a metallic capillary forming a hemispherical drop at the end of the orifice. An electrical field is applied between the capillary and a conducting plate held perpendicular to the axis of the orifice. Above a critical field intensity a fine continuous jet of molten polymer is drawn; rapid crystallization ensues and a continuous fiber is formed. For fibers spun in an uncontrolled thermal environment, corresponding to ambient air temperature, and at electric field intensities of 6 and 7 kV cm⁻¹, the properties are typically those of unoriented or slightly oriented polyolefin fibers, such as would be obtained in a conventional fiber spinning process.

The flow field in an electrically driven jet has been examined and quantitatively analyzed. Using a model fluid, the nature of the streamlines and magnitude of the stream velocities were investigated with the aid of tracer particle photography. It was found that the velocity field is not purely extensional, but contains rotational components as well. Furthermore, the only portion of the jet completely free of any rotational component is the region about the symmetry axis. The extensional strain rate along the symmetry axis increases rapidly with the applied electric field intensity and can attain values in excess of 50 sec⁻¹. This suggests that it might be possible to draw continuous oriented fibers from polymer melts by this technique if the jet can be operated at sufficiently high electric field intensity. It has been previously shown that fine jets can be drawn from polymer melts with the aid of an electric field. In an effort to understand the mechanism of jet formation, preliminary experiments have been carried out on the deformation of pendant drops of molten polymers (nylon 12 and polyethylene) subjected to an electric field. The drop deformation was

measured as a function of field intensity and frequency, and the results were interpreted in terms of a theory due to Torza et al.[32]. It is shown that there is qualitative agreement between the theory and experimental observations. This permits the identification of the parameters influencing the drop deformation and leads to a qualitative picture of the mechanism of deformation.

Bornat [33] in 1982 described the electrostatic spinning process as a new way for obtaining novel synthetic blood vessel useful in medical field. Solidified polymer filaments of fluorinated hydrocarbons, i.e. PTFE and also polyurethans, were electrospun on the rotating collector to form a tubular product. Moreover a few years later Bornat patented a slightly different apparatus provided with an auxiliary electrode causing a different fiber pattern so that higher proportions of the fibers are circumferential rather than longitudinal.

In 1985 How et al.[34], proposed an apparatus to make synthetic vascular grafts by an electrostatic spinning process of polyurethane. In this application the collector was a rotating mandrel and the syringe could translate at a constant linear speed along the length of the mandrel. In order to study the effect of process parameters on their mechanical properties, different conditions in term of mandrel rotation(1500 r.p.m-9000 r.p.m.), traverse speed (2 cm/s-40cm/s)and polymer solution concentration(12wt%-16.6wt%) were tested. It has been shown that the speed of the rotation mandrel affect the anisotropy of the manufactured grafts, such as at low rotation, the circumferential modulus is less than the longitudinal modulus suggesting that there is a preferential alignment of fibres in the longitudinal direction.

Moreover, the effect of an applied electric field on pendant and flowing drops (through a capillary) were studied in 1987 Hayati [35] by observing the droplet profile as a function of applied voltage. The effect of liquid conductivity, applied voltage, flow rate, and capillary diameter on the stability of jets was investigated by measuring the critical voltage, ϕ_c , at which transition from the pulsating mode to the stable jet mode occurred. By measuring the current carried by the jet, the charge-to-mass ratio could also be calculated. Some measurements of droplet size distribution were made using a practical sprayer and a particle measuring system for measuring droplet diameters in flight. These measurements were made as a function of applied voltage, conductivity, and flow rate. The results obtained clearly demonstrate the importance of applied voltage, liquid conductivity and flow rate in the formation of stable jets and the subsequent process of electrohydrodynamic atomization. At a given voltage and flow rate an optimum conductivity range is necessary for producing the most stable jet, the narrowest size distribution, and the smallest droplet size. This could be accounted for in terms of the electric forces acting on the liquid, which are related to the relaxation time of the liquid. The influence of flow rate on the production of stable jets and the subsequent atomization could also be understood in terms of the inertial and electrostatic forces which act in the same

direction. At a given conductivity and voltage, stability is enhanced by increasing the flow rate, but at the expense of producing larger droplets.

The same authors [35 b] also investigated the stability of the jet looking at a probable mechanism to explain it, by observing the motion of the liquid in a jet close to the capillary tip from which it emerges under the influence of an electric field. Streak photographs were taken of a stable jet and from their analysis it has been pointed out an axisymmetric circulation of the liquid in the conical base of the jet, in contrast with previous theories that proposed a uniform velocity profile in the liquid cone. In order to explain this behaviour of the liquid in the jet, interfacial electrical shear stresses were considered. Both tangential and normal fields on the cone were determined thanks to the knowledge of the jet profile and current, and the obtained results showed the normal force from five-fold to ten-fold greater than the shear force which was found to be inversely proportional to the increase of the applied voltage. This trend has been explained in terms of the reduction of tangential shear force with an increase in applied voltage, thus reducing jet stability [35 b].

After a brief gap of a decade or so, maybe because of the improved knowledge on the potential application of electrospun nanofibers in different areas, such as filtration, wound dressing, protective clothing, reinforcing in composite materials, nanocatalysis and nano-electronics, Reneker and his co-workers revived interest in this technology. In 1995 Doshi and Reneker [36] described the electrospinning conditions that affect this phenomena, fiber morphology and some possible use of electrospun fibers. They dealt with electrospinning of poly(ethylene oxide) (PEO) in aqueous solutions having concentration in the range of 1% to 7%(w/w) and they studied the morphology of the fibers as well as the electric potentials limits among which a stable jet is obtained. Moreover, the jet diameter was measured as a function of distance from the apex of the cone and it has been pointed out a decrease in diameter jet by about a factor of 5 at distance of 10 mm from the tip of the cone, indicating a large amount of stretching and orientation of polymer molecules in the jet.

Then, as it has been previously exposed, since 1980s and especially in recent years, the electrospinning process has gained interest from several research groups, maybe because of the major interest on the nanotechnology field. A survey of open publications related with electrospinning in the past 10 years is given in Figure 2, whereas those publication distributions all over the world are shown in Figure 3. These literature data were obtained based on IsiKnowledge search system. The data demonstrate a growing up trend since 2003, just looking at the high number of publications in 2006 which is 389.

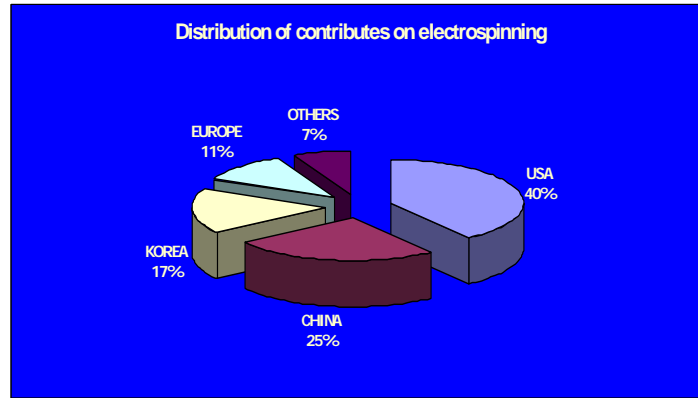


Figure 2 General trend of publications concernine electrospinning since 1995 to 2006.

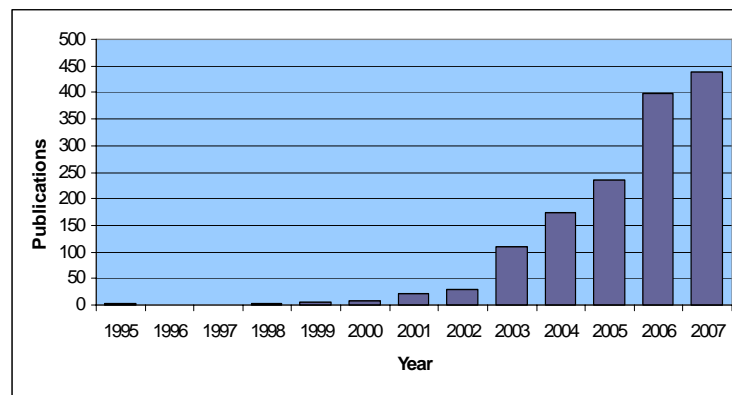


Figure 3 Publication distribution around the world based on IsiKnowledge search system.

1.2 Electro spraying of nanoparticles

There is growing interest in the creation and deposition of nanoparticles [37].

A review by Grace and Marijnissen [38] presented the electro spraying of many different liquids but also concluded that the method was poorly understood. Since then, however, there have been great advances in the understanding and application of the method.

More recently, the successful spraying of individual colloidal nanoparticles was reported by Lenggoro et al (39), Schulz et al (40) and Suh et al (41) using home-built electro spray units. In addition, carbon nanotubes [42], biomolecules [43] and proteins [44] have been successfully sprayed.

Moreover a great deal of research has been done in the last decade by different groups in an attempt to manufacture and characterise semiconductor quantum dots or nanoparticles with size-dependent physical properties intermediate between those of the bulk solid and molecules [45,50]. This size-dependent variation of physical properties can be explained by a quantum confinement effect. Confinement of electrons and holes within a sufficiently small potential well leads to the disappearance of the continuum of states used to describe a bulk solid. As a result, conduction and valence bands are replaced by two sets of discrete energy levels separated by an energy gap, which is approximately inversely proportional to the square of the particle size [51].

This size dependence of energy levels allows one to control properties of nanomaterial that can be applied, for example, to build novel light-emitting devices, electro-optical modulators and lasers [52,54].

Electro spraying is not the common way for nanoparticles deposition; however this kind of systems have the following advantages over conventional mechanical atomisers [55]:

1. Droplets can be smaller than those available from mechanical atomisers, and for fine capillaries, the droplets can be smaller than 1 μm .
2. The size distribution of the droplets is usually narrow, and a train of monodispersed droplets can be easily obtained through synchronised excitation with pulse voltage.
3. Charged droplets are subjected to auto-dispersion in the space, that results in absence of droplet coagulation.
4. The motion of charged droplets can be easily controlled (including deflection or focusing) by electric fields.
5. The deposition efficiency of the droplets on an object is manifold higher than for uncharged droplets.

6. The charge and size of the droplets can be controlled to some extent by adjusting the voltage and liquid flow rate. An apparatus for electro spraying is very simple and can be easily made in a portable version.

The main disadvantage of electro spray systems, limiting their application in industry, is their low throughput. Some industrial applications, for example electrostatic painting or coating, fuel atomisation, agriculture chemical spraying or electrostatic scrubbing require much larger amount of liquid than that available from a single nozzle. Several inventions have been proposed to overcome this shortcoming. The most important are mechanical atomisers (pneumatic, or rotary) with induction charging. However, such devices produce droplets of larger size and lower charge than those obtained by electro spraying. Multi-nozzle electro spray systems were, therefore, proposed. In such systems, the charged jets and sprays interact due to Coulomb repulsive forces that can disturb the electro spraying process.

In spite of great practical importance of charged sprays, the problem of jets and sprays interaction has not been considered in the literature, except in a couple of papers. Snarski and Dunn (1991) [56] investigated two interacting sprays of charged ethanol droplets generated by the electrohydrodynamic method. They discovered that the spray plume from each nozzle was wider than that from a single nozzle operating independently. An increase in the distance between the nozzles caused the axial velocity of the droplets to decrease, whereas the lateral velocity component and the Sauter mean diameter were not noticeably affected by the distance variations. Rulison and Flagan (1993) [57] used a linear array of capillaries to increase the flow rate of aerosol. The authors noticed that the voltage at which the Taylor cone is formed increased with decreasing distance between the capillaries. The current emitted from each cone was almost independent of the inter-capillary distances. Regele et al. (2002) [58] considered the effect of distance between four capillary nozzles on the cone-jet electro spray. Three capillaries were positioned at the vertices of an equilateral triangle, and the fourth one in the triangle centre. When the capillaries became close to each other, the voltage required for spraying in the cone-jet mode initially increased, reached its maximum for the distance between the capillaries of about three to four times of capillary diameter, and then started to drop again. Hubacz and Marijnissen (2003) [59] used also a linear array of four nozzles in two versions—one with two parallel bar extractor electrodes, and one without an extractor. The photographs indicated skewed shape of the plumes at the array periphery. To control the shape of these plumes, the authors placed two additional, non-spraying needles on both sides of the array.

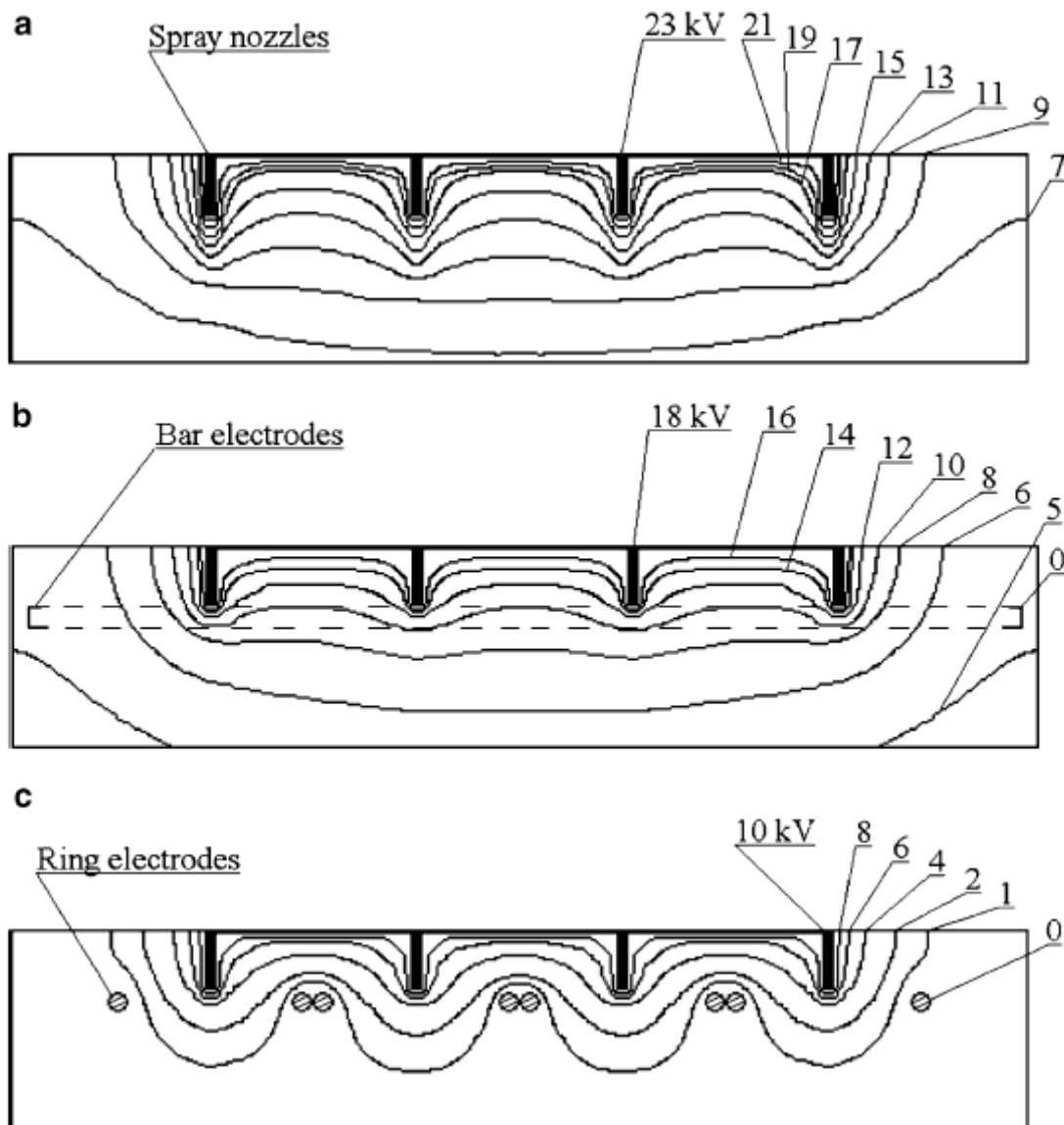


Figure 4 Electric potential distribution in the plane of capillary nozzles. a Nozzle-plate system; nozzle voltage 23 kV. b System with two bar induction electrodes; nozzle voltage 18 kV. c System with ring induction electrodes; nozzle voltage 10 kV

Looking at the electric potential distributions in the plane of capillary (Figure 4) for three different systems [55], that is spray nozzles located above a plate, spray nozzles with two bar induction electrodes (extractors) and spray nozzles with ring induction electrodes, it can be gathered that the spray plume is wider in the latter than in the other two systems, because the electric field between the induction electrodes and the plate diminishes at a short distance from the rings (cf. Fig. 4c), and the droplets are dispersed only due to their mutual repulsion. Additionally, close beneath the rings, the horizontal component of the electric field vector is higher than the vertical ones, and this component drives the droplets outside. Due to their high electric charge, the droplets are easily bent to other grounded elements located nearby, including induction electrodes, thus causing an aerosol loss. Wide plume indicates that the specific charge (q/m ratio) of the spray could be very high. The

system with ring induction electrodes operates at lower voltages than other two systems tested which is a result of short inter-electrode distance. Such system can be advantageous to electrostatic scrubbing applications.

1.3 Process of fiber production

As previously mentioned, electrospinning is a versatile approach that exploits electrostatic forces to produce fibers with diameters ranging in nanometers scale by forcing a molten polymer or a solution through a spinnerette under the influence of an electric field.

In order to understand the basic fundamental of this process it is necessary to remember that several forces play a role during electrospinning especially the coulombic, electric field, viscoelastic, surface tension, air drag and gravitational forces respectively. So, in the conventional view, when the voltage overcomes a threshold value depending on the specific system, electrostatic charging of the fluid at the tip of a nozzle results in the formation of the well-know Taylor cone, from the apex of which a single fluid jet is ejected [60]. The jet moves towards a ground plate acting as counter electrode. It is believed that excess charge is essentially static with respect to the moving coordinate system of the jet [61].

This means that the electrospinning jet can be essentially thought of as a string of charged elements connected by a viscoelastic medium, with one end fixed at a point of origin and the other end free.

The controlling parameters of the process are hydrostatic pressure in the capillary tube and external electric field. Viscosity, conductivity, dielectric permeability, surface tension, and temperature gradient affect the process as well. The parameters effect on the process, will be discuss in the next section.

As shown in Figure 5, a typical experimental setup for electrospinning consists of a syringe-pump apparatus where the polymer solution is fed. An electrode dipped in the polymer solution or in contact with the needle, is connected to a high voltage supply.

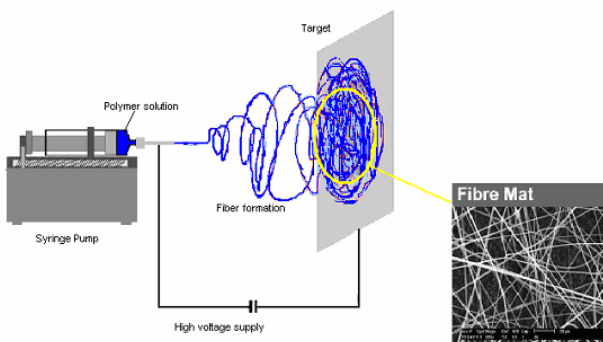


Figure 5 Experimental set up for electrospinning.

When the high voltage supply is turned on, the electrode induces free charges into the polymer solution. Consequently, these charged ions move in response to the applied electric field towards the electrode of opposite polarity, thereby transferring tensile forces to the polymer liquid [60].

Typical operating conditions results on internal diameter of the needle usually 0.7 – 1mm, flow rates of 0.002-0.2 ml/min, electric potential from 5 KV to 30 KV and distances tip-collector of 10 – 30 cm. The target or the collector screen can be at a ground potential or be kept at a polarity opposite respect to the polymer solution. Different types, shapes and sizes of target have been utilized (see next section).

But let's see in detail which mechanisms are involved in electrospinning process. Several authors have just studied them, developing theoretical model for predicting the behaviour of the jet and consequently the diameter of the electrospun fibers. Doshi and Reneker [36], proposed that as the jet accelerates and thins in the electric field, radial charge repulsion results in splitting of the primary jet into multiple filaments, in a process known as "splaying". Hence, in this view, the final fiber size is determined primarily by the number of secondary jets formed.

Usually the electrospinning process involves two stages. The first one, involve the acceleration and smooth stretching, by electrostatic forces, of the polymer jet issued from the nozzle. In the second stage, a "bending instability" occurs farther downstream when the jet gets sufficiently thin, and the fiber spirals violently. The enormously increased contour length produces a very large stretch ratio and a nanoscale diameter [62].

In order to explain and model the behaviour of the jet during electrospinning, fundamentals were proposed by Sir Taylor [12,63], in the mid of 1960s, who introduced the leaky dielectric model to characterize the disintegration of liquid drops in strong electric fields, looking at the conditions under which a conical point could exist in equilibrium. It has been found the elongation of the drop in the direction of the field, whereas for some fluids the drop actually shortened in the field direction. Moreover, detailed studies on the electrodynamic stability problems were performed by Melcher [64] and Saville [65].

Yarin and co-workers [66], beginning with Taylor's assumptions, showed the existence of an other critical shape of the liquid drop, different from the conical shape previously referred by Taylor [63]. An axisymmetric liquid body kept at a potential $\Phi_0 = \varphi_0 + \text{const.}$, placed at a distance a_0 from an equipotential plane (Figure 5), and supposed to be that of equilibrium, was considered in order to evaluate a general form for the distribution of the electric potential Φ at any point all around the liquid body:

$$\Phi = (T_s R)^{1/2} \Psi(\theta) + \text{const.} \quad \text{Eq. (1.1)}$$

Where $\Psi(\theta)$ is a dimensionless function, T_s is the surface tension coefficient, r, z cylindrical coordinates and R, θ the spherical coordinates. According to Taylor's model, a self-similar solution of Eq. (1.1) leads to find out the fluid body in Figure 6 is enveloped by a cone with a half angle at the tip equal to $\alpha=49.3^\circ$. Self-similarity is guaranteed since $\Omega \rightarrow \infty$ as $R \rightarrow \infty$.

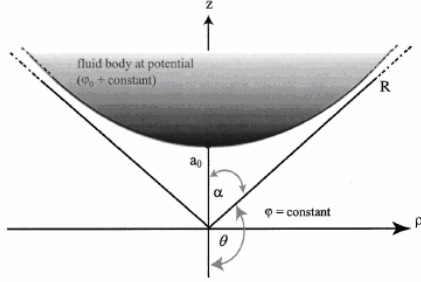


Figure 6 Axisymmetric “infinite” fluid body kept at potential $\Phi_0 = \varphi_0 + \text{const.}$ at a distance a_0 from an equipotential plane kept at $\Phi = \text{const.}$

However, it has been demonstrated by the same authors [66], there exist nonself-similar solutions which do not tend toward a Taylor cone. Supposed the droplet shape as a hyperboloid of revolution, and the space charge effects negligible, the electric potential (using prolate spheroidal coordinates η, ξ , Figure 7) between the free surface of a hyperboloidal liquid body and the equipotential surface $z=0$ yields:

$$\Phi = \varphi_0 \frac{\ln\left[\frac{1+\xi}{1-\xi}\right]}{\ln\left[\frac{1+\xi_0}{1-\xi_0}\right]} + \text{const.} \quad \text{Eq.(1.2)}$$

where φ_0 was assumed in the case of an “infinite” hyperboloid with its tip at a distance a_0 from an equipotential surface $z=0$, (T_{surf} , surface tension coefficient) to have the form:

$$\varphi_0 = (T_s a_0)^{1/2} (4\pi)^{1/2} \ln\left(\frac{1+\xi_0}{1-\xi_0}\right) (1-\xi_0^2)^{1/2} \quad \text{Eq.(1.3)}$$

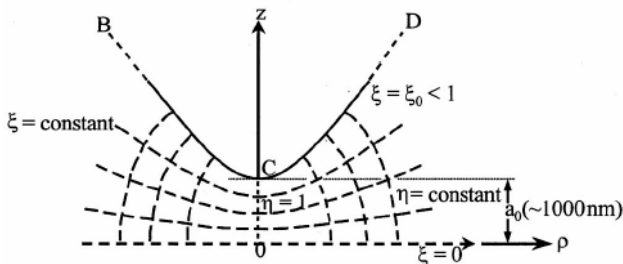


Figure 7 Prolate spheroidal coordinate system about a hyperboloidal liquid body BCD.

Since the asymptotic value ($R \rightarrow \infty$) of Φ is finite, it means that it is a nonself-similar solution and the maximal potential at which a stationary shape can exist corresponds to the critical hyperboloid $\xi_0^* = 0.834$ which is related to the hyperboloid equation as follows:

$$\frac{a_0}{b_0} = \frac{\xi_0^*}{(1-\xi_0^{*2})^{1/2}} = 1.51 \quad \text{Eq.(1.4)}$$

Therefore the half angle at the tip of the cone is given by (Figure 5):

$$\alpha_* = \frac{\pi}{2} - \arctan(1.51) \quad \text{Eq. (1.5)}$$

It means $\alpha_*=33.5^\circ$ which is significantly smaller than the angle for the Taylor cone $\alpha_T=49.3^\circ$. Experimental comparison with the critical angle α_* has been shown resolving that the critical half angle does not depend on fluid properties for Newtonian fluids, since an increase in surface tension is always accompanied by an increase in the critical electric field. However, the sharpness of the critical hyperboloid depends on elastic forces and surface tension in elastic fluids or in unrelaxed viscoelastic fluids.

For the steady stretching in stage one, Spivak and Dzenis [67], published a simple electrohydrodynamic model of a weakly conductive viscous jet accelerated by an external electric field supposed uniform and constant and unaffected by the charges carried by the jet.

It has been assumed that the jet flow is an extensional axisymmetric flow in the direction of the external electric field and the electrical current, due to electronic or ionic conductivity of the fluid, is small if compared to the current provided by the convective charge transfer with moving jet particles. However, the conductivity is sufficient for the electric charges to migrate the short distance to the jet surface. The bulk electric charge has been considered zero, in the asymptotic limit. The pulling force responsible for jet acceleration results from the interaction between the surface charge and the external electric field. The balance equations averaged over the jet cross section and assuming all quantities depending only on the axial position z result:

Equation of mass balance

$$\pi R^2 v = Q \quad \text{Eq.(1.6)}$$

where Q is the constant volumetric flow rate, R is the jet radius, v is average jet velocity in the cross section;

Linear momentum balance equation (averaged over the jet cross-section)

$$\frac{d}{dz} \left[\frac{\rho}{2} \pi R^2 v^2 + \pi R^2 p - \mu \pi R^2 \left(\frac{dv}{dz} \right)^{m-i} \frac{dv}{dz} \right] = 2\pi R \sigma E_0 \quad \text{Eq.(1.7)}$$

where ρ is fluid density, σ is the surface charge density, E_0 is the electric field, p is hydrostatic pressure determined by the surface tension and transverse electric repulsion; p is approximated for a slender jet by $p = \frac{T_s}{R} - \frac{\sigma^2}{2\epsilon_0}$ where T_s is the surface tension coefficient, and ϵ_0 is the dielectric permeability of vacuum.

However Spivak and Dzenis momentum equation, has been developed missing several terms: the viscous normal stress; the surface tension term in the z equation; and the normal electrostatic traction in both axial and radial balances. Those terms are not, in general, smaller than the terms retained and they were explained by Hohman et al. [68], and Feng [62].

Electric charge balance yields

$$\pi R^2 KE + 2\pi Rv\sigma = I \quad \text{Eq.(1.8)}$$

where K is the electrical conductivity of the fluid, I is the constant total electric current.

A general nonlinear rheologic constitutive equation (Oswald-deWaele's law) is used to describe polymer fluid.

$$\hat{\tau}^c = \mu (II_{\dot{\gamma}})^{\frac{m-1}{2}} \dot{\gamma} \cdot \mathbf{i} \quad \text{Eq.(1.9)}$$

Where μ is the apparent viscosity, $II_{\dot{\gamma}}$ is the second invariant of the rate of strain tensor $\dot{\gamma}$, m is the flow index, p is hydrostatic pressure and i is the unit tensor.

Then, a differential equation for jet radius was derived [67] and analyzed as follows:

$$\frac{d}{d\tilde{z}} \left\{ \tilde{R}^{-4} + (We\tilde{R})^{-1} - Y\tilde{R}^2 - Re^{-1} \left(\frac{1}{2} \frac{d\tilde{R}^{-2}}{d\tilde{z}} \right)^m \right\} = 1 \quad \text{Eq.(1.10)}$$

where \tilde{R} is the dimensionless jet radius, \tilde{z} is the dimensionless axial coordinate, We, Y and Re are, respectively, the Weber number, Euler number, and the effective Reynolds number. The Bernoulli integral obtained from Eq. (1.10) is

$$\tilde{R}^{-4} + We\tilde{R}^{-1} - YR^2 - Re^{-1} \left(\frac{1}{2} \frac{d\tilde{R}^{-2}}{d\tilde{z}} \right)^m = \tilde{z} + C \quad \text{Eq.(1.11)}$$

where the integration constant C is determined by the boundary conditions. A power-law asymptote $\tilde{R} \approx \tilde{z}^{-\alpha}$ (the exponent α is a positive constant) for the jet radius was replaced in Eq. (1.7) obtaining:

$$\tilde{z}^{4\alpha} + We\tilde{z}^{\alpha} - Y\tilde{z}^{-2\alpha} - \frac{\alpha^m}{Re} \tilde{z}^{(2\alpha-1)m} - \tilde{z} = O(1) \quad \text{Eq.(1.12)}$$

The power balance at $\tilde{z} \rightarrow +\infty$ yields

$$4\alpha = \max[1, (2\alpha - 1)m] \quad \text{Eq.(1.13)}$$

The solutions of the latter equation, which represent two asymptotic regimes of the jet motions, depend on the fluid behavior: for pseudoplastic and dilatant fluid with the flow index m in the range from zero to two, $\alpha = 1/4$. For dilatant fluids with the flow index greater than 2, the solution is

$$\alpha = \frac{1}{2} m / (m - 2).$$

In order to compare the results with experimental data, electrospinning of the 4wt% aqueous solution of poly(ethylene oxide) (PEO) was performed. The jet was illuminated with a laser and the

variation of the jet radius with coordinate was measured over the distance of approximately 15 cm, using magnified optical images. It has been found a good agreement between model predictions and experimental observation.

Moreover, since for a polymer with high molten temperature thermal effects must be considered, Wan-Guo-Pan [69] developed a rigorous thermo-electro-hydrodynamics model that takes into account the thermal effect and the air drag.

Other authors dealt with the steady stretching process because it is important in that it not only contributes to the thinning directly, but also sets up the conditions for the onset of the bending instability. Hohman et al. [68,70], developed a slender-body theory for electrospinning that couples jet stretching, charge transport, and the electric field. The governing hydrodynamic equations of the model (obtained working on conservation of mass, conservation of charge and differential momentum balance) were made non-dimensional by choosing a length scale r_0 , where r_0 was the diameter of the capillary; a time scale t_0

$t_0 = \sqrt{\frac{\rho r_0^3}{T_{surf}}}$, where T_{surf} was the surface tension and ρ was the density of the fluid; an electric field strength, $E_0 = \sqrt{T_{surf} / (\epsilon - \bar{\epsilon}) r_0}$

where $\epsilon(\bar{\epsilon})$ was the permittivity of the fluid (air); and a surface charge density $\sqrt{T_{surf} \bar{\epsilon} / r_0}$.

Moreover four dimensionless parameters were used for material properties characterization such as $\beta = \epsilon / \bar{\epsilon} - 1$, the dimensionless viscosity μ^* [68], the dimensionless gravity g^* and the dimensionless conductivity K^* .

The dimensionless balance equations were considered as follows [70]:

Mass balance

$$\partial_z (h^2) + (h^2 v)' = 0 \quad \text{Eq.(1.14)}$$

Charge balance

$$\partial_z (\sigma h) + \left(\sigma h v + \frac{K^*}{2} h^2 E \right)' = 0 \quad \text{Eq.(1.15)}$$

Navier-Stokes equation

$$\partial_z v + v v' = - \left(\frac{1}{h} - h'' - \frac{E^2}{8\pi} - 2\pi \sigma^2 \right) + \frac{2\sigma E}{h\sqrt{\beta}} + g^* + \frac{3v^{*2}}{h^2} (h^2 v)' \quad \text{Eq.(1.16)}$$

where $h(z)$ was the radius of the jet at axial coordinate z ; $v(z)$ was the axial velocity of the jet and was assumed to be constant across the jet cross-section; $\sigma(z)$ was the surface charge density and $E(z)$ was the electric field in the axial direction. The prime (') denotes differentiation with respect to z .

The dimensionless tangential field inside the jet was derived according to the Coulomb's law in the form:

$$E = E_\infty + \int ds \frac{\lambda(s)}{|x-r(s)|} \approx E_\infty + \ln \frac{r}{L} \left(\frac{\beta}{2} (h^2 E) - \frac{4\pi}{\varepsilon} h \sigma \right) \quad \text{Eq.(1.17)}$$

where $\lambda(s)$ was the linear charge density along the jet, parameterized by the arclength s that varied over a length scale L much larger than the jet radius.

In order to work on the linear stability analysis the authors [68], axisymmetric perturbations (see Figure 8) of the form $h^* / h = 1 + h_\varepsilon e^{\omega t + ikz}$ were applied to the radius, velocity and surface charge density where $h\varepsilon$ was assumed to be small. Moreover, a local electric field strength was also introduced within the governing hydrodynamic equation obtaining the following dispersion relation for axisymmetric instabilities:

$$\begin{aligned} & \omega^3 + \omega^2 \left[\frac{4\pi K^* \Lambda}{\delta \sqrt{\beta}} + 3v^* k^2 \right] + \omega \left[\frac{3v^* k^2}{\delta \sqrt{\beta}} 4\pi K^* \Lambda + \frac{k^2}{2} (k^2 - 1) + 2\pi \sigma_0^2 k^2 \left(\frac{8l}{\delta} - 1 \right) + \frac{\Lambda}{\delta} \frac{\Omega_0^2}{4\pi} k^2 \right] \\ & + \frac{4\pi K^* \Lambda}{\delta \sqrt{\beta}} \left[\frac{k^2}{2} (k^2 - 1) + 2\pi \sigma_0^2 k^2 + \frac{\delta}{\Lambda} \frac{\Omega_0^2}{4\pi} k^2 + E_0 \sigma_0 \frac{ik}{\sqrt{\beta}} \left(\frac{1}{l} - 4 \right) \right] = 0 \end{aligned} \quad \text{Eq.(1.18)}$$

where σ_0 was the dimensionless unperturbed charge density and $1/\chi$ was the local aspect ratio of the jet assumed small according to the long wavelength instabilities. Eq. (1.18) worked for arbitrary values of conductivity, dielectric constant, viscosity and field strength, as long as the tangential electrical stress was smaller than the radial viscous stress.

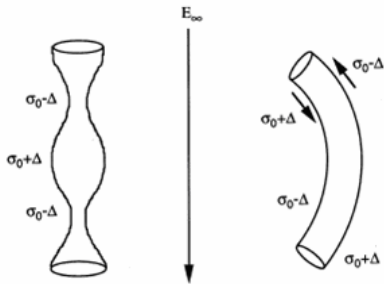


Figure 8(a) Axisymmetric and (b) non-axisymmetric instabilities in a fluid jet in an external electric field (E_∞). Δ denotes perturbations of the surface charge density (σ). The arrows in (b) indicate the local torque that bends the jet.

In a second part of their work, Hohman and co-workers extended the model to non-axisymmetric disturbances that results in a more complicate form of the balance equations shown previously (Eq (1.14), Eq. (1.15), Eq.(1.16)). This is due to the charge density that cannot be considered no longer uniform around the circumference of the jet in the presence of a dipolar component, $P(z)$, orientated perpendicular to the jet axis. These dipoles involve in a localized torque that bends the jet and consequently oscillations of the bending instability account for the whipping motion of the jet

[68,70] (see Figure 7). In this case the centreline of the jet is described in non-dimensional coordinates by $\underline{r}(z, y) = z\hat{z} + \varepsilon e^{\omega t + ikz} \hat{x}$ where \hat{x} and \hat{z} are unit vectors in a Cartesian coordinate system. The final form of the dispersion relation for the non-axisymmetric disturbances yields.

$$\omega^2 + \frac{3}{4}v^* \omega k^4 + 4\pi\sigma_0^2 k^2 \ln(k) + ik \frac{2\sigma_0 \Omega_0}{\sqrt{\beta}} + \frac{ik\Omega_0}{\sqrt{\beta}} (\sigma_0 k^2 + C) + k^2 - \left[\Omega_0 \left(-\frac{1}{4\pi} + \frac{(\beta+1)k^2}{16\pi\beta} \right) + \frac{ik\sigma_0}{\beta} \right] \times \frac{\sqrt{\beta}}{\beta+2} \left[k^2 \Omega_0 \sqrt{\beta} + ik(4\pi C + 2\pi\beta\sigma_0 k^2) \right] = 0$$

$$\text{with } C = \frac{ik \frac{2K^* E_0}{\beta+2} + \frac{4\pi K^* \sqrt{\beta}}{\beta+2} \sigma_0 k^2}{\frac{4\pi K^* \sqrt{\beta}}{\beta+2} + \omega} \quad \text{Eq.(1.19)}$$

The model encounters difficulties, however, with the boundary condition at the nozzle. Steady solutions may be obtained only if the surface charge density at the nozzle is set to zero or a very low value [62]. Even after this drastic assumption, no steady solution was possible for fluids with higher conductivities. This is probably due to the underestimation of the axial field, that ignores the effects of the charges carried by the polymer and the spinneret upstream of the nozzle and consequently the radial repulsion of the charges rise to the ballooning instability.

Therefore, Feng revisited the problem with the Newtonian model of Hohman et al. and proposed a simplified model [62] that unexpectedly does not suffers from the unrealistic ballooning instability. This has been explained noting that the potential equation shown by Feng, is a pragmatic approach that avoids the need to account for the effects of upstream charges or details of the device.

$$\phi(z) \approx \phi_\infty(z) + \ln \chi \left(\frac{1}{\varepsilon} \sigma R - \frac{\beta}{2} \frac{d(ER^2)}{dz} \right) \quad \text{Eq.(1.20)}$$

shown by Feng is a pragmatic approach that avoids the need to account for the effects of upstream charges or details of the device. Eq. (20) represents an asymptotic estimation of the potential along the centerline of the jet, due to the total surface charge $\sigma + \sigma_{ind}$. ϕ_∞ is the potential due to the external field in the absence of the jet, $\beta = \varepsilon / \bar{\varepsilon} - 1$ where ε and $\bar{\varepsilon}$ are the dielectric constants of the jet and the ambient air respectively; σ is the surface charge density, χ is the aspect ratio $\chi = L/R_0$, R_0 being the characteristic radius of the jet.

Moreover, after a further investigation on the effects of the dimensionless parameters on Newtonian solutions, Feng extended his theoretical model introducing non-Newtonian rheology and the effects of extension thinning, extension thickening, and strain hardening has been examined. He depicted these three different behaviours:

- a) extension-thinning causes enhanced stretching for mildly stretched jet and has the opposite effect for severely stretched jets behave differently.
- b) extension thickening results in stretching hampered by the higher viscosity for both mildly and severely stretched jets.
- c) strain hardening affects the viscosity and enhances stretching upstream and damps it downstream. As a consequence, thicker fibers result even if this effect is not so remarkable.

However this model is going to be improved in order to overcome some limitations, such as the toughness of treating the physics near the nozzle directly as well as the need to integrate the problem with viscoelastic constitutive equations.

Still regarding the first stage of electrospinning, He and co-workers [71], proposed a rational theory, which can predict simply the length of the straight jet in the initial stage of electrospinning, in which electrical force is dominant over other forces acting on the jet. The application of the Chauchy's inequality to the force balance (thanks to suitable assumptions) results on the critical straight length (L , see Figure 9) from the capillary orifice to the point where instability occurs:

$$L = z_{cr} = \frac{1}{\beta} \left[\left(\frac{\pi k \rho E}{2 \sigma Q} \right)^{2/3} - r_0^{-2} \right] = \frac{4kQ^3}{\pi \rho^2 I^2} \left[\left(\frac{\pi k \rho E}{2 \sigma Q} \right)^{2/3} - r_0^{-2} \right] = \frac{4kQ^3}{\pi \rho^2 I^2} (R_0^{-2} - r_0^{-2}) \quad \text{Eq.(1.21)}$$

where $R_0 = (2\sigma Q / \pi k \rho E)^{1/3}$, k is the dimensionless conductivity of the fluid, σ the surface charge, E the applied electric field, I the current passing through the jet, Q the flow rate, r the radius of the jet, ρ is the liquid density and β is defined as minimal radius number $\beta = \pi \rho^2 I^2 / 4kQ^3$.

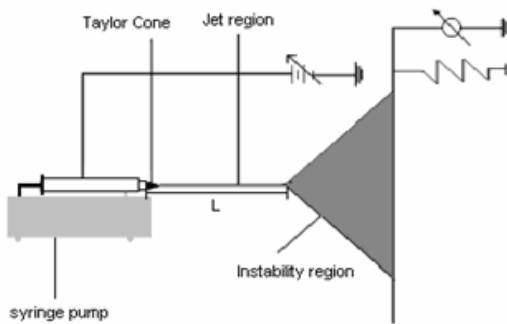


Figure 9 Electrospinning set up.

For stage two, the jet instability has been carefully documented by two groups (Reneker et al. [61]; Shin et al. [60]). Thanks to the slender body theory proposed by Hohman et al. [68], the growth rates for two types of instability modes has been predicted evaluating the behaviour of the radius and centreline of the jet. It is called varicose instability when the centreline of the jet remains

straight but the radius of the jet is modulated and whipping instability, or *bending instability* when the radius of the jet is constant but the centerline is modulated. Three unstable modes were described that is the *Rayleigh mode*, which refers to an axisymmetric extension of the classical Rayleigh instability when electrical effects are important; and two conducting modes named *axisymmetric conducting mode*; and *whipping conducting mode* which are enhanced by increasing the surface charge density. Fluid parameters of the jet (viscosity, dielectric constant, conductivity) as well as the static charge density, strongly affect the dominant instability. In order to have a better understanding, it has been reported as example of a high conductivity fluid, in which the varicose mode dominates the whipping mode due to the lack in static charge density on the jet. But when a large static charge density appears, the axisymmetric Rayleigh mode is suppressed and the whipping mode tends to dominate [68].

Reneker et al.[61], explained the observed bending instability modelling the electrospun jet as a system of connected viscoelastic dumbbells (see Maxwell model that describes rheological behaviour of polymeric systems [72]). The beads, ‘A’ and ‘B’(Figure 10 (a))interacted with each other according to Coulomb’s law and they are subjected to the electrical forces from the electrical field created between the pendant droplet and the target by the imposed potential difference; the stress, σ , pulling B back to A has been expressed in the form:

$$\frac{d\sigma}{dt} = G \frac{dl}{dt} - G \frac{\sigma}{\mu} \quad \text{Eq.(1.22)}$$

where l is the filament length, t is the time, G is the elastic modulus and μ is the Newtonian viscosity. The momentum balance on B yields:

$$m \frac{dv}{dt} = -\frac{e^2}{l^2} - \frac{eV_o}{h} + \pi a^2 \sigma \quad \text{Eq.(1.23)}$$

where m and e are the mass and charge on the bead respectively, a is the cross-sectional radius of the filament and v was the velocity of the bead B that satisfied the relation $\frac{dl}{dt} = -v$.

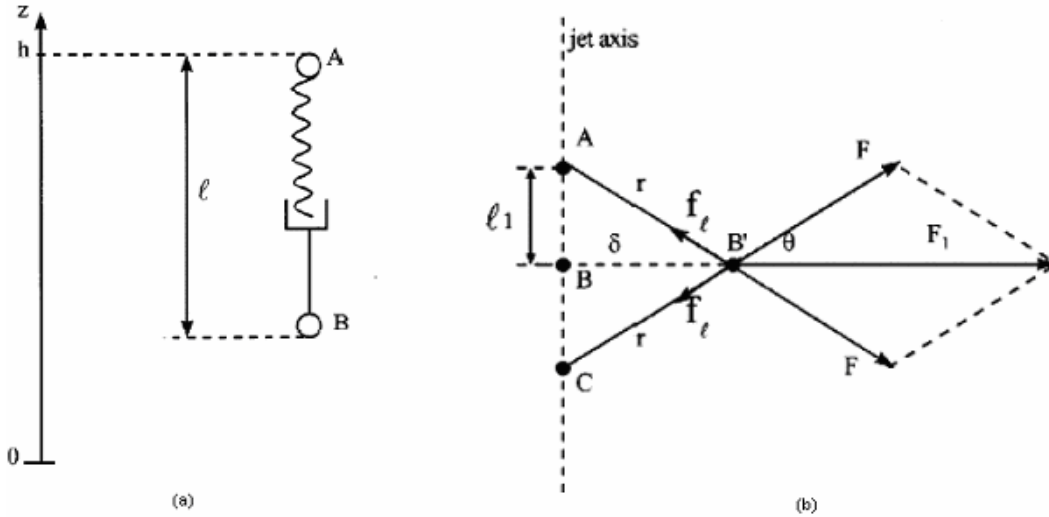


Figure 10(a) Viscoelastic dumbbell representing a rectilinear liquid jet; (b) Earnshaw instability, leading to bending instability of the jet.

Others forces such as surface tension, electrostatic forces, air friction and gravity must be considered even though the compressive stress along the jet axis of the air drag was found to be negligibly small in comparison with the stretching due to gravity and electrical forces.

Reneker and co-worker suggested that the electrical charges can be studied as a static system of charges interacting mainly by Coulomb's law; such systems are unstable according to the general Earnshaw theorem. As a result there will always be a lateral force component that will cause the jet to deviate from its original initiated path into a looping spiraling trajectory. In order to explain the Earnshaw instability, three point-like charges, originally in a straight line, has been considered by Reneker and coworkers [61]. As shown in Figure 10, the charges at A, B and C carried the same charge e and two Coulomb forces having magnitudes $F = e^2/r^2$ are imposed on charge B from opposite directions. Moreover if a perturbation caused the point B to move off the line by a distance δ to B', a net force

$$F_1 = 2F \cos \theta (= 2e^2 / r^3) \delta \quad \text{Eq.(1.24)}$$

results on the charge B in a direction perpendicular to the line, and consequently B moves towards the direction of the perturbation away from the fixed charges, A and C. The growth of the small bending perturbation characterized by δ is well described in the linear approximation expressed by the equation

$$m \frac{d^2 \delta}{dt^2} = \frac{2e^2}{l_1^3} \delta \quad \text{Eq.(1.25)}$$

where m is the mass and l_1 is the distance A-B, as shown in Figure 10. The solution of this equation showed that small perturbations increased exponentially and this is sustained because the electrostatic potential energy of the system decreased as e^2/r when the perturbations grew. It has

been assumed that this mechanism well explains the observed bending instability of jets in electrospinning.

Therefore, in order to describe adequately three-dimensional equations of the dynamics of the electrospun jets, the model proposed above has been generalized as follows: the electrospun jet is modeled as a series of charged beads connected by viscoelastic elements and according Newton's second law, the equation governing the radius vector of the position of the i^{th} bead $\mathbf{r}_i = ix_i + jy_i + kz_i$ assumes the form

$$m \frac{d^2 \mathbf{r}_i}{dt^2} = \sum_{j=1, N; j \neq i} \frac{e^2}{R_{ij}^3} (\mathbf{r}_i - \mathbf{r}_j) - e \frac{V_o}{h} \mathbf{k} + \frac{\pi a_{ui}^2 \sigma_{ui}}{l_{ui}} (\mathbf{r}_{i+1} - \mathbf{r}_i) - \frac{\pi a_{di}^2 \sigma_{di}}{l_{di}} (\mathbf{r}_i - \mathbf{r}_{i-1}) - \frac{\alpha \pi (a^2)_{av} k_i}{(x_i^2 + y_i^2)^{1/2}} \text{ Eq.(1.26)}$$

$$\times [\mathbf{i}|x_i|sign(x_i) + \mathbf{j}|y_i|sign(y_i)]$$

where the first term on the right side of the equation is the contribute of the Coulomb force, the second one is the electric force imposed, the third one is the viscoelastic force and the last one is the surface tension [61].

Both spatial and temporal perturbations of an established jet have been modeled [61] in order to have a complete description of the phenomena. The equations proposed has been solved numerically for jet path and trajectory and the results were compared to the experiments performed on a 6wt% PEO solution in 60/40 water/ethanol electrospun at a field strength of 1kV/cm. The predicted motion of the jet was in good agreement with the experimental data until about 2-3 ms after jet initiation. After 3 ms, the predicted motion deviated from the experimentally observed results. As concerns the jet velocity, theoretical value was bigger (1-2 m/s) if compared with the experimental one (0.8-1.1 m/s) in the first 8 ms after jet initiation. The predicted maximum lateral excursion and the lateral velocity of the jet were at least two orders of magnitude higher than the experimental data. Also Warner et al. [73], performed measurements of the average jet velocity and it has been pointed out the value 15 m/s for electrospun PEO aqueous solution (2 wt%). Some considerations were carried out about the area reduction ratio (defined as the ratio of the cross sectional area of the upper end of a segment to the cross-sectional area at the lower end of the same segment) in the loops of the bending instability; it has been found out that the total draw ratio is very high (about 60.000) and the associated strain rate (calculated at different places of the jet) has an high value as well.

However, this work was done neglecting evaporation and solidification effects; then Yarin [74], accounted for them in a subsequent study considering that the equation describing variation of the jet volume:

$$\frac{\partial f \lambda}{\partial t} = -D_a \cdot 0.495 \cdot \text{Re}^{1/3} \cdot \text{Sc}^{1/2} [c_{s,eq}(T) - c_{s\infty}] \pi \lambda \quad \text{Eq.(1.27)}$$

where $f = \pi a^2$ is the cross-sectional area, λ is the geometrical stretching ratio, $c_{s,eq}(T)$ is the saturation vapor concentration of solvent at temperature T , $c_{s\infty}$ is the vapor concentration in atmosphere far from the jet, D_a is the vapor diffusion coefficient in air, Re and Sc , are Reynolds and Schmidt number respectively.

As concerns the solidification process due to solvent evaporation, it has been accounted by employing the following correlation for the viscosity, μ , dependent on polymer concentration:

$$\mu = 10^A \times 10^{Bc_p^m} \quad \text{Eq.(1.28)}$$

($m=0.1-1$, the order of magnitude estimate of B is $B=O(10)$, the value of A is unimportant, since the initial value of the viscosity is assumed to be known and is used for scaling) and replacing this equation in the rheological constitutive equation for the normal stress in the jet cross section $\sigma_{\tau\tau}$:

$$\frac{\partial \sigma_{\tau\tau}}{\partial t} = G \frac{1}{\lambda} \frac{\partial \lambda}{\partial t} - \frac{G}{\mu} \sigma_{\tau\tau} \quad \text{Eq.(1.29)}$$

where G is the modulus of elasticity and λ as the meaning previously cited.

On other hand, Shin et al. [60], shown that the phenomena responsible for the onset of whipping are revealed by a linear instability analysis [68] that describes the jet behavior in terms of known fluid properties and operating conditions. The approach presented described the stability characteristics of the jet as a function of realistic and measurable values of the fluid properties and operating parameters. The most important characteristics of the fluid are found to be viscosity and conductivity. The main operating parameters are the applied electric field and flow rate. The relevant process variables are the jet radius, axial velocity, charge distribution, and displacement of the centerline of the jet as a function of the axial distance from the nozzle.

An ‘‘operating diagram’’ summarizes how the amplification factor $\Gamma(E_\infty, Q)$ for a particular instability depends on the applied electric field E_∞ and flow rate Q for a given set of fluid parameters. From the growth rate equation, we estimate $d \ln A / dt = \omega(h, E, \sigma)$ where $A(t)$ is the amplitude of a perturbation at time t . Approximating $dA/dt \sim U dA/dz$, where $U = Q/\pi h^2$, we obtain the amplification factor for a perturbation convected a distance d downstream:

$$\Gamma(E_\infty, Q) = \ln \left[\frac{A(d)}{A(0)} \right] = \int_0^d \frac{\omega(h, E, \sigma) \pi h^2}{Q} \quad \text{Eq.(1.30)}$$

By plotting contour lines of the amplification factors for the various instability modes, a map of the jet behavior has been obtained as shown in Figure 11.

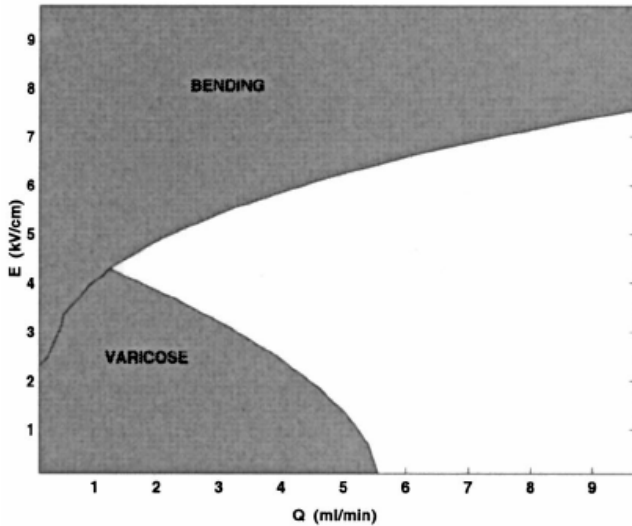


Figure 11 Operating diagram showing stability transitions for a 2 wt% solution of PEO.

He et al. [75], proposed a scaling relation between electric current and solution flow rate, which is able to describe a complex dynamic process from the theory, and it requires less empirical or semi-empirical input. Of course the authors understand that no matter how rigorous, some experimental verification is needed to validate the model. The relation of I and Q can be expressed as

$$I = \beta Q^{\frac{2(\delta+1)}{\alpha(2\delta+1)}} \quad \text{Eq. (1.31)}$$

where β is a constant. The three parameters (β, α and δ) in Eq.(1.31) can be determined experimentally.

Moreover He [76] dealt with allometric scaling of electrospinning process, predicting the radius of the jet in two different cases i.e. case of full surface charge and case of part surface charge. The balance force has been managed conveniently and the relationship between radius r of jet and the axial distance z from nozzle has been proposed for the two cases:

$$r \sim z^{-1/2} \text{ (case of full surface charge)}$$

$$r \sim z^{-\alpha/(1+\alpha)} \text{ (case of part surface charge) where } \alpha \text{ is a surface charge parameter.}$$

In an other study [77], it has been focused on the same relationship between r and z in different stages of the process, predicting for the initial stage, when electrically generated force is dominant, $r \sim z^{-0.5}$, for the instability stage $r \sim z^{-1/2}$ (the latter is valid if the resultant force of the electric and viscous forces approximately vanishes and if the acceleration can be approximated to zero), and for the terminal stage, when $z \rightarrow \infty$, $r \sim z^0$. These predictions also agree with the experimental data. Moreover an allometric scaling relation between the current and voltage is also obtained from He and co-workers [78]:

$$I = E^{a(2\delta+1)/(a(2\delta+1)-2(\delta+1))} \quad \text{Eq.(1.32)}$$

where a and δ are two parameter experimentally determined and only two set of data (I, E) are necessary.

All the models discussed above are fundamental in understanding basic principles of electrospinning because the dimensions and the structure of the electrospun nanofibers are closely related to the prevalence of one of the different instabilities which occur during the process. However, the plurality of the forces which play a role in the process as well as the interactions among them, whose modeling is still hard, require more efforts in this branch.

1.4 Nanofibers structure and characterization

The morphology of the electrospun fibers depends on different parameters and even though electrospinning has been carried out on molten polymer [31] usually this process considers polymer solutions. Because of this, a first broad distinction can be made between polymer solution parameters (molecular weight and solution viscosity, surface tension, solution conductivity, solvent dielectric constant), processing conditions (applied voltage, flow rate, nozzle collector distance) and ambient conditions (temperature, pressure, humidity, type of atmosphere).

Although the fiber morphology results as a synergic effect of the parameters all in this section we try to understand how every single parameter contributes to the fiber structure.

1.4.1 Polymer solution parameters

1.4.1.1 Molecular weight and solution viscosity

The molecular weight of the polymer strongly affects the fiber size and spinnability in general because one of the necessary conditions for a good outcome in the process is the presence of a suitable viscoelastic force in the polymer that means sufficient molecular weight and viscosity. The ejected jet from Taylor cone undergoes stretching during its path towards the collector and then the role of the entanglements of the molecule chains is to prevent the charged jet from breaking up into small droplets and then to guarantee a continuous and stable jet.

As reported by Michelson [79], both viscosity and conductivity play vital roles in the electrostatic atomization process, and can influence the 49.3° equilibrium angle determined by Taylor and other aspects of the process [80].

The solution viscosity can be increased throughout two ways that is considering the same polymer with higher molecular weight rather than increasing the polymer concentration. The latter results in addition of entanglements within the solution. In order to explain this idea, Figure 12 shows that fibers formation is more difficult working with low molecular weight (LMw) (M_w 34000 by GPC) polymer solutions of poly(methylmethacrylate)-co-metacrylic acid (PMMA-co-MAA) even though the polymer concentration has been increased from 10 to 20 wt%.

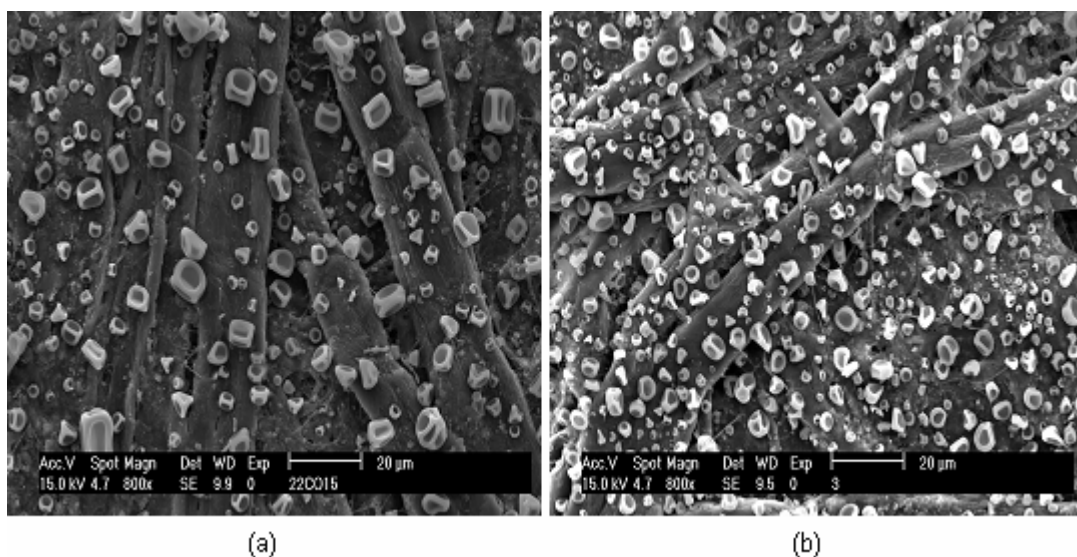


Figure 12 No fibers formation working on low molecular weight polymer solutions of (PMMA-co-MMA) at different concentrations (a) 10wt % (b) 20wt %.

On the other hand, Figure 13 reports a SEM micrograph of the same polymer mixed to an higher molecular weight fraction (HM_w) of the same one (MW 5,000,000-10,000,000 by GPC). The ratio HM_w/LM_w considered is 1/8 that means a small amount of high molecular weight polymer promote fibers formation.

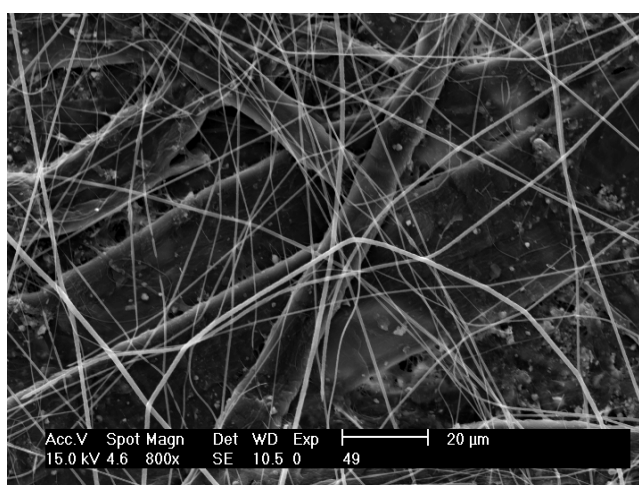


Figure 13 SEM image of PMMA-co-MAA with $HM_w/LM_w=1/8$.

As concerns viscosity solution, the upper limit is represented by a value over which processing is prohibited by an inability to control and maintain the flow of a polymer solution to the tip of the needle and by the cohesive nature of the high viscosity as well as the drying of the solution after a short time from the process beginning [81].

Different authors related on the morphology changes with the polymer concentration [80-83] as well as with the molecular weight [83-88] and it can be pointed out that polymer chain entanglements affect the presence of beads on the fibers.

For instance Fong et al. [89], reported SEM micrographs of poly(ethylene) oxide (PEO)/water system (Figure 14) that well explain the changes on morphology due to the viscosity.

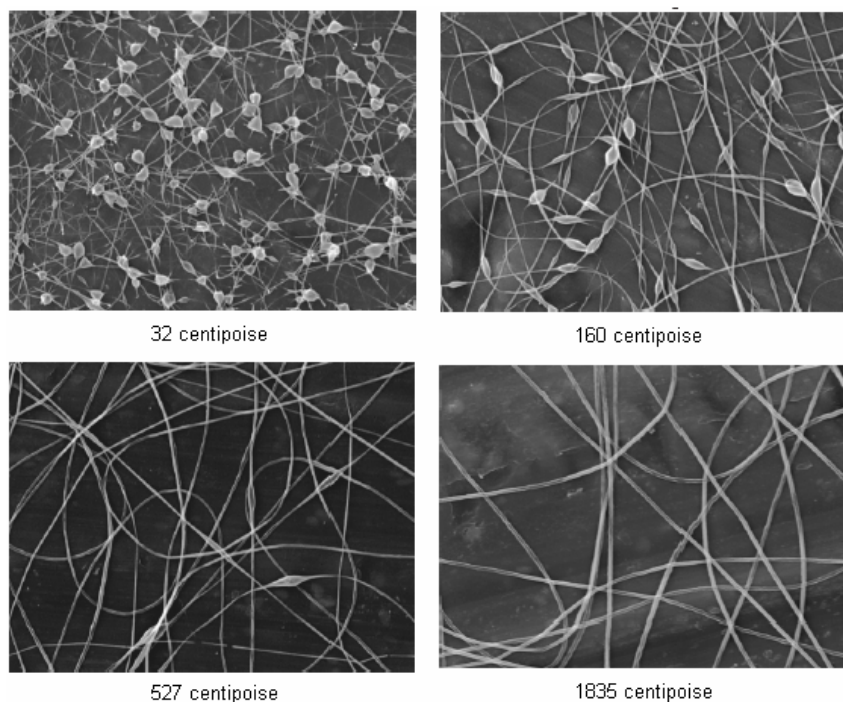


Figure 14 The morphology of beaded fibers versus solution viscosity. The horizontal edge of each image is 20 microns long.

Moreover solution parameters were previously correlated with fiber morphology by Baumgarten in 1971 [26], who determined the limits of spinnability for a poly(acrylonitrile)/DMF solutions and also observed a dependence of the fiber diameter, d , from the solution viscosity η as $d \sim \eta^{0.5}$. Deitzel et al. [90], in their experiments on PEO/water system, used a power law relationship with an exponent of about 0.5 to relate solution concentration to the average diameter of electrospun nanofibers. It has been noticed, a bimodal size distribution at concentrations of above 7 wt% PEO/water.

As concerns fibers morphology, an irregular, undulating morphology with large variations in diameter along a single fiber and the presence of numerous junctions and bundles of fibers has been observed at low concentration ($\eta < 1$ poise) since surface tension is the dominant influence on fiber morphology. On the contrary, a regular, cylindrical morphology and more uniform diameters were obtained at the high concentration ($\eta > 20$ poise), near the end of the processing window. The apparent change in morphology has been explained thanks to the lower surface tension and solvent content in the high concentration solutions.

Different exponents for the power law relationship fiber diameter-concentration, that is average diameter = (concentration)³, were also used from Demir at al. [91], who investigated the polyurethaneurea (PUU) copolymers/DMF system. Also in this study, fiber morphology varied with concentration solution and at high concentrations fibers exhibited curly, wavy and straight structure.

An inverse relationship between molecular weight and concentration for poly(ethylene oxide)/water system has been identified by Doshi [92], who concluded that jet break up depends on the viscosity so that lower viscosity solutions break up into droplets more readily.

Although the range of concentrations that produce fibers will obviously vary depending on the polymer/solvent system used, the forces of viscosity and surface tension will determine the upper and lower boundaries of processing window, if all other variables are held constant.

Gupta et al [83], explored scaling relationships between viscosity and concentration for a series of different linear homopolymers of poly(methylmethacrylate) ranging from 12,470 to 365,700 g/mol MW and they also investigated the impact of these relationships on fiber formation during electrospinning. All the polymers were characterized by hydrodynamic radius and radius of gyration measurement in order to determine the crossover concentration between the dilute and the semidilute concentration regimes, c^* . Experimental values of c^* were compared with the

theoretically determined values calculated by the criteria $c^* \sim \frac{1}{[\eta]}$ where $[\eta]$ is the intrinsic viscosity estimated from the Mark–Houwink parameters, K and a (at 25 °C in dimethyl formamide) are known (they may be obtained from the literature). Three different solution regimes were identified such as dilute ($c/c^* < 1$), semidilute unentangled ($1 < c/c^* < 3$) and semidilute entangled ($c/c^* > 3$). Since the crossover between semidilute unentangled and semidilute entangled regimes in their investigation occurred at $c/c^* \sim 3$, the onset of the critical chain entanglement concentration was marked as c_e according to the procedure utilized by Colby and co-workers[93].

It has been shown that the insufficient chain overlap results on beads formation in the dilute regime, and uniform fibers were obtained when $c/c^* \sim 6$ for all the narrow molecular weight distribution (MWD) polymers (MW of 12,470–205,800 g/mol) but for the relatively broad MWD polymers (MW of 34,070 and 95,800 g/mol), uniform fibers were not formed until higher concentrations, $c/c^* \sim 10$, were utilized. Dependence of fiber diameter, d , on concentration and viscosity was found as $d \sim (c/c^*)^{3.1}$ and $d \sim \eta_0^{0.71}$ (where η_0 is the zero shear viscosity) respectively. The latter was according to the relationship worked out by McKee and co-workers [94] who investigated branched and linear copolymers of poly(ethylene terephthalate-co-ethylene isophthalate) PET-co-PEI and obtained $d \sim \eta_0^{0.8}$. High concentration is also liable for a smaller deposition area because as the solution viscosity is higher, as the bending instability is discouraged and then it spreads over a smaller area; moreover the jet path is reduced resulting in a larger fiber diameter.

Even though viscosity strongly affects fibers formation, it is quite difficult to determine the concentration at which fibers are formed during electrospinning because it depends on molecular weight of the polymer and on all processing conditions considered.

1.4.1.2 Surface tension

As mentioned in previous section, jet ejection from the drop solution at the end of the needle occurs when electrostatic charges overcome its surface tension. Moreover, surface tension, along viscoelastic properties, is liable for the beads formation along the fibers because, according to fluid mechanics [95], the free molecules on interface tend to aggregate to make the surface area per unit mass smaller thus changing the jets into spheres. On the contrary, viscoelastic forces of polymer solution oppose resistance and then at high viscosity the solvents molecules are distributed over the entangled polymer molecules. Then it can be noticed that the choice of a solvent characterized by a low surface tension may encourage the formation of smooth fibers and then solvent properties in terms of surface tension, dipole moment and conductivity as well, may affect the “beads on string” morphology (Jarusuwannapoom et al. [96]). Sometimes, by changing the pure solvent by a mixture of two miscible solvents with different properties, may result in variation of the fiber morphology as shown by Fong et al. [89], with the mixing water/ethanol and increasing ethanol concentration, makes the solution viscosity higher and the surface tension lower. Both these effects favor the formation of smooth filaments. The effect of the presence of two solvents in the polymeric solution can strongly affect the fibers formation as shown in Figure 14. Electrospinning of starched based polymer, called Mater-Bi®, was performed at Chemical Process Engineering Department, University of Padova, Italy [97], varying the kind of solvent mixed. Looking at Figure 15, it can be pointed out that the solvent properties (especially in term of surface tension and conductivity) strongly affect the obtained result and sometimes the best conditions were found to be a mixture of two solvents. Figure 15 (A) showed the electrospun mat obtained with a pure solvent whereas Figure15 (B) and (C) reported the result of an increase and a decrease in surface tension respectively, which was achieved adding precise amount of different solvents.

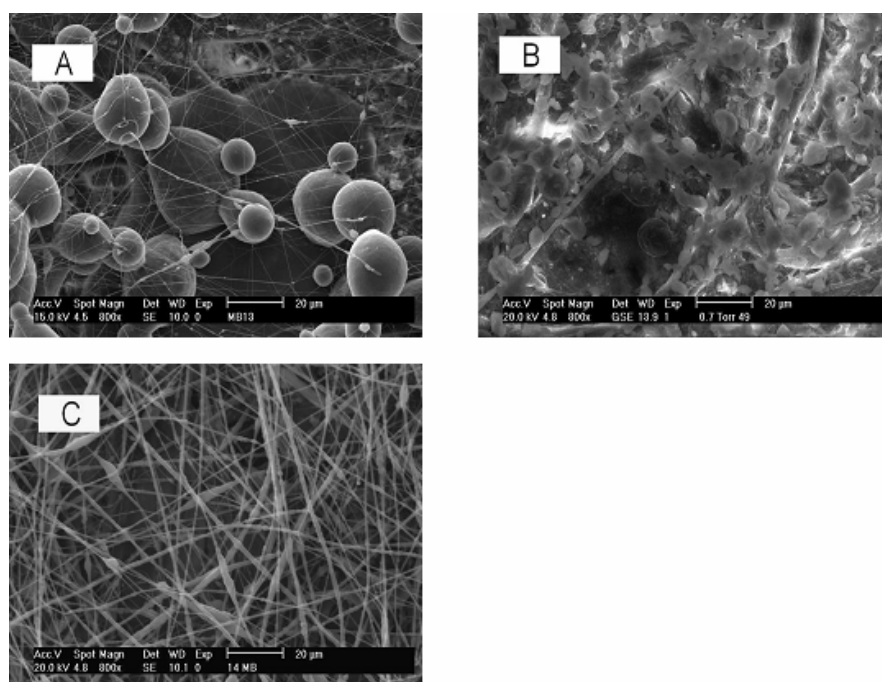


Figure 15 SEM images of Mater-Bi® (10 wt.%) electrospinning. Effect of the solvent properties fiber production. (A) Pure solvent, (B) two mixed solvents resulting in higher surface tension than the pure one, (C) two mixed solvents resulting in lower surface tension than the pure one.

Another way to reduce surface tension is to exploit the ability of surfactants to lower the surface/interfacial tension of the medium in which they are dissolved. In fact, an ionic surfactant, having an ionic hydrophilic head, interacts with the polymer molecules altering the rheological properties of the solution. A small concentration of surfactant improves the conductivity of the solution as well [98].

1.4.1.3 Solution Conductivity

Solution conductivity is related to the net charge density of the jet and it affects the formation of beads because it deals the whipping instability mainly destabilizing the jet and stretching it thinner. Usually, the conductivity is increased by ions addition [98]. Several examples have been reported in literature that show as a small amount of salt induces an increase of the charge density carried by the jet and thus, stronger elongation forces are imposed to the jets due to the self-repulsion of the excess charges under the electrical field, resulting in a substantially straighter shape and smaller diameter of electrospun fibers [99]. However, the effect of conductivity on the fiber diameter might be limited above a critical value because of the viscoelastic forces that act against the coulombic forces of the charges. Another effect of salt addition results in a greater bending instability and then an increase of the deposition area. Moreover electrospinning can occur for a lower critical voltage and the minimum concentration of polymer to prepare fibers via electrospinning decrease as suggested by Son et al. [100].

However the solution conductivity depends also on the solvent conductivity. Jarusuwannapoom et al. [96] noted that solutions prepared using solvents of higher conductivity generally yield fibers without beads while from solutions characterized by zero conductivity, no fibers are obtained.

Another fundamental aspect regards the size of the ions that can affect the resulting fiber diameter. Ions with smaller atomic radius have a higher charge density and thus a higher mobility under an external electric field. Zong et al.[81] investigated the effect of different salts that is NaCl, NaH₂PO₄, KH₂PO₄ and it has been pointed out that sodium and chloride ions have smaller radius than potassium and phosphate ions. Thus the elongational forces imposed on the jet with sodium chloride should be higher than that with potassium phosphate and that means a smaller average diameter for electrospun fiber of solution with NaCl while the fibers spun from the solution added with KH₂PO₄ had the largest fiber diameter.

The pH of the solution also involves a variation on conductivity. An example of this effect has been present by Son et al. [101] who investigated electrospinning of cellulose acetate (CA) under basic conditions, adding NaOH, rather than neutral conditions. The presence of OH⁻ ions, due to the deacetylation of CA under basic conditions, improves the conductivity of the solution and then the jets stretch resulting in fibers diameters reduction.

1.4.1.4 Solvent dielectric constant

The dielectric constant of the solvents, and then of the resultant solutions, may influence electrospinning because it affects the stability of the jet in term of an increase on bending instability. The dielectric constant is a measure for the polarity of solvent. Charges have a much greater effect to a polar solvent than to a non-polar one. It is considered that solvent with a larger dielectric constant have a higher net charge density in solution and then results in thinner electrospun fibers [100]. Lee et al. [102], also indicated that an increase of the solution dielectric constant affects the spinnability and the electrospun fibers diameter. In their experiments dimethylformamide (DMF) ($\epsilon = 39$) has been added to rise the dielectric constant of the whole solution and different ratio methylene chloride (MC)/(DMF) were tested as reported in the micrographs of Figure 16.

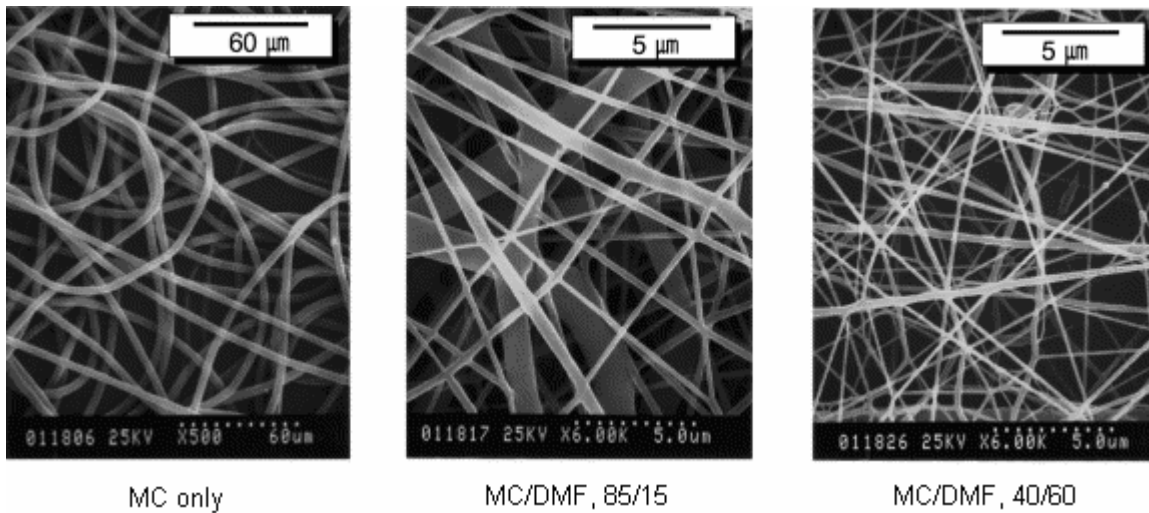


Figure 16 Micrographs of of electrospun poly (1 -caprolactone) (PCL) nonwoven mats from three types of solvent system.

1.4.2 Processing conditions

1.4.2.1 Applied voltage

The applied voltage represents a fundamental parameter in electrospinning because as mentioned in the previous section, a high voltage induces the charge of the solution and when the electrostatic force in the solution overcomes the surface tension of the solution a jet is ejected from the Taylor cone resulting in electrospinning.

As previously mentioned, various instability modes occurs during the fiber forming process depending on the shape of the jet initiating surface and the degree of instability, which effectively produces changes in the fiber morphology. The charge transport in electrospinning is mainly due to the flow of the polymer jet towards the collector since the ionic conduction in the polymer solution is generally negligible [103].

Depending on the feed rate, there is a critical potential that made a stable jet. Deitzel et al. [90], demonstrate that an increase in applied voltage modifies the shape of jet initiation point and also the morphology of the poly(ethylene oxide) (PEO) fibers undergoes a change from a defect free fiber at 5.5 kV to a highly beaded structures at 9.0 kV as shown in Figure 17. Beads formation was related to a steep increase in the spinning current, which strongly affects this phenomenon.

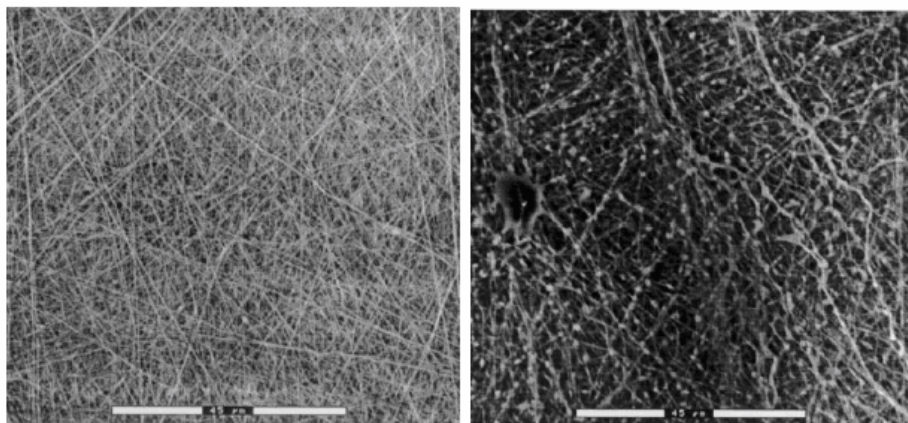


Figure 17 SEM images of electrospun PEO at (a) 5.5kV and (b) 9kV by Deitzel et al.

In order to avoid changes of the jet initiating surface, Jaeger et al. [104], proposed a different set up made up of a ring electrode between the nozzle and the collector. Thanks to this modification a field free space has been created and then the jet instability at the initiation stage is reduced even though the bending instability is still dominant during the second stage. A similar apparatus was proposed by Deitzel et al. [105] who introduced eight copper grids in series, held at different potentials, between the nozzle and the collector in order to damp the bending instability. The scope of this setup was converging the field lines to a center line above the collection target by the applied potential to the ring electrodes. They also used multiple field technique for obtaining lower diameter fibers as well as a reduced depositing area on the collector due to the dampening of the bending instability.

Other researchers focused on the voltage dependence of the fiber morphology and, for instance Megelski et al. [106] noticed a fiber diameter reduction as the voltage was increased from 5 to 12kV. A similar trend was observed from Buchko et al. [80] with electrospun polymer fiber with fibronectin functionality (SLPF). Generally it has been assumed that an increase of voltage applied results in a greater deposition rate due to high mass flow from the needle tip. Moreover, if electrospinning is carried out with low viscosity solutions, tests performed at different increased voltage showed a fiber diameter reduction because of the formation of secondary jets during the process.

This trend can also be noted in Figure 18 that represents electrospun fiber of polylactic acid carried out in our Laboratories (Chemical Process Engineering Department, University of Padova, Italy).

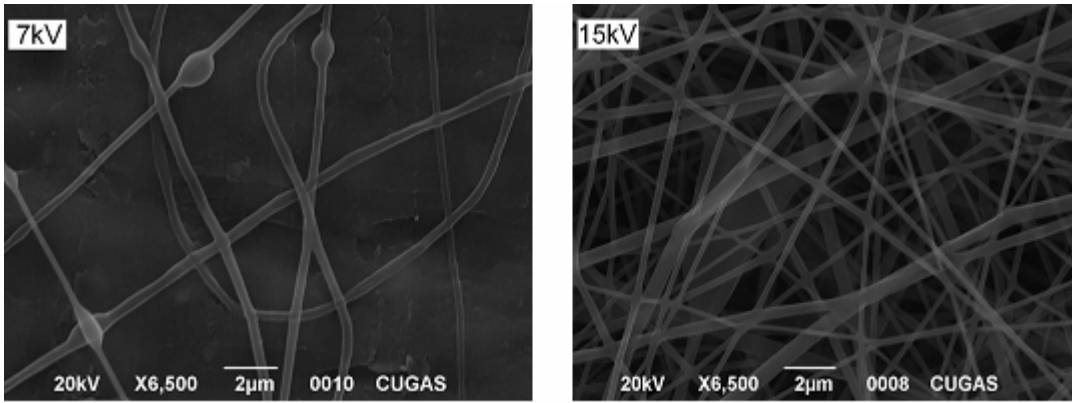


Figure 18 SEM images of electrospun poly(lactic acid) at 8 wt. % concentration, flow rate of 5 µl/min and 15 cm nozzle-collector distance.

Kessick et al. [107], performed electrospinning of poly(ethylene oxide) (PEO) solutions using both DC potential and AC potential and they noticed that only the latter was capable of producing significant coverage on the insulating substrate, possibly due to a reduction in the amount of surface charging. The AC potential resulted in a significant reduction in the amount of fiber ‘whipping’ and the resulting mats exhibited a higher degree of fiber alignment (Figure 19) but were observed to contain more residual solvent. In order to explain the reduction of the instability they suggested that, under AC potentials, the net charge on the fiber is reduced as well as the electrostatic forces producing the fiber instability. Due to the alternating polarity of the applied potential, the AC spun fiber should consist of short charge segments of alternating polarity, with the length of the charge segments depending on the fiber production rate as well as the frequency of the AC potential [107].

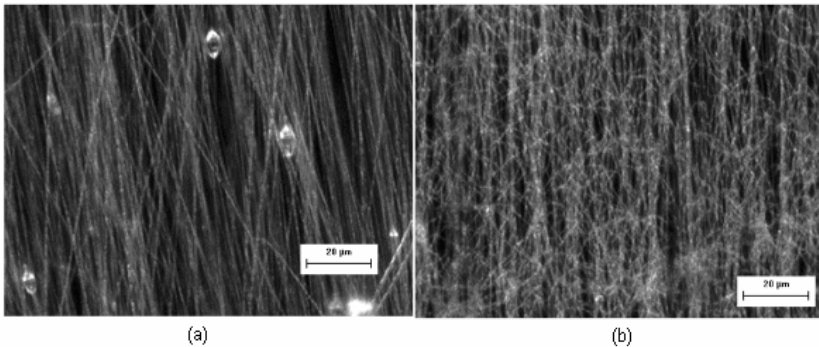


Figure 19 Optical microscope images of a mat of PEO fibers produced by (a) AC and (b) DC electrospinning.

The applied voltage affected also the crystallinity of the polymer fiber (Zhao et al. [108]) because its increase causes more order of the polymer molecules and then a greater crystallinity will characterize the fibers. Otherwise, there is also an opposite effect over a certain voltage value because higher potential results on acceleration of the jet and consequently on a reduction of the flight time of the jet. Then, this means that the polymer molecules will be on the collector before their alignment takes place, thus leading to a lower crystallinity.

1.4.2.2 Flow rate

The flow rate of the polymer melt or solution influences the jet velocity and the material transfer rate. An increase of feed rate results in a greater fiber diameter or beads size as well as a longer time for the jet drying due to a major volume of solution that comes out from the tip of the needle as shown in Figure 20. This example regards electrospinning of polylactic acid and it was performed at Polymers laboratories of Chemical Process Engineering Department, University of Padova, Italy.

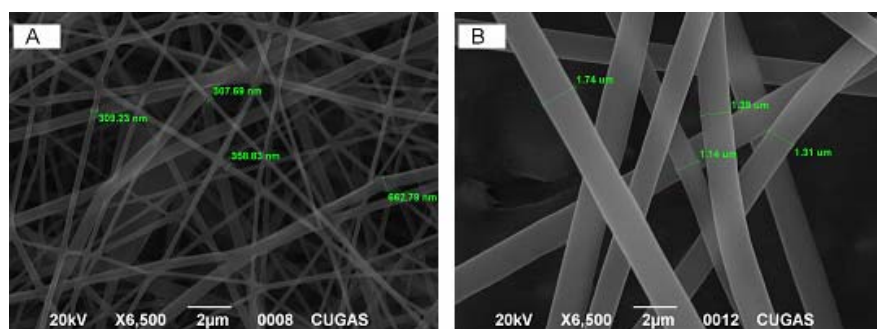


Figure 20 SEM images of electrospun polylactic acid at 8 wt.% concentration, 15 kV voltage and 15 cm nozzle-collector distance. Effect of the increased flow rate from 5 $\mu\text{l}/\text{min}$ (A) to 20 $\mu\text{l}/\text{min}$ (B).

Moreover if the solvent does not have enough time for evaporation fusion of different fibers takes place forming webs.

1.4.2.3 Nozzle collector distance

The distance between the tip of the needle and the collector affects both the flight time and the electric field strength. In order to permit the fibers formation as the specific requirements, it is necessary a suitable time for solvent evaporation. If the distance is too low, excess solvent may cause the fusion of separate fibers and beads formation occurs as reported by Megelski et al. [106], Deitzel et.al. [90], and Zong et al. [81]. This effect may be a consequence of the increase field strength. This condition is represented in Figure 21 which shows the effect of nozzle collector distance on the fibers morphology of polylactic acid electrospun from solution at 8 wt% concentration. It is clearly observable that a low distance results on wet fibers.

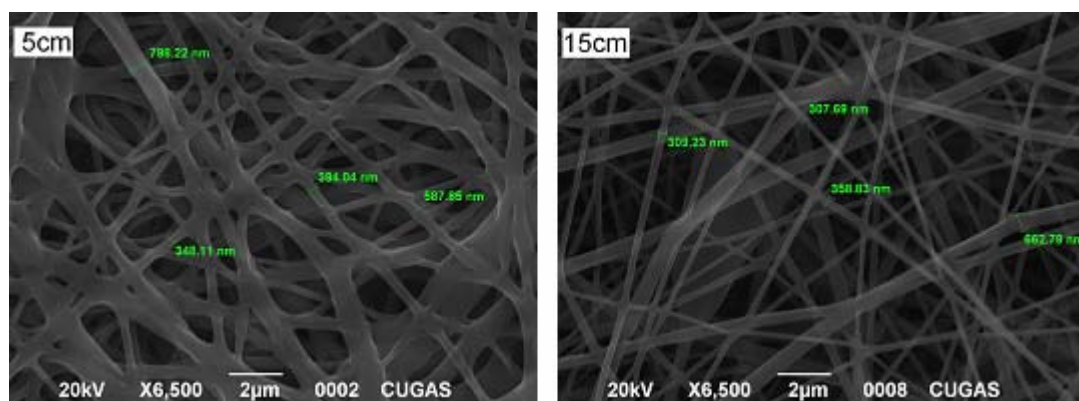


Figure 21 SEM images of electrospun polylactic acid at 8 wt.% concentration, 15 kV voltage and flow rate of 5 $\mu\text{l}/\text{min}$. Effect of the nozzle collector distance, 5cm and 10cm, on the nanofibers morphology.

On the contrary Jaruswannapoom et al. [96] noticed that the amount of beads on the fibers and the areal density of the fibers increased with increasing collection distance as shown in Figure 22. This contrasting behavior may be explained remarking that all the parameters are strongly related each other and scanning electron micrographs show only the global and final result of that.

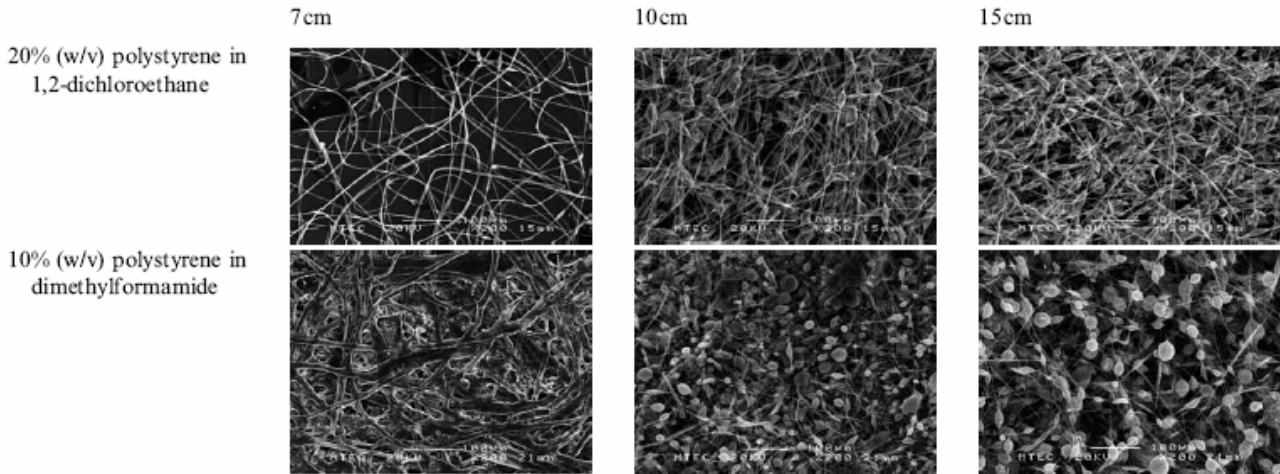


Figure 22 Effect of increased collection distance for a fixed applied potential of 20 kV.

Also the diameter dimension of the fibers as a function of collection distance presents contrasting trend depending on the specific studied system. Zhao et al. [108] and Reneker et al. [61] reported a decrease of average diameter as the increased distance and they explained it considering that a longer flight time means more stretching time for the jet. Again Lee et al. [109] noticed an increase of average diameter as the distance increases and this is due to the less field strength that results in less stretching of the fibers.

1.4.3 Ambient parameters

1.4.3.1 Temperature

Effects of the temperature on the electrospinning process were investigated from Larrondo and Manley[31], who dealt with melt electrospinning and observed that the fiber diameter decrease with increasing melting temperature. Moreover a study of the temperature effect on the electrospinning of polymer solutions revealed that it affects the morphology and the spinnability of the solution. Demir et al. [91] reported that an increase of processing temperature results on higher deposition rate and consequently higher film thickness of the nonwoven mats. As regards fiber morphology, a major uniformity of diameter distribution has been noted, probably due to the lower viscosity of the solution and greater solubility of the polymer in the solvent that allow more stretching of the solution. Smaller diameters of the electrospun fibers can be related to greater stretching forces as well [110]. However it could pointed out that room temperature electrospinning is more sustainable process and usually the temperature play a fundamental role if melt electrospinning is carried out.

1.4.3.2 Humidity

The humidity of the electrospinning chamber may influence the process in term of fibers morphology. This is because high humidity induces water condensation presence on the fibers surface when electrospinning occurs. Some examples are reported by Megelski et al. [106], Bognitzki et al. [111], and Casper et al. [112]. The latter concluded that in the presence of humidity electrospun fibers contained submicron surface features and understanding the link between humidity and fiber morphology a better control over the properties of electrospun fibers could be allowed. The obtained data shown an increase of both pore diameter and pore size distribution as the humidity increased. They also provided additional information concerning the depth of the pores performing atomic force microscopy (AFM) analysis that revealed proportionality from the depth of the pores to the humidity and molecular weight as shown in Figure 23.

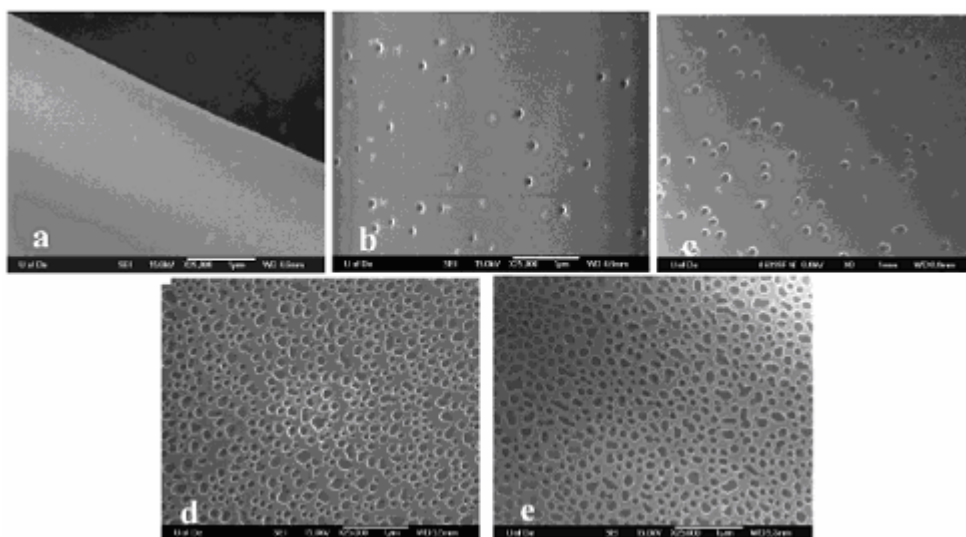


Figure 23 Micrographs of 190 000 g/mol PS/THF fibers electrospun under varying humidity: (a) <25%, (b) 31-38%, (c) 40-45%, (d) 50-59%, (e) 60-72%.

The humidity affects also the evaporation rate of the solvent. The solvent dries quickly if the humidity is very low and then if the evaporation rate is faster than the removal of the solvent from the tip of the needle, the latter could be clogged after a few minutes since the beginning of the process [26].

Others authors (Li et al. [113,114]) suggested that high humidity and fibers discharge can be related as well as the accumulation of residual charges on the electrospun fibers, but nowadays there are not enough tests that prove and explain these relationships.

1.4.3.3 Pressure and type of atmosphere

The effect of the pressure on the electrospinning process can be evaluated under enclosed conditions and it has been noted that is not expedient work with very low pressure because of the

discharge of the electrical charges. Moreover reduction in the pressure promotes the instability of jet initiation and also bubbling of the solution at the tip may occur.

Usually electrospinning experiments are carried out at normal atmosphere because using different gases must be considered their behavior under electric field applied. Helium cannot be used due to its break down under these conditions, but some examples have been reported in literature about the use of others gases (Piperno et al.[115], and Baumgarten [26]).

Nanofibers characterization: morphology

Morphology

Nanofibers produced by electrospinning usually show a solid interior and smooth surface. Depending on the their specific application, several morphology can be obtained choosing a suitable system (polymer-solvent) that results on a specific secondary structures of nanofibers such as porous, flatted or ribbon-like, branched, helical, hollow and core-shell, that will be discuss in this sub-section.

Several authors reported of flatted or ribbon like fibers Several authors reported of flatted or ribbon like fibers[110,117-120. Different polymers have been tested, among which polystyrene (PS [110]), polyether-imide (PEI [116]), polyamides PA [117], polyvinyl alcohol PVA [118], and elastin protein [119,120] as well. The typical flat-ribbon like structure is showed in Figure 24 [116,117].

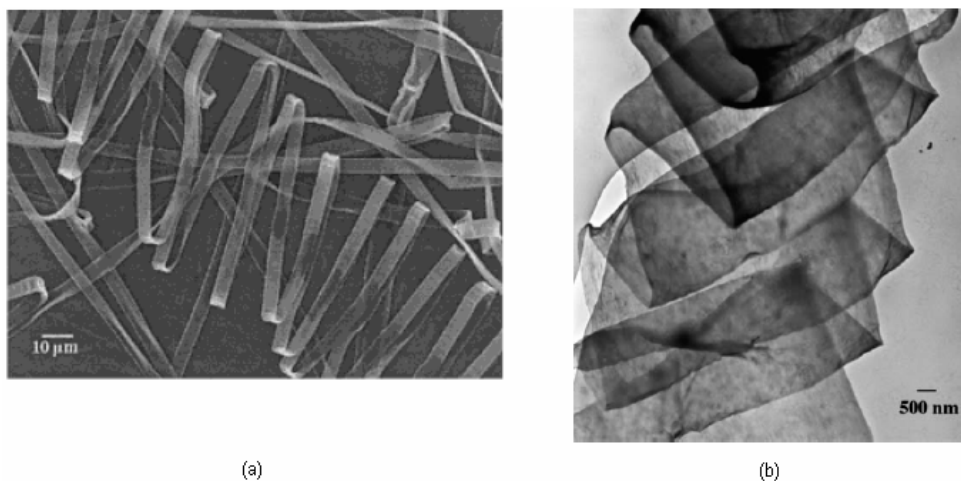


Figure 24 (a) Ribbons from 10% poly(ether imide) inhexafluoro-2-propanol.

Koombhongse et al. [116] explained the ribbon like structure considering the presence of a thin, mechanically distinct polymer skin on the liquid jet. When solvent evaporation occurs, a tube structure took place and because of the atmospheric pressure the latter collapsed and the circular cross section became elliptical and then flat forming a ribbon with a cross-sectional perimeter nearly the same as the perimeter of the jet [116] (Figure 25(a)-(d)). Sometimes a web, made from the skin, connected the two tubes as shown in Figure 25(e).

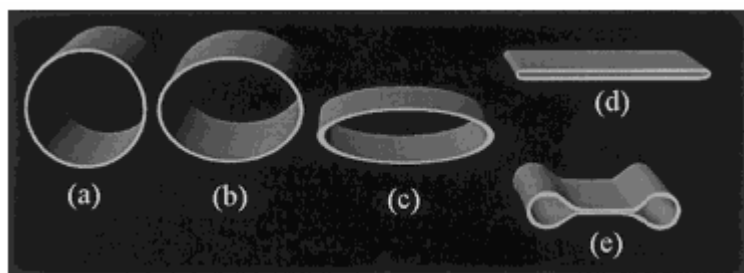


Figure 25 Figure 24 Collapse of the skin on a jet.

Moreover, Koski et al. [118], and Huang [120], related the flat structure of ribbon-like fibers to the concentration increase, in particular Koski indicated that the transition from round to flat fibers occurs at $[\eta]\text{Conc.}$ values between 9 and 10.

In his work, Koombhongse [116] also observed the formation of branched jet and fibers, and this behavior has been explained considering the jet instability. During the elongation of the jet, the evaporation of the solvent takes place and the balance between the main forces, such as electrical forces and surface tension, can shift causing a decrease of its local charge per unit surface area by ejecting a smaller jet from the surface of the primary jet (Figure 26 (a)) or by ejection from the surface of a charged bead (Figure 26(b)).

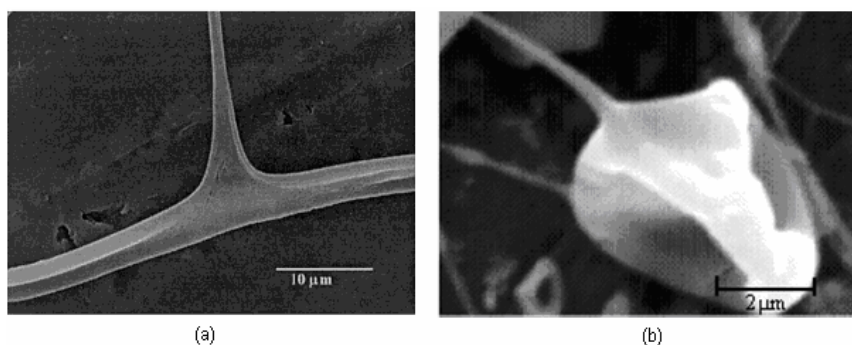


Figure 26 (a) SEM micrograph of branched fibers. Reprinted

Kessick and Tepper [121] observed the formation of helical coil fibers consisting of a composite of one conducting, poly(ethylene oxide) (PEO) and one nonconducting polymer, poly (aniline sulfonic acid) (PASA). Their experience suggested that the electrochemical property of PASA played a fundamental role on helical structures formation and the mechanism that took place involved once again the forces balance on polymer jet. In particular the equilibrium between electrostatic forces and viscoelastic forces is disquieted because of the charges of PASA regions transferred to the fiber surface. Consequently a structural rearrangement is promoted in order to reinstate the equilibrium.

As concerns porous structures, the exact mechanism is complex and many variables should be considered. Two different approaches have been reported to explain pore formation. The first one involved breath figures form due to evaporative cooling that occurs as a result of solvent evaporating as the electrospinning jet is being propelled toward the target. The surface of the jet

cools and water from the air condenses on the surface of the fiber [112]. The second one counted the phase separation of different polymers during electrospinning thanks to the application of suitable parameters.

Some authors [106,112] extend the breath figures theory to the explanation of the presence of three dimensional structures on fibers surface. Srinivasarao et al. [123] produced a thin film by evaporating a PS solution in a volatile solvent and passing humid air across the surface of the film. The resulting film contained hexagonally ordered arrays of pores; on the contrary the pores obtained on the surface of an electrospun fiber are not ordered arrays of uniformly shaped pores. This difference in breath figure have been explained considering the motion and elongation of the jet through the moist air and the charges carried on the fibers that may affect the ordering of the pores and their density [4].

However the concept of breath figures alone does not fully explain the pore size differences seen when changing the molecular weight of the polymer. If pore formation was based solely on breath figures, pore size would primarily be a function of humidity and molecular weight would not play a major role in determining the size or shape of porous structures [112].

Because of this, an other mechanism based on phase separation has been considered. The formation of nano- and microstructures by phase separation in membrane preparation processes has been widely discussed in the literature [124-129].

There are four main phase separation mechanisms to produce porous membranes: thermally induced phase separation (TIPS), immersion precipitation, air-casting of the polymer solution and precipitation from the vapor phase [124]. A detailed discussion of each type of phase separation in relation to pore formation was published by Megelski et al. [106]. Thermodynamic instability is the driving force behind phase separation leading the formation of a polymer rich and a polymer lean phase. During fiber formation, the concentrated phase solidifies shortly after phase separation and forms the matrix, whereas the polymer lean phase forms the pores. A phase diagram coupled with thermodynamic and kinetic aspects provides information about structure formation in membranes [106].

Bognitzki et al. [111] reported the formation of pores due to phase separation in electrospun poly-L-lactide, polycarbonate and polyvinylcarbazole when dissolved in dichloromethane. Thermally induced and vapor induced phase separations (TIPS and VIPS respectively) are the most pertinent phase separation processes that Casper et al. [112] mentioned to explain the pore formation in the PS/THF electrospun fiber. Vapor induced phase separation involves the penetration of a nonsolvent vapor causing phase separation of the polymer solution. In their system, water is the nonsolvent, which induced the phase separation of the homogeneous mixture of PS and THF [126]. Rapid

evaporation of the solvent as the jet is being projected from the needle causes lowering of the temperature on the fiber, thus making TIPS a viable explanation for pore formation as well. During the evaporation of solvent, pore formation begins when the temperature reaches the bimodal temperature and continues to grow until the crystallization temperature is reached [127]. Phase separation occurs by the mechanisms of nucleation and growth (NG) and/or spinodal decomposition (SD). Generally, an interconnected pore structure is characteristic of the NG mechanism while closed pores are produced by SD [126,129]. As concerns the viscosity effect and molecular weight effect on pore formation it is not clear at all if the changes in pore size and shape are due to their synergic effect or not. Research is currently in progress to investigate this issue [112].

It is evident that neither the phase separation theory nor the formation of breath figures alone fully explains the phenomena of pore formation in electrospun fibers. Rather, the porous surface of electrospun fibers is due to combination of both phase separation and breath figure formation.

Also Han et al. [130] (Figure 27) produced ultrafine porous cellulose triacetate (CTA) fibers via electrospinning with methylene chloride (MC) as solvent and suggested their application in nanofiltration since cellulose acetate and its derivatives have found extensive use in membranes for separation.

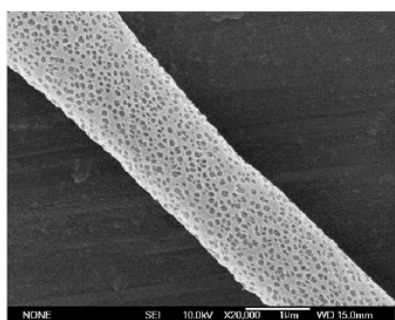


Figure 27 SEM images of CTA porous fibers.

In another work, Xia and Li [113] obtained porous ceramic nanofibers by a different spinneret system. In this case the mechanism of formation was slightly different because thanks to the solvents evaporation during fibers formation, two polymer phases were separated to generate nanoscale domains of PS embedded in a continuous TiO_2 /PVP matrix. Once the PS phase has been removed by calcinations, the resultant fibers became highly porous in the PS-rich region (Figure 28(a)). This and other demonstrations suggest that the secondary structure of electrospun fibers can be controlled by varying the polymer contained in the core and sheath solutions.

Xia and Li also obtained core/sheath or hollow structure using the same co-electrospinning process. In a typical procedure [113] mineral oil and an ethanol solution of PVP/ titanium tetra(isopropoxide) ($\text{Ti}(\text{OiPr})_4$) have been used as the source materials for core and sheath, and they were ejected at the same time through the double capillary system. After solvent extraction of the oil phase, the

obtained product resulted in hollow fibers consisting of TiO_2 /PVP composite walls (Figure 28(b)). Sheath thickness and inner in the nanometers scale diameter could be modulated by controlling the spinning conditions. Then, it has been pointed out [113] that the presence of a sol-gel precursor such as $\text{Ti}(\text{OiPr})_4$ affected the formation of stable, coaxial jets and robust tubular structures because it improves the stability of the jet and lead to the formation of uniform diameters.

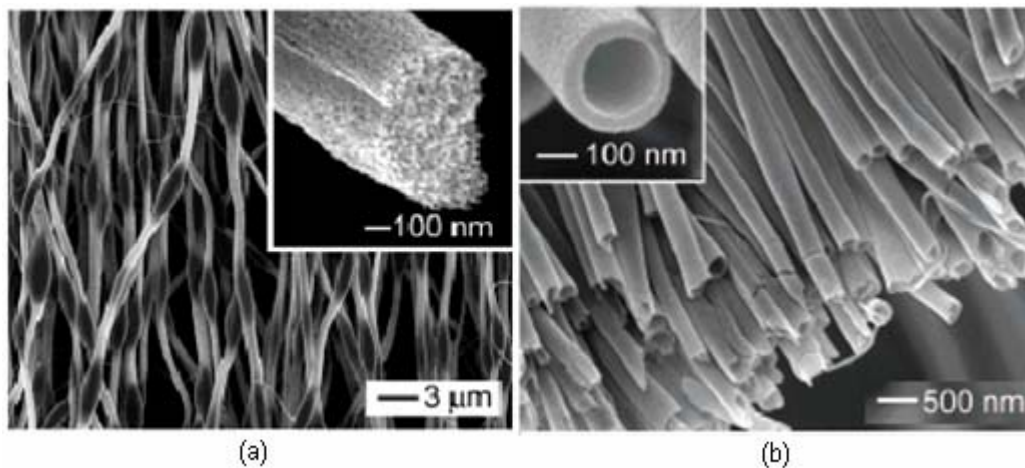


Figure 28 (a) SEM images of TiO_2 fibers fabricated by electrospinning, with a DMF/THF solution of PS (0.12 g/mL) as the core and an ethanol solution of $\text{Ti}(\text{OiPr})_4$ /PVP as the sheath. (b) SEM image of a uniaxially aligned array of anatase hollow fibers that were collected across the gap between a pair of electrodes.

Moreover, thanks to its hydrolysis, an inorganic gel network can be formed in the polymer sheath as the compound jet is spun, enhancing the sheath strength to prevent the oil from smearing out during the fibers formation, increasing the viscosity of the PVP solution and the transmission of the viscous stress between core-sheath interface.

Also Larsen and co-workers [132] produced hollow silica-based fibers (SiO_2) by co-electrospinning using an inorganic sol as outer fluid and an immiscible liquid (oil or glycerin) as inner. The resultant tubular structures were characterized by diameters in the order of 500 nm and an average shell thickness of about 70 nm. They found out that the monodispersity in the diameter of the fibers seems to be connected to the absence of jet instability because of low electrical charge level on jet surface.

Beyond co-axial electrospinning, chemical vapor deposition (CVD) method has been tied to electrospinning in order to have hollow nanofibers. Examples are reported by Hou et al. [133] who worked on poly(L-lactic acid) (PLA) nanofibers as template for CVD of poly(p-xylene) (PPX). The obtained fibers have been process by annealing for PLA core removing and consequently PPX hollow nanofibers with outer diameter of 55nm and the inner one of 7nm were obtained.

As regards core-shell structures, many examples have been reported up to now [134-138]. For instance Yu et al.[134] dealt with three different systems i.e. polyacrylonitrile/poly(acrylonitrile-co-styrene) (PAN/PAN-co-PS), poly(aniline sulfonic acid)/poly(vinyl alcohol) (PAni/PVA) and

silk/poly(ethylene oxide) (silk/PEO) obtaining core-shell nanofibers. Sung et al.[135] electrospun core-sheath structures from a poly(carbonate) (PC)/poly(butadiene) solution. Sun and co-workers [136] proposed an experimental set up characterized by a polymer storage bath with two air inlets for obtaining core-shell fibers, made of two identical polymers (PEO) added in different amount of bromophenol in order to gain optical contrast. The diameter of the fibers was around 3000 nm for the outer shell and 2000 nm for the inner. In a similar way PEO (shell)/poly(dodecylthiophene) (core) were processed and transmission electron microscopy (TEM) characterization revealed 1000 nm diameter for the shell and 200 nm for the core. It has been pointed out that the mixing of the solutions can be avoid by the low diffusion coefficients of polymer chains because during electrospinning there is not enough time for the mixing process. Another setup proposed for coaxial electrospinning was reported by Zhang et al. [137] and it is shown in Figure 29 (a). Bi-component biodegradable nanofibers made of gelatin and PCL, as the core and shell polymers, were obtained and a TEM image of their results has been reported in Figure 29 (b).

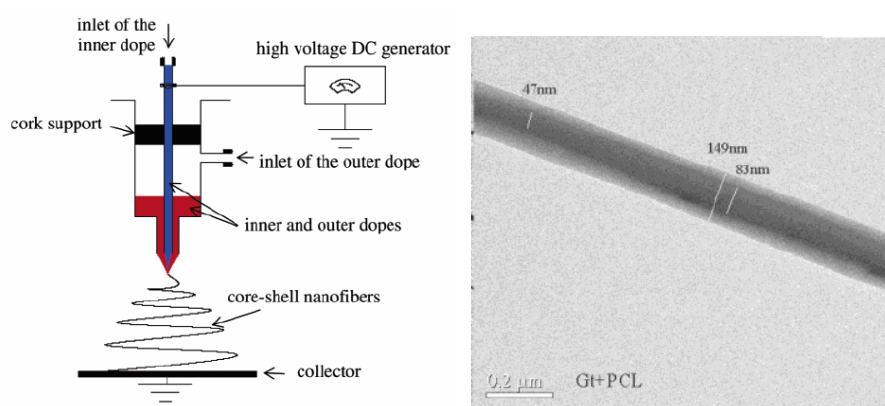


Figure 29 (a) Coaxial electrospinning apparatus by Zhang et al. (b) TEM image of core-shell nanofiber of gelatine and PCL respectively.

Nanofibers characterization: thermal and mechanical properties

Nanofibers exhibit marked differences in their thermal and mechanical properties if compared to regular fibers and bulk properties. Nowadays data about these properties are reported by few authors but more tests are necessary in order to whole understand the behavior of electrospun nanofibers. Especially for mechanical testing the conventional instruments cannot be used because their set up, while thermal properties can be tested without any difficult.

Thermal properties

Thermal analysis has been carried out on a number of electrospun nanofibers in order to understand the relationship between nanostructures and thermal properties (Subbiah et al. [103]).

Zong et al. [81] reported thermal properties of PLA fibers and it has been pointed out that their crystallinity, melting temperature (T_m), glass transition temperature (T_g) are lower than semicrystalline PLA resins. The decrease of T_g is probably due to the large surface volume ratio of

the fibers with air as the plasticizer. As regard the crystallinity, it has been related to the high evaporation rate of the solvent and then rapid solidification of the fibers and wide angle X-Ray diffraction (WAXD) analysis also revealed that crystallinity has been retarded by electrospinning.

Decrease in T_g and T_m were also determined for electrospun poly(ethylene terephthalate) (PET) and poly(ethylene naphthalate) (PEN) by Kim et al. [138] explaining this behavior with the increase of segmental mobility. Moreover thermal degradation analysis of these polymers performed before and after electrospinning revealed a reduction of the intrinsic viscosities of both PET and PEN that can be also the reason of T_g decrease.

Deitzel et al. [90] showed a lower melting temperature and heat fusion of poly(ethylene oxide) (PEO) if compared to PEO powder as well as a decrease of crystallinity has been noted despite the same crystal structure as PEO powder.

Mechanical properties

Nanofibers made from different polymers are used for a wide range of applications such as tissue engineering, filtration, catalysis, reinforcement in nanocomposite and micro/nano-electro mechanical systems and then they are subjected to stresses and strains from the surrounding media during their service lifetime. Because of this, it is necessary to characterize the mechanical properties of single nanofibers.

Of all the mechanical tests, tensile test, bend tests and nanoindentation can be performed on nanofibers. The use of atomic force microscopy (AFM) cantilevers for tensile test is suitable for fibers ranging from tens of nanometers to several hundred nanometers in diameter and can be used with SEM or optical microscopes depending on size of nanofibers. One disadvantage of this method is that it is time consuming and it is difficult to manipulate and test single fibers. As regards bend tests it can be performed by different techniques such as three-point bend test (samples tested using this method of preparation include conductive polymer nanofibers [139,140] biological materials [141], and biodegradable polymer nanofibers [142]).

Nanoindentation is perhaps the most convenient test to perform as the sample can be prepared for testing by simply depositing the nanorods, nanowires and nanofibers on a hard and flat substrate, with sufficient adhesion between the substrate and the nanomaterials. The elastic and elastic-plastic behavior of the material can be obtained from nanoindentation data. Nanoindentation of nanofibers has not been widely studied due to the difficulty in probing the curved surface of the fiber (Tan et al. [143]).

Electrospun polycaprolactone (PCL) fibers by Tan et al. [144] were found to exhibit a tensile modulus of 120 ± 30 MPa, tensile strength of 40 ± 10 MPa, strain at break of $200 \pm 100\%$ strain, yield stress of 13 ± 7 MPa and yield strain of $20 \pm 10\%$ strain.

A decrease in the tensile strength has been reported by Buchko et al. [80] with silk-like polymer with Fibronectin functionality (SLPF) fibers. Kim et al. [145] measured the effect of electrospun nanofibers of PBI (polybenzimidazole) on mechanical properties of two different matrixes, such as epoxy matrix and Styrene-Butadiene rubber (SBR). The first one (epoxy matrix) revealed higher fracture toughness and modulus if compared to the PBI whisker-like particle epoxy composite whereas the reinforced elastomeric matrix had Young's modulus 10-fold greater than the neat SBR.

1.5 Electrospinning design

One dimensional nanostructures have gained more attention in the last few years by the scientific community and much efforts have been made in ordered nanostructures making. This is because the ability to electrospun various materials into uniaxially aligned nanofibers opens the door to the exploration of a wide range of properties, as the anisotropic behavior, and applications such as photonic devices, tissue engineering scaffold and composite reinforcing, to cite only a few of them.

A complete review on the strategies for obtaining ordered structures has been reported by Teo and Ramakrishna [146] and this sub-section will relate some of the main examples about that.

Alignment of the fibers can be essentially achieved following two different ways: by using a rotating collector and by the manipulation of the electric field changing the configuration of the collector electrode.

Different authors referred about rotating device [87,147] and it has been shown the rotating speed of the mandrel affects the degree of fibers alignment [147], as well as the crystallinity and the mechanical properties of electrospun fibers [87]. As regards the fibers alignment, Matthews et al. [147] noted that if the rotating speed is less than 500 rpm, random mats of electrospun fibers are collected; then if speed is increased to 4500 rpm, which correspond to a surface velocity of the mandrel of 1,4 m/s, deposition of collagen fibrils into linear, parallel arrays has been achieved. Thanks to mechanical testing along the principal axis fibril alignment and across fibers orientation, it has been demonstrated that the values of the peak stress and the average modulus in the first case are two fold than the second one and it means that it is possible to tailor subtle mechanical properties into a matrix by controlling fiber orientation.

Kim et al. [87] electrospun poly(ethylene terephthalate) (PET) and mechanical properties were found to be increased as a function of the linear velocity of drum surface in the same way as the crystallinity of the nanofibers. However, over a velocity limit of 30 m min^{-1} , it has been pointed out that the mechanical properties tend to decrease. A possible explanation can be found in a Zussman's work [149] on poly(ethylene oxide), where he noted that an high rotation speed of the disc collector may results in necking of the nanofibers which is essentially attributed to a strong stretching of solidified nanofibers by the tapered accumulating wheel, if its rotation speed becomes too high.

Moreover, Fong et al [117], fabricated aligned yarns of nylon-6 nanofibers by rapidly oscillating a grounded frame within the jet and Deitzel et al. [105], dealt with yarns of aligned poly(ethylene oxide) fibers by introducing an electrostatic lens element to stabilize the liquid jet. Different rotating collector was also proposed by Katta et al. [150] who exploited wire drum collector in order to enhance the fiber alignment maintaining low rotating speed (just 1 rpm).

Rotating devices not only assume considerable importance as a good way for fibers alignment, they are also useful in biomedical applications such as for the production of vascular scaffolds for clinical application as suggested by Kidoaki et al. [151] (as reported in the previous section) and Stitzel et al. [152]. The latter [152] extensively investigated these constructs, made of random nanofibers mat of collagen, elastin, and poly (D,L-lactide-co-glycolide) blends, by testing material distribution, biomechanical properties in vitro and in vivo biocompatibility, obtaining good performance.

As regards the manipulation of the electric field changing the configuration of the electrode(s) Li et al. [153,154] proposed a complete study to generate nanofibers as uniaxially aligned arrays that could be further stacked layer-by-layer into hierarchical architectures. Their electrospinning set up was made of two pieces of conductive silicon strips separated by a void gap as collector. Across the gap, which had a width from some hundreds of micrometers to several centimeters, the obtained fibers had been aligned with the longitudinal axis oriented perpendicular to the edges of the silicon strips [153]. Since this kind of set up works well just in case of the fibers thickness higher than 150 nm, Li et al. [154] proposed a new design in which two parallel gold electrodes were directly fabricated on the surface of an insulator by thermal evaporation through a physical mask. Then, poly(vinylpyrrolidone) (PVP) nanofibers with diameters smaller than 10 nm were deposited on the surface of substrate characterized by a resistivity greater than $10^{22} \Omega \text{ cm}$ such as quartz or polystyrene. In order to explain the mechanism for the alignment, the same authors [154] detected three principal electrostatic forces which are involved during fibers formation.

The effect of the insulating gap has been found to change the structure of the external electric field because the electric field lines split into two fractions pointing toward opposite edges of the gap. Then the charged fibers, moving toward the electrodes, induce image charges on the surfaces of the two grounded electrodes which consequently cause the stretching of the nanofiber across the gap to assume perpendicular position to the edge of the electrode. Moreover, observing the degree of alignment as a function of the collection time, it has been found that the residual charges on the fibers after that span the gap, may cause repulsion between deposited and the upcoming fibers, and then enhance the parallel alignment which correspond to the lowest energy configuration.

Thanks to this approach, uniaxially aligned arrays of nanofibers could be deposited on a highly insulating substrate controlling the test pattern for the electrodes and multi-layered films were also successfully obtained as shown in Figure 30. Li et al. investigated the spatial orientation and position of nanofibers stack supported by a quartz wafer, varying alternatively and altogether the grounded electrodes pairs (1-3 and 2-4). The results can be sighted in Figure 30 B and Figure 30 C, D respectively.

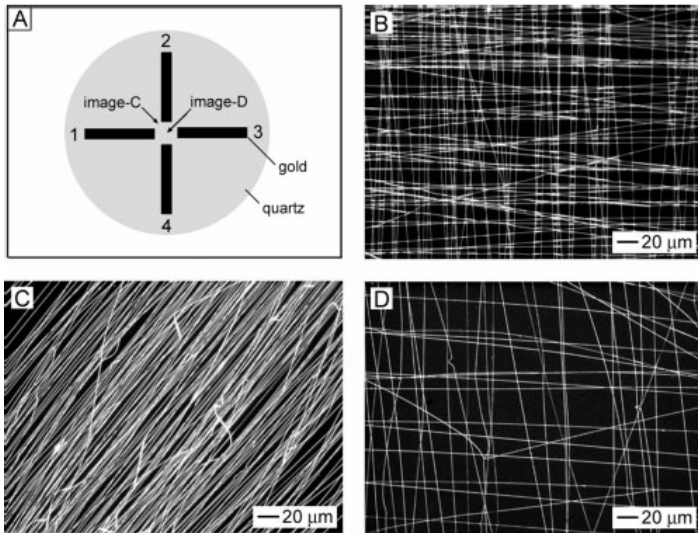


Figure 30 (A) Schematic illustration of the test pattern composed of four electrodes deposited on quartz wafer; (B) Optical micrograph of a mesh of PVP nanofibers collected in the centre area of the gold electrodes grounding alternatively the electrodes pairs 1-3 and 2-4; (C, D) Optical micrographs of a mesh of PVP nanofibers collected in different regions indicate in (A), grounding all the electrodes at the same time.

Teo and Ramakrishna [155] proposed another simple set up wherein the gap was created between two blades in line which were in turn connected to a high negative voltage in order to exert an additional attractive force on the positively charged jet. However, it has been found a threshold value of the negative applied voltage over which no fibers are collected on the blades, probably because of the ionization of the air that could entail a net negative charge appearance on the spun jet and consequently the repulsion by the negatively charged blades. A further packaging of the electrospun fibers was achieved exploiting the surface tension of the water dipping the fibers after collection.

Another interesting manipulation of the electric field has been carried out using two rings placed in parallel as shown in Figure 31 (a) by Dalton and co-workers [156] who produced oriented and continuous fibers across the gap with diameters of $1.26 \pm 0,19 \mu\text{m}$. The rotation of one of the rings was useful to obtain the conversion of the suspended fibers into a multi-filament yarns with a diameter below $5 \mu\text{m}$ and a length of 50 mm as shown in Figure 31 (b) which have a potential in medical application.

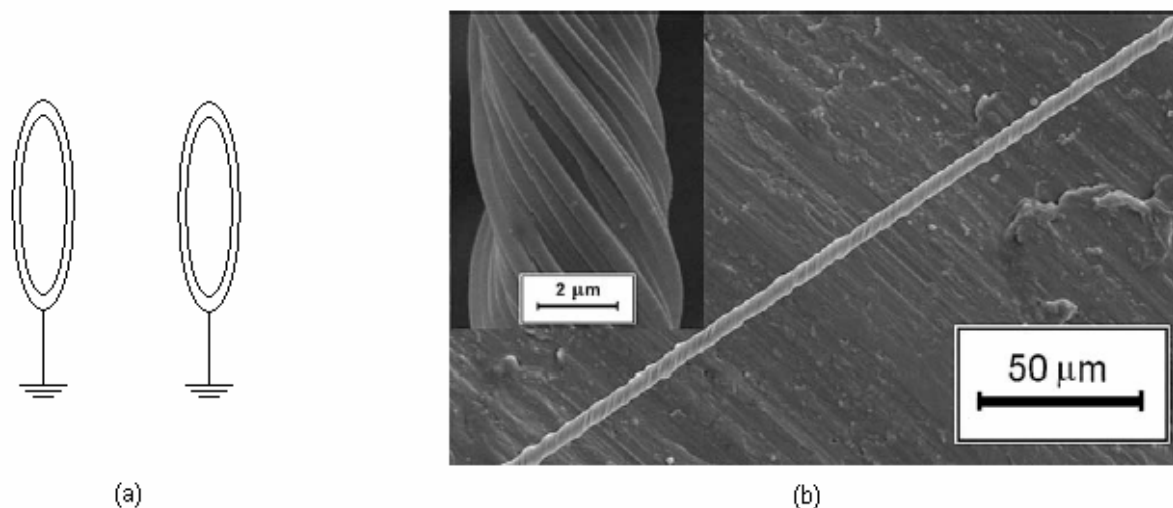


Figure 31 (a) Dual-grounded ring configuration; (b) Micrograph of a multi-filament yarn.

Different setups that combine a variation in the electric field lines with dynamic collectors were proposed by Teo et al. [157] and Theron et al. [158] who investigated the effect of a knife-edged auxiliary electrode on the deposition of electrospun fibers on a tube and a disc collector respectively. A similar concept has been also studied by Sundaray et al. [159] who combined the effect of a sharp pin placed in the rotating collector with the further lateral movement imposed to the rotating collector, obtaining a thick patterned fiber mesh.

A fundamental issue in electrospinning technology regards the productivity of the process as well as the possibility to obtain multi-component mats (Ding et al. [160]); both can be achieved considering multi-jet electrospinning which involve, as suggested by the name, a set up composed of several spinnerets. However, in spite of the practical implementation of multiple jets, detailed physical understanding of the outcome of jet–jet interaction needs to be delved and different authors are dealing hereof. For instance, Theron et al. [161] proposed an experimental investigation and modeling of multiple jets during the electrospinning of polymer solutions of poly(ethylene oxide) (PEO), working on two different arrangements of the multiple nozzles as shown in Figure 32.

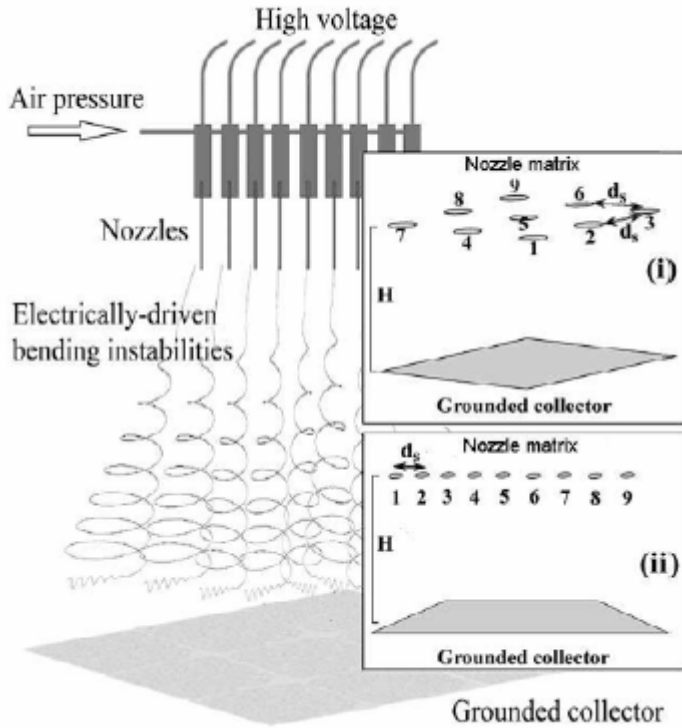


Figure 32 Schematic drawings of multiple-nozzle electrospinning proposed in two arrangements: (i) 3x3 matrix with each nozzle attached to a syringe with polymer solution; (ii) syringes in a row (a 9x1 and a 7x1 linear array).

Thanks to numerical simulations, it has been demonstrated that the mutual Coulombic interactions influence the paths of individual electrified jets in electrospinning and, at the same time, induce the repulsion among them. The latter is inversely proportional to the inter-nozzle distance, but it has been shown that this effect is reduced by the introduction of more jets. Moreover, the decrease in the inter-nozzle distance results on the delay of the bending instability onset, which could be compensate by an increase of the nozzle-collector distance and consequently it might result in a broad collection area. The matrix arrangement has been found to lead more uniformity of the produced non-woven mat and as regards the case of several jets electrospun in a row, the squeezing of the envelope cones of the inner jets along the line on which the nozzles were located has been predicted and observed.

Different configurations of the multiple nozzles have been investigated by Tomaszewski and co-workers [162] who proposed serials, elliptic and concentric multi-jet electrospinning heads. The concentric configuration revealed best performance in term of both efficiency and quality of the process producing 1.0 ± 0.2 mg of dry nanofibers of PVA from one spinning pipe during one minute, and 12 ± 3 mg of such material with respect to the whole electrospinning head during one minute (data obtained with respect to the elliptic head referred as a production of 0.4 ± 0.1 mg of dry nanofibers from one spinning pipe during one minute, and 11 ± 3 mg of such material with respect to the whole electrospinning head and its work during one minute).

Then, in order to enhance the stability of the jets when a multiple nozzles configuration is schemed and consequently to obtain high production rate, Kim et al. [163] tested the use of a cylindrical electrode connected with multiple nozzles and they noted that the initial stream line had stable jet-motion without interferences due to the near charged jets, the environmental conditions, and the interferences of near dielectric/conductive materials.

Another innovative method for increasing the electrospinning rate was proposed by Dosunmu et al. [164] who applied air pressure in order to force the feed solution through the numerous pore of a cylindrical tube a shown in Figure 33. Since the solution approached the outer surface of the tube was charged by an electrode, numerous jets were formed and the electrospun nanofibers were collected on the inner surface of the cylindrical tube. A wide range of materials and polymer can be process with this set up even it has been noted a broader diameter distribution compared to the distribution from the single jet.

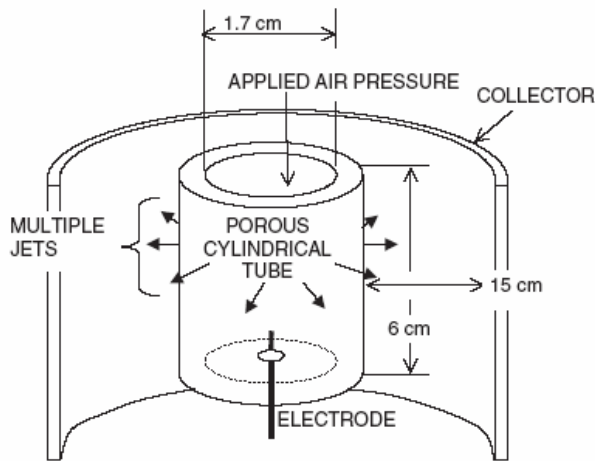


Figure 33 Schematic view of the apparatus with the porous tube proposed by Dosunmu et al.

1.6 Applications

The simplicity and versatility of electrospinning united to the wide range of materials that can be processed, as well as the unique and interesting features associated with electrospun nanofibers, all make this technique attractive for a huge number of applications. In this section, an overview on the developed applications of nanofibers are presented, focusing on nanofiber-based filtration and membranes, nanofiber-based sensors and supports for enzyme and catalysis, nanofiber-based reinforced composites concluding with biomedical usage that represents the main field of nanofibers application up to now.

1.6.1 Filtration and membranes

For more than twenty years, industrial, consumer and defense filtration applications have been made use of polymers nanofibers with fiber diameter of 0.25 μm [165].

Since 1986, some companies have been invested on nanofiber filter media for a broad range of filtration applications and an increase of filter life and more contaminant holding capacity have been revealed. The oldest US patent has been filed by Firma Carl Freudenberg [166] and then Fiber Mark Gessner GmbH & Co., produced multi-layer composites filters which is be able to capture particle with diameter in the nanoscale range [167].

Electrospun nanofibrous membranes have several attractive attributes that make them very attractive in separation technology, such as high porosity, pore sizes ranging from tens of nanometer to several micrometers, interconnected open pore structure, high permeability for gases and a large surface area per unit volume. All these properties make this kind of constructs as a good candidate in high performance air filters development.

Increased filtration efficiency has been explained considering the effect of slip flow at fiber surface [168] that is liable for a lower pressure drop as well as higher diffusion, interceptional and inertial impaction efficiencies. Donaldson Company, USA [169] has already commercialized nanofiber filter media called Ultra-Web® and the improved filters efficiency has been tested as regards airborne contamination and two different filters: standard cellulose and cellulose/nanofibers filters respectively have been compared. The latter provided an improvement in worker protection because four times less penetration of sub-micron dust occurred.

The filtration efficiency of conventional melt blown fabrics (35 g/m² density), respect to NaCl aerosol containing 100 nm particles, was compared with electrospun poly(ethylene oxide) nanofiber webs, 3 g/m², by Tsai and co-workers [170]. It has been pointed out that the performance was similar, but if the PEO nanofiber webs were increased to 16 g/m², its efficiency is comparable with high-efficiency–particulate-air (HEPA) filters made of non-woven glass fiber meshes.

Conventional air filter media were also covered with polyamide fibers (Hajra et al. [171], Li et al., [172]) in order to investigate filter performances. Hajra et al. [171] demonstrated that by the addition of nanofiber with average diameter of 150 nm affects the filter efficiency in term of quality factor (which is defined regardless of the filter thickness) which tends to increase. The improved filtration efficiency and its relationship with nylon fibers weight facing (from 0.03 to 0.5 g/m²) was also proved by Li and co-workers [172] who produced covering fibers with average diameters ranging from 120 to about 700 nm. The filter life was also improved, especially at weight coverage level of 0.1g/m² or lower due to the sufficient adhesion between the nylon-6 fibers and air filter media fibers.

Nanofibrous filtering media have been prepared and characterized by Barhate and co workers [173] who pointed out that the structural and transport properties of electrospun membrane depends on the distribution, deposition and orientation of nanofibers and then on the processing parameters. They were able to control the pore size distribution by controlling the drawing and collection rates. Further attention to electrospun membranes has been given by Gopal et al. [174] who proved Polyvinylidene fluoride (PVDF) nanofibers based membrane in order to separate 1.5 and 10µm polystyrene particles. Other polymers for filtering application were successfully electrospun by Schlossberger and co workers [175], who dealt with polystyrene (PS) and polyhedral oligomeric silsesquioxane (POSS) nanofibers which were characterized by a highly porous structure.

Small fibers in the submicron range, in comparison with larger ones, are well known to provide better filter efficiency at the same pressure drop in the interception and inertial impaction regimes. For nanometer-scale fibers, a second factor has to be taken into account that is the effect of slip flow at the fiber surface [176]. Filtration theory generally relies on an assumption of continuous flow around the fiber, with a no-slip condition at the fiber surface. The theory starts to break down when the scale of the fiber becomes small enough that the molecular movements of the air molecules are significant in relation to the size of the fibers and the flow field. Using a slip-flow model at the fiber surface can extend the useful range of continuous flow theory. The Knudsen number is used to describe the importance of the molecular movements of air molecules at the fiber surface to the overall flow field. The Knudsen number can be written as

$$Kn = \frac{\lambda}{r_f}$$

where λ is the gas mean free path (the dimension of the non-continuous nature of the molecules), and r_f is the radius of the fiber. When Kn becomes non-negligible, the continuous flow theory, which does not take into account the molecular nature of air, starts to break down. While there is no exact Kn above which slip flow will prevail, it generally needs to be considered when $Kn > 0.1$, and

definitely needs to be considered when Kn is around 0.25. For air at standard conditions, the mean free path is 0.066 microns; therefore, for fibers with diameters smaller than 0.5 microns, slip flow must be considered. In slip flow, the air velocity at the fiber surface is assumed to be non-zero. In other words, the air slips at the fiber surface as shown in Figure 34

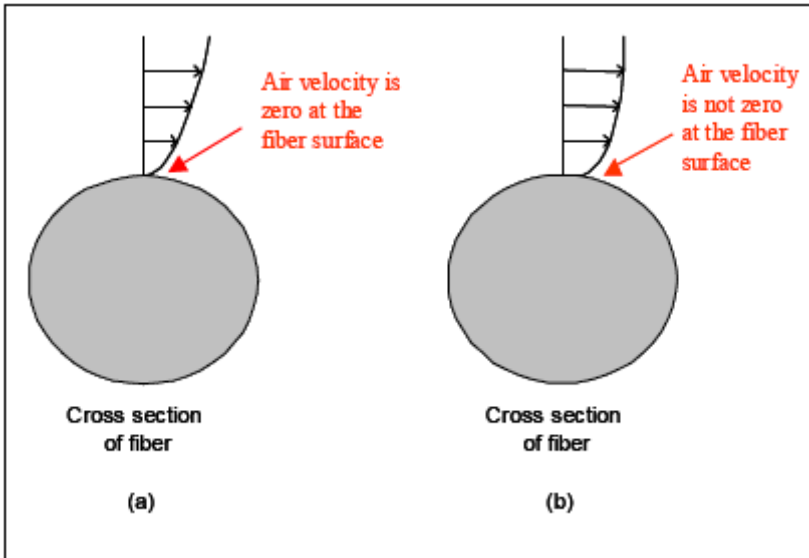


Figure 34 Velocity profiles at the fiber surface for (a) non-slip flow; and (b) slip flow

Due to the slip at the fiber surface, drag force on a fiber is smaller than that in the case of non-slip flow, which translates into lower pressure drop. On the other hand, the slip flow makes the portion of the air flowing near the fiber surface larger than that in the case of non-slip flow, which translates into more particles traveling near the fiber, resulting in higher diffusion, interception and inertial impaction efficiencies. The effects of slip flow on pressure drop and efficiency can be further illustrated by applying mathematical equations such as those by Stechina and Pich [177,178] in their valid range, although such results are not presented here as they are beyond the scope of this paper. Thus, the benefit of achieving better filter efficiency at the same pressure drop actually accelerates when fiber sizes are reduced below half micron.

Therefore, due to the dependence of efficiency and pressure drop on fiber sizes, and due to the benefit of having slip flow at the fiber surface, small fiber sizes such as those of 0.2 to 0.3 micron are highly desired for filtration applications.

In a fibrous filter the resistance or pressure drop of the filter is a result of the combined effect of each fiber resisting the flow of air past it. The pressure drop is based on total drag force of all the fibers and is given by Davies (1973):

$$\Delta P = \frac{\eta t U_0 f(\alpha)}{d_f^2}$$

where η is the viscosity, t is the filter thickness, df is the mean fibers diameter, U_0 is the face velocity defined by the ratio Q/A (Q the volumetric flow through the filter and A the cross-sectional area of the filter expose to the airstream) and $f(\alpha) = 64\alpha^{1.5}(1 + 56\alpha^3)$ for $0.006 < \alpha < 0.3$. However this empirical formula doesn't take in account the effect of gas slip at the fiber surface and because of this is quite difficult compare experimental results for pressure drop to the theoretical ones.

Electrospun nanofibers could be useful for enhancing ultrafiltration/nanofiltration membrane performance that usually exhibit low-flux and high-fouling. In this sense, Yoon et al. [179] presented a new type of high flux ultrafiltration/nanofiltration medium based on an electrospun nanofibrous scaffold (e.g. polyacrylonitrile, PAN) coupled with a thin top layer of hydrophilic, water-resistant, but water-permeable coating (e.g. chitosan) as shown in Figure 35. The membrane, based on electrospun PAN scaffold with an average diameter from 124 to 720 nm and a porosity of about 70%, together with a chitosan top layer having a thickness of about 1 μm , although not yet fully optimized, exhibited a flux rate that is an order magnitude higher than commercial nanofiltration membranes in 24 h of operation, while maintaining the same retention efficiency ($> 99.9\%$) for oily waste-water filtration [179].



Figure 35 Fabrication schematics of the electrospun PAN scaffold with a chitosan coating layer.

Madhugiri et al. [180] applied electrospinning process in the production of molecular sieve fibers using different organic templates and silica sources in order to reproducibly obtain a high density mesoporous molecular sieves, such as SBA-15, and DAM-1 (Dallas Amorphous Materials #1, a novel, hexagonal mesoporous material) and the fibers were characterized by diameters in the range of a micron to a few hundred nanometers.

These are only a few example of the high potential of nanofibers in filtration and it was estimated the future filtration market up to US \$700 billion by the year 2020 [181].

Moreover, thanks to their properties, electrospun nanofibers membranes have been found to be a good candidate for protective clothing processing in order to adsorb deadly chemical agents such as mustard gases (iprite), nerves agents, radioactive alpha and beta particles and, at the same time, they result to be permeable to water vapor and air and insoluble in all solvents. The neutralization of chemical agents can be attributed to their great surface area (due to the high surface to volume ratio) as suggested by Smith et al. [182], and the high porosity of the electrospun nanofibers allows a good resistance to the penetration of chemical harm agents in aerosol form (Gibson et al. [183]). Other studies performed by Gibson and co-workers [184,185], revealed a minimal impedance to moisture vapor diffusion and a greater trapping aerosol particles if compared with conventional textiles.

Electrospun nanofibers can also be exploited in filter mask processing. The conventional designs contain activated charcoal impregnated media and, if a High Efficiency Particulate Air (HEPA) is included, particles ranging from 0.13-15 μm can be absorbed. Nanofibers, because of their high surface area, could improve the capture of chemical agents as well as block out the biological warfare agents [186].

Several research centers are working on nanotechnologies development in order to improve the protective clothing properties. The Institute for Soldier Nanotechnologies (ISN), a division of the Massachusetts Institute of Technology (MIT), USA, has a millions contract from the U. S. Army for developing light weight and high-tech battle suit. The National University of Singapore (NUS) deals with protective systems for chemical and biological defense in term of functionalized nanofibers for selective binding to the warfare agents and their decomposition into non-toxic products [1]. The latter can be achieved and increased thanks to the high surface area and the light weights of the nanofibers. A selectively permeable face mask has been developed made of two distinct groups of fibers, one of which is able to capture and decompose mustard gases and the other one oxidizes and deactivates nerve agents. Thank to nanofibers pore size, less than 500 nm, bacterial spore can be blocked out and the high porosity of the filter media, combined to the increased permeability, seems to be enough to avoid the issues related to the low oxygen permeability [1].

Since the potential of the nanostructured materials, high efforts are in progress to improve nanofiber properties for high tech materials development.

Electrospun nanofibers could be a good candidate for affinity membrane applications, especially for protein purification purpose, as suggested by different authors such as Bamford et al. [187] who functionalized electrospun polyurethane with protein A for IgG purification. Also Ma et al. [188]

investigated electrospinning of cellulose acetate as affinity membrane; a nonwoven mat with diameter ranging from 200 nm to 1 μm was produced by electrospinning, and after a heat and alkaline treatments respectively, which were necessary to obtain regenerated cellulose (RC) nanofiber, a general dye ligands, Cibacron blue F3GA (CB), was covalently attached on the surface of RC membrane (RC) that was characterized in term of mechanical properties, porosity, water permeability. The investigation on the activity of the CB was carried out looking on its interaction with serum albumins (BSA) and bilirubin that were tested by batch wise adsorption method and results of the static adsorption tests are shown in Figure 36.

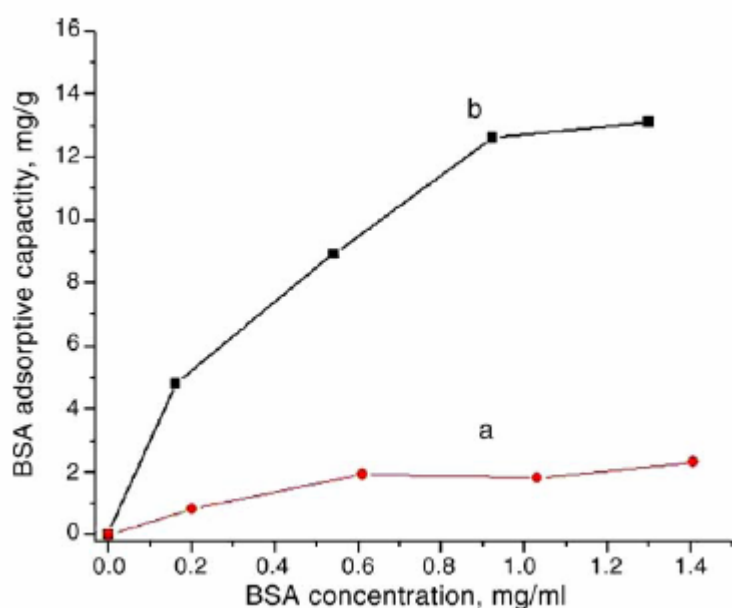


Figure 36 BSA adsorption capacity on the (a) RC nanofiber membrane and (b) CB immobilized RC nanofiber membrane.

1.6.2 Catalysis and sensors

Chemical reactions employing catalysis are a fundamental part in chemical processes due to the possibilities of increased reaction rate as well as mild processing conditions. Immobilized catalysts are extensively used due to their stability, easiness separation and their availability for continuous processes. Their efficiency depends both on the pore size and distribution and on the diffusion limitations of the substrate material [189]. In this terms, nanofibers represent a good candidate as catalysts support because of their great surface area and their size, in nanoscale range, that allow to neglect the diffusion term. Moreover nanofibers can also be characterized by high catalyst loading [189].

Since chemical and physical properties of nanoscale metal clusters are quite different from those of bulk metals, they have been gained attention from several research groups as regards their catalytic activities. So electrospun nanofibers are used as a scaffold for nanoparticles immobilization. For instance nanoclusters of palladium on poly (acrylonitrile) and acrylic acid (PAN-AA) nanofibers

were synthesized by direct reduction of PdCl₂ in aqueous hydrazine media by Demir et al. [190]. The catalytic properties of PAN-AA copolymer containing Pd nanoclusters (the amount of Pd on the electrospun fiber mat was estimated on the order of 50 mg/g) were investigated via hydrogenation of dehydrolinalool (3,7-dimethyloktaen-6-in-1-ol-3) (DHL). It has been reported that the catalyst PAN-AA (5.4% AA) containing 0.4% of reduced Pd (without additional modification) is more active and selective if compared to the current catalyst, i.e., Pd particles on Al₂O₃ supports, as confirmed by the reaction rate data in term of m³ H₂/mol Pd·mol DHL.

It has also been reported the production of electrospun PAN/Ag nanoparticles [191-193]. Yang et al. [191] obtained and characterized by TEM analysis the PAN/Ag nanofibers using AgNO₃ as a precursor of Ag nanoparticles, as shown in Figure 37. Differently Lee et al. [192] developed a simple one-step method of preparing of ultrafine PAN fibers containing Ag nanoparticles, using dimethylformamide both as a solvent and as reduction agent of the AgNO₃. Then, further investigation by Wang et al. [193] led the structural characterization of PAN/Ag nanocomposite film in term of average diameter of Ag nanoparticles (10 nm) and graphitization of PAN that probably was affected by the function of Ag nanoparticles as a catalyst for dehydrogenation of hydrocarbon compound.

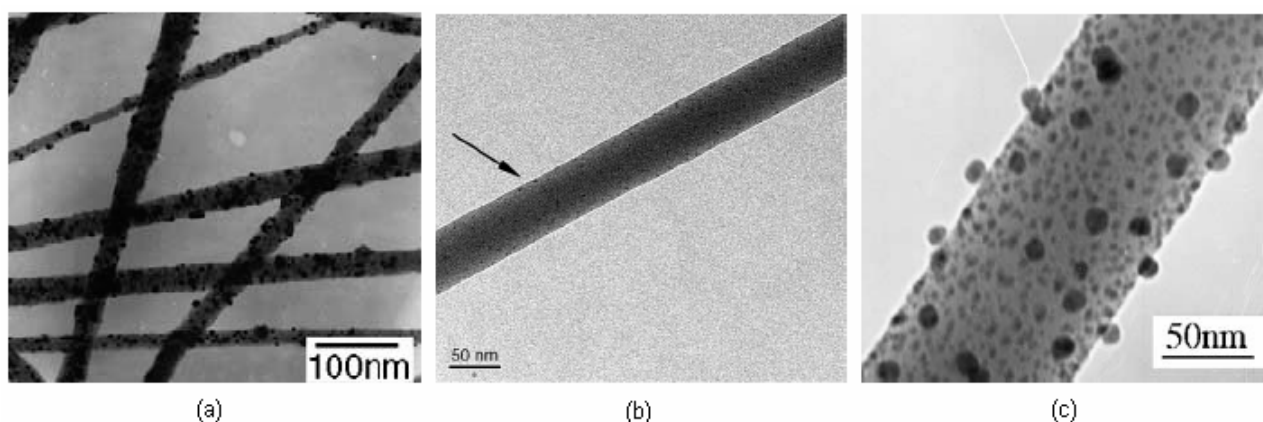


Figure 37 (a)TEM micrograph of PAN/Ag nanofibers by Yang et al. (b) TEM micrograph of ultrafine PAN/Ag nanofibers by Lee et al. (c) TEM micrograph of a single PAN nanofiber embedded Ag nanoparticles.

Since metallic nanostructures with various shapes have been shown to have catalytic properties useful in heterogeneous catalysis, biological labeling and photonics, Li et al. [194] proposed a different way for metal/semiconductor composites fabrication by deposition of gold nanoparticles on electrospun nanofibers of titania through the photocatalytic reduction of HAuCl₄ in the presence of an organic capping reagent which controlled the final nanostructure produced (gold nanoparticles, fractal nanosheets or nanowires) as shown in Figure 38.

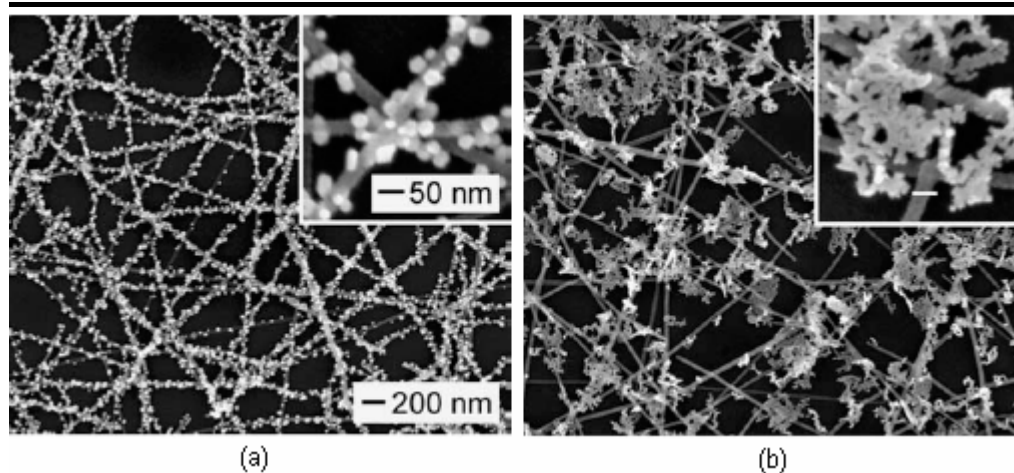


Figure 38 (a) SEM images of gold nanoparticles on TiO₂ nanofibers; (b) fractal nanosheets or nanowires of gold on TiO₂ nanofibers obtained for low concentration ($< 5.0 \cdot 10^{-6} \text{M}$) of capping reagents.

One-dimensional arrangements of Au nanoparticles arrays within poly(ethylene oxide) nanofibers were also obtained via single-step processing route by Kim et al. [195] who electrospun a PEO/Au solution in chloroform using the intrinsic nature of semicrystalline PEO as a template to arrange the Au nanoparticles within the fibers during electrospinning. One-dimensionally arranged chainlike arrays of Au nanoparticles were revealed by TEM analysis as shown in Figure 39 and it has been pointed out that Au nanoparticles affected the PEO molecular conformation which changed from helix to trans planar zigzag structure, since they acted as nucleating site during PEO crystallization. Graphitic carbon nanofibers were also used (Rodriguez et al. [196]) as a catalyst support of iron particles and the conversion of hydrocarbons has been strongly increased if compared with active carbon and γ -alumina.

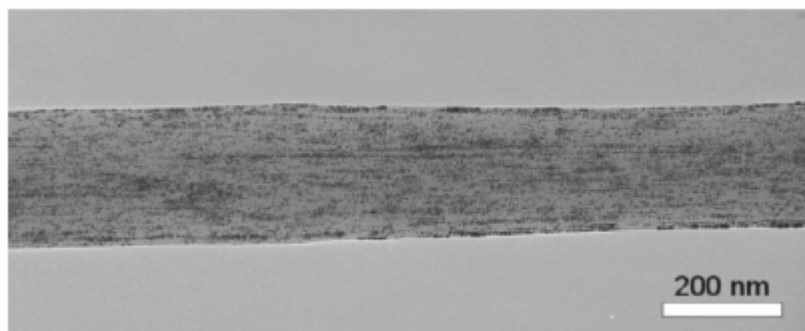


Figure 39 TEM micrograph of 1D chainlike arrays of Au nanoparticles.

However nanofibers can be in their own way catalysts, just look at to the cerium dioxide (CeO₂) nanofibers produced by Yang et al. [197] that could be used in automotive catalysts because of its unique characteristic of facile Ce IV and Ce III switching. These oxide nanofibers were obtained by using calcination treatment of electrospun thin fibers of polyvinyl alcohol (PVA)/cerium nitrate composite as precursor. The CeO₂ nanofiber mat was characterized by high surface area and small

pore size, thus an high catalytic activity has been expected and it may also has possible a potential use of these nanofibers in high-storage capacitor devices.

Among metal oxides, titanium oxide has gained much interest since its potential applications in catalysis, sensors and high photovoltaic performances as reported in literature [198,199]. Madhugiri and co-workers [198] investigated the preparation of mesoporous titanium dioxide fibers by electrospinning; their characterization (by microscopy and vibrational spectroscopy) and photocatalytic experiments of calcinated TiO₂ nanofibers activity on the oxidation of phenol and formic acid were carried out in a traditional annular quartz liquid-phase photocatalytic reactor. Although photocatalytic properties of the calcinated TiO₂ fibers fall well below those of commercial catalysts an improved reactivity could be achieve working on fiber size and porosity. Li et al. [113] proposed the production an the characterization of TiO₂ nanofibers using a poly(vinyl pyrrolidone) with titanium tetra(isopropoxide) (Ti(OiPr)₄) solution as precursor. Moreover He and Gong [199] studied TiO₂-Pt based photocatalysts that has been demonstrated to enhance the degradation of plastic materials such as poly(vinyl alcohol) (PVA) under UV irradiation. They noted that the effectiveness of photocatalytic degradation for composite nanofiber is much greater compared with that for composite film under the same conditions and the mechanism proposed was the direct oxidation pathway by direct electron transfer from reaction substrates to hole on the photocatalyst surface under UV irradiation.

Jia et al. [200] dealt with bioactive polystyrene (PS) nanofibers with a typical diameter of 120 nm and their catalytic efficiency for biotransformation was tested. The electrospun nanofibers were functionalized by chemical attachment of a model enzyme α -chymotrypsin. Moreover, a high catalytic activity and improved enzyme stability have been noticed.

In the present literature electrospun polymer nanofibers have gained more attention in sensors processing, probably thanks to their high surface volume ratio and then high sensivity, as well as quick response time with a targeted material, can be expected from them.

Nanofibers based sensors translate a physical or chemical responses resulting from a reaction between a target material and a sensing material. An electrical signal has produced as output and a quantitative measurement of the tested substances can also be allowed [1].

The principle of nanofibers sensors is to translate a physical or chemical responses resulting from a reaction between a target material and a sensing material. The latter produces an electrical signal as output and a quantitative measurement of the tested substances can also be allowed [1]. Then electrospun nanofibers play a fundamental role in gas sensors, chemical sensors, optical sensors and biosensors processing. As regards gas sensors, several examples have been reported about NH₃ because its determination is very important not only for environmental monitoring, but also gas

alerting in industrial and defense field. Among sensing materials for ammonia detecting, various examples have been reported but not all these prepared sensors are able to detect ammonia at ppb level [201]. Ding and co-workers [202] proposed a novel gas sensor composed of electrospun nanofibrous membranes of poly(acrylic acid) (PAA) and poly(vinyl alcohol) (PVA) and quartz crystal microbalance (QCM). The latter is one of the acoustic wave techniques that can detect the mass change as a function of the reaction between a coating material and the target gas. The choice of the polymer blend solution has been explained because of the probable interaction between the carboxyl groups of the PAA and ammonia. The nanofibrous membranes coated QCM sensors sensing properties were investigated at 50 ppm NH_3 level by measuring the resonance frequency shifts of QCM which is due to the additional mass loading. Their sensitivity was depending on different factors such as the content of PAA component and the relative humidity. In particular an increase in PAA concentration results in increased sensitivity even though the first exposure was markedly different from the subsequent exposures, due to an irreversible absorption processes originated from some strong interactions between NH_3 molecules and carboxyl groups of PAA that caused the shift of the base line frequency. In a subsequent work, the same authors [201] improved the sensitivity of QCM sensors at ppb level of NH_3 covering the latter with only PAA electrospun nanofibers. The sensitivity of fibrous membranes coated QCM is four times higher than sensitivity of casting film coated QCM sensors.

Still regarding NH_3 detection, Liu and co-workers [203] utilized the semiconductor properties of polyaniline (PANI) for developing nanowire sensors. This can be possible because electron-supplying gases such as NH_3 reduce the charge-carrier concentration and consequently the conductivity of the conducting polymer. Scanning tip electrospinning was used in order to deposit isolated and oriented polymeric nanowires of polyaniline/poly-(ethylene oxide) (PANI/PEO) and NH_3 detection was performed for gas concentrations as low as 0.5 ppm with rapid response and recovery time.

In response to the growing demand of cheaper, simpler and higher sensitivity detection device architectures, many advances are in progress for chemical and biological sensors. Aussawasathien et al. [204] investigated the sensing properties for humidity of lithium perchlorate (LiClO_4) doped-poly (ethylene oxide) (PEO) ionically-conducting electrospun nanofibers. The sensing device was made of a glass substrate upon which an interdigitated comb-shaped aluminum electrode took place as a collector of the electrospun nanofibers. All the tests were performed taking as a reference the corresponding film-type humidity sensor of the same PEO/ LiClO_4 solution spin-casting. Results showed higher sensitivity probably due to the higher surface area.

Kwoun et al. [205] also modified the conventional piezoelectric sensors in order to detect chemicals. A poly-lactic-acid-co-glycolic acid (PLA-GA) electrospun mat were deposited on a sensing interface and its hydrophobic properties against water, and hydrophilic properties against propanol are exploited for chemicals detection such as benzene gas.

As regards biosensors, Aussawasathien et al. [204] exploited the conductivity changes of the camphosulfonic acid (HCSA) doped polyaniline/polystyrene (PANI/PS) nanowires as a component for glucose sensors. The electrospun non-woven mat was put on a sticky tape and after drying, glucose oxidase was immobilized on this substrate. It has been proved that the amperometric response from the latter sensing device was greater than the HCSA-PANI/PS film sensor.

Since the urea levels are very important in medical diagnosis, environmental and bioindustrial analysis, Sawicka et al. [206] proposed a study regarding an innovative technique for enzyme immobilization which uses electrospinning process. Polyvinylpyrrolidone (PVP) in ethanol solution was added in urease and then electrospun on a collector in order to obtain a non-woven mat. The electrospun membrane acted as catalyst in the hydrolysis of various urea solutions and it has been suggested that the activity of the enzyme has been preserved as well as excellent biosensing properties due to the large surface area that offers an improved adsorption rate and therefore reduces the response time.

Moreover, still regarding sensors, Ramakrishna et al. [1] recently developed Nylon 6 nanofibers incorporated with gold particles for glucose sensing. The reaction between glucose and glucose oxidase can be traced looking at the hydrogen peroxide (H_2O_2) or oxygen concentration [1] since H_2O_2 is further decomposed to oxygen and two protons and electrons. Using gold particles on the nanofibers surface, thus enhancing the conductivity of the fibers, the detection of glucose level may be done through a potentiostat instead of measuring H_2O_2 or O_2 level, which is more difficult. An improvement in biosensor sensitivity has been achieved (Lala and Sanstry [207]) thanks to the electrostatic interactions between the Au/nanofibers and a tetrameric protein “avidin” and the further high affinity biotinylated glucose oxidase-avidin. The developed sensor measured glucose concentrations from solutions ranging from 1 M to 1 μ M with a response time of 130s and sensitivity levels of 0.113 μ V/mM [1].

Wang et al. [208] combined the techniques of electrospinning and electrostatic layer-by-layer adsorption in order to produce a highly sensitive optical sensor by assembling fluorescent probes onto electrospun cellulose acetate electrospun mat, which showed fluorescent quenching as function of the concentration exposure of both methyl viologen and cytochrome c in aqueous solutions. Thanks to its high surface area/volume ratio and the strong interaction between the fluorescent conjugated polymer and the analytes, very low concentrations (at ppb level) of analytes can be

detected. Optical sensors, which exploit the fluorescence quenching of the sensing material against the targeted chemical molecules, have also been reported in literature by Lee et al. [209], and Wang et al. [210]. The first group investigated fluorescent emission response of acrylate polymers with dinitrotoluene (DNT) which is a toxic chemical occasionally noted in drinking water. The second one dealt with electrospun membrane based on the cross-linked poly(acrylic acid)-pyrene methanol (PAA-PM) and polyurethane for metal ions (Fe^{3+} , Hg^{2+}) and DNT detecting. It has been pointed out that the sensitivities of electrospun membranes are 2 to 3 orders of magnitude higher than those obtained previously from the thin film sensors.

1.6.3 Electrical applications

Since the increased necessity of limiting environmental problems related to the CO₂ emissions of developed countries, many efforts are in progress in the “clean energy system” research. This means looking at different energy system such as wind generator, solar power generator, hydrogen battery and polymer batter. Several conductive polymer as Poly(vinylidene fluoride) (PVDF), Poly(acrylonitrile) (PAN), and poly(methyl methacrylate) (PMMA) have been extensively studied for applications in rechargeable batteries.

Choi and co-workers [211] produced microporous fibrous membranes from PVDF solutions with different polymer contents, using the electrospinning technique. Electrospun nanofibers, with average diameter included from 0.45 to 1.38 μm , presented an increase in ionic conductivity as a function of the decrease in average diameter of the fibrous membrane, probably due to its high electrolyte uptake. The interaction between the electrolyte molecules and the PVDF with a high crystalline content may have had a minor effect on the lithium ion transfer in the fibrous polymer electrolyte, unlike in a nanoporous gel electrolyte.

The prototype cells were assembled by sandwiching a given fibrous polymer electrolyte between two stainless steel blocking electrodes (2 cm \times 2 cm), and was vacuum sealed with a polyethylene-coated aluminum pouch. The cell performance of the fibrous polymer electrolytes was evaluated throughout cycle tests with cutoff voltages of 4.2V for the upper limit and 2.75V for the lower limit at the C/2-rate (1.67 mA/cm²) cycles. It has been noted a very stable charge–discharge behavior and little capacity loss under current constant voltage conditions.

As regards the interfacial resistance between lithium and the fibrous polymer electrolytes generally increased with the storage time and it is relatively lower compared to other gel polymer electrolyte. It has been reported that increasing the pore size of the PVDF matrix can help to enhance the ionic conductivity and thus improve cell rate capability. Choi et al. [212] carried out a further investigation on a thermal treatment of electrospun PVDF nanofibers mats in order to improve their

physical properties and dimensional stability that are usually lower because of the absence of interfiber bonding.

However conducting polymers are extensively investigated from different research groups as active electric components in the fabrication of the field effect transistor (FET). The reason that leads to use conducting electrospun polymers can be found in the necessity of size reduction of these devices. This goal can be achieved increasing component density in circuits due to electrospun nanofibers (differently to thin film form) and then the obtained design is going to be one-dimensional. Gonzalez et al. [213] compared electrical properties of nanofibers based FET to the conventional thin film FET. The conducting polymer chosen was the poly(3-hexylthiophene-2,5-diyl)(P3HT) that was electrospun onto a doped Si/SiO₂ wafer and electrically contacted to the source and drain finally to form a FET. Up to now, thin FET film still reveals better characteristics in comparison to FET nanofibers because of the high surface volume ratio, which makes it more susceptible to being doped by atmospheric oxygen and the current –voltage (I–V) curves affected by adsorbed water vapor. In order to avoid this condition, pure starting materials and inert environment could be helpful for maintaining the superior performances seen in thin film FET.

Electrospun piezoelectric polymers are being developed for use as a component on lightweight wings for micro-air vehicles (MAV) as reported by Pawlowski et al. [214]. They electrospun a copolymer of PVDF and trifluoroethylene (TrFE) onto MAV wings (Figure 40). Strength and elasticity of the fibrous coatings have been shown to be consistent with the small diameter of the individual fibers and the complex network that the fibers created. Moreover because of the fibrous nature of the mats, it has been noticed a property knockdown compared to the film, and in preliminary attempts at fiber actuation, the fiber-coated wing frames exhibited a perceptible vibration upon excitation with a 2 kV (peak-to- peak) sine wave at 6.7 Hz [214].

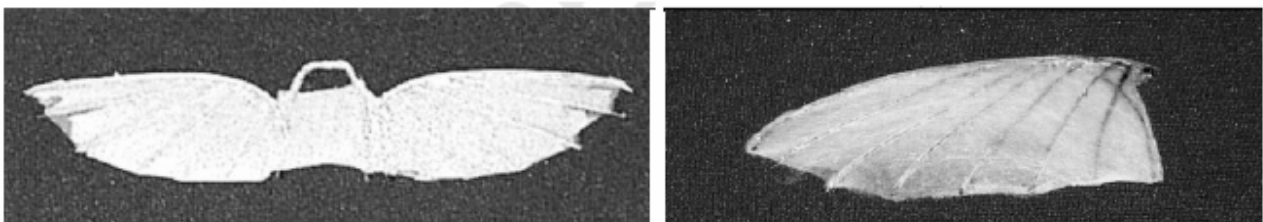


Figure 40 Trifluoro Graft Elastomer (TrF1) fibers electrospun onto MAV wing frames; (a) double wing configuration, (b) single wing configuration.

Research in electric field moves also toward the development of novel electrode materials for high storage capacitors devices as reported by Kim et al. [215] and Guan et al. [216]. Since carbonaceous materials in their various form (powder, fabric and carbon nanotube based nanocomposites) are candidates for electrodes of the supercapacitor, Kim et al. [215] focused their studies on the production of nanofibers carbon web which could be easily used for electrodes of supercapacitor

and secondary battery without further treatments, and therefore they should provide high performance due to their large specific surface area and low electrical resistivity. Activated carbon nanofibers (ACNFs) were successfully produced by the steam supplied activation of electrospun nanofibers of polybenzimidazol (PBI). The performances of the electrochemical double layer capacitor from PBI-based ACNFs were evaluated, and it has been pointed out that the specific surface area increased with the activation temperatures of 700-800 °C from 500 to 1220 m²/g and then decreased with further increase in activation temperature. However the ACNFs activated at 850°C exhibited the highest capacitance at high discharge current density and the lowest electrical resistance values. This behavior has been supposed because the capacitor properties are function of activation conditions which affected the porous structure of the nonwoven mat.

According to Guan and co-workers [216] nanofibers of NiCo₂O₄ were obtained using the composite fibers of poly(vinyl alcohol) (PVA)/cobalt acetate/nickel acetate as a precursor, due to their potential as electrode for oxygen reduction and water electrolysis. It has been supposed they present greater electrocatalytic properties due to their high surface areas.

1.6.4 Composite reinforcing

Reinforced fibers materials are extensively used in several applications field because they show superior structural properties such as both high modulus and strength if compared with conventional materials. To this end, nanofibers represent a good candidate for reinforcing composite, as revealed from Kim and Reneker [145] who tested the reinforcing effects of electrospun nanofibers of polybenzimidazole (PBI) in an epoxy matrix and in a rubber matrix. The results regarding the fracture toughness and the modulus of the nanofiber (15 wt%) reinforced epoxy composite showed an increased value of both in comparison to an epoxy composite made with PBI-whisker-like particles.

Tests carried out on filled elastomeric matrix (styrene-butadiene rubber, SBR) with the same PBI chopped nanofibers, also revealed a positive effects on the mechanical properties, such as the Young's modulus and tear strength were ten times and twice higher, respectively, than the pure SBR. Electrospun nanofibers of PBI were also used by Dzenis and Reneker [217] in order to modify the interlaminar fracture resistance of unidirectional laminated carbon-epoxy composites and an increase of the critical energy release rate by 15% in the Mode I (opening mode) and by 130% in the Mode II (forward mode) was noticed, where Mode I and Mode II are two crack surface displacement modes usually employed in fracture composites testing.

Bergshoef and Vancso [218] dealt with Nylon 4,6 nanofiber reinforced epoxy composite films, and mechanical tests were performed using monolithic matrix films as a reference; a considerable increase of both tensile stiffness and strength have been reported.

Still regarding Nylon nanofiber reinforced composite materials, Fong et al. [219] reported a research on a dental restorative composite resins based on BIS-GMA/TEGDMA (extensively 2,20-bis-[4-(methacryloxypropoxy)-phenyl]-propane with tri (ethylene glycol) dimethacrylate) that was impregnated with electrospun Nylon 6 nanofibers (50/50, mass ratio). Flexural strength, elastic modulus and work of fracture were respectively 36%, 26%, and 42% higher than the obtained values for the neat resin. A difference on morphology of fracture was also noted by SEM analysis (Figure 41) and it was suggested that the presence of nanofibers deflected the crack and the numerous fracture lines and steps noted on the fracture surface, suggested the energy consumption during breaking.

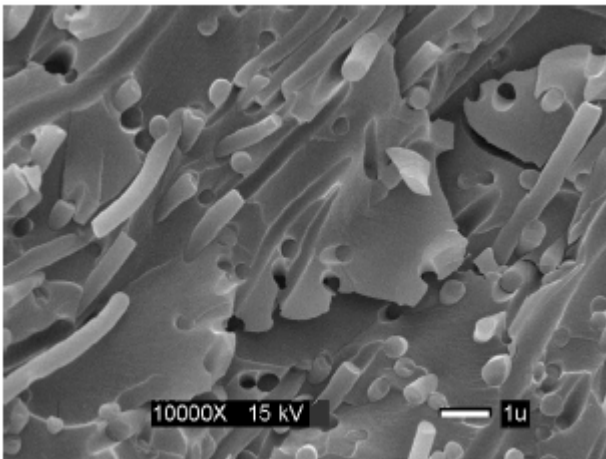


Figure 41 SEM image of the fracture surface. It has been shown the presence of the nanofibers in the composite resin.

Another idea that seems to be very promising from a mechanical and electrical perspective, regards the dispersion or alignment of carbon nanotubes in a nanofibers matrix to form a reinforced composite. Mathew and co-workers [220] investigated electrospun poly(butylene terephthalate) (PBT) reinforced with 5 wt% of multi-walled carbon nanotubes. This idea comes from the excellent properties of carbon nanotubes such as stiffness and strength. The resultant fibers have shown broader distribution in diameter compared to no-reinforced electrospun PBT, rougher surface morphology, improved thermal stability and mechanical modulus, which increased nearly three times. Also PAN were embedded with single wall carbon nanotubes (SWNT) by Ko et al. [221] who reported an increased on thermal stability, respect pure electrospun PAN, and a strong reinforcement effect by doubling the tensile modulus with less than 10 wt% reinforcement. It has been suggested that the reinforcing action of carbon nanotubes depends on the nanotubes distribution in the matrix as well as the interfacial adhesion between nanotubes and polymers. Thus,

they are liable for reduced stress concentration, dissipation of energy by pullout and hindering crazing extension.

Besides nanotubes, also graphite nanoplatelets were used in polymer electrospinning for enhancing mechanical properties. Nanoplatelets/PAN nanocomposite fibrils were characterized in term of elastic properties by Mack et al. [222] who dispersed graphite nanoplatelets in a 7 wt% PAN solution in DMF, that was subsequently electrospun. It has been reported that the elastic modulus of the nanocomposites was directly depending on the different contents in nanoplatelets (from 1 to 4 wt%), increasing from 77 to 133 GPa.

In another work Ko et al. [223] processed carbon nanotube reinforced spider silk. Transgenic spider silk with different combinations of silk protein was electrospun adding a small amount, 1wt%, of SWNT; random and aligned nanofibers with diameters of 10 nm were obtained. Tensile testing showed a 10-fold increase in modulus, 5-fold increase in strength, and 3-fold increase in toughness compared to the reference.

Single-walled carbon nanotube have also been investigated by Haddon et al. [224], who reinforced polystyrene (PS) and polyurethane (PU) matrix prepared by electrospinning. SWNT filled polystyrene nanofibers have been prepared wherein the SWNT bundles are oriented parallel to the nanofiber axis. The effects of SWNT on the mechanical properties were studied on the SWNT-PU composites membranes which showed a significant enhancement in the mechanical properties when compared to the pure polymer membrane depending on the type of SWNTs used (as prepared AP-SWNT and an ester functionalized EST-SWNTs were tested). For example, composites membrane showed an increase of tensile strength by 46 % and 104 % with AP-SWNTs and EST-SWNTs respectively, if compared to pure PU membrane and the tangent moduli were found to be 215 % for AS-SWNT composites, and 250 % for EST-SWNT composites, higher than pure PU membranes. It has been suggested that better mechanical properties for the EST-SWNT composites could be due to improved dispersion of the SWNTs, but could also be due to the polar functionalities in the SWNT ester groups which give the opportunities for hydrogen bonding between the polymer and matrix or to amidation reactions between free amine in the polyurethane and the ester functionality in the SWNTs [224]. As regards the reinforcement capability, Chronakis et al. [225] remarked that it is strongly related to the intrinsic crystalline quality and the straightness of the embedded nanotubes as well as their final orientation in the polymer matrix.

1.6.5 Bioapplications

Because of their peculiar structure properties, electrospun nanofibers have gained much attention in biomedical research area, especially for tissue engineering, wound dressing, affinity membranes and drug release.

Before starting this sub-section covering some of the bioapplication features, it is important to understand the reasons that make electrospinning one of the best available techniques employed in current research. Since almost all of the human tissues and organs are deposited in hierarchical fibrous forms or structures realigned in nanometer scale, electrospinning represents a good candidate for these applications thanks to the opportunity of processing a huge variety of polymers. On the other hand, core-shell nanofibers have been shown to be useful in drug release as well as electrospun nanofibers could also act as a bacterial barrier in wound dressing or could promote the wound healing. In any case biological applications count the electrospinning of a wide range of natural and synthetic polymers such as collagen, chitosan, (PCL), (PU), (PLGA), (PLA), (PGA), and various blends of them, characterized by good biocompatibility, biodegradability and good mechanical properties.

1.6.5.1 Tissue engineering scaffold

As suggested by Langer and Vacanti's definition, tissue engineering is an interdisciplinary field that applies the principles of engineering and the life science toward the development of biological substitutes that restore, maintain or improve tissue function [226]. Thus, the fundamental purpose of a synthetic scaffold is to mimic mechanical and biological properties of the native extracellular matrix in order to modulate cellular behavior until repair or regeneration occurs. The first property required is biocompatibility which is a complex notion that has to be interpreted as a series of events or interactions happening at the tissue/material interface whose outcome must be satisfactory or optimal [227]. Moreover the materials used in this application shall have a high surface/volume ratio united to a high porosity of the scaffold, in order to enhance cells adhesion as well as their proliferation and their capability of exchange nutrients in vitro and in vivo culture. The last, but not the least important property required is the biodegradability of the tissue scaffold in order to avoid a second removing surgery, and the rate of degradation should be of the same order of the neo-tissue formation rate [228].

In order to produce structure with similar behavior of the natural extra cellular matrix, several biopolymer based scaffold were studied. For instance, Bhattarai et al. [229] investigated a novel biodegradable poly(p-dioxanone-co-l-lactide)-block-poly(ethylene glycol) (PPDO/PLA-b-PEG) copolymer scaffold (characterized by nanofibers of average diameters of 380 nm, median pore size of 8 μm , porosity more than 80% and mechanical strength 1.4 MPa), as well as fibroblast NIH 3T3

cell proliferation and morphology of cell–matrix interaction with the electrospun nanofibrous matrix. Their data suggested that fibroblast cell seeded on the structure tend to maintain phenotypic shape and cell growing has been guided according to nanofiber orientation; all these considerations make this scaffold as a good candidate to substitute extracellular matrix.

Bhattarai et al. [229] presented also chitosan-based (chitosan/polyethylene oxide (PEO)) electrospun nanofibers with an average fiber diameter controllable from a few microns down to 40 nm. Cell adhesion and spreading of osteoblast and chondrocytes, as well as cells interaction with the nanofibrous membrane, were studied by SEM analysis as reported in Figure 42.

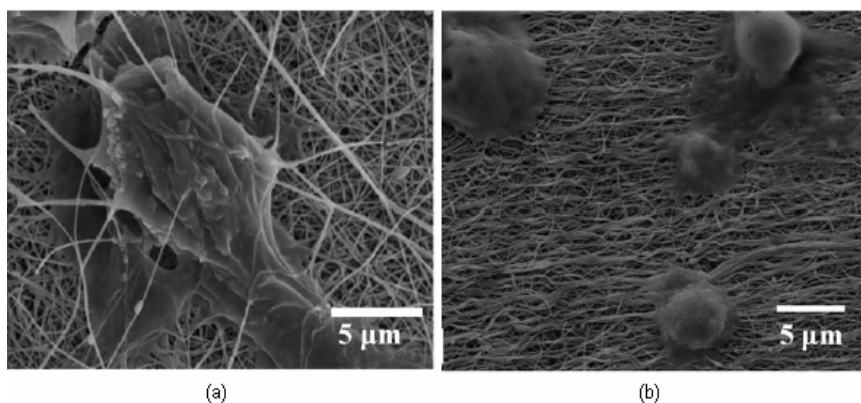


Figure 42 SEM image of osteoblasts (MG-63) (a) and chondrocytes (HTB-94) (b) seeded on the chitosan/PEO(90/10) scaffold after 5 days culture.

The issue for which an electrospun scaffold could be design regards blood vessels, cartilage, bone, nerve or skin.

Artificial blood vessel can be based on collagen scaffolds or biodegradable scaffolds. Kidoaki et al. [151] investigated multi-layering electrospinning and mixing electrospinning (Figure 43) for a mesoscopically ordered structure scaffolds composed of nano- and microscale fiber meshes. A trilayered electrospun nano/microfiber mesh (type I collagen, ST-gelatin, and segmented polyurethane, SPU) and a mixed electrospun-fiber mesh segmented polyurethane (SPU) and poly(ethylene oxide) (PEO) were produced. A bilayered tubular construct that could be a prototype scaffold of artificial grafts of miming the native structure of the blood vessel [231] has been fabricated, using thick SPU microfiber mesh as an outer layer and a thin type I collagen nanofiber mesh as an inner layer as shown in Figure 44.

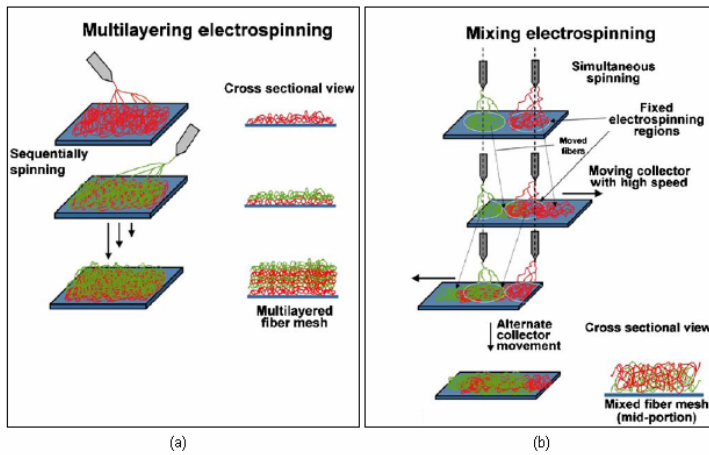


Figure 43 Multi-layering and mixing electrospinning techniques.

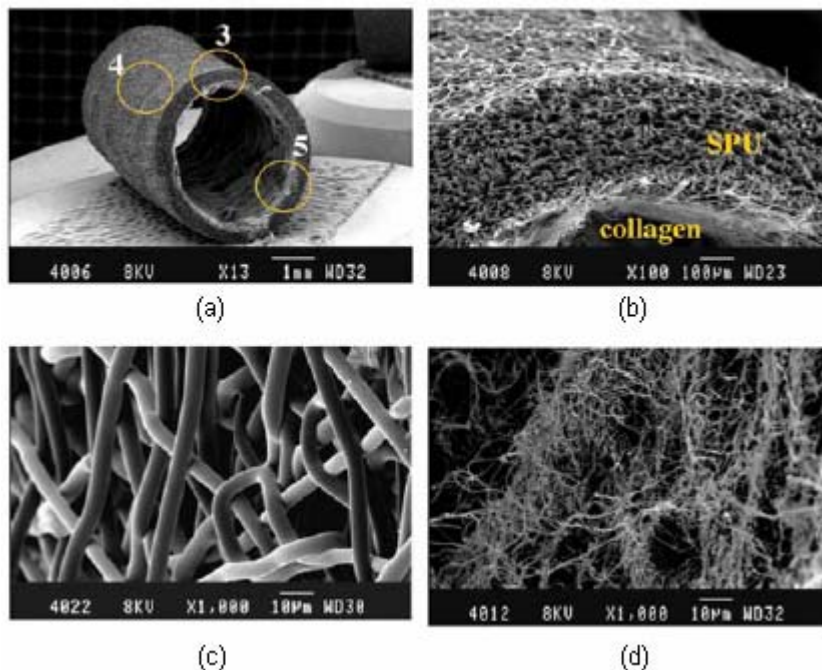


Figure 44 Figure 43 Fabricated bilayered tubular construct of SPU/collagen. (a) SEM image of the tube; (b) Magnified image of region 3 in photo (a); (c) Magnified images of the outer layer of region 4 in photo (a); (d) Magnified images of the inner layer of region 5 in photo (a).

Moreover Vaz et al. [232] proposed another candidate for blood vessel repair, which was a bi-layered tubular scaffold composed of a stiff and oriented PLA outside fibrous layer and a pliable and randomly oriented PCL fibrous inner layer (PLA/PCL). It has been obtained performing a sequential multilayering electrospinning on a rotating mandrel-type collector. The capability to promote cell attachment, proliferation and migration, was tested seeding the scaffolds with 3T3 mouse fibroblasts and later human venous myo-fibroblasts (HVS). In both cases, the cell-polymer constructs were cultured under static conditions and after 4 weeks culture time, the quantitative protein analysis of the extracellular matrix revealed values of collagen and glycosaminoglycans reaching 8 and 26%, respectively, of those found on native valve tissue (porcine pulmonary valve was used as a reference). However, the cell content was high in the constructs (64% of the native

value), possibly reflecting that tissue growth is still in progress. The findings suggest the feasibility of multi-layering electrospinning to design scaffolds with a hierarchical organization through a layer-by-layer process and control over fibers orientation. The resulting scaffolds achieved the desirable levels of pliability (elastic up to 10 % strain) and proved to be capable to promote cell growth and proliferation.

As regards conventional materials used in vascular grafts, Ma et al. [233] proposed polyethylene terephthalate (PET) for obtaining non-woven nanofiber mat and compared its performance with PET nanofibers activated throughout gelatin grafting method. Cell proliferation and viability of endothelial cells (ECs) were studied and it has been observed that the gelatin grafting method can improve the spreading and proliferation of the ECs on the PET nanofiber mat as well as the EC's phenotype can be preserved.

Because of their ability to differentiate into multiple cell lineages, marrow stromal cells (MSC) are extensively used for cartilage and bone engineering strategies. Some authors [234,235] reported electrospun scaffolds that can enhance MSCs adhesion and proliferation. The electrospun polymer used for this purpose was PCL, since it seems able to support and permit the differentiation of the MSCs into adipogenic, chondrogenic or osteogenic lineages by culturing in specific differentiation [234]. In a subsequent work, Li et al. [235] added a growth factors, β (TGF- β) that played critical roles in chondrogenesis of the MSCs tested. As result, the differentiation level was comparable to that observed for MSCs maintained as cell aggregates or pellets.

As regards bone tissue engineering, PCL electrospun scaffold were obtained and subsequently seeded with (MSCs) derived from the bone marrow of neonatal rats [236]. The cell-polymer constructs were cultured with osteogenic supplements under dynamic culture conditions, maintaining the size and the shape of the original scaffolds. After 4 weeks culture, SEM showed that the surfaces of the cell-polymer constructs were covered with cell multilayers and at the same time mineralization and type I collagen were noticed.

The same authors [237] presented an *in vivo* study with similar constructs, which were implanted in the omenta of rats for 4 weeks. Histological, immunohistochemical and SEM characterization were performed on the explanted constructs. It has been noted that constructs maintained the same size and shape of the original scaffolds and, as regards its morphology, the constructs appeared as a bone-like rigid structure. Moreover extracellular matrix (ECM) formation were noted throughout the constructs.

Lee et al. [238] obtained aligned polyurethane electrospun fibers using a rotating collector that were seeded with human ligament fibroblast (HLF) and the influence of HLF alignment and strain direction on mechano-transduction was evaluated. As shown in Figure 45, no significant

histological differences between the strained and unstrained aligned HLFs were noticed except in the amount of matrix in the intercellular regions. On the contrary, cells spread on the randomly oriented nanofibers reorganized their spindle-shape when strain was applied (Figure 46).

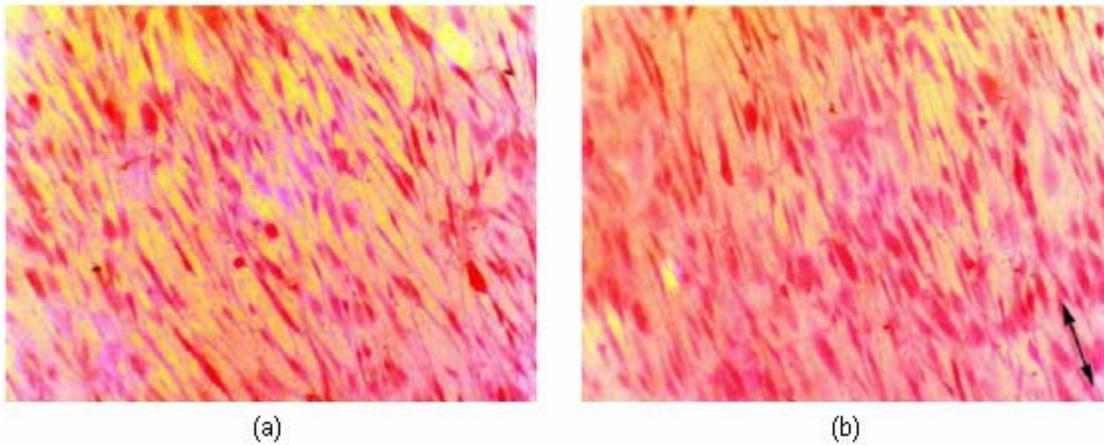


Figure 45 Morphology of fibroblasts seeded on aligned nanofibers: (a) before stretching, (b) longitudinal stretching.

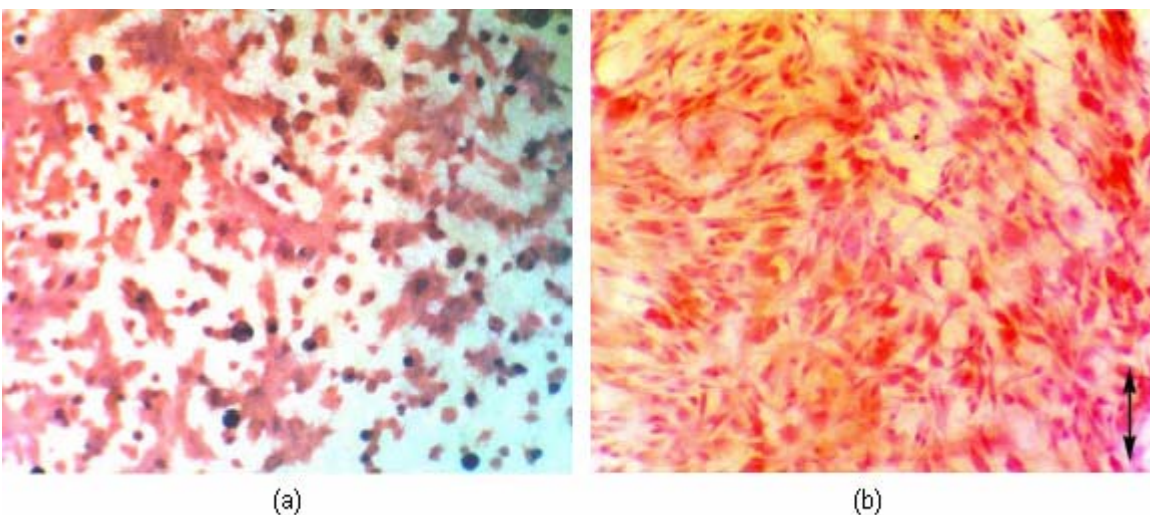


Figure 46 Morphology of fibroblasts seeded on randomly oriented nanofibers: (a) before and (b) after stretching. The fibroblasts were reorganized into their spindle-shape reflecting the effect of stretching the fibers.

As regards scaffolds for cardiac tissue engineering, Zong et al. [239] deduced that nano- and micro-structured electrospun non-woven scaffolds provide both flexibility and guidance for cardiomyocytes (CMs) growth and can be successfully applied to obtain structurally and functionally competent cardiac tissue constructs. They proposed biodegradable non-woven poly(lactide)-and poly(glycolide)-based (PLGA) scaffolds in different formulations seeded with primary CMs in order to test the effects on cell attachment structure and functions. Post-processing steps (mechanical stretch of the electrospun membranes) were also performed to achieve oriented scaffold texture, enforcing anisotropic cell growth. CMs resulted to be very sensitive to the composition of the electrospun PLGA- based scaffolds, with a preference to relatively hydrophobic

surfaces. Moreover Stankus et al. [240] proposed a different way to achieve a highly cellularized construct, suitable for cardiovascular tissue engineering, providing at the same time elastomeric mechanical support. Then, they developed a microintegration approach wherein a meshwork of sub-micron elastomeric fibers of a biodegradable poly(ester urethane)-urea (PEUU) was electrospun concurrently with cellular placement of vascular smooth muscle cells (SMCs) by electrospraying. Two different configurations were tested: side by side capillarity n (Figure 47(a)) and perpendicular configurations (Figure 47(b)). It has been noted that, when the streams arrived from different directions, repulsion was minimized and the combination of rotation and translation of the mandrel target induced component mixing even further. The obtained results showed higher cell numbers with perfusion culture with 131% and 98% more viable cells versus static culture at 4 and 7 days; strong microintegration as well as good mechanical properties of the construct (tensile strengths ranging from 2.0 to 6.5 MPa and breaking strains from 850 to 1700% dependent on the material axis) were also observed.

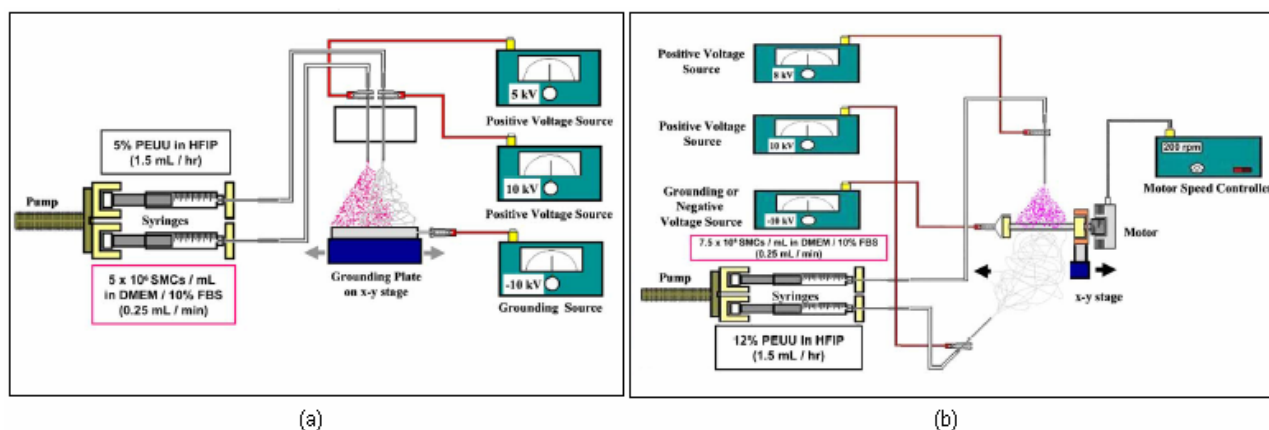


Figure 47 (a) Side-by-side capillary configuration for electrospinning polymer and electrospraying cells onto a flat target moving on an x-y stage; (b) perpendicular configuration for electrospinning polymer and electrospraying cells onto a rotating mandrel moving on a linear stage.

Another interesting study was reported by Nicholson and Jayasinghe [241] who electrospun living organisms under stable threading conditions at a level of resolution that is constrained only by the size of the cells being electrospun. This has been possible employing coaxial-electrospinning and using poly(dimethylsiloxane) (PDMS) as the driving medium which is able to guarantee the cell protection during electrospinning (Figure 48). In-vitro tests demonstrated the effective cellular activity and then the possibility to generate scaffolds comprising living cells.

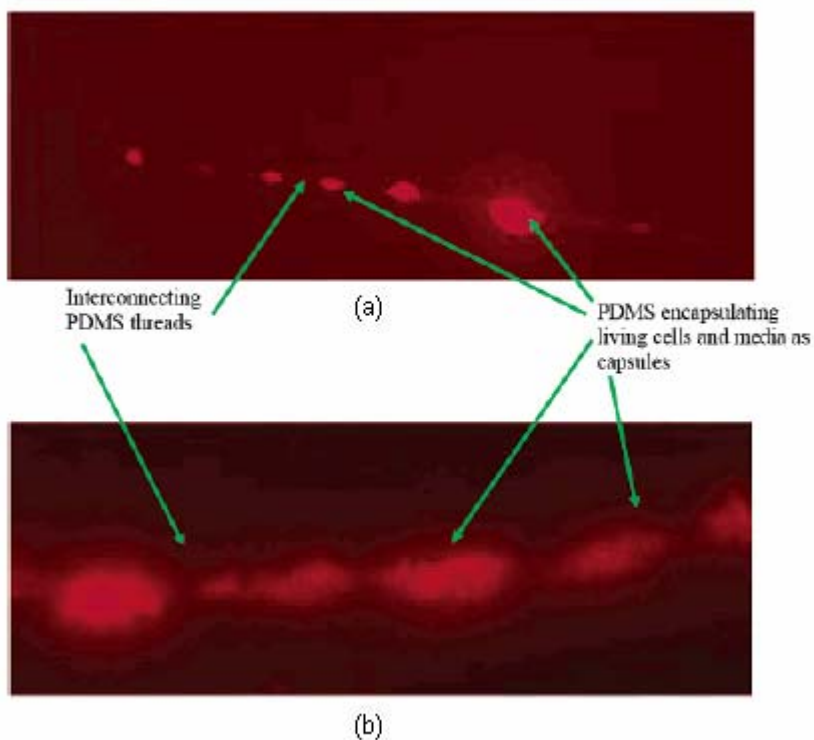


Figure 48 Characteristic fluorescent micrographs showing the variation in fiber diameter that results from cell encapsulations. Experiments were conducted at an applied voltage of 9,5 kV under two different flow rate conditions: (a) Inner needle flow rate $10^{-12}(\text{m}^3\text{s}^{-1})$ –Outer needle flow rate $10^{-11}(\text{m}^3\text{s}^{-1})$; (b) Inner needle flow rate $10^{-8}(\text{m}^3\text{s}^{-1})$ –Outer needle flow rate $10^{-7}(\text{m}^3\text{s}^{-1})$.

The effect of nanofiber surface coatings on the cell's proliferation behavior was investigated by Zhang et al. [242] who developed collagen coated poly(ϵ -caprolactone) (PCL) core-shell nanofibers and a soaked collagen-coated PCL nanofibrous matrix as reference scaffold. It has been pointed out that coatings of collagen on PCL nanofibrous matrix definitely favored cells proliferation and the efficiency depended on the coating. A linear increased of the human dermal fibroblast density by 19.5% (2 days), 22.9% (4 days) and 31.8% (6 days) was revealed on collagen-r-PCL nanofiber membrane compared to PCL. In contrast, the roughly collagen-coated PCL increased only by 5.5% (2 days), 11.0% (4 days) and 21.0% (6 days). So it has been evident the enhancement of integration between cells and collagen-PCL nanofibers scaffold.

Since the renewed interested on Poly(glycolic acid) (PGA), poly(L-lactic acid) (PLA) and poly(lactic-co-glycolic acid) (PLGA) as potential use in biomedical fields, due to their good biodegradability, biocompatibility and mechanical properties, these polymers and their blends have been studied [243,245] in order to characterize the degradation behavior of electrospun nanofibers [243], the nanofibers morphology (high porosity) [244] as well as the infiltration of interstitial cells into different scaffolds [245]. You et al. [243] revealed an increased degradation rate of PGA/PLA blend for decreased PLA content. As regards PGA nanofibers, which were obtained by removing the PLA content from the PGA/PLA blend via dissolution in a selective solvent [244], their

morphology resulted in nanofibers with circular shaped and three-dimensionally interconnected porous structure that can strongly affect the biodegradability of the scaffolds.

Telemaco et al. [245] prepared cylindrical electrospun constructs with electrospun collagen, gelatin, PGA, PLA, and electrospun PGA/PLA co-polymer. The produced scaffolds exhibited similar average pore areas, ranging from 2,000 to 6,000 μm^2 , with an average pore dimension (distance between adjacent fibers) of less than 10 μm in diameter for most of them. Implant studies were performed on the constructs after seven days in vivo implant, to evaluate their ability in supporting cellular migration and infiltration. It has been noted the presence of fibrotic capsules developed in association with electrospun PGA and the PGA/PLA co-polymer and then cells penetration was physically blocked and inflammatory response could also occur because of the hydrolytic by-products release from the synthetic materials. So, without further processing to skirt these biophysical limitations, the structural and chemical properties of the synthetic polymers based-scaffolds make them unfitting for many tissue engineering applications. On the contrary, collagen seems to support rapid cellular infiltration because this material can initiate, or potentiate, physiological signals that promote cell migration.

1.6.5.2 Wound dressing

Electrospun nanofibers exhibit a potential use in wound dressing and wound healing as suggested by various authors (Khil et al. [246], Rho et al. [247], Barnes et al. [251], and Grewal et al. [253]).

Because of the necessity to high porosity and good barrier properties preserving at the same time oxygen permeability, wound dressing materials must be carefully selected. Khil et al. [246] studied the unique properties of polyurethane nanofibers membranes that showed controlled evaporative water loss, excellent oxygen permeability and promoted fluid drainage ability, even blocking out exogenous microorganism.

Collagen and chitosan are two naturally derived polymers that are most commonly used in tissue engineering as well as in wound dressing and wound healing. Rho et al. [247] investigated the electrospinning of type I collagen to fabricate a biomimetic nanofibrous extracellular matrix. Effects on cytocompatibility, cell behavior, cell and collagen nanofiber interactions and open wound healing in rats were studied. It has been revealed that early-stage healing in the collagen nanofiber group was faster than that of the control group.

Chitosan is an N-deacetylated product of chitin, the second-most abundant natural polysaccharide next to cellulose. Both have been successfully electrospun by Geng et al. [84] and Noh et al. [248], respectively. Noh et al. produced chitin nanofibrous matrices for biodegradability and cell behavior tests. It has been proved that chitin, alone or with extracellular matrix proteins (particularly type I collagen), promoted cell attachment and spreading of normal human keratinocytes and fibroblasts,

probably as a consequence of the high surface area available for cell attachment, growth and proliferation. Also Min and co workers[249] investigated and compared morphology and microstructure of electrospun chitin nanofibers mat (diameters in the range from 40 to 640 nm) that was subsequently chemically deacetylated without dimensional change. In another study, Park et al. [250] electrospun silk fibroin/chitosan blends, with different composition ratios and with formic acid as a solvent. They performed the electrospinning of this blend, because chitosan can improve mechanical and physical properties of the brittle silk fibroin film. Moreover, the influence of the methanol treatment on the secondary structure was also determined and it has been noted a conformational change in the electrospun blend compared with the pure silk fibroin. This might be the result of an intermolecular interaction between chitosan and silk fibroin.

Electrospinning of globular proteins such as hemoglobin and myoglobin (responsible for binding and releasing oxygen in the blood and muscles, respectively) has been carried out for preparing a biological construct that could be potentially an oxygen delivering scaffold for optimal wound healing as suggested by Baernes and co-workers [251].

Another interesting protein which play a key role in wound healing, that is fibrinogen, has been successfully electrospun by Wnek et al. [252] who produced a nanofibers mat processing different formulations of bovine fibrinogen, obtaining nanofibers diameters ranging from 70 to 800 nm.

Grewal et al. [253] proposed a study regarding a prospective treatment of chronic or unhealing ulcers that need proteins which are able to enhance the normal wound healing. Since the failure healing is related to the lack of a glycoprotein called fibronectin, an electrospun scaffold composed of crosslinked Hyaluronic Acid and Type III fibronectin could allow the regular healing process. In order to evaluate the effectiveness of the scaffold for cell adhesion and migration, dermal fibroblasts were applied to the electrospun matrix and after 24hours of incubation it has been noted that cell are able to migrate into the scaffold and then proliferate. Because of its unique rheological properties and complete biocompatibility, Hyaluronic Acid (HA) has been used quite extensively in many biomedical applications and also Um and Wang [254,255] reported tests regarding parameters investigation on electrospun HA nanofibers, using a different apparatus that was equipped with an air blowing system that introduced a large additional pulling force for the jet formation and enhanced solvent evaporation.

1.6.5.3 Drug release

Polymeric drug delivery systems present some advantages related to the controlled release of the drugs exclusively in a localized area. Moreover there are other two fundamental implications: first, nanofibers drug delivery system result on directly embedded drugs into the scaffold which is the

nanofibers based construct; second, the efficiency in drug release is promoted by the high surface/volume ratio that is peculiar of nanofibers.

Many efforts have been made in this field, as reported in the following examples. The conventional technique applied for this kind of application is the coaxial electrospinning, that leads the formation of core-shell nanofibers. For instance, Jiang et al. [256] investigated the incorporation and controlled release of two model proteins, bovine serum albumin (BSA) and lysozyme, from biodegradable core-shell nanofibers with poly ϵ -caprolactone (PCL) as shell and protein-containing Poly(ethylene glycol) (PEG) as core. The latter was chosen because of its excellent fiber-former property and also because it could guarantee protection to the proteins during electrospinning and also thanks to the potential detrimental effect of the degradation by products of PCL. As regards proteins release from the scaffold, a slight burst release during the first day has been observed and then a relatively steady release was pointed out. Feed rate of PEG/protein solution affected the release rate in term of increased protein release as the feed rate grew up and BSA and lysozyme presented almost the same release rate.

Verreck et al. [257] prepared drug-embedded nonbiodegradable nanofiber; itraconazole and ketanserin were selected as model compounds while a segmented polyurethane (SPU) was chosen as the nonbiodegradable polymer. For both itraconazole and ketanserin, an amorphous nanodispersion with SPU was obtained when the drug/polymer solutions were electrospun from dimethylformamide (DMF) and dimethylacetamide (DMAc), respectively. The collected nonwoven fabrics were shown to release the drugs at various rates and profiles based on the nanofiber morphology and drug content. The data, obtained using a specially designed release apparatus based around a rotating cylinder, shown that at low drug loading itraconazole was released from the nanofibers as a linear function of the square root of time suggesting Fickian kinetics and initial drug burst was not observed (Figure 49). As regards the second tested drug, ketanserin, biphasic release pattern was observed in which two sequential linear components were noted. These release phases may be temporally correlated with both the drug diffusion through the polymer and the drug diffusion through formed aqueous pores (Figure 50).

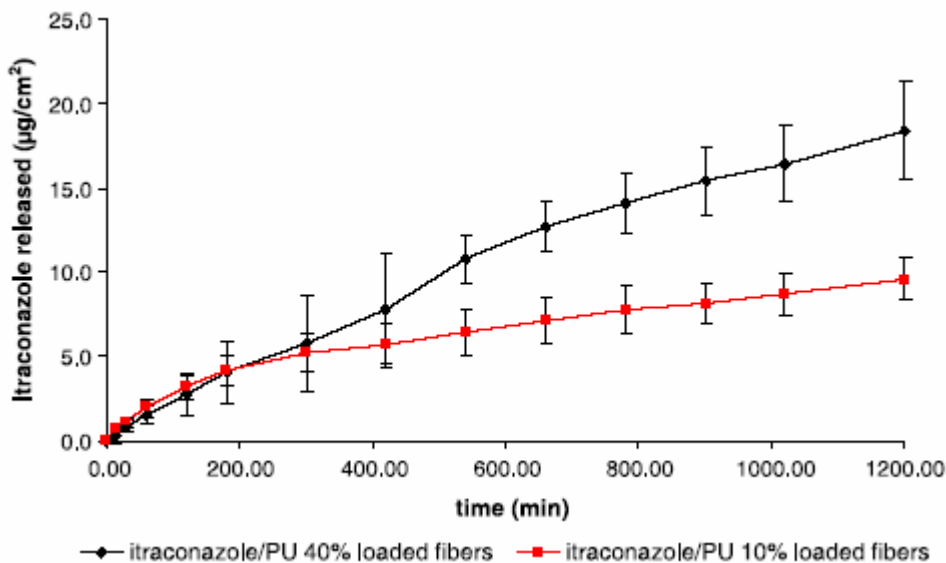


Figure 49 In vitro drug release of itraconazole/PU 10 wt.% and 40 wt.% electrostatic spun fabrics.

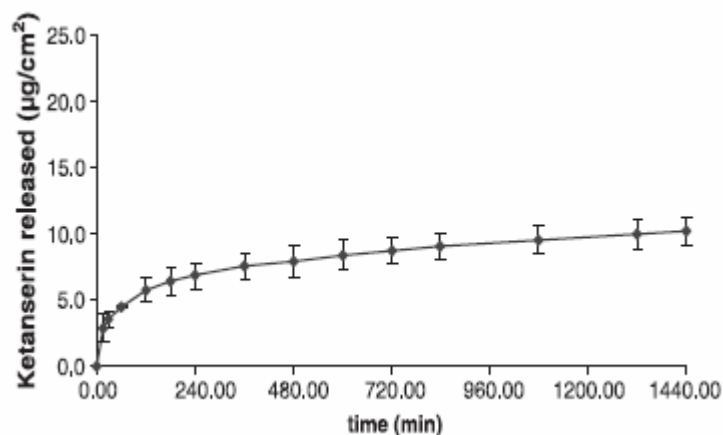


Figure 50 In vitro drug release of ketanserin/PU 10% w/w electrostatic spun fabric.

Also antitumoral agents could be carried by electrospun nanofibers. Its evidence has been provided by Xu et al. [258] who produced nanofibers from water-in-oil emulsion in which the oily phase was a chloroform solution of amphiphilic poly (ethylene glycol)-poly (l-lactic acid) (PEG-PLLA) diblock copolymer while aqueous phase contained water-soluble doxorubicin hydrochloride (Dox) anticancer agent. Nanofibers with average diameter in the range from 300 nm \div 1 μ m were collected and it has been proved that the drug was entirely (concentrations tested from 1-5%wt) encapsulated. The release rate from the fibers was monitored considering both the combined diffusion mechanism and the enzymatic degradation mechanism that became predominant only after a characteristic time, before which diffusion predominated. Another important result confirm that the Dox has been released without losing cytotoxicity as tests about its antitumoral activity on glioma cells (C6 cell lines) confirmed.

As regards polymer used in drug deliver, electrospun poly(L-lactic acid) (PLA) fibers were also tested by Zeng et al. [] who explore the influences of surfactants and typical drugs on the average

fiber diameter. As previously mentioned, the effect of surfactants results in diameter reduction since the surface tension as well as the conductivity of the solution have been changed. Drug release experiments were carried out on rifampin, contained in 15 or 25wt% concentration in 0.05 M Tris–HCl buffer solution containing 3 Ag/ml of proteinase. In this case, it has been supposed that diffusion and permeation throughout carriers didn't occur and the release mechanism was attributed essentially to the PLA degradation in the specific experimental conditions. It has also been revealed that the high rifampin concentration probably affected the fibers morphology because experiments with drug amount of 50% or higher resulted in twin fibers morphology. Moreover, solubility and compatibility of the drug in the drug–polymer–solvent system have been shown to be decisive factors that may affect the presence of the drug within the carrier instead on the surface. This purpose was derived for tests performed with other anticancer agents[259,260] such as doxorubicin hydrochloride and paclitaxel. The latter is a lipophilic and high soluble drug, as well as rifampin; on the contrary doxorubicin is a hydrophilic drug that after electrospinning resulted dispersed exclusively on the fiber surface.

Poly(lactide-co-glycolide) (PLGA)-based nanofibrous scaffold (such as PLGA and PLGA/PLA/PEG-b-PLA, 80:5:15) has been used as drugs carrier by Kim et al. [261] and the study on incorporation, sustained release of a hydrophilic antibiotic drug (Mefoxin ®, cefoxitin sodium) from this supports as well as its antimicrobial effects on *Staphylococcus aureus* cultures were investigated. The morphology and the density of the electrospun scaffolds were found to be dependent on the concentration of the drug which was added in the salt form that consequently affects the conductivity of the solution (see Section II). Drugs release tests confirmed the structural integrity and functionality (Figure 51) as well as an effective inhibition of *Staphylococcus aureus* bacteria growth in both a static (agar) and dynamic (liquid) environment was noticed as shown in Figure 52.

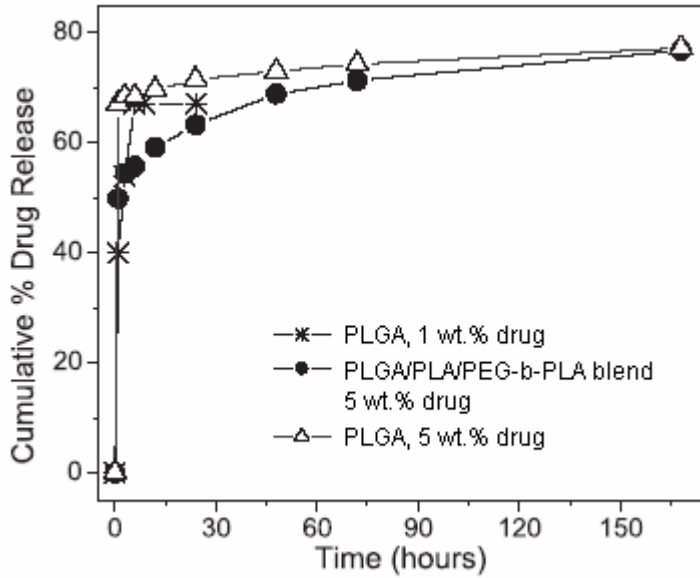


Figure 51 The drug (cefoxitin sodium) release profiles (cumulative curve-top and differential curve-bottom) from medicated electrospun scaffolds.

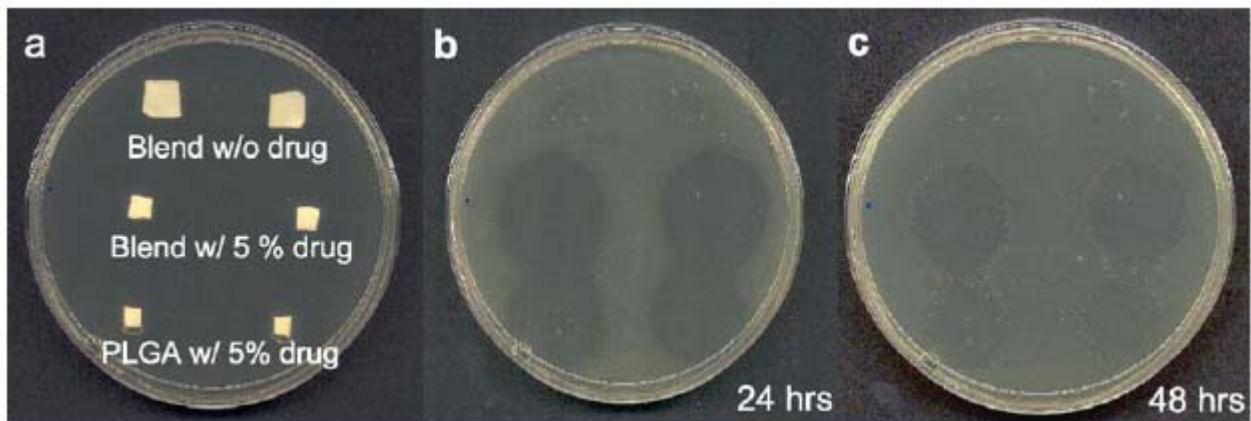


Figure 52 Inhibition of bacterial growth on agar plates.

Drug delivery of tetracycline hydrochloride has been explored by Kenawy et al. [262], who used electrospun mats of either poly(lactic acid) (PLA), poly(ethylene-co-vinyl acetate) (PEVA), or a 50:50 blend of the two as a drug carriers.

Comparing the release profile of tetracycline hydrochloride to the commercial drug delivery system profiles or cast films of various formulations, it has been pointed out that the release rate of the drugs from this delivery system is almost the same of commercial system and the mechanism involved is the molecular diffusion of the drug out of the electrospun fibers. Regarding the comparison with cast film, the release rate was relatively higher because of the high surface/volume ratio of the nanofibers scaffold.

Electrospun nanofiber scaffolds were also proposed as proteins carriers as suggested by Zeng and co-workers [263] who investigated by absorption spectroscopy the release of fluorescein isothiocyanate labeled bovine serum albumin (FITC-BSA) from poly(vinyl alcohol) (PVA) nanofibers coated with

different thickness of Poly(p-xylylene) (PPX) by chemical vapor deposition techniques. The study of protein release is reported in Figure 53 as a function of the different thickness of PPX and it can be noted an increase in FITC-BSA release with the thinner thickness.

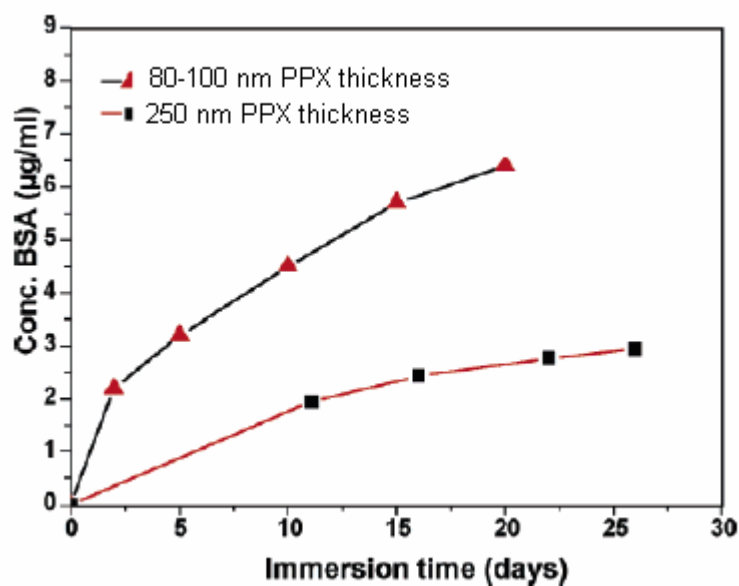


Figure 53 Release of FITC-BSA from PPX coated PVA/BSA nanofibers.

Luu et al. [264] applied electrospinning in order to produce synthetic polymer/DNA composite scaffolds for therapeutic application in gene delivery for tissue engineering. The scaffold was composed of poly(lactide-co-glycolide) (PLGA) random copolymer and a poly(D,L-lactide)-poly(ethylene glycol) (PLA-PEG) block copolymer and plasmid DNA (extracted from cultured *E. coli*). Release was controlled and it was typically 68-80% of the initial loading. Transfection studies were conducted using a preosteoblastic cell line for testing plasmid integrity and activity, in term of b-galactosidase gene expression and translation into protein by the cells.

In a subsequent work, Liang et al. [265] delved into transfection efficiency studies of plasmid DNA in pure PLGA and PLA/PGA/PLA triblock copolymer, emphasizing that in vitro gene delivery to cells was enhanced by attracting the cells to a scaffold that was capable of supporting cellular adhesion. It has been shown that the scaffold protected plasmid DNA during electrospinning and the network structure modulated its release before transfection.

This brief review on the potential applications of electrospinning can be useful to the reader in order to taste the real actuality of this technique even if more efforts are necessary to improve the process control as well as the scale up of the process. Up to now, most of the applications regard the biomedical field, since nanofibers mat may emulate the structure and the properties of the native extracellular matrix that play a fundamental role in all the regenerative processes. Especially for tissue scaffold design, the ability to control fiber formation and cell distribution need to be addressed for improving the performance of the scaffolds. At the same time, drug release

throughout electrospun nanofibers seems to be very promising because of the possibility to process biocompatible and biodegradable polymers that can be used as drug carriers towards a specific target.

Moreover conductive nanofibers obtained from electronic polymers and/or their blends with conventional organic polymers represent good candidate for applications in micro-optoelectronics and electronic device fabrication thanks to the ability of electrospinning to produce photo-responsive polymeric nanofibers suitably functionalized.

However the integration of nanofibers into nanodevice involve a good knowledge of their size and orientation as well as the reproducibility of the array. At this end, new design of collectors is still now a part of the ongoing work in this field.

In addition, recent studies have been demonstrate how electrospinning can be implemented combining this simple technique with cryogenic collection and sol-gel processing in order to enable new nanostructured materials which exhibit a wide range of properties.

1.7 Conclusive remarks on future challenges

Nanoscience and nanotechnology represent up to now one of the most interested fields for the scientific community due to the growing demand of new materials development in nanoscale range characterized by improved mechanical, electrical, chemical and biological properties. Within the general perspective, electrospinning technique seems to be a very simple, economic and versatile method for nanofibers making, to be more precise one dimensional nanostructures which find a wide range of potential applications as filter media, catalysis support or catalysts, sensing component, smart clothes components, composite reinforcing and tissue engineered scaffold. The future of their applicability depends on the ability to produce well-controlled fibers diameter as well as to tailor the morphologies and the internal structure as a function of the specific purpose. At this regard, the production of various types of fibers with porous surface distribution, hollow interiors, core-shell structure open the way for the growing application as drug carriers because nanofibers can modulate the controlled release on a specific target.

Much efforts have been made in order to exploit the effect of the process, solution and ambient parameters on the spinning process, but it can be noted that there are several interactions among them that affect the final nanofiber structure; then very often it is quite difficult to establish a mathematical equation to look upon all of them and this means a systematical preliminary investigation is still essential to check out the best experimental conditions. Theoretical modeling has been also progressed to provide a better understanding of the instabilities phenomena that occur during the process and consequently to achieve an improved control on the size of the nanofibers. Moreover, even a large variety of materials can be successfully electrospun, this process is still bound by their molecular weight which strongly affects the dividing line from electrospraying to electrospinning.

Progress and research have also moved to design various electrospinning set-ups to obtain different fibrous assemblies and in particular ordered nanostructures. As a consequence of the improved ability to control the electrospun jet into various fibrous assemblies, more applications may find nanofibers as a good candidate for developing and improving current technology.

Future challenges regard a detailed study of the nanofibers organization into hierarchical architectures in order to best exploit their potential application in nanodevice production and at the same time it will be important to develop the scale up of the process for improving the productivity of the method.

Furthermore, since electrospinning process could be combined with other well-known techniques and thanks to the improved knowledge of the whole process, functional materials could be obtained,

then, it will be involved an extensive cooperation among different research fields and as a result, it will get to be one of the most powerful tool for developing nanostructured materials with a huge range of properties and applications.

The present work proposed a complete review on the submitted literature and the research activity on electrospinning developed until now. It is hoped that this overview will be useful for everybody who works in this field as well as for people who firstly approach to this technique providing the basic fundamentals for planning their own work.

CHAPTER 2 Response Surface Methodology

2.1 Introduction

Response Surface Methodology (RSM) is a collection of statistical and mathematical techniques useful for developing, improving, and optimizing processes [266].

The most extensive applications of RSM are in the particular situations where several input variables potentially influence some performance measure or quality characteristic of the process. Thus performance measure or quality characteristic is called the response. The input variables are sometimes called independent variables, and they are subject to the control of the scientist or engineer. The field of response surface methodology consists of the experimental strategy for exploring the space of the process or independent variables, empirical statistical modeling to develop an appropriate approximating relationship between the yield and the process variables, and optimization methods for finding the values of the process variables that produce desirable values of the response. In this section we will concentrate on the second strategy: statistical modeling to develop an appropriate approximating model between the response y and independent variables $\xi_1, \xi_2, \dots, \xi_k$. In general, the relationship is

$$y = f(\xi_1, \xi_2, \dots, \xi_k) + \varepsilon; \quad \text{Eq.(2.1)}$$

where the form of the true response function f is unknown and perhaps very complicated, and ε is a term that represents other sources of variability not accounted for in f . Usually ε includes effects such as measurement error on the response, background noise, the effect of other variables, and so on. Usually ε is treated as a statistical error, often assuming it to have a normal distribution with mean zero and variance σ^2 . Then

$$E(y) = \eta = E[f(\xi_1, \xi_2, \dots, \xi_k)] + E(\varepsilon) = f(\xi_1, \xi_2, \dots, \xi_k); \quad \text{Eq.(2.2)}$$

The variables $\xi_1, \xi_2, \dots, \xi_k$ in Equation (1.2) are usually called the natural variables, because they are expressed in the natural units of measurement, such as degrees Celsius, pounds per square inch, etc. In much RSM work it is convenient to transform the natural variables to coded variables x_1, x_2, \dots, x_k , which are usually defined to be dimensionless with mean zero and the same standard deviation. In terms of the coded variables, the response function (2.2) will be written as

$$\eta = f(x_1, x_2, \dots, x_k); \quad \text{Eq.(2.3)}$$

Because the form of the true response function f is unknown, we must approximate it. In fact, successful use of RSM is critically dependent upon the experimenter's ability to develop a suitable approximation for f . Usually, a low-order polynomial in some relatively small region of the independent variable space is appropriate. In many cases, either a first-order or a second-order model is used.

The first-order model is likely to be appropriate when the experimenter is interested in approximating the true response surface over a relatively small region of the independent variable space in a location where there is little curvature in f . For the case of two independent variables, the first-order model in terms of the coded variables is

$$\eta = \beta_0 + \beta_1 + \beta x_1 + \beta_2 x_2, \tag{Eq.(2.4)}$$

The form of the first-order model in Equation (2.4) is sometimes called a main effects model, because it includes only the main effects of the two variables x_1 and x_2 . If there is an interaction between these variables, it can be added to the model easily as follows:

$$\eta = \beta_0 + \beta_1 + \beta x_1 + \beta_2 x_2 + \beta_{12} x_1 x_2, \tag{Eq.(2.5)}$$

This is the first-order model with interaction. Adding the interaction term introduces curvature into the response function.

Often the curvature in the true response surface is strong enough that the first-order model (even with the interaction term included) is inadequate. A second-order model will likely be required in these situations. For the case of two variables, the second-order model is

$$\eta = \beta_0 + \beta_1 + \beta x_1 + \beta_2 x_2 + \beta_{11} x_1^2 + \beta_{22} x_2^2 + \beta_{12} x_1 x_2, \tag{Eq.(2.6)}$$

This model would likely be useful as an approximation to the true response surface in a relatively small region.

The second-order model is widely used in response surface methodology for several reasons:

1. The second-order model is very flexible. It can take on a wide variety of functional forms, so it will often work well as an approximation to the true response surface.
2. It is easy to estimate the parameters (the β 's) in the second-order model. The method of least squares can be used for this purpose.
3. There is considerable practical experience indicating that second-order models work well in solving real response surface problems.

In general, the first-order model is

$$\eta = \beta_0 + \beta_1 + \beta x_1 + \beta_2 x_2 + \dots + \beta_k x_k \tag{Eq.(2.7)}$$

and the second-order model is

$$\eta = \beta_0 + \sum_{j=1}^k \beta_j x_j + \sum_{j=1}^k \beta_{jj} x_j^2 + \sum_{i < j=2}^k \sum_{j=2}^k \beta_{ij} x_i x_j \tag{Eq.(2.8)}$$

In some infrequent situations, approximating polynomials of order greater than two are used.

The general motivation for a polynomial approximation for the true response function f is based on the Taylor series expansion around the point $x_{10}, x_{20}, \dots, x_{k0}$.

Finally, let's note that there is a close connection between RSM and linear regression analysis. For example, consider the model

$$y = \beta_0 + \beta_1 + \beta x_1 + \beta_2 x_2 + \dots + \beta_k x_k + \varepsilon \quad \text{Eq.(2.9)}$$

The β 's are a set of unknown parameters. To estimate the values of these parameters, we must collect data on the system we are studying. Because, in general, polynomial models are linear functions of the unknown β 's, we refer to the technique as linear regression analysis.

2.1.2 Response Surface Methodology and Robust Design

RSM is an important branch of experimental design. RSM is a critical technology in developing new processes and optimizing their performance. The objectives of quality improvement, including reduction of variability and improved process and product performance, can often be accomplished directly using RSM.

It is well known that variation in key performance characteristics can result in poor process and product quality. During the 1980s [267,268] considerable attention was given to process quality, and methodology was developed for using experimental design, specifically for the following:

For designing or developing products and processes so that they are robust to component variation.

For minimizing variability in the output response of a product or a process around a target value.

For designing products and processes so that they are robust to environment conditions.

By robust means that the product or process performs consistently on target and is relatively insensitive to factors that are difficult to control.

Professor Genichi Taguchi [267,268] used the term robust parameter design (RPD) to describe his approach to this important problem. Essentially, robust parameter design methodology prefers to reduce process or product variation by choosing levels of controllable factors (or parameters) that make the system insensitive (or robust) to changes in a set of uncontrollable factors that represent most of the sources of variability. Taguchi referred to these uncontrollable factors as noise factors. RSM assumes that these noise factors are uncontrollable in the field, but can be controlled during process development for purposes of a designed experiment.

Considerable attention has been focused on the methodology advocated by Taguchi, and a number of flaws in his approach have been discovered. However, the framework of response surface methodology allows easily incorporate many useful concepts in his philosophy [266].

There are also two other full-length books on the subject of RSM [269,270].

In our technical report we are concentrated mostly on building and optimizing the empirical models and practically do not consider the problems of experimental design.

2.1.3 The Sequential Nature of the Response Surface Methodology

Most applications of RSM are sequential in nature.

The first step concerns about the specification of factors or variables that could be important in response surface study. It is usually called a screening experiment. The objective of factor screening is to reduce the list of candidate variables to a relatively few so that subsequent experiments will be more efficient and require fewer runs or tests. The purpose of this phase is the identification of the important independent variables.

In the subsequent phase 1, the experimenter's objective is to determine if the current settings of the independent variables result in a value of the response that is near the optimum. If the current settings or levels of the independent variables are not consistent with optimum performance, then the experimenter must determine a set of adjustments to the process variables that will move the process toward the optimum. This phase of RSM makes considerable use of the first-order model and an optimization technique called the method of steepest ascent (descent).

Phase 2 begins when the process is near the optimum. At this point the experimenter usually wants a model that will accurately approximate the true response function within a relatively small region around the optimum. Because the true response surface usually exhibits curvature near the optimum, a second-order model (or perhaps some higher-order polynomial) should be used. Once an appropriate approximating model has been obtained, this model may be analyzed to determine the optimum conditions for the process.

This sequential experimental process is usually performed within some region of the independent variable space called the operability region or experimentation region or region of interest.

2.2 Building Empirical Models

2.2.1 Linear Regression Model

In the practical application of RSM it is necessary to develop an approximating model for the true response surface. The underlying true response surface is typically driven by some unknown physical mechanism. The approximating model is based on observed data from the process or system and is an empirical model. Multiple regression is a collection of statistical techniques useful for building the types of empirical models required in RSM.

The first-order multiple linear regression model with two independent variables is

$$y = \beta_0 + \beta_1 x_1 + \beta_2 x_2 + \varepsilon \tag{Eq.(2.10)}$$

The independent variables are often called predictor variables or regressors. The term "linear" is used because Equation (2.10) is a linear function of the unknown parameters $\beta_0, \beta_1,$ and β_2 .

In general, the response variable y may be related to k regressor variables. The model

$$y = \beta_0 + \beta_1 x_1 + \beta_2 x_2 + \dots + \beta_k x_k + \varepsilon \tag{Eq.(2.11)}$$

is called a multiple linear regression model with k regressor variables. The parameters β_j , $j=0,1,\dots,k$, are called the regression coefficients.

Models that are more complex in appearance than Equation (2.11) may often still be analyzed by multiple linear regression techniques. For example, considering adding an interaction term to the first-order model in two variables

$$y = \beta_0 + \beta_1 x_1 + \beta_2 x_2 + \beta_{12} x_1 x_2 + \varepsilon \tag{Eq.(2.12)}$$

As another example, consider the second-order response surface model in two variables

$$y = \beta_0 + \beta_1 x_1 + \beta_2 x_2 + \beta_{11} x_1^2 + \beta_{22} x_2^2 + \beta_{12} x_1 x_2 + \varepsilon \tag{Eq.(2.13)}$$

In general, any regression model that is linear in the parameters (the β -values) is a linear regression model, regardless of the shape of the response surface that it generates.

2.2.1.1 Estimation of the Parameters in Linear Regression Models

The method of least squares is typically used to estimate the regression coefficients in a multiple linear regression model. Suppose that $n > k$ observations on the response variable are available, say y_1, y_2, \dots, y_n . Along with each observed response y_i , we will have an observation on each regressor variable, let x_{ij} denote the i^{th} observation or level of variable x_j (see Table 2.1).

The model in terms of the observations may be written in matrix notation as

$$\mathbf{y} = \mathbf{X}\boldsymbol{\beta} + \boldsymbol{\varepsilon} \tag{Eq. (2.14)}$$

where

\mathbf{y} is an $n \times 1$ vector of the observations,

\mathbf{X} is an $n \times p$ matrix of the levels of the independent variables,

$\boldsymbol{\beta}$ is a $p \times 1$ vector of the regression coefficients, and

$\boldsymbol{\varepsilon}$ is an $n \times 1$ vector of random errors.

y	x_1	x_2	\dots	x_k
y_1	x_{11}	x_{12}	\dots	x_{1k}
y_2	x_{21}	x_{22}	\dots	x_{2k}
\cdot	\cdot	\cdot	\dots	\cdot
\cdot	\cdot	\cdot	\dots	\cdot
\cdot	\cdot	\cdot	\dots	\cdot
y_n	x_{n1}	x_{n2}	\dots	x_{nk}

Table 2.1: Data for Multiple Linear Regression

We wish to find the vector of least squares estimators, \mathbf{b} , that minimizes

$$L = \sum_{i=1}^n \varepsilon_i^2 = \boldsymbol{\varepsilon}'\boldsymbol{\varepsilon} = (\mathbf{y} - \mathbf{X}\boldsymbol{\beta})'(\mathbf{y} - \mathbf{X}\boldsymbol{\beta})$$

After some simplifications, the least squares estimator of $\boldsymbol{\beta}$ is

$$\mathbf{b} = (\mathbf{X}'\mathbf{X})^{-1} \mathbf{X}'\mathbf{y} \tag{Eq.(2.15)}$$

It is easy to see that $\mathbf{X}'\mathbf{X}$ is a $p \times p$ symmetric matrix and $\mathbf{X}'\mathbf{y}$ is a $p \times 1$ column vector. The matrix $\mathbf{X}'\mathbf{X}$ has the special structure. The diagonal elements of $\mathbf{X}'\mathbf{X}$ are the sums of squares of the elements in the columns of \mathbf{X} , and the off-diagonal elements are the sums of cross-products of the elements in the columns of \mathbf{X} . Furthermore, the elements of $\mathbf{X}'\mathbf{y}$ are the sums of crossproducts of the columns of \mathbf{X} and the observations $\{y_i\}$.

The fitted regression model is

$$\hat{\mathbf{y}} = \mathbf{X}\mathbf{b} \tag{Eq.(2.16)}$$

In scalar notation, the fitted model is

$$\hat{y}_i = b_0 + \sum_{j=1}^k b_j x_{ij}, \quad i = 1, 2, \dots, n$$

The difference between the observation i y and the fitted value \hat{y}_i is a residual, $e_i = y_i - \hat{y}_i$.

The $n \times 1$ vector of residuals is denoted by

$$\mathbf{e} = \mathbf{y} - \hat{\mathbf{y}} \tag{Eq.(2.17)}$$

2.2.2 Hypothesis testing in multiple regression

In multiple linear regression problems, it is always necessary to examine the usefulness of the model and if it provides an adequate approximation to the true system; hypothesis-testing procedures require that the errors ε_i in the model is normally and independently distributed with mean zero and variance σ^2 .

2.2.2.1 Properties of the Least Squares Estimators

The method of least squares produces an unbiased estimator of the parameter $\boldsymbol{\beta}$ in the multiple linear regression model. The important parameter is the sum of squares of the residuals

$$SS_E = \sum_{i=1}^n (y_i - \hat{y}_i)^2 = \sum_{i=1}^n e_i^2 = \mathbf{e}'\mathbf{e} \tag{Eq.(2.18)}$$

Because $\mathbf{X}'\mathbf{X}\mathbf{b} = \mathbf{X}'\mathbf{y}$, we can derive a computational formula for SS_E :

$$SS_E = \mathbf{y}'\mathbf{y} - \mathbf{b}'\mathbf{X}'\mathbf{y} \tag{Eq.(2.19)}$$

Equation (2.19) is called the error or residual sum of squares.

It can be shown that an unbiased estimator of σ^2 is

$$\hat{\sigma}^2 = \frac{SS_E}{n - p} \tag{Eq.(2.20)}$$

where n is a number of observations and p is a number of regression coefficients.

2.2.2.2 Test for Significance of Regression

The test for significance of regression is a test to determine if there is a linear relationship between the response variable y and a subset of the regressor variables x_1, x_2, \dots, x_k . the appropriate hypotheses are

$$\begin{aligned} H_0: \beta_1 = \beta_2 = \dots = \beta_k = 0 \\ H_1: \beta_j \neq 0 \text{ for at least one } j \end{aligned} \tag{Eq.(2.21)}$$

Rejection of H_0 in (2.21) implies that at least one of the regressor variables x_1, x_2, \dots, x_k contributes significantly to the model. The test procedure involves partitioning the total sum of squares

$$SS_T = \sum_{i=1}^n (y_i - \bar{y})^2$$

into a sum of squares due to the model (or to regression) and a sum of squares

due to the residual, say

$$SS_T = SS_R + SS_E \tag{Eq.(2.22)}$$

If the null hypothesis H_0 is true, then SS_R / σ^2 is distributed as χ^2_k , where the number of degrees of freedom for χ^2 is equal to the number of regressor variables in the model. The test procedure for $H_0: \beta_1 = \beta_2 = \dots = \beta_k = 0$ is to compute

$$F_0 = \frac{SS_R / k}{SS_E / (n - k - 1)} = \frac{MS_R}{MS_E}$$

and to reject H_0 if F_0 exceeds $F_{\alpha, k, n-k-1}$. Alternatively, one could use the P-value approach to hypothesis testing and, thus, reject H_0 if the P-value for the statistic F_0 is less than α .

This test procedure is called an analysis of variance because it is based on a decomposition of the total variability in the response variable y.

A computational formula for SS_E and consequently for SS_R can be derived from Equation (2.19) and then the total sum of squares is

$$SS_T = y'y - \frac{(\sum_{i=1}^n y_i)^2}{n} = \sum_{i=1}^n y_i^2 - \frac{(\sum_{i=1}^n y_i)^2}{n} \tag{Eq.(2.23)}$$

Then the coefficient of multiple determination R^2 is defined as

$$R^2 = 1 - \frac{SS_E}{SS_T} \quad \text{Eq.(2.24)}$$

R^2 is a measure of the amount of reduction in the variability of y obtained by using the regressor variables x_1, x_2, \dots, x_k in the model. From inspection of the analysis of variance identity equation (Equation (2.14)) we can see that $0 \leq R^2 \leq 1$. However, a large value of R^2 does not necessarily imply that the regression model is good one. Adding a variable to the model will always increase R^2 , regardless of whether the additional variable is statistically significant or not. Thus it is possible for models that have large values of R^2 to yield poor predictions of new observations or estimates of the mean response.

Because R^2 always increases as we add terms to the model, some regression model builders prefer to use an adjusted R^2 statistic defined as

$$R_{adj}^2 = 1 - \frac{SS_E / (n - p)}{SS_T / (n - 1)} = 1 - \frac{n - 1}{n - p} (1 - R^2) \quad \text{Eq.(2.25)}$$

In general, the adjusted R^2 statistic will not always increase as variables are added to the model.

In fact, if unnecessary terms are added, the value of R_{adj}^2 will often decrease. When R^2 and R_{adj}^2 differ dramatically, there is a good chance that nonsignificant terms have been included in the model.

We are frequently interested in testing hypotheses on the individual regression coefficients.

Such tests would be useful in determining the value of each of the regressor variables in the regression model. For example, the model might be more effective with the inclusion of additional variables, or perhaps with the deletion of one or more of the variables already in the model.

Adding a variable to the regression model always causes the sum of squares for regression to increase and the error sum of squares to decrease. We must decide whether the increase in the regression sum of squares is sufficient to warrant using the additional variable in the model.

Furthermore, adding an unimportant variable to the model can actually increase the mean square error, thereby decreasing the usefulness of the model.

2.2.2.3 Residual Analysis

The residuals from the least squares fit, defined by $e_i = y_i - \hat{y}_i, i = 1, 2, \dots, n$ play an important role in judging model adequacy. Many response surface analysts prefer to work with scaled residuals, in contrast to the ordinary least squares residuals. These scaled residuals often convey more information than do the ordinary residuals.

The standardizing process scales the residuals by dividing them by their average standard deviation. In some data sets, residuals may have standard deviations that differ greatly. There is some other way of scaling that takes this into account. Let's consider this. The vector of fitted values \hat{y}_i corresponding to the observed values y_i is

$$\hat{y} = Xb = X(X'X)^{-1} X'y = Hy \tag{Eq.(2.26)}$$

The $n \times n$ matrix $H = X(X'X)^{-1} X'$ is usually called the hat matrix because it maps the vector of observed values into a vector of fitted values. The hat matrix and its properties play a central role in regression analysis.

Since $e = y - \hat{y}$ there are several other useful ways to express the vector of residuals

$$e = y - Xb = y - Hy = (I - H)y \tag{Eq.(2.27)}$$

The prediction error sum of squares (PRESS) proposed in [271-272], provides a useful residual scaling

$$PRESS = \sum_{i=1}^n \left(\frac{e_i}{1 - h_{ii}} \right)^2 \tag{Eq.(2.28)}$$

From Equation (2.28) it is easy to see that the PRESS residual is just the ordinary residual weighted according to the diagonal elements of the hat matrix h_{ii} . Generally, a large difference between the ordinary residual and the PRESS residual will indicate a point where the model fits the data well, but a model built without that point predicts poorly.

2.3 Variable Selection and Model Building in Regression

In response surface analysis it is customary to fit the full model corresponding to the situation at hand. It means that in steepest ascent we usually fit the full first-order model, and in the analysis of the second-order model we usually fit the full quadratic.

Nevertheless, an experimenter may encounter situations where the full model may not be appropriate; that is, a model based on a subset of the regressors in the full model may be superior. Variable selection or model-building techniques usually is used to identify the best subset of regressors to include in a regression model [273,274]. Now we give a brief presentation of regression model-building and variable selection methods, introduce our method of variable selection and illustrate their application to a response surface problem. We assume that there are K candidate regressors denoted x_1, x_2, \dots, x_k and a single response variable y . All models will have an intercept term β_0 , so that the full model has $K + 1$ parameters.

There is a strong motivation for correctly specifying the regression model: leaving out important regressors introduces bias into the parameter estimates, while including unimportant variables weakens the prediction or estimation capability of the model.

2.3.1 Procedures for Variable Selection

Now we will consider several of the more widely used methods for selecting the appropriate subset of variables for a regression model. We will also introduce our approach based on the optimization procedure used for selecting the best model from the whole set of models and finally we will discuss and illustrate several of the criteria that are typically used to decide which subset of the candidate regressors leads to the best model.

2.3.1.1 All Possible Regression

This procedure requires that the analyst fit all the regression equations involving one candidate regressors, two-candidate regressors, and so on. These equations are evaluated according to some suitable criterion, and the best regression model selected. If we assume that the intercept term β_0 is included in all equations, then there are K candidate regressors and there are 2^K total equations to be estimated and examined. For example, if $K = 4$, then there are $2^4 = 16$ possible equations, whereas if $K = 10$, then there are $2^{10} = 1024$. Clearly the number of equations to be examined increases rapidly as the number of candidate regressors increases.

Usually the analysts restrict the candidate variables for the model to those in the full quadratic polynomial and require that all models obey the principal of **hierarchy**. A model is said to be hierarchical if the presence of higher-order terms (such as interaction and second-order terms) requires the inclusion of all lower-order terms contained within those of higher order. For example, this would require the inclusion of both main effects if a two-factor interaction term was in the model. Many regression model builders believe that hierarchy is a reasonable modelbuilding practice when fitting polynomials.

2.3.1.2 Stepwise Regression Methods

Because evaluating all possible regressions can be burdensome computationally, various methods have been developed for evaluating only a small number of subset regression models by either adding or deleting regressors one at a time. These methods are generally referred to as stepwise-type procedures. They can be classified into three broad categories: (1) forward selection, (2) backward elimination, and (3) stepwise regression, which is a popular combination of procedures (1) and (2).

Forward Selection

This procedure begins with the assumption that there are no regressors in the model other than the intercept. An effort is made to find an optimal subset by inserting regressors into the model one at a time. The first regressor selected for entry into the equation is the one that has the largest simple correlation with the response variable y . Suppose that this regressor is x_1 . This also the regressor

that will produce the largest value of the F-statistic for testing significance of regression. This regressor is entered if the F-statistic exceeds a preselected F-value, say F_{in} (or F-to-enter). The second regressor chosen for entry is the one that now has the largest correlation with y after adjusting for the effect of the first regressor entered (x_1) on y . We refer to these correlations as partial correlations. They are the simple correlations between the residuals from the regression $\hat{y} = \hat{\beta}_0 + \hat{\beta}_1 x_1$ and the residuals from the regressions of the other candidate

regressors on x_1 , say $\hat{x}_j = \hat{a}_{0j} + \hat{a}_{1j} x_1, j = 2, 3, \dots, K$

In general, at each step the regressor having the highest partial correlation with y (or equivalently the largest partial F-statistic given the other regressors already in the model) is added to the model if its partial F-statistic exceeds the preselected entry level F_{in} . The procedure terminates either when the partial F-statistic at a particular step does not exceed F_{in} or when the last candidate regressor is added to the model.

Backward Elimination

Forward selection begins with no regressors in the model and attempts to insert variables until a suitable model is obtained. Backward elimination attempts to find a good model by working in the opposite direction. That is, we begin with a model that includes all K candidate regressors. Then the partial F-statistic (or a t-statistic, which is equivalent) is computed for each regressor as if it were the last variable to enter the model. The smallest of these partial F-statistics is compared with a preselected value, F_{out} (or F-to-remove); and if the smallest partial F-value is less than F_{out} , that regressor is removed from the model. Now a regression model with $K - 1$ regressors is fitted, the partial F-statistic for this new model calculated, and the procedure repeated. The backward elimination algorithm terminates when the smallest partial F-value is not less than the preselected cutoff value F_{out} .

Backward elimination is often a very good variable selection procedure. It is particularly favored by analysts who like to see the effect of including all the candidate regressors, just so that nothing obvious will be missed.

Stepwise Regression

The two procedures described above suggest a number of possible combinations. One of the most popular is the stepwise regression algorithm. This is a modification of forward selection in which at each step all regressors entered into the model previously are reassessed via their partial F- or t-statistics. A regressor added at an earlier step may now be redundant because of the relationship between it and regressors now in the equation. If the partial F-statistic for a variable is less than F_{out} , that variable is dropped from the model.

Stepwise regression requires two cutoff values, F_{in} and F_{out} . Some analysts prefer to choose $F_{in} = F_{out}$, although this is not necessary. Sometimes we choose $F_{in} > F_{out}$, making it more difficult to add a regressor than to delete one.

General Comments on Stepwise-Type Procedures

The stepwise regression algorithms described above have been criticized on various grounds, the most common being that none of the procedures generally guarantees that the best subset regression model of any size will be identified. Furthermore, because all the stepwise-type procedures terminate with one final equation, inexperienced analysts may conclude that they have found a model that is in some sense optimal. Part of the problem is that it is likely that there is not one best subset model, but several equally good ones.

The analyst should also keep in mind that the order in which the regressors enter or leave the model does not necessarily imply an order of importance to the variables. It is not unusual to find that a regressor inserted into the model early in the procedure becomes negligible at a subsequent step. For example, suppose that forward selection chooses x_4 (say) as the first regressor to enter.

However, when x_2 (say) is added at a subsequent step, x_4 is no longer required because of high positive correlation between x_2 and x_4 . This is a general problem with the forward selection procedure. Once a regressor has been added, it cannot be removed at a later step.

Note that forward selection, backward elimination, and stepwise regression do not necessarily lead to the same choice of final model. The correlation between the regressors affects the order of entry and removal. Some users have recommended that all the procedures be applied in the hopes of either seeing some agreement or learning something about the structure of the data that might be overlooked by using only one selection procedure. Furthermore, there is not necessarily any agreement between any of the stepwise-type procedures and all possible regressions.

For these reasons, stepwise-type variable selection procedures should be used with caution.

Some analysts prefer the stepwise regression algorithm followed by backward elimination. The backward elimination algorithm is often less adversely affected by the correlative structure of the regressors than is forward selection. They also found it helpful to run the problem several times with different choices of F_{in} and F_{out} . This will often allow the analyst to generate several different models for evaluation.

2.4 Steps of Response Surface Methodology

1. Approximate the simulation response function in the current region of interest by a first-order model. The first-order model is described by Equation (2.7). Estimators of the regression coefficients (the β 's) are determined by using ordinary least squares. To this end, the objective

function is evaluated in the points of an experimental design, which is a specific arrangement of points in the current region of interest. Although there are many designs to choose from, usually a fractional two-level factorial design [275] is used, often augmented by the center point of the current region of experimentation [266]. The advantages of this design are that it is orthogonal, what means that the variance of the predicted response is minimal, gives unbiased estimators of the regression coefficients and can quite easily be augmented to derive a second-order design.

2. Test the first-order model for adequacy. Before using the first-order model to move into a direction of improved response, it should be tested if the estimated first-order model adequately describes the behavior of response in the current region of experimentation. It is necessary to remember that the total number of observations should be always larger than the number of regression coefficients. Moreover, multiple observations are needed in the center point of the region of experimentation. Estimation of adequacy is usually performed using the analysis of variance (ANOVA) table. It allows decide when to accept the first-order model. The decisions include choosing the significance levels for the test involved.

3. Perform a line search in the steepest descent direction. If the first-order model is accepted, then this model is used for determining the direction where improvement of the simulation response is expected. The steepest descent direction is given by $(-b_1, \dots, -b_k)$. A line search is performed from the center point of the current region of experimentation in this direction to find a point of improved response. This point is taken as the estimator of the optimum of the simulation response function in the n th iteration, and is used as the center point of the region of the experimentation in the $(n + 1)^{\text{th}}$ iteration. The line search is stopped when no further improvement is observed.

4. Solve the inadequacy of the first-order model. If the first-order model is not accepted, then either there is some evidence of pure curvature or interaction between the factors in the current region of experimentation. Usually, this is solved by approximating the simulation response by a second-order polynomial. However, the optimization algorithm becomes less efficient especially if it occurs very early during the optimization process. There is alternative solution that recommends reduce the size of the region of experimentation by decreasing the step sizes. In this way this region can possibly become small enough to ensure that a first-order approximation is an adequate local representation of the simulation response function. Another solution is to increase the simulation size used to evaluate a design point or to increase the number of replicated observations done in the design points. This may ensure that a significant direction of steepest descent is indeed found. At the start of the algorithm it should be decided which actions will be taken when the first-order model is rejected. For example, depending on the p-value found for the lack-of-fit test, one could

decide to apply a second-order approximation or to decrease the size of the region of experimentation.

5. Approximate the objective function in the current region of experimentation by a second-order model. The coded second-order model is given by the Equation (2.8). The regression coefficients of the second-order model are again determined by using ordinary least squares method applied to observations performed in an experimental design. The most popular class of second-order designs is the central composite design (CCD) [266]. This design can be easily constructed by augmenting the fractional factorial design that is used for estimating the first-order model.

6. Testing the second-order model for adequacy. Similar to the first-order model, it should be tested if the estimated second-order model adequately describes the behaviour of the response in the current region of experimentation before using the model.

7. Solve the inadequacy of the second-order model. If the second-order model is found not to be adequate, then one should reduce the size of the region of experimentation or increase the simulation size used in evaluating a design point. In RSM it is not customary to fit a higher than second-order polynomial.

8. Perform canonical analysis. If the second-order model is found to be adequate, then canonical analysis is performed to determine the location and the nature of the stationary point of the second-order model. The estimated second-order approximation can be written as follows:

$$\hat{Y} = b_0 + \mathbf{x}'\mathbf{b} + \mathbf{x}'\mathbf{B}\mathbf{x} \quad \text{Eq.(2.29)}$$

where b_0 , \mathbf{b} , and \mathbf{B} are the estimates of the intercept, linear, and second order coefficients, respectively.

The stationary point \mathbf{x}_s of the second-order polynomial is determined by

$$\mathbf{x}_s = -\frac{1}{2}\mathbf{B}^{-1}\mathbf{b} \quad \text{Eq.(2.30)}$$

If all eigenvalues of \mathbf{B} are positive(negative), then the quadratic surface has a minimum(maximum) at the stationary point \mathbf{x}_s . If the eigenvalues have mixed signs, then the stationary point \mathbf{x}_s is a saddle point.

Perform ridge analysis. It is not advisable to extrapolate the second-order polynomial beyond the current region of experimentation, because the fitted model is not reliable outside the experimental region [266]. Therefore, if the stationary point is a minimum that lies outside the current region of experimentation, it is not accepted as the center of the next region of experimentation. In the case if the stationary point is a maximum or a saddle point, then the stationary point is rejected as well. In

these cases, ridge analysis is performed, which means a search for a new stationary point x_s on a given radius R such that the second order model has a minimum at this stationary point [266].

Using Lagrange analysis, the stationary point is given by

$$(\mathbf{B} - \mu \mathbf{I})\mathbf{x} = (-\frac{1}{2}) \mathbf{b}$$

As a result, for a fixed μ , a solution x of Equation (4.3) is a stationary point on $R = (\mathbf{x}'\mathbf{x})^{1/2}$. In the working regions of μ , namely $\mu > \lambda_k$ or $\mu < \lambda_1$, where λ_1 is the smallest eigenvalue of B and λ_k is the smallest eigenvalue of B , R is a monotonic function of μ . As a result, a computer algorithm for ridge analysis involves the substitution of $\mu > \lambda_k$ (for a design maximum response) and increases μ until radii near the design perimeter are encountered. Future increases in μ results in coordinates that are closer to the design center. The same applies for $\mu < \lambda_1$ (for desired minimum response), with decreasing values of μ being required.

10. Accept the stationary point. The stationary point will be used as the center point of the next experimental region. The analyst should decide whether the first-order or a second-order model is used to approximate the simulation response surface in this region. This decision can be based on the results of the canonical analysis. For example, if a minimum was found, it could be useful to explore a region around this minimum with a new second-order approximation. Opposite, if a maximum or a saddle point was found, the optimum could still be located far away from the current experimental region. In this case, approximating this region with a first-order model and consequently performing a line search would be preferable. Allowing this we return to the first phase of our algorithm. It is considered to be a powerful selfcorrection mechanism.

11. An enhanced algorithm is introduced in [276]. In this algorithm the authors use the gradient of the second-order model in the center point of the current region and the results of the canonical analysis to determine the direction of steepest descent. Next, they perform a line search using this direction, resulting in a new center of an experimental region. In this region they already approximate the simulation response surface by a first-order model.

12. Stopping criterion. Usually it is recommended ending the optimization process if the estimated optimal simulation response value does not improve sufficiently anymore or if the experimental region becomes too small. In the case of restricted budget we can stop if a fixed number of evaluations has been performed. Next, a confidence interval on the response at the estimator for the optimum can be determined.

Very often the natural sequential deployment of RSM allows the user to make intelligent choices of variable ranges. What is often even more important is for the response surface analysis to reveal important information about the nature of the simulation model and the roles of the variables. The computation of a stationary point, a canonical analysis, or a ridge analysis may lead to important

information about the simulated process, and in the long run it might be very valuable. Using of RSM as an automated validation tool also helps to make the validation process of the simulation model less time and resource consuming and less prone to bias. Using the RSM equivalent rather than the multi-agent simulation model on some stages of simulation process also eliminates the wait time for generating results under a variety of conditions and to address a number of policy issues.

CHAPTER 3 Photocatalytic oxidation

3.1 Semiconducting nanomaterials

Since its commercial production in the early twentieth century, titanium dioxide (TiO_2) has been widely used as a pigment and in sunscreens, paints, ointments, toothpaste, etc. In 1972, Fujishima and Honda discovered the phenomenon of photocatalytic splitting of water on a TiO_2 electrode under ultraviolet (UV) light. Since then, enormous efforts have been devoted to the research of TiO_2 material, which has led to many promising applications in areas ranging from photovoltaics and photocatalysis to photo-/electrochromics and sensors. These applications can be roughly divided into “energy” and “environmental” categories, many of which depend not only on the properties of the TiO_2 material itself but also on the modifications of the TiO_2 material host (e.g., with inorganic and organic dyes) and on the interactions of TiO_2 materials with the environment [277].

An exponential growth of research activities has been seen in nanoscience and nanotechnology in the past decades. New physical and chemical properties emerge when the size of the material becomes smaller and smaller, and down to the nanometer scale. Properties also vary as the shapes of the shrinking nanomaterials change. Many excellent reviews and reports on the preparation and properties of nanomaterials have been published recently. Among the unique properties of nanomaterials, the movement of electrons and holes in semiconductor nanomaterials is primarily governed by the well-known quantum confinement, and the transport properties related to phonons and photons are largely affected by the size and geometry of the materials. The specific surface area and surface-to-volume ratio increase dramatically as the size of a material decreases. The high surface area brought about by small particle size is beneficial to many TiO_2 -based devices, as it facilitates reaction/interaction between the devices and the interacting media, which mainly occurs on the surface or at the interface and strongly depends on the surface area of the material. Thus, the performance of TiO_2 -based devices is largely influenced by the sizes of the TiO_2 building units, apparently at the nanometer scale.

As the most promising photocatalyst, TiO_2 materials are expected to play an important role in helping solve many serious environmental and pollution challenges. TiO_2 also bears tremendous hope in helping ease the energy crisis through effective utilization of solar energy based on photovoltaic and water-splitting devices. As continued breakthroughs have been made in the preparation, modification, and applications of TiO_2 nanomaterials in recent years, especially after a series of great reviews of the subject in the 1990s.

Moreover various n-type semiconductor metal oxides, such as TiO_2 , ZnO , CdS , SnO_2 , and WO_3 , have been tested for photocatalytic elimination of organic pollutants in water and air.

The drawbacks to using these metal oxides are their (a) large band gap, often requiring near-UV light ($\lambda < 400$ nm) to induce electron photoexcitation, (b) instability in aqueous medium, leading to photocatalyst decomposition, and (c) high electron-hole recombination rates. Miyauchi and co-workers [278] tested 12 metal oxide (MO) thin films in air for surface wettability and oxidation of methylene blue coated on the MO surface. Only TiO₂, ZnO, and SnO₂ exhibited both photocatalytic oxidation (PCO) and photoinduced superhydrophilicity (PSH) qualities when illuminated under 2 mW/cm² UV irradiance, making them good catalyst candidates for “self-cleaning” surfaces in air. Zinc oxide in water self-deactivates when reacted with photogenerated holes to form Zn²⁺ ions which dissolve into solution [279,280]. A similar photocorrosion effect is seen for CdS in solution, releasing toxic Cd²⁺ into the aqueous medium [279,281]. Tin oxide has lower relative photoactivity compared to TiO₂ because of its wider band gap of 3.5-4.2 eV (350-300 nm) versus 3.2 eV (TiO₂), which utilizes a lesser fraction of UVA light [282]. Titanium dioxide is widely accepted as the best photocatalyst because of its chemical stability, strong oxidizing power, non-toxicity, and low cost. Moreover metaloxide nanoparticles such as magnesium oxide, aluminium oxide, etc. are actively destroy the chemical and biological warfare agents into nontoxic products and the activity is found to be more when compared to bulk materials [283]. These nanoparticles possess high reactivity (when compared to bulk material) not only due to high surface area alone, rather specific types of defects (highly reactive edge and corner defects), shapes (small irregular-shaped particles), and residual presence of OH and –OCH₃ groups [284]. It is reported that magnesium oxide degrades nerve agents, mustard gas, and biological spores effectively [285]. Mechanism of degradation of chemical warfare agent simulant (such as paraoxon) is found to be destructive adsorption and much faster than activated charcoal, which physisorb and does not degrade destructively. It was reported in literature that magnesium hydroperoxyacetate was easily dispersed in water and hand sprayed on the PET/cotton cloth and tested as an antibacterial agents [286,287]. This hydroperoxyacetate was stable up to 50 laundries in which cotton has the tendency to withhold the hydroperoxide during laundry time. However, the better uniformity could not be achieved by using handspray technique [287].

3.2 Photocatalytic oxidation (PCO)

Figure 54 [288] presents the diagram of photocatalytic oxidation. For the photocatalytic oxidation, an important step of photoreaction is the formation of hole–electron pairs which need energy to overcome the band gap between the valence band (VB) and conduction band (CB). When the energy provided (photon) is larger than the band gap, the pairs of electron–holes are created in the semiconductor, and the charge will transfer between electron–hole pairs and adsorbed species

(reactants) on the semiconductor surface, then photooxidation happens. A good photocatalyst is characterised by its capability to adsorb simultaneously two reactants, which can be reduced and oxidised by a photonic activation through an efficient absorption ($h\nu > E_g$). Currently, for the photocatalytic reaction, TiO_2 is the most important and widely used catalyst. Other semiconductors such as ZnO , ZnS , CdS , Fe_2O_3 , SnO_2 are also commonly used catalysts.

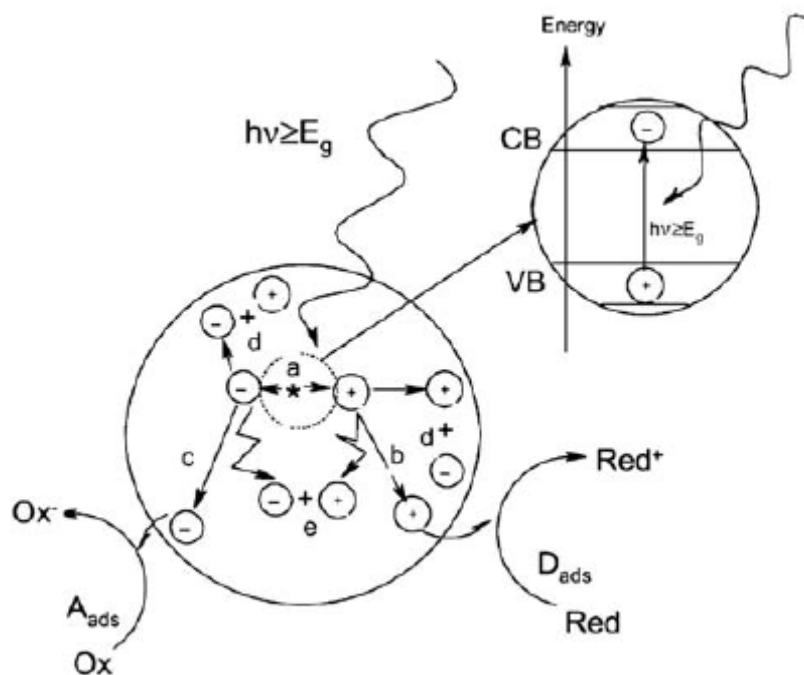


Figure 54 Main processes occurring on a semiconductor particle: (a) electron-hole generation; (b) oxidation of donor (D); (c) reduction of acceptor (A); (d) and (e) electron-hole recombination at surface and in bulk, respectively

The PCO property is activated by photocatalyst absorption of UV photons of energy greater than the TiO_2 band gap energy (EBG). Electron photoexcitation from the TiO_2 valence band (VB) to the conduction band (CB) produces electron (e^-_{CB}) - hole (h^+_{VB}) pairs (Eq. 3.1). For anatase phase TiO_2 , $\text{EBG} = 3.2 \text{ eV}$ ($\lambda = 385 \text{ nm}$), while rutile phase TiO_2 has a $\text{EBG} = 3.0 \text{ eV}$ ($\lambda = 410 \text{ nm}$). The redox potential for h^+_{VB} is $+2.53\text{V}$ with respect to the standard hydrogen electrode (SHE), which is sufficiently oxidizing to overcome the $+2.27\text{V}$ SHE binding energy of e^- in OH^- to form a hydroxyl radical OH^\bullet (EB,VB) from water [288], shown in Eq. (3.2). Similarly, e^-_{CB} (-0.52V SHE redox potential) is sufficiently reductive to react with O_2 to form O_2^- (EB,CB = -0.28V SHE) [288], shown in Eq. (3.3). The O_2^- in turn may react with H^+ to form the perhydroxyl / hydroperoxyl radical HO_2^\bullet (Eq.3.4). All E values are reported for $\text{pH} = 7$.



The overall PCO process is shown schematically in Figure 54. The mobile $\text{OH}\cdot$ reacts with adsorbed, oxidizable species to form volatile and/or water soluble products. The $\text{HO}_2\cdot$ is also reactive, but weaker than $\text{OH}\cdot$. The $\text{HO}_2\cdot$ also can combine with another H^+ to form yet less reactive H_2O_2 . The full PCO reaction sequence for TiO_2 is detailed by Turchi and Ollis [290].

The TiO_2 PSH property, as designated by Fujishima et al. [288], has been rationalized by two proposed mechanisms. In one explanation, electrons reduce Ti(IV) cation sites to Ti(III) and holes oxidize O_2^- anions to O_2 . The molecular O_2 are ejected, creating surface vacancies on which water can adsorb as OH groups, giving the TiO_2 surface its hydrophilic nature [288,291]. This process is summarized in Eq. (2) taken from Mills et al. [291]. In fact, the illuminated TiO_2 surface exhibited amphiphilicity [292] caused by creation of alternating hydrophilic/hydrophobic domains. Fujishima and coworkers [288] showed that in the absence of UV illumination, the water contact angle for TiO_2 was $72^\circ \pm 1^\circ$ (hydrophobic), while UV illumination of $1 \mu\text{W}/\text{cm}^2$ dropped the contact angle to $0^\circ \pm 1^\circ$ (hydrophilic).

Alternatively, Zubkov et al. [293] hypothesized that absorbed trace-level hydrocarbon contaminants on the initial TiO_2 surface were photooxidized by O_2 to reveal a wettable surface. A water droplet on hydrocarbon-covered TiO_2 experienced a sudden decrease (< 1 s) in contact angle after an initial period of hydrophobic behavior. This induction period occurred because the pre-absorbed hydrocarbon layer must be removed before the TiO_2 surface became wetted.

3.3 VOCs exposure in indoor environment

Indoor air was defined as the air in non-industrial areas of dwellings, offices, schools, and hospitals. Recently, air quality in cars and aircraft cabins has also raised much concern, because these vehicles are also typical indoor environments. According to the definition of the World Health Organisation (WHO), VOCs are referred as all organic compounds in the boiling point range of $50\text{--}260^\circ\text{C}$, and excluding pesticides. Figure 55 lists the classes of VOCs identified in indoor air, in which aromatics, aldehydes, and halocarbons are the most occurring compounds.

Since the 1970s, a lot of investigations have been carried out for measurement of the indoor air concentrations of VOCs all around the world [294]. It is found that indoor air typically contains a greater number of VOCs at higher concentrations than outdoor air. The concentrations of VOCs are dependent on the environment. The mean concentration of each VOC in established buildings is generally below $50 \mu\text{g}/\text{m}^3$, but higher than $5 \mu\text{g}/\text{m}^3$. The mean concentrations of VOCs and total VOCs in established buildings are generally greater than those established public buildings and VOC concentrations in new buildings are much greater than those in established buildings [294].

VOC class	Environment and sources
Aliphatic and cyclic hydrocarbons	1, 2, 4, 5, 7, 9–11
Aromatic hydrocarbons	1–7, 9, 11, 12
Aldehydes	1–12
Terpenes	1–4, 7–10
Alcohols	1–9, 11
Esters	1, 2, 4, 7–9
Halocarbons	1, 2, 7, 11
Glycols/glycolethers/glycolesters	1–4, 7, 9
Ketones	1–4, 6–12
Siloxanes	11
Alkene	2, 7
Organic acids	2, 3, 7–9, 11
Ethers	9
Other VOCs	1, 2, 4, 7, 11

Figure 55 Classes of VOCs and their possible emission sources [294]:

1: Established buildings, **2:** new and renovated buildings, **3:** school, **4:** new car interiors, **5:** carpets, **6:** floor coverings, **7:** wood-based panel and furniture, **8:** solid woods, **9:** paints, **10:** cleaning products, **11:** unflued gas heaters and electric ovens, **12:** office equipment.

Compound	Source material(s)
Paradichlorobenzene	Moth crystals, room deodorants
Methylene chloride	Paint removers, solvent usage
Formaldehyde	Pressed wood products, foam
Styrene	Insulation, textiles, disinfectants, plastics, paints
Acetaldehyde	Glues, deodorants, fuels, preventives, mold growth on leathers
Acrolein	Component of oak-wood, by-product of the combustions of wood, kerosene and cotton
Toluene diisocyanate	Polyurethane foam, aerosols
Phthalic acid anhydride	Epoxy resins
Trimellitic acid	
Triethylene tetraamine	
Benzyl chloride	Vinyl tiles plasticized with butyl benzyl phthalate
Benzyl chloride	
Ethylene oxide	Sterilizers (hospitals)
Amines (cyclohexylamine, diethylaminoethanol, morpholine)	Volatilized with the steam boiler systems (corrosion inhibitors of steam pipes and other equipment)
Volatile amines	Putrefactive degradation of casein-containing building materials
Benzene	Smoking
Tetrachloroethylene	Wearing or storing dry-cleaned clothes
Chloroform	Chlorinated water (showering, washing clothes, dishes)
1,1,1-trichloroethane	Wearing or storing dry-cleaned clothes, aerosols sprays, fabric protectors
Carbon tetrachloride	Industrial strength cleaners
Aromatic hydrocarbons (toluene, xylenes, ethylbenzene, trimethylbenzenes)	Paints, adhesives, gasoline, combustion sources
Aliphatic hydrocarbons (octane, decane, undecane)	Paints, adhesives, gasoline, combustion products
Terpenes (limonene, α -pinene)	Scented deodorizers, polishes, fabrics, fabric softeners, cigarettes, food beverages
Chloropyrifos (Dursban)	Household insecticides
Chlordane, heptachlor	Termicide
Diazinon	Termicide
PCBs	Transformers, PCB-containing fluorescent light ballasts, ceiling tiles
PAHs	Combustion products (smoking, woodburning, kerosene heaters)
Polychlorinated dibenzofurans (PCDFs)	Incinerator stack emission
Polychlorinated dibenzo- <i>p</i> -dioxins (PCDDs)	Contamination of pentachlorophenol used as wood preservative
Acrylic acid esters, epichlorohydrin, vinyl chloride	Monomers may escape from polymers
Alcohols	Aerosols, window cleaners, paints, paint thinners, cosmetics and adhesives
Ketones	Lacquers, varnishes, polish removers, adhesives
Ethers	Resins, paints, varnishes, lacquers, dyes, soaps, cosmetics
Esters	Plastics, resins, plasticizers, lacquers solvents, flavors, perfumes
Pentachlorophenol	Wood preservative agent
Lindane	Wood preservative formulations

Figure 56 Specific indoor sources of organic vapours [295]

The exposure level of VOCs in indoor environment is also significantly dependent on the sources and emission rates. There is a variety of sources of VOCs in indoor air. The emission of volatile organic compounds from building material has been recognised as the largest source of indoor air pollutants. In some cases, contributions from outdoor air can be an important component through leakages and makeup air in ventilation systems. Indoor sources vary tremendously depending on the nature of the facility and are too diverse for any simple classification. In summary, a variety of VOCs including alcohols, aromatics, aldehydes, and halocarbons will occur in indoor environment. The VOCs concentrations in indoor environments such as home, office, public buildings, and mobile cabins are much similar. The individual VOC is usually lower than $50 \mu\text{g}/\text{m}^3$, however, total VOCs are much higher. The building materials and coverings are the major contributors to indoor VOCs with various emission rates.

CHAPTER 4 Materials

4.1 Macromolecular materials for electrospinning

As regards nanofibers processing, three different polymer have chosen:

Polysulfone PSU (Mw 34.000 g/mol), was purchased by Aldrich, USA and N,N-dimethylformamide (DMF) provided by Sigma-Aldrich, USA, was used as a solvent after dehydration by storage with molecular sieves. PSU solutions 18wt% have been prepare and then processed by electrospinning.

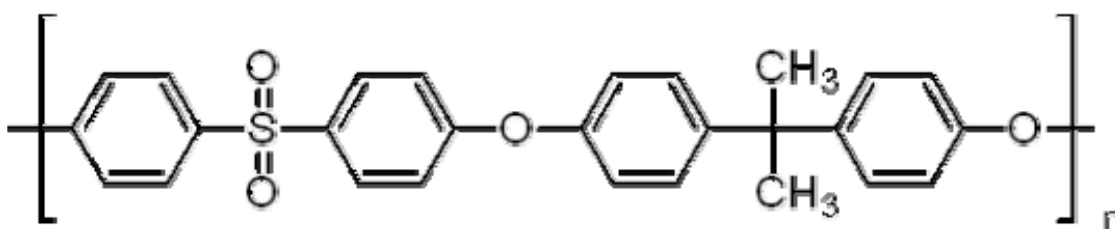


Figure 57 PSU chemical structure

Polymethylmethacrylate co methacrylic acid (PMMAcoMAA) (Mw 34.000 g/mol, inherent viscosity 0.19 dl/g, T_g=105°C, molar ratio MMA:MAA= 1:0.016) was purchase by SigmaAldrich, USA. This polymer has been chosen because of the presence of carboxylic groups within the mamomolecular chain, which may interact with the hydroxyl group on the nanoparticles surface and then improve their binding. Since the solutions properties are affected by solvent properties, herein we just cite the used solvent and their specific properties (Table XX) but details regards how they affect the resulting electrospun nanofibers will be discuss in Chapter 7.

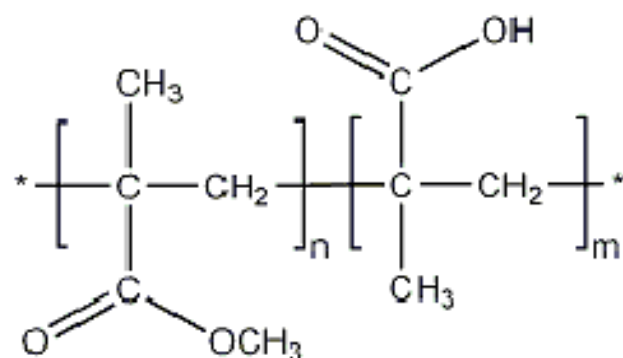


Figure 58 PMMAcoMAA chemical structure

Solvent	Surface Tension at 20 °C [mN/m]	Dielectric constant	Boiling Temperature [°C]	Viscosità at 20°C [mPas]
Acetone	25,2	20,7	56,2	3,06
Methanol	22,6	32,7	64,7	0,6
N,N Dimetilformamide	37,1	38,3	153	9,2

Table4. 1 Solvent properties

Poly (acrylonitrile-co-vinyl acetate) was purchased by Montefibre s.p.a and it has been chosen in order to improve some properties (see Chapter 7) of the produced multistructured membrane. The solvent used for preparing the solutions is DMF and details regards the operating conditions are reported in Chapter 7.

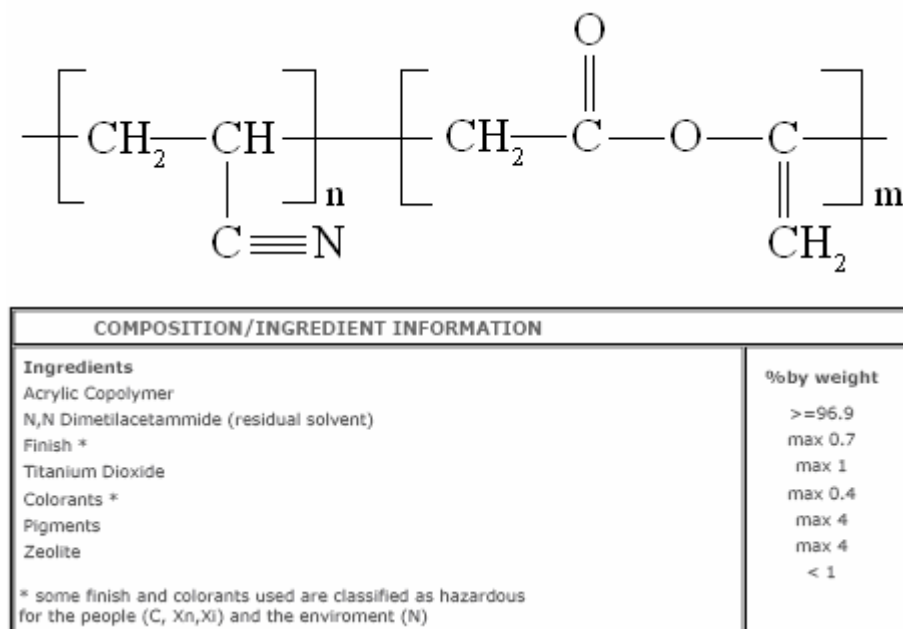


Figure 59 PANcoAc chemical structure and composition information

4.2 Nanoparticles

4.2.1 Titanium dioxide nanoparticles

The inorganic nanoparticles used in this project are Titanium dioxide P25 (mean surface area 50 ± 15 m²/kg, average primary particle size, 21nm, 80% anatase and 20% rutile) purchased by Degussa, Germany. In order to suspend these nanoparticles, methanol from was used as a solvent without any further purification. In order to have more details about TiO₂ crystallites properties and structure the reader may refer to the extensive literature [296].

4.2.2 Magnesium Oxide nanoparticles production via aerogel technique

MgO is a unique solid owing to its highly ionic nature, simple stoichiometry, and crystal structure. It can be prepared in widely variable particle sizes and shapes. MgO prepared by the aerogel route (AP-MgO) [297] possesses surface area in the range of 300-500 m²/g and consists of very small weakly aggregated crystallites (about 4 nm in size) that appear more irregular with polyhedral shapes. AP-MgO possesses numerous surface sites such as crystal corners, edges, or ion vacancies, which lead to inherently high surface reactivity per unit area. AP-MgO nanocrystals isolated in powder form exist as porous aggregates of 1-2 microns in size.

AP-MgO procedure. In a three-necked 2 L creased round bottom flask equipped with a mechanical stirrer, water cooled condenser, and N₂ inlet with a three-way stopcock was placed 300 mL of toluene. In another flask, 2.4 g (0.10 mol) of Mg turnings was allowed to react with 100 mL of CH₃OH under N₂. The resultant 1 M solution of Mg(OCH₃)₂ was added dropwise to the toluene with vigorous stirring under N₂. Then 2.8 mL of distilled water was added dropwise from a syringe over a 10 min period. This solution was stirred at room temperature under N₂ overnight. The resultant slightly milky solution (gel-like) was placed in an autoclave parr reactor. The ramp and soak heating condition for the experiments was the following: ramp from room temperature to 220 °C at 1°C/min; soak at 220 °C for 5 h; ramp from 220 to 500 °C at 1°C/min; soak at 450 °C for 5 h.

4.2.3 Dispersant agent

A dispersant agent was used for improving nanoparticles dispersion in order to avoid their aggregation. 3-Methacryloxypropyltrimethoxysilane (MEMO) provided by Evonik-Degussa, Germany has been chosen within the silane family and its structure is show in Figure 60. Its properties to interact with nanoparticles will be explained in detail in Chapter 7.

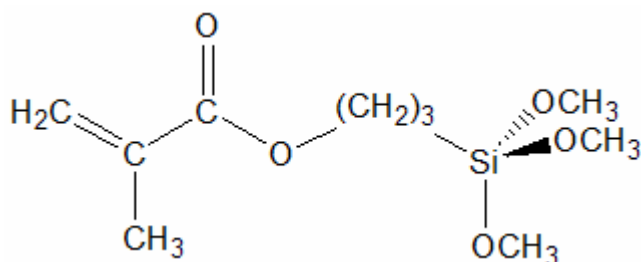


Figure 60 3-Methacryloxypropyltrimethoxysilane (MEMO) chemical structure

CHAPTER 5 Methods

In the present Chapter basic principles of the main techniques used during membrane processing as well as for the evaluation of photocatalytic performances will be shortly reviewed. Dynamic light scattering have been used for monitoring the nanoparticles suspension properties before electrospinning while Scanning electron Microscopy was useful for membrane characterization (both morphology and elementary microanalysis).

As regards the analytic techniques employed in photocatalysis studies, UV spectrophotometer and High performance liquid chromatography (HPLC) were used for liquid phase analysis and Gas spectroscopy coupled with mass spectrometry was the analytic techniques chosen for gas phase studies.

5.1 Characterization techniques

5.1.1 *Dynamic light scattering*

Dynamic Light Scattering is also known as Photon Correlation Spectroscopy.

This technique is one of the most popular methods used to determine the size of particles [304].

Classical electromagnetic theory tells us that incident light which impinges on a nonconducting, nonmagnetic, nonabsorbing molecule induces a fluctuating dipole in the molecule which then radiates light of the same frequency in all directions. In the case of polymer solutions, this elastically scattered light contains information on the size and shape of the scattering molecules (static light scattering). However, the light is not only scattered elastically, but also inelastically (Brillouin and Raman scattering) and quasielastically (dynamic light scattering) by the motions of the polymers in solution due to the Doppler effect. In the case of Brillouin and Raman scattering, the frequency of the scattered radiation is shifted from the incident frequency by sound waves in the fluid (Brillouin) and vibrational motions of the molecules (Raman).

Dynamic light scattering, also called quasielastic light scattering (QELS) or photon correlation spectroscopy (PCS), is the study of the very small shifts of the Rayleigh (elastic) scattered light caused by the translations and rotations of molecules. These shifts are on the order-of 10^{-5} cm^{-1} (compared to 1000 cm^{-1} for Raman spectroscopy), too small to be measured by standard spectroscopic techniques, and thus are usually measured in the Fourier-transformed time domain using correlation functions (hence the term photon correlation spectroscopy).

Dynamic light scattering (DLS) determines the frequency distribution of the scattered light at a given angle, $I(\omega, \theta)$, whereas static light scattering (SLS) involves measurement only of the total

intensity of light scattered at that angle, $I(\theta)$, essentially the integration of the DLS spectrum over the entire frequency range.

The scattered light impinging on a photomultiplier tube (PMT) outputs a current, $i(t)$, which is proportional to the intensity of the scattered light, $I_s(t)$. Since the intensity of the light is equal to the square of the electric field, $I_s(t) = E_s(t)^2 \propto i(t)$. The output of the PMT is then fed into a correlator which computes the intensity autocorrelation function,

$$\langle i(0)i(\tau) \rangle = B \langle |E_S(0)|^2 |E_S(\tau)|^2 \rangle$$

where B is a proportionality constant. This correlation function is similar to an exponential decay curve, and a single (or distribution of) characteristic decay times (τ_c) can be extracted via data analysis routines. The Fourier transform of this correlation function is the power spectrum or spectral density, and τ_c is related to the linewidth of the power spectrum through $\Gamma = 2\pi/\tau_c$.

This linewidth (or distribution of linewidths) can be related to the rotational and translational diffusion causing the line broadening of the Rayleigh scattered light. For simple translational diffusion, each Γ is related to a translational diffusion coefficient D_T , which is related to the hydrodynamic size of the scattering molecule. Thus, DLS can be used to determine particle size distributions or in certain cases, molecular weight distributions.

The scattered electric field is proportional to the molecular polarizability of the molecule, $\alpha(t)e^{iqr(t)}$. This tensor has two components: $\alpha(t)$, the polarizability of the molecule along the initial and final polarization directions, and $e^{iqr(t)}$, the component which changes as the molecule translates, where $r(t)$ is the molecule's position at time t . The scattering wave vector (q) is defined as $(4\pi n/\lambda)\sin(\theta/2)$, where λ is the wavelength of the scattering radiation, n is the refractive index of the scattering medium, and θ is the angle at which the scattered light is detected.

When the product of the wave vector and the radius of the scattering particle is less than unity ($qR \ll 1$, usually the case for synthetic macromolecules using visible radiation), the time correlation function is sensitive to fluctuations occurring on the time-scale associated with center-of-mass diffusion. In this case, the diffusion coefficient of the molecule can be simply related to the experimentally determined linewidth via $\Gamma = Dq^2$. If spherical particles are assumed, the Stokes-Einstein equation can be used to convert D to a hydrodynamic radius, R_h .

When qR exceeds unity (particles are very large, or scattering is from shorter wavelength radiation or is detected at large angles), the motions of the scattering particle cannot be attributed to translational diffusion alone, internal motions of the particle become important, and rotational diffusion coefficients (Θ) may be calculated.

In many applications of dynamic light scattering, the interpretation of the experimentally determined linewidths cannot be simply related to translational and rotational diffusion coefficients

or to particle sizes. However, it is still useful to determine the distribution of linewidths, particularly when there are bimodal distributions present, because it is an indication of different size particles, which might be interpreted as due to aggregation or other phenomenon.

5.1.2 Scanning electron microscopy

The scanning electron microscope (SEM) uses a focused beam of high-energy electrons to generate a variety of signals at the surface of solid specimens [304]. The signals that derive from electron-sample interactions reveal information about the sample including external morphology (texture), chemical composition, and crystalline structure and orientation of materials making up the sample. In most applications, data are collected over a selected area of the surface of the sample, and a 2-dimensional image is generated that displays spatial variations in these properties. Areas ranging from approximately 1 cm to 5 microns in width can be imaged in a scanning mode using conventional SEM techniques (magnification ranging from 20X to approximately 30,000X, spatial resolution of 50 to 100 nm). The SEM is also capable of performing analyses of selected point locations on the sample; this approach is especially useful in qualitatively or semi-quantitatively determining chemical compositions (using EDAX), crystalline structure, and crystal orientations (using diffracted backscattered electrons, EBSD).

5.1.2.1 Electron-Sample Interactions

Electrons accelerated onto a material result in a number of interactions with the atoms of the target sample. Accelerated electrons can pass through the sample without interaction, undergo elastic scattering and can be inelastically scattered (Figure 61) [306].

As the name implies, elastic scattering results in little ($<1\text{eV}$) or no change in energy of the scattered electron, although there is a change in momentum. Since momentum, $p=mv$, and m doesn't change, the direction of the velocity vector must change. The angle of scattering can range from 0-180 degrees, with a typical value being about 5 degrees.

Elastic scattering occurs between the negative electron and the positive nucleus. This is essentially Rutherford scattering. Sometimes the angle is such that the electron comes back out of the sample and these represent backscattered electrons. During inelastic scattering, energy is transferred to the electrons surrounding the atoms and the kinetic energy of the energetic electron involved decreases. A single inelastic event can transfer a various amount of energy from the beam electron ranging from a fraction to many kiloelectron volts. The main processes include phonon excitation, plasmon excitation, secondary electron excitation, continuum X-ray generation, and ionization of inner shells. In all processes of inelastic scattering, energy is lost, though different processes lose energy at varying rates. Consequently elastic and inelastic scattering result in a number of signals that are

used for imaging, quantitative and semi-quantitative information of the target sample and generation of an X-ray source. Typical signals used for imaging include secondary electrons (SE), backscattered electrons (BSE), cathodoluminescence (CL), Auger electrons and characteristic X-rays. Quantitative and semi-quantitative analyses of materials as well as element mapping typically utilize characteristic X-rays. As previously mentioned characteristic X-rays are generated when an energetic beam of electrons interacts with the inner shell electrons by inelastic scattering with enough energy to excite inner shell electrons to outer shell orbitals, leaving inner-shell vacancies (Figure 62). As outer-shell electrons fall to the various inner shell orbitals, characteristic amounts of energy are generated that are a function of the target element and the type of orbital decay. Much of the energy is emitted from the atom or some may be internally absorbed and knock out another outer shell electron (Auger electron) with additional energy emissions.

Bremsstrahlung (continuum) radiation is a continuous spectrum of X-rays from zero to the energy of the electron beam, and forms a background in which characteristic X-ray must be considered. Further, X-rays generated from a specific target material are used as the roughly fixed-wavelength energy source for X-ray diffraction (XRD) and X-ray fluorescence (XRF) investigations.

Where an electron beam impinges on a sample, electron scattering and photon- and X-ray-production develops in a volume (the electron interaction volume) that is dependent on several factors. These include:

- The energy of the incident beam (accelerating potential) increases the interaction volume, but decreases the elastic scattering (e.g. backscattering).
- The interaction volume decreases as a function of the mean atomic weight.
- Smaller and more asymmetric interaction volumes develop in samples tilted relative to the impinging electron beam.

Each of the signals used for imaging or X-ray generation is generated from different electron interaction volumes and, in turn, each of the signals has different imaging or analytical resolution. Auger and Secondary images have the best imaging resolution, being generated in the smallest volume near the surface of the sample. Backscattered electrons are generated over a larger volume resulting in images of intermediate resolution. Cathodoluminescence is generated over the largest volume, even larger than Bremsstrahlung radiation, resulting in images with the poorest resolution.

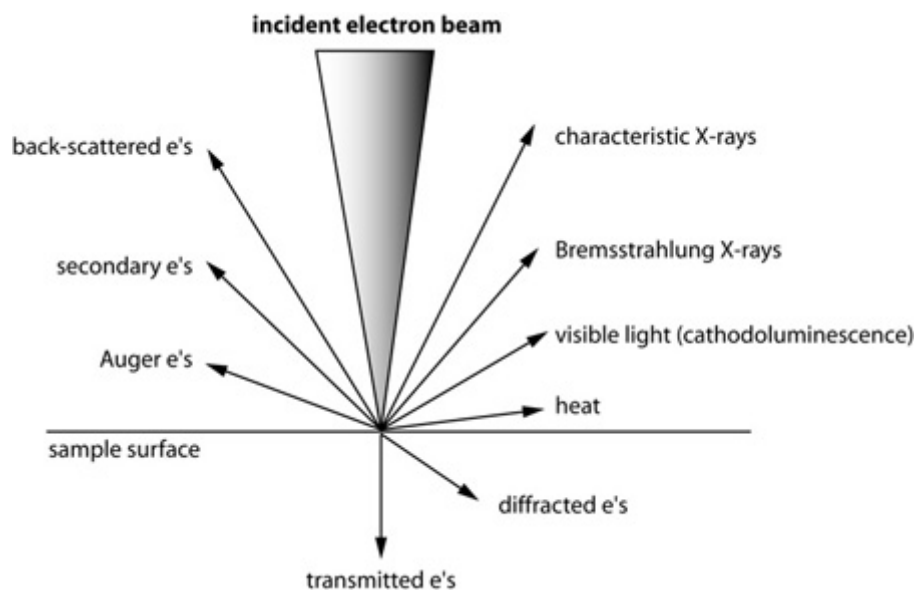


Figure 61 Types of interactions between electrons and a sample

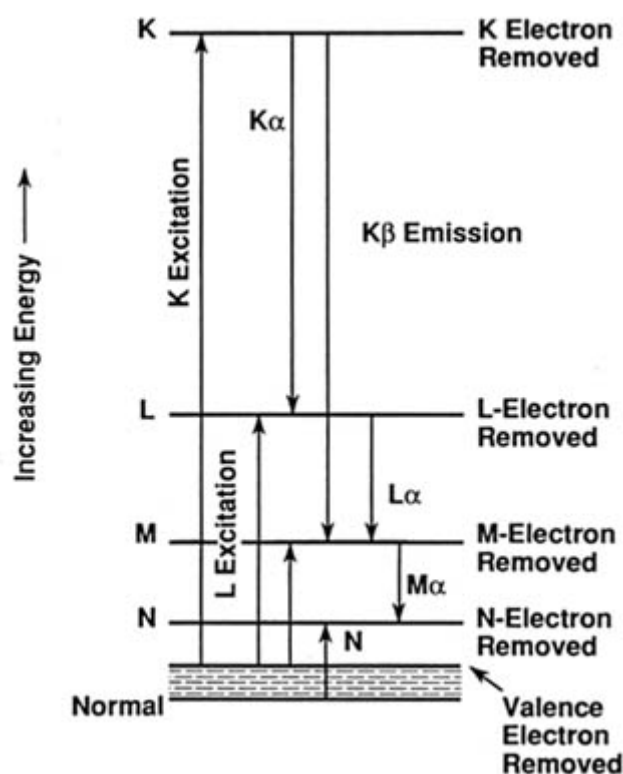


Figure 62 Energy shells

5.1.2.2 Fundamental Principles of Scanning Electron Microscopy (SEM)

Accelerated electrons in an SEM carry significant amounts of kinetic energy, and this energy is dissipated as a variety of signals produced by electron-sample interactions when the incident electrons are decelerated in the solid sample. These signals include secondary electrons (that produce SEM images), backscattered electrons (BSE), diffracted backscattered electrons (EBSD that are used to determine crystal structures and orientations of minerals), photons (characteristic X-rays that are used for elemental analysis and continuum X-rays), visible light

(cathodoluminescence-CL), and heat. Secondary electrons and backscattered electrons are commonly used for imaging samples: secondary electrons are most valuable for showing morphology and topography on samples and backscattered electrons are most valuable for illustrating contrasts in composition in multiphase samples (i.e. for rapid phase discrimination). X-ray generation is produced by inelastic collisions of the incident electrons with electrons in discrete orbitals (shells) of atoms in the sample. As the excited electrons return to lower energy states, they yield X-rays that are of a fixed wavelength (that is related to the difference in energy levels of electrons in different shells for a given element). Thus, characteristic X-rays are produced for each element in a mineral that is "excited" by the electron beam. SEM analysis is considered to be "non-destructive"; that is, x-rays generated by electron interactions do not lead to volume loss of the sample, so it is possible to analyze the same materials repeatedly.

Essential components of all SEMs include the following (Figure 63) [307,308]:

- Electron Source ("Gun")
- Electron Lenses
- Sample Stage
- Detectors for all signals of interest
- Display / Data output devices
- Infrastructure Requirements:
 - A. Power Supply
 - B. Vacuum System
 - C. Cooling system
 - D. Vibration-free floor

Room free of ambient magnetic and electric fields

SEMs always have at least one detector (usually a secondary electron detector), and most have additional detectors. The specific capabilities of a particular instrument are critically dependent on which detectors it accommodates.

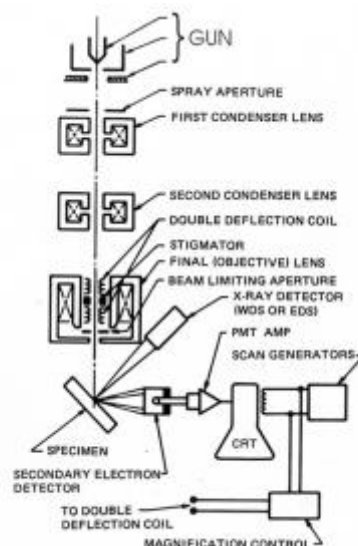


Figure 63 SEM components

5.2 Analytical techniques

5.2.1 UV spectroscopy

5.2.1.1 General principles

Absorption of incident radiation by bonding/non-bonding electrons represents a high energy (~ 100 kcal/mole) transition. This corresponds to a high frequency, i.e. low wavelength, absorption band which is observed at $200 \sim 800$ nm in the UV and visible range of detection.

The absorption of UV or visible radiation corresponds to the excitation of outer electrons. There are three types of electronic transition which can be considered (Figure 64) [309];

- Transitions involving π , σ , and n electrons
- Transitions involving charge-transfer electrons
- Transitions involving d and f electrons

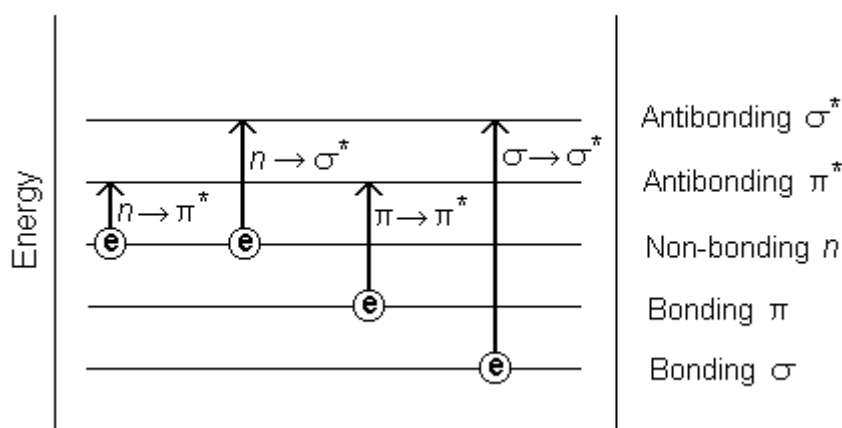


Figure 64 Possible electronic transitions

In solution, electronic absorption spectra are found with broad, generally unresolved bands. These contrast with the vibration fine structure in the vapour phase and with a series of sharp peaks within a continuum in non-polar solvents.

For a solution of an absorbing substance, an absorptivity ratio at a monochromatic wavelength is defined as: $\{(incident\ light, I_0)/(transmitted, I)\}$ and this is logarithmically related to concentration and optical path-length by the Beer Lambert law [310]: Absorbance (A) = $\log_{10}(I_0/I) = k.c.l.$, where c mg/ml is the concentration of solute and l cm is the distance travelled between parallel optical faces of a suitable cell, and k is a proportionality constant. It is frequently convenient to normalise to a concentration $c = 10$ mg/ml [i.e. 1%] and $l = 1$ cm, which is expressed as the specific absorbance [$A^{1\%}_{1cm}$]. Molar absorptivity is defined by the coefficient $\epsilon = M_r.(A/cl)$, and is related to the relative molecular mass, M_r . This coefficient is computed for each wavelength maximum, and also at minima if this is of diagnostic value. It may be useful in showing relationships within an homologous series.

For light source emissivity, the common radiation source is a deuterium lamp covering the operating range 180~ 350 nm and supplemented by a tungsten filament lamp in the near UV, through the visible, into the near-IR, i.e. over the range 320~1000 nm. Stray light is usually checked with a 1.2% potassium chloride solution, where the absorbance for 1 cm path length should exceed 2.0 at 200 nm against a water reference. This solution can be replaced by 1% NaBr or NaI at the more accessible wavelengths of 215 or 240 nm respectively. Glass optics absorb UV light below about 300 nm and quartz systems are used to extend the working range down to 200 nm, and even to 185 nm if there are high quality optics and stray light control. At lower wavelengths, absorption of UV-radiation by air requires the use of vacuum systems in research instruments. For practical UV-vis spectrophotometry, the effective working range is 200~800 nm.

5.2.1.2 Operating conditions

Selection of a suitable solvent is influenced by the wavelength expected to be studied. Water and the lower (polar) alcohols, through diethyl ether and dioxan to nonpolar cyclohexane and light petroleum ('aromatic free' in a spectroscopic grade) can be used above 190 nm, whereas chloroform absorbs below ~245 nm.

The choice of cells depends on the target range. Silica is essential for measurements at UV wavelengths but glass is acceptable in the visible region; air must be evacuated below ~200 nm. The matched pair required for test solution and solvent reference path should demonstrate effectively identical absorbance when filled with the same solvent. The optical faces of the cells should be parallel; the absorbance of a matched pair of cells containing the same solvent should not differ by more than 0.005 units. In quantitative work all solutions should be at the same temperature;

conveniently, they are transferred from a waterbath at, say, 20° C and the absorbance measured immediately. Sensitivity of the solution to laboratory and natural lighting should be established in a pilot experiment.

5.2.1.3 Quantitative procedures

UV photometry is a frequently used assay technique. Provided that proper calibration checks are maintained, the UV-vis technique is particularly useful for assay of formulations after extraction or separation of the active substance by suitable chromatography. In the assay calibration, there may be some deviation from Beer's Law. This may be attributable to association in solution or an effect of slit width. The latter should be large enough to gain a reasonable I-value but remain small compared with the (half-) bandwidth for the absorption measured. If in doubt, reduce the slit width slightly and check if the apparent absorbance increases. UV photometric data can also be of value in determining the kinetics of a process, or in following a reaction sequence, such as the disappearance of an absorption peak representing starting material.

Light absorption' measurements also provide a semi-quantitative test of identity. This relies on the specific absorbance (defined above as the $A_{1\text{cm}}^{1\%}$ value), or sometimes absorbance at a nominated concentration and path length, either exactly at a specified wavelength, or at the absorption maximum close to a named wavelength. The absorption spectrum may be sensitive to control of pH. Chromophores involving an acidic or basic group will be affected by pH, e.g. the bathochromic shift (to longer wavelength) and hyperchromic peak (greater intensity) of phenates compared with their parent phenol

In subtractive spectrophotometry, the difference between two (or more) spectra measures multicomponent mixtures and is especially useful in formulated product assays. This should be distinguished from the use of second derivative spectroscopy, in which there is computer differentiation of the algebraic function equivalent to the change of slope (i.e. second differential) of the digitalised spectrum [311]. This display sharpens separation of individual UV bands and thereby facilitates lower levels of control. In other applications of computer-aided spectroscopy, modern equipment will provide 'smoothing', deconvolution and regression (least squares) analysis.

5.2.2 High Performance Liquid Chromatography (HPLC)

5.2.2.1 General principles

High Performance Liquid Chromatography (HPLC) is one mode of chromatography, the most widely used analytical technique. Chromatographic processes can be defined as separation techniques involving mass-transfer between stationary and mobile phases.

HPLC utilizes a liquid mobile phase to separate the components of a mixture. These components (or analytes) are first dissolved in a solvent, and then forced to flow through a chromatographic column under a high pressure. In the column, the mixture is resolved into its components. The amount of resolution is important, and is dependent upon the extent of interaction between the solute components and the stationary phase. The stationary phase is defined as the immobile packing material in the column. The interaction of the solute with mobile and stationary phases can be manipulated through different choices of both solvents and stationary phases. As a result, HPLC acquires a high degree of versatility not found in other chromatographic systems and it has the ability to easily separate a wide variety of chemical mixtures.

In general, HPLC is a dynamic adsorption process. Analyte molecules, while moving through the porous packing bead, tend to interact with the surface adsorption sites. Depending on the HPLC mode, the different types of the adsorption forces may be included in the retention process:

Hydrophobic (non-specific) interactions are the main ones in reversed-phase separations.

Dipole-dipole (polar) interactions are dominated in normal phase mode.

Ionic interactions are responsible for the retention in ion-exchange chromatography.

All these interactions are competitive. Analyte molecules compete with the eluent molecules for the adsorption sites. So, the stronger analyte molecules interact with the surface, and the weaker the eluent interaction, the longer analyte will be retained on the surface.

SEC (size-exclusion chromatography) is a special case. It is the separation of the mixture by the molecular size of its components. In this mode any positive surface interactions should be avoided (eluent molecules should have much stronger interaction with the surface than analyte molecules).

It is well recognized now that column band broadening originates from three main sources:

- multiple path of an analyte through the column packing;
- molecular diffusion;
- effect of mass transfer between phases.

In 1956 J.J. Van Deemter introduced the equation which combined all three sources and represented them as the dependence of the theoretical plate height (HETP) on the mobile phase linear velocity. Originally, it was introduced for gas chromatography, but it happened that the same physical processes occurs in HPLC, and this equation is perfectly fit for liquid chromatography.

There are two basic approaches for thermodynamic description of the HPLC retention phenomena, one is based on the partitioning theory and another is based on adsorption.

Partition is a concentrational changes in the system due to the distribution of the components between two (or more) phases;

Adsorption is the concentrational changes in the system in presence of interface with another phase and due to the surface forces;

Phase is a form of matter that is uniform throughout in chemical composition and physical state.

In HPLC we have two main phases:

mobile phase (eluent) which is a liquid solvent or mixture of solvents which is moving through the chromatographic column and carrying analytes;

stationary phase (adsorbent) which is a solid porous media which consists of the rigid porous particles, usually silica based, with the specific surface properties (surface chemistry).

Adsorbent particles are considered to be nonpermeable and nonsoluble for the eluent and analyte molecules. It only introduces surface forces in the system.

Consideration of the HPLC process based on the partitioning theory was transferred from GC (gas chromatography) theory, where we usually have a mobile gas phase and stationary liquid phase, and where a true partitioning occurs.

Usual description of liquid chromatography on the partitioning basis consider the assumption of the existence of the separate liquid phase which is close to the adsorbent surface. Chemically bonded phases are usually considered by this manner. The most popular bonded phase is octadecylsilica, where relatively long (21 Å) alkyl chains are chemically bonded to the silica surface. The main partitioning concept is that analyte molecules can penetrate between these alkyl chains. This process thermodynamically considered as dissolving of the analyte molecules in the surface alkyl phase.

Two restrictions exists for application of this approach in thermodynamic description:

the bonded chains have a certain thickness (about 3.8 Å in diameter) and depending on the bonding density the layer may not behave as a liquid;

monomolecular layer would not be considered a phase in classical thermodynamics.

Actually an application of the partitioning theory leads to the certain controversy in the description of some HPLC data.

5.2.2.2 Instrumentation

HPLC instrumentation includes a pump, injector, column, detector and recorder or data system, connected as shown in the Figure below. The heart of the system is the column where separation occurs. Since the stationary phase is composed of micrometer size porous particles, a high pressure pump is required to move the mobile phase through the column.

The chromatographic process begins by injecting the solute onto the top of the column. Separation of components occurs as the analytes and mobile phase are pumped through the column. Eventually, each component elutes from the column as a narrow band (or peak) on the recorder. Detection of the eluting components is important, and this can be either selective or universal, depending upon

the detector used. The response of the detector to each component is displayed on a chart recorder or computer screen and is known as a chromatogram. To collect, store and analyze the chromatographic data, computers, integrators, and other data processing equipment are frequently used. For having more details we suggest to refer to the extensive literature [312].

5.2.3 Gas spectroscopy-Mass spectrometry

Gas chromatography-mass spectroscopy (GC-MS) is one of the so-called hyphenated analytical techniques. As the name implies, it is actually two techniques that are combined to form a single method of analyzing mixtures of chemicals. Gas chromatography separates the components of a mixture and mass spectroscopy characterizes each of the components individually. By combining the two techniques, an analytical chemist can both qualitatively and quantitatively evaluate a solution containing a number of chemicals.

Mass spectrometry is an analytic techniques which find a broad range of applications for:

- identification of the elementary composition of the analyzed sample;
- identification of samples constituents
- determination of the inorganic, organic structure of the biological molecules

It is commonly coupled with separative techniques, such as gas chromatography and High permeation liquid chromatography (HPLC) or more recently with ionization techniques such as induction plasma. A scheme of mass spectrometer coupled with gas chromatography is shown in Figure 65

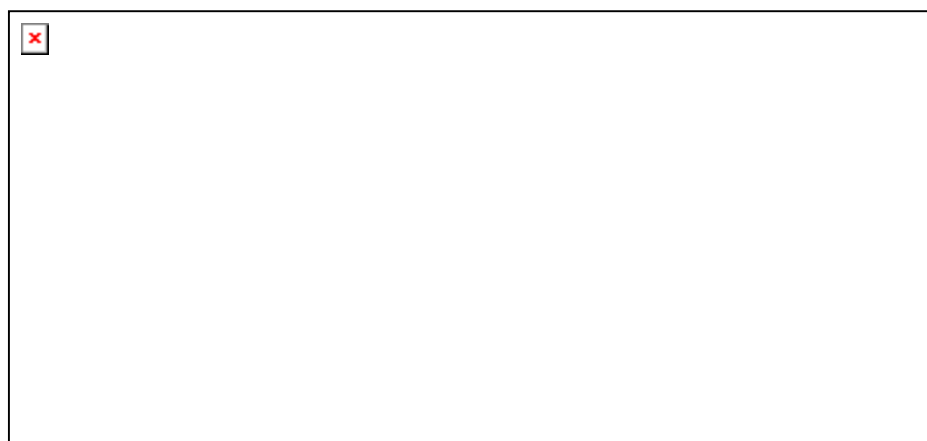


Figure 65 GC/MS scheme

The basic principles of mass spectrometry is the ability to separate a mixture of ions as a function of their mass to charge ratio employing static or oscillating magnetic fields. The most common mode of ionisation is electron impact ionisation. Molecules in the gas phase (at a pressure of typically 10^{-4} Pa) are subjected to bombardment by electrons, normally at energy of 70 eV, generating a radical cation. The mass spectra show the abundance of each ion according to its characteristic mass to charge ratio.

The mass spectrometer has four main sections:

- Injection zone
- Ionization chamber
- Analyzer
- Detector

As regards the injection phase, the amount of sample to inject is just few micrograms. In these conditions most analytes are in gas phase and solid samples which do not sublime are usually vaporized by injection close to ion source. In this specific study the exit of a GC is the inlet of the mass spectrometer, so the sample goes in directly in gas phase or throughout a vaporizer immediately before the column.

Following acceleration of a pulsed beam of ions, those of different mass to charge ratio will arrive at different times, the lightest ions being the first to arrive. The ionisation techniques may generate positive or negative ions and they can be distinguished as:

Hard Techniques: high energy involved and strong fragmentation,

Soft Techniques: low energy involved and soft form of ionisation

According to the ion source, the primary ionisation of the sample can be schematized as shown in Table5. 1.

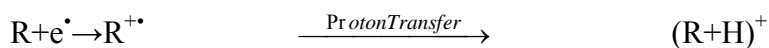
	Ionization mode
HARD TECHNIQUES	<ul style="list-style-type: none"> • Electron Ionization (EI)
SOFT TECHNIQUES	<ul style="list-style-type: none"> • Chemical Ionization(CI) • Fast atom bombardment (FAB) • Thermospray ionization (TSP) • Elettrospray ionization(ESI) • Atmospheric Pressare Chemical ionization (APCI) • Matrix-assisted laser desorption / ionization (MALDI)

Table5. 1 Ionisation techniques

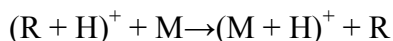
The analyte ionisation may occur according different phenomena: electron impact ionisation, protonation, deprotonation, cationization. The expulsion of electrons generates a radical ion instable which may fragment, while the others generate a pseudomolecular ion.

Chemical ionisation is a less energetic (soft) form of ionisation producing much less fragmentation.

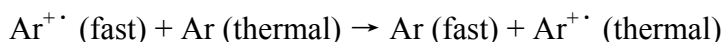
A reactant gas (R) at a relatively high pressure (100 Pa) is ionised by electron impact as shown:



An ion molecule reaction then produces ionisation of compound molecule M:



The technique of fast atom bombardment is a particularly soft form of ionisation. A beam of heavy ions such as Ar⁺. is produced by ionising argon atoms and passing them through an electric field to accelerate them. These fast ions are then passed through a chamber containing argon where charge exchange occurs:



The beam of fast atoms then bombards a metal plate coated with the sample and the high kinetic energy of the atoms is transferred to the sample molecules on impact. This energy is dissipated in various ways, some of which leads to volatilisation and ionisation of the sample.

As regards the mass analyzer, it is possible to distinguish:

- Magnetic analyzer
- Quadrupole analyzer
- Ion trap analyzer
- Time of flight analyzer

The quadrupole mass analyser (of which the ion trap is a three dimensional variant) consists of four hyperbolic rods arranged in a parallel radial array. Each pair of opposite rods are electrically connected to a d.c. voltage on which an oscillating radio-frequency voltage is superimposed. Ions introduced into the quadrupole field undergo oscillations and for a certain value of these fields a stable trajectory will result for ions of a particular m/z value resulting in their transmission to the detector. The mass range is scanned by varying the d.c. and RF fields whilst keeping the voltage ratio and oscillator frequency constant. This produces a low resolution spectrum. In the ion trap ions are stored within the trap in stable trajectories. Raising the RF potential renders successive m/z values unstable; they are then ejected from the trap and detected.

In the time of flight mass spectrometer, which is generally of low resolution, ions of different masses are separated by virtue of their different velocities after acceleration through a potential (V).

The mass spectrometer work in high vacuum depending on the specific section of the instrument:

10⁻⁴ mmHg in the ionisation zone (with the exception of Atmospheric Pressure ionisation system i.e. APCI and plasma (ICP)); 10⁻⁸ in the analyzer and detector zones. This is necessary because mass spectrometer analyzes according to the momentum and the presence of atmospheric gas could interfere with the ions, changing their kinetic energy and getting worse signal to noise ratio.

As previously mentioned the mass spectrometer is coupled with a gas chromatography (GC) which allows an analytical separation of the components. All chromatography techniques, it is based on the partition of the analyte from a stationary to a mobile phase according its affinity to the inert gas carrier.

Basic principles on gas chromatography are basically two [313]:

Adsorption: the stationary phase is a solid and over its surface there are active sites which are able to induce weak bonds formation (dipole-dipole, hydrogen bond, Van der Waals, etc..) to the analytes (Gas-solid chromatography).

Partition: the stationary phase is an immobilized liquid, the analyte will solubilize and split between the two phases according to its affinity for them (Gas-liquid chromatography)

The main sections of the instruments are:

Injection sample zone

Separation column

Detector

There are two general types of column, packed and capillary (also known as open tubular). Packed columns contain a finely divided, inert, solid support material (commonly based on diatomaceous earth) coated with liquid stationary phase. Most packed columns are 1.5 - 10m in length and have an internal diameter of 2 - 4mm.

Capillary columns have an internal diameter of a few tenths of a millimeter. They can be one of two types; wall-coated open tubular (WCOT) or support-coated open tubular (SCOT). Wall-coated columns consist of a capillary tube whose walls are coated with liquid stationary phase. In support-coated columns, the inner wall of the capillary is lined with a thin layer of support material such as diatomaceous earth, onto which the stationary phase has been adsorbed. SCOT columns are generally less efficient than WCOT columns. Both types of capillary column are more efficient than packed columns. In 1979, a new type of WCOT column was devised - the Fused Silica Open Tubular (FSOT) column. These have much thinner walls than the glass capillary columns, and are given strength by the polyimide coating. These columns are flexible and can be wound into coils. They have the advantages of physical strength, flexibility and low reactivity.

There are many detectors which can be used in gas chromatography. Different detectors will give different types of selectivity. A non-selective detector responds to all compounds except the carrier gas, a selective detector responds to a range of compounds with a common physical or chemical property and a specific detector responds to a single chemical compound. Detectors can also be grouped into concentration dependant detectors and mass flow dependant detectors. The signal from

a concentration dependant detector is related to the concentration of solute in the detector, and does not usually destroy the sample Dilution of with make-up gas will lower the detectors response. Mass flow dependant detectors usually destroy the sample, and the signal is related to the rate at which solute molecules enter the detector. Table 5.2 summarized the main detectors available. In particular in the present study we have used a FID detector where The effluent from the column is mixed with hydrogen and air, and ignited. Organic compounds burning in the flame produce ions and electrons which can conduct electricity through the flame. A large electrical potential is applied at the burner tip, and a collector electrode is located above the flame. The current resulting from the pyrolysis of any organic compounds is measured. FIDs are mass sensitive rather than concentration sensitive; this gives the advantage that changes in mobile phase flow rate do not affect the detector's response. The FID is a useful general detector for the analysis of organic compounds; it has high sensitivity, a large linear response range, and low noise. It is also robust and easy to use, but unfortunately, it destroys the sample. More detail about the chromatography techniques can be found in literature [313,314].

Detector	Type	Support gases	Selectivity
Flame ionization (FID)	Mass flow	Hydrogen and air	Most organic cpds.
Thermal conductivity (TCD)	Concentration	Reference	Universal
Electron capture (ECD)	Concentration	Make-up	Halides, nitrates, nitriles, peroxides, anhydrides, organometallics
Nitrogen-phosphorus	Mass flow	Hydrogen and air	Nitrogen, phosphorus
Flame photometric (FPD)	Mass flow	Hydrogen and air possibly oxygen	Sulphur, phosphorus, tin, boron, arsenic, germanium, selenium, chromium
Photo-ionization (PID)	Concentration	Make-up	Aliphatics, aromatics, ketones, esters, aldehydes, amines, heterocyclics, organosulphurs, some organometallics
Hall electrolytic conductivity	Mass flow	Hydrogen, oxygen	Halide, nitrogen, nitrosamine, sulphur

Table5. 2 GC detectors

CHAPTER 6 Optimization of Electrospinning parameters via RSM

6.1 Introduction

In an engineering production process, efforts are often directed toward the goal of optimization. When the response of a process is affected by more than one manipulable variable, it is often desired to find out the particular combination of variable settings that would give the expected response which satisfied specific requirements. A common approach is the one-variable-at-a-time method in which the individual effect of each of the variables is studied alternately and separately. This method has the drawback of being time-consuming, inefficient and even capable of yielding misleading conclusion. At this regard, response surface methodology results a powerful and versatile tool if the parameters effect and their interaction effect on the final response is not clear at all. As suggested in Section I, few parameters affect electrospinning process and consequently the nanofibers morphology. The purpose of this study is to obtain a maximum control over the variables and parameters that govern this process and to have a better understanding of the interaction among different structural configurations.

The early stage of the optimization process has exploited a set of screening experiments in order to evaluate the range of parameters, both solution and process parameters, within which fiber morphology is obtained. Moreover it is possible to define which parameters mainly affect the response, that is the mean fiber diameter, and then decide on the factors for the next response surface analysis. Two systems have been consecutively studied:

- Polymer/solvent system
- Polymer/solvent/salt system

and the results of screening experiments significance will be discuss in the next paragraphs. Subsequently Response Surface analysis for both the systems has been carried out and the parameters effect and their interactions have been extensively studied.

6.2 Case study: Polymer/solvent system

6.2.1 Screening experiments for the Polymer/solvent system

The first screening experiments have been carried out for evaluating the proper conditions in term of minimum concentration of entanglements, electrical conductivity and surface tension of the polymer solution. The latter are strictly connected to the solvents used, the properties of which have

been shown in Chapter 2. In detail, acetone addition turns down the surface tension of the solution and the results for different ratio DMF/acetone are shown in Table6. 1.

DMF/Ac. ratio	Surface tension (Dyne/cm)
1:1	32
2:1	34
1:2	27

Table6. 1 Surface tension of different ratio of solvents

The polymer chosen for this study is the Polymethylmethacrylate-co-Methacrylic Acid (PMMA-co-MAA) and the tested conditions of the first screening stage are reported in Table 6.2.

ID	Polymer Concentration [w/w]	Solvents ratio DMF:Acetone	Voltage [kV]	Flow rate [ml/hr]
1	20	1:1	14	3
2			14	1
3			17	1
4		2:1	17	1
12			14	3
13			14	1
5	25	1:1	14	3
6			14	1
7			17	1
8		2:1	17	1
14			14	3
15			14	1
9	30	1:1	14	3
10			17	1
18			14	1
11		2:1	17	1
16			14	3
17			14	1

Table6. 2 Screening experiments data set

From the literature review previously exposed, it stands to reason all the solution properties are fundamental for obtaining proper fiber morphology and the micrographs of the electrospun samples (see Appendix A) showed that for every sample with polymer concentration of 20% by weight and 25% by weight, beads morphology is predominant and then it means that the critical entanglement concentration, c_e , which marks the distinct onset of significant chain entanglements in solution, is ranging from 25 to 30 % by weight. Moreover, in these conditions, it is not possible to assess the effect of different solvents ratio or the process parameters control.

In order to evaluate the critical entanglement concentration, c_e , a second screening stage has been designed, according to Table 6.3 which summarizes all the electrospun samples.

ID	Polymer Concentration [w/w]	DMF/Acetone Ratio	Voltage [kV]	Flow rate [ml/hr]
33	26	1:1	14	3
34			14	1
35			17	1
36		2:1	14	3
37			14	1
38			17	1
21	27	1:1	14	3
22			14	1
23			17	1
24		2:1	14	3
25			14	1
26			17	1
27	28	1:1	14	3
28			14	1
29			17	1
30		2:1	14	3
31			14	1
32			17	1
39	29	1:1	14	3
40			14	1
42			17	1
42		2:1	14	3
43			14	1
44			17	1

Table6. 3 Second screening experiments data set

Within this second stage of screening, the effect of different solvents ratio has been also evaluated, even if it is not possible to ensure that this parameter is completely independent of the others. SEM micrographs of the electrospun samples are shown in Table 6.4 and Table 6.5. Table 6.4 summarizes the results obtained with DMF:Ac ratio equal to 2:1. Increasing the polymer concentration from 26 to 29wt%, it can be observed a substantial reduction of beads number and dimension. For every concentration, an increase of applied voltage or flow rate doesn't affect substantially the fiber morphology but more significant and quantitative results will be gleaned from the response surface analysis in paragraph 6.3.

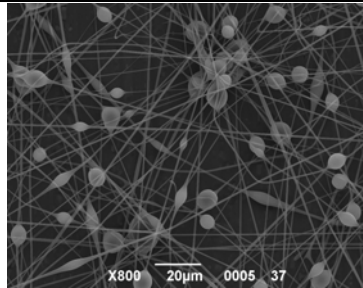
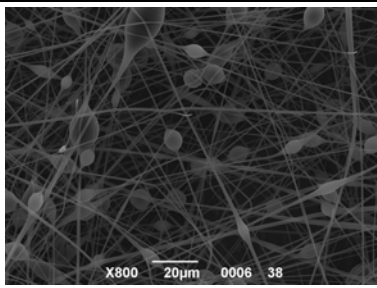
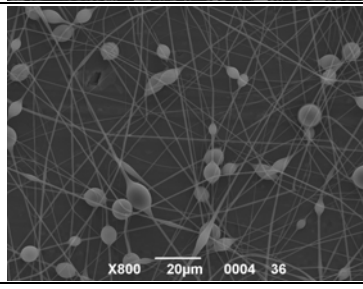
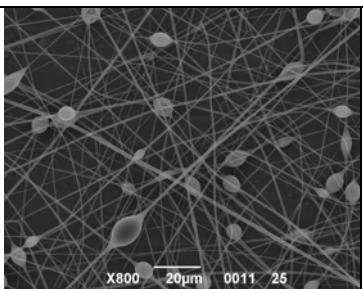
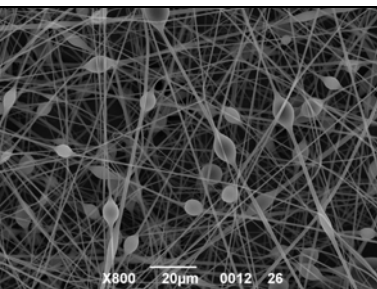
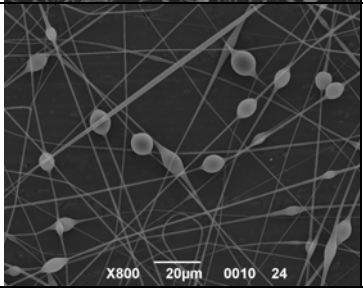
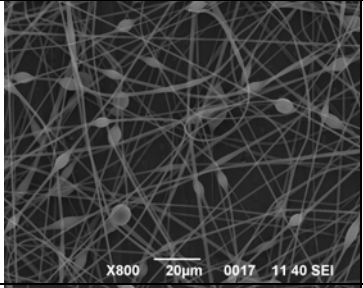
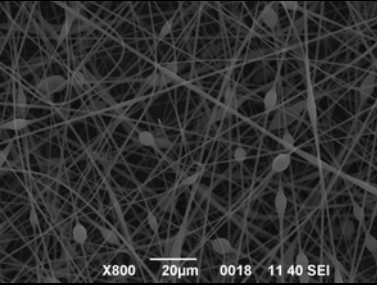
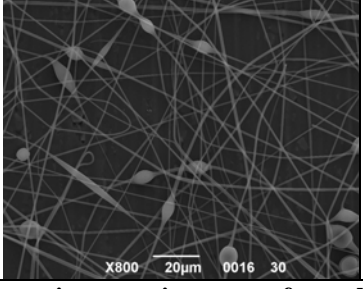
DMF:Ac. ratio	[PMMAcMAA]	Voltage [kV]		Flow rate [ml/hr]
		14	17	
2:1	26%w			1
				3
2:1	27%w			1
				3
2:1	28%w			1
				3

Table 6. 4 SEM micrographs of the screening experiments performed with DMF:Ac=2:1

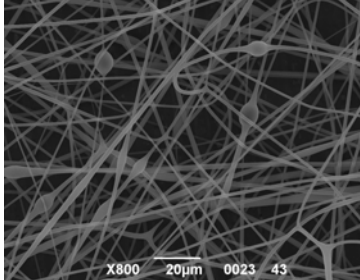
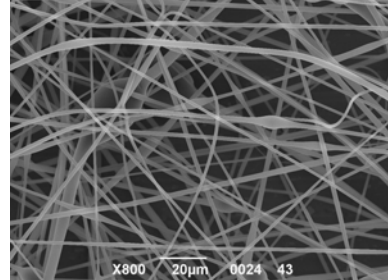
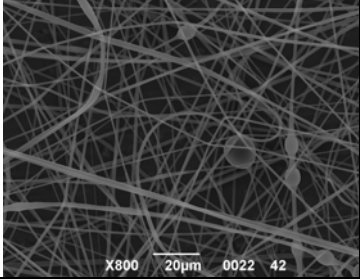
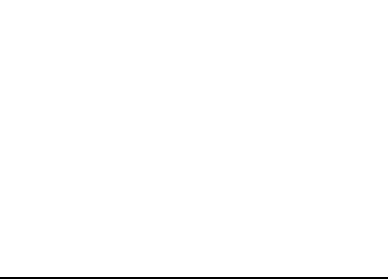
DMF:Ac. ratio	[PMMAcoMAA]	Voltage [kV]		Flow rate [ml/hr]
		14	17	
2:1	29%w			1
				3

Table6. 5 (-Continuated-) SEM micrographs of the screening experiments performed with DMF:Ac=2:1

As regards the solvents ratio 1:1 it can be observed “beads on string” morphology, where the defects are stretched within the fiber structure. According to the theory, better results in term of fiber morphology are obtained with higher electrical conductivity and lower surface tension. When the ratio of two different solvents is changed, both these properties are affected and in this system, a substantial decrease of surface tension by Acetone addition to DMF (with a ratio 1:1) results on better fiber morphology, other conditions being equal.

Moreover, looking at the micrographs of Table 6.5, the electrospun samples at 26%w and 27%w show higher beads formation if the applied voltage rises to 17 kV. This could be explained considering that the excess electrical charges carried with the jet create a strong elongational flow, and may either stabilize or destabilize the capillary instability, depending on the wavelength of the bead-forming instability. Looking at this set of samples, the crossover of concentration from the semi-dilute unentangled to semi-dilute entangled regime ranges from 27%w to 28%w and this information is useful for moving to a response surface analysis for the system polymer/solvent.

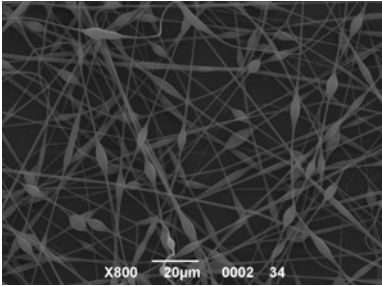
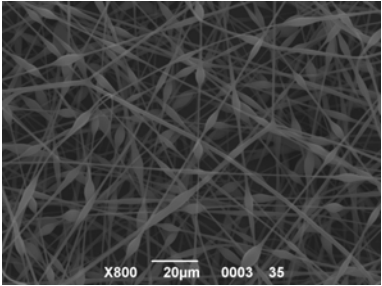
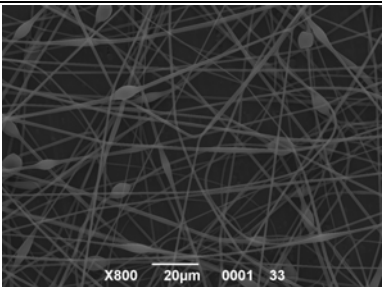
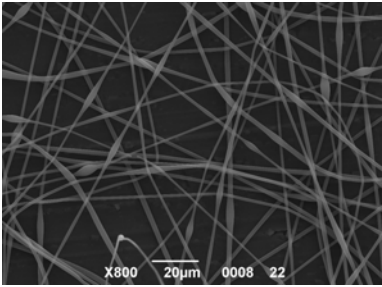
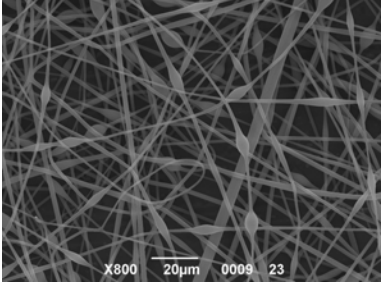
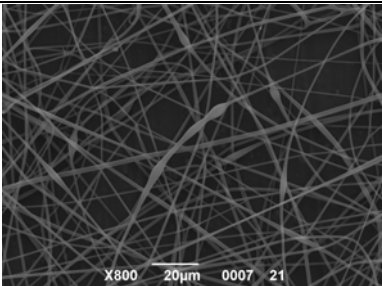
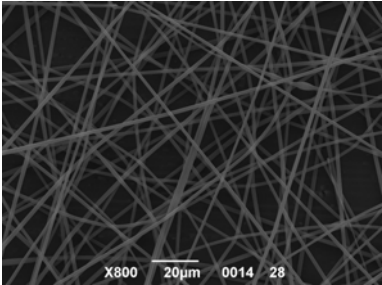
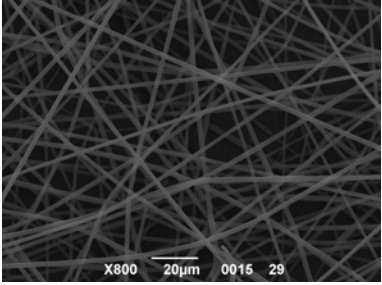
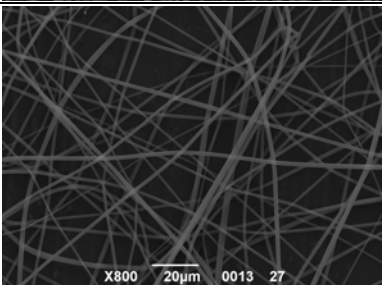
DMF:Ac ratio	[PMMAcO ₂ MAA]	Voltage [kV]			
		14	17		
1:1	26%w			1	Flow rate [ml/hr]
				3	
1:1	27%w			1	Flow rate [ml/hr]
				3	
1:1	28%w			1	Flow rate [ml/hr]
				3	

Table6. 6 SEM micrographs of the screening experiments performed with DMF:Ac=2:1

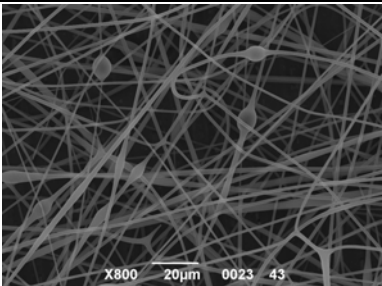
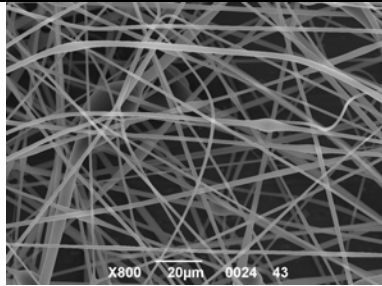
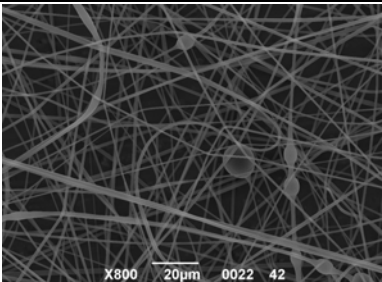
DMF:Ac ratio	[PMMAcO ₂ MAA]	Voltage [kV]		Flow rate [ml/hr]
1:1	29%w			
1:1				3

Table 6.5 (-continued-) SEM micrographs of the screening experiments performed with DMF:Ac=2:1

6.2.2 RSM for polymer-solvent system

6.2.2.1 Design Summary

Box-Behnken Design has been chosen within the family of efficient three-level designs for fitting second order response surfaces. The class of designs is based on the construction of balanced incomplete block design and it represents an efficient option and indeed an important alternative to the central composite design. All the modelling analysis have been performed Minitab® software and Statease® statistical software for design of experiments.

The station in which experiments have been carried out is stationary and is placed in a controlled environment, where relative humidity (UR) and temperature are monitored with a precision of $\pm 2\%$ UR and $\pm 0.3^\circ\text{C}$ respectively, distance tip-collector is accurately measured by fixed horizontal digital scale 300mm length (precision 0.01mm). Natural variables, Uncontrollable Variables and fixed variables are defined as shown in Table 6.6.

Natural Variables	Fixed Variables	Uncontrollable Variables
Applied Voltage 14 – 20 kV	DMF/Ac =1:1	Temperature (°C)
Distance tip-collector (15 – 30 cm)		Relative Humidity (%)
Volumetric flux (1 – 4ml/h).		
[PMMAcO ₂ MAA] 28 ÷ 32 % w/w		

Table6. 7 Natural Variables, Fixed Variables and Uncontrollable Variables for Polymer/solvent system

Box-Benhken design was consequently based on 4 factors, 3 levels each, 6 replicates at central points (Table 6.7). Replicates are useful because they provide an estimate of pure error, or experimental error, which serves as a benchmark to determine whether observed differences in the data are statistically different.

Design Summary									
Study Type	Response Surface	Runs	30	Replicates	6				
Initial Design	Box.Behenken	Blocks	No Blocks						
Design Model	Quadratic								
Factor	Name	Units	Type	Low Actual	High Actual	Low Coded	Mean Coded	High Coded	Mean
A	Volt	kV	Numeric	14.00	20.00	-1.000	0	1.000	17.070
	[PMMAcO ₂ MAA]	%w/w	Numeric	28.00	32.00	-1.000	0	1.000	30
B	flow rate	ml/hr	Numeric	1.0	4.0	-1.000	0	1.000	2.5
C	Distance	cm	Numeric	15.00	30.00	-1.000	0	1.000	22.5

Table6. 8 Design Summary

The design of experiment counted 30 runs (see Table 6.8) and for every sample the response, that is the fiber diameter, has been recorded from SEM micrographs processed by an image software analyzer. The mean diameter set as a response is the mean value resulting from 200 measurements. A distribution curve for “Diameter” has been obtained and then the Standard deviation reflects the variability of every response.

RunOrder	Voltage [KV]	[PMMAcO ₂ MAA [% w/w]	Distance [cm]	Flow rate [ml/h]	Diameter [micron]	Dev. St.
1	20	28	22,5	2,5	1,335	0,346
2	14	30	15	2,5	1,861	0,380
3	17	30	22,5	2,5	1,979	0,454
4	17	30	22,5	2,5	1,975	0,795
5	17	30	22,5	2,5	2,406	0,586
6	20	30	22,5	1	2,042	0,832
7	20	30	30	2,5	2,016	0,420
8	20	30	15	2,5	2,113	0,353

9	17	28	22,5	1	1,658	0,353
10	17	32	22,5	1	2,641	1,084
11	17	32	15	2,5	2,790	0,525
12	14	30	30	2,5	2,229	0,455
13	17	30	30	1	2,028	0,494
14	20	32	22,5	2,5	3,266	1,754
15	17	28	15	2,5	1,335	0,330
16	17	32	22,5	4	2,514	0,422
17	17	30	30	4	2,323	0,519
19	20	30	22,5	4	2,208	0,575
18	17	30	22,5	2,5	3.	1,910
20	14	30	22,5	4	2,382	0,871
21	17	30	15	4	2,109	0,365
22	14	30	22,5	1	1,759	0,598
23	17	30	22,5	2,5	2,590	0,533
24	17	28	22,5	4	1,930	0,407
25	17	28	30	2,5	1,555	0,314
26	14	28	22,5	2,5	1,582	0,356
27	17	30	22,5	2,5	2,287	0,476
28	14	32	22,5	2,5	2,624	0,375
29	17	30	15	1	2,139	0,372
30	17	32	30	2,5	2,980	0,812

Table6. 9 Data set and responses of Box-Behnken design for the Polymer/solvent system

Before doing the modelling of the response, interactions plot (a plot of means for each level of a factor with the level of a second factor held constant) are useful for judging the qualitative presence of interaction. Interaction is present when the variance of the response at a factor level is affected upon the level(s) of other factors. Parallel lines in an interactions plot indicate no interaction. The greater the departure of the lines from the parallel state, the higher the degree of interaction. Figure 66 summarizes the matrix of interaction plot for four factors. The response is on Y axis, while the factors are on the rows of the matrix. Looking at “Voltage” column, it can be observed that a possible interaction with distance and flow rate can be expected while the polymer concentration effect seems to be independent to voltage as well as to other factors. Moreover the main effect plot (Figure 67) for [PMMAcoMAA] reveals a strong interaction to the response (0.883) and it probably has a higher order with respect to the others. In fact, from the scatter plot it is possible to highlight a specific trend moving from the low level to the third one regardless of other factors. However these plots will be used just for a qualitative intent and more information will result later on.

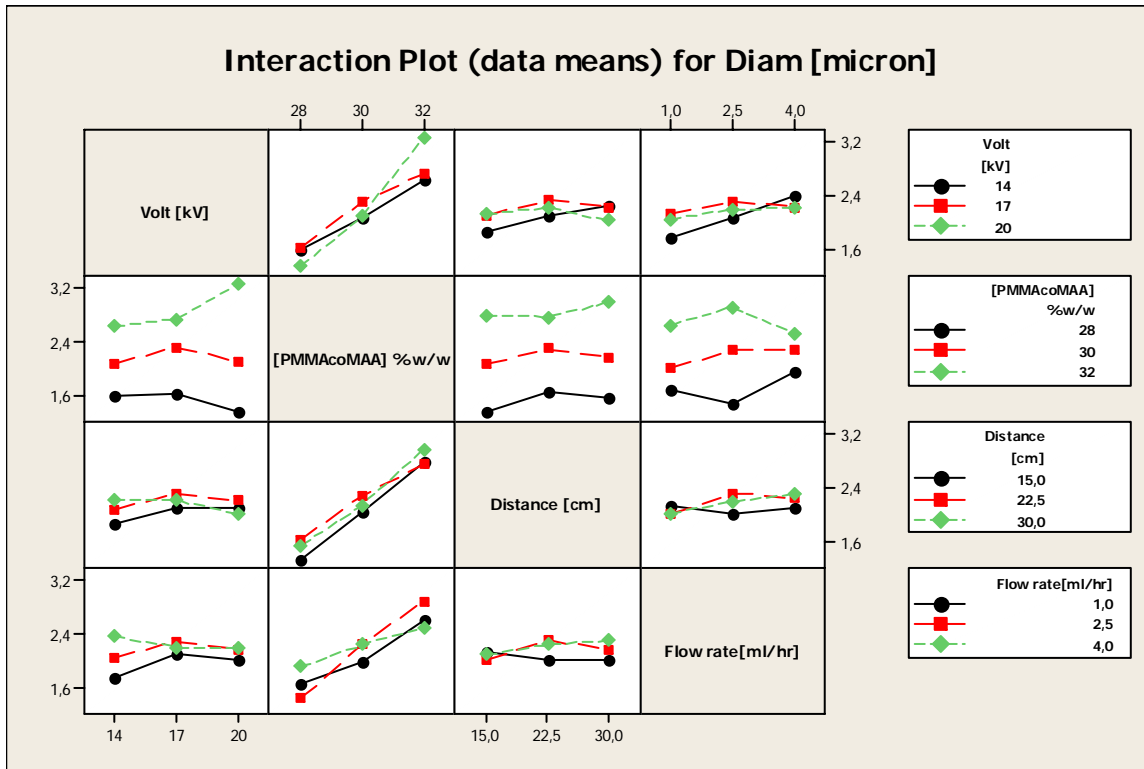


Figure 66 Interaction plot for polymer/solvent system

Design-Expert® Software

Correlation: 0.883

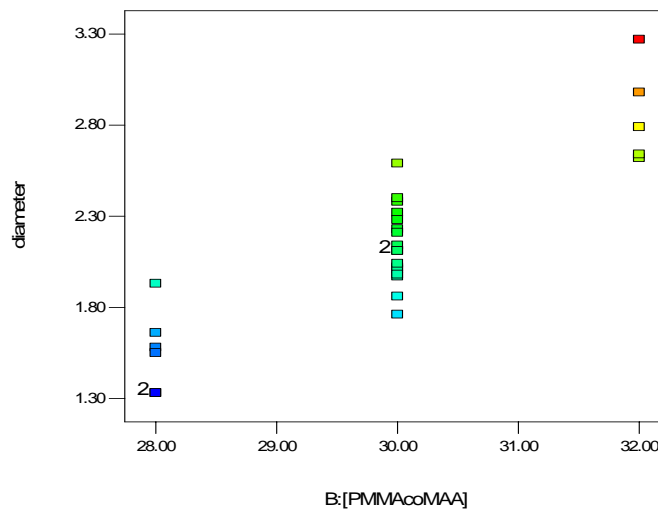


Figure 67 Main effect graph for [PMMAcoMAA]

Looking at the response of the central points (Figure 68) it has been emphasized that the experimental runs are not consistent, probably due to some external uncontrollable variables or because of the presence of outliers. However the responses have been processed and this aspect will be explained by response surface analysis.

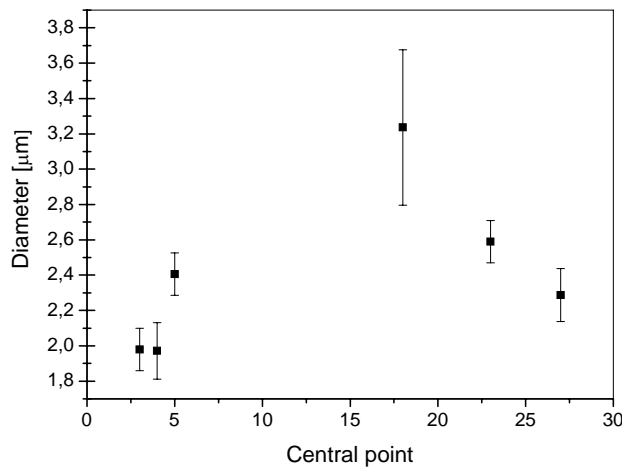


Figure 68 Response at central points

6.2.2.2 Model adequacy checking

The response surface analysis based on listed experiments (Table 6.8) has been performed considering a quadratic model for fitting the response. The result showed here comes from an iterative methodology which leads the identification of outliers and then their removal from the modelling. Two outliers were identified, Run 16 and Run 18, looking at DFFITS which provides, with Leverage and Cook's Distance, another measure to determine whether an observation is unusual. It uses the leverage and deleted (Studentized) residual to calculate the difference between the fitted value calculated with and without the i^{th} observation. DFFITS represents roughly the number of estimated standard deviations that the fitted value changes when the i^{th} observation is removed from the data. Comparing DFFITS values of run 16 and 18 to one another, it has been pointed out they are extremely large relative to the others. Consequently they have been removed from the design and the observations were examined accurately for understanding why they were unusual.

Table 6.9 summarized the results of reliability of the proposed model.

Std. Dev.	0,190	R-Squared	0,919
Mean	2,146	Adj R-Squared	0,833
C.V. %	8,866	Pred R-Squared	0,720
PRESS	1,638	Adeq Precision	13,031

Table 6.10 Results of reability of the model

The "Pred R-Squared" of 0.720 is in reasonable agreement with the "Adj R-Squared" of 0.833. The latter indicates the signal to noise ratio greater than 4 and it means an adequate signal and then the model is able to represent the design space.

The analysis of variance for the selected model is shown in Table 6.10. The model is significant and Values of "Prob > F" less than 0.0500 indicate model terms are significant. In this case B ([PMMAcO₂MAA], C (Flow rate), AB(Voltage-[PMMAcO₂MAA]) are significant

ANOVA for Response Surface Quadratic Model							
Analysis of variance table [Partial sum of squares - Type III]							
Source	Sum of Squares	df	Mean Square	F Value	p-value	Prob > F	
Model	5,375	14	0,384	10,60	< 0.0001	significant	
A-volt	0,024	1	0,024	0,67	0.4274		
B-[PMMAcO₂MAA]	4,657	1	4,657	128,62	< 0.0001		
C-Flow rate	0,267	1	0,267	7,36	0.0177		
D-Distance	0,049	1	0,049	1,36	0.2637		
AB	0,203	1	0,203	5,59	0.0343		
AC	0,051	1	0,051	1,40	0.2582		
AD	0,055	1	0,055	1,53	0.2387		
BC	0,020	1	0,020	0,56	0.4691		
BD	0,000	1	0,000	0,01	0.9384		
CD	0,027	1	0,027	0,75	0.4016		
A ²	0,090	1	0,090	2,49	0.1386		
B ²	0,032	1	0,032	0,89	0.3629		
C ²	0,001	1	0,001	0,04	0.8476		
D ²	0,081	1	0,081	2,24	0.1587		
Residual	0,471	13	0,036				
Lack of Fit	0,181	9	0,020	0,28	0.9494	not significant	
Pure Error	0,290	4	0,073				
Cor Total	5,846	27					

Table6. 11 ANOVA for Response Surface Quadratic Model

The predictive models in terms of coded versus actual factors are shown side-by-side in Table 6.11.

Final Equation in Terms of Coded Factors:			Final Equation in Terms of Actual Factors:		
diameter	=		diameter	=	
2,244			21,547		
0,682	* B		-1,472	* [PMMAcO ₂ MAA]	
0,163	* C		-0,563	* Flow rate	
0,225	* A * B		0,038	* volt * [PMMAcO ₂ MAA]	

Table6. 12 Final equation of the predictive model

Plotting the predicted values versus actual values (Figure 69) we can view the good predictivity of the proposed model but the error bars suggest that is necessary to be aware.

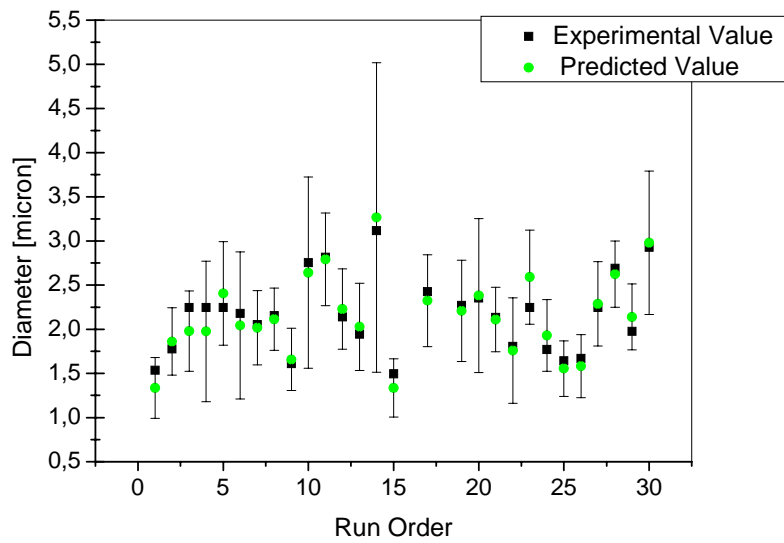


Figure 69 Experimental and predicted value of the response

The only interaction which seems to be valid is the interaction between Voltage and [PMMAcoMAA] and the 3D surface plot is shown in Figure 70 where factor C and D are kept constant to the mean level. The surface trend provides some information about the scaling relationship order of those factors with respect to the forces they act on and consequently to the response. As regards the polymer concentration, within the semidilute entangled regime, it is possible to identify a threshold value over which the viscoelastic forces increase drastically and strongly overhang the other forces. For instance, at the low level of B, an increase of Voltage results on diameter reduction, as confirmed by contour plot analysis in Figure 71. Moving up to the second level of B, a new wide region may be detected, where voltage effect is not significant. This means that the power law dependences have such a different order, that factor B prevails on the response. If the dependence orders of the factors on the response are strongly different, is not possible to have interaction anymore.

Design-Expert® Software

diameter

● Design points above predicted value

○ Design points below predicted value



X1 = A: volt

X2 = B: [PMMAcoMAA]

Actual Factors

C: Flow rate = 2.50

D: Distance = 22.50

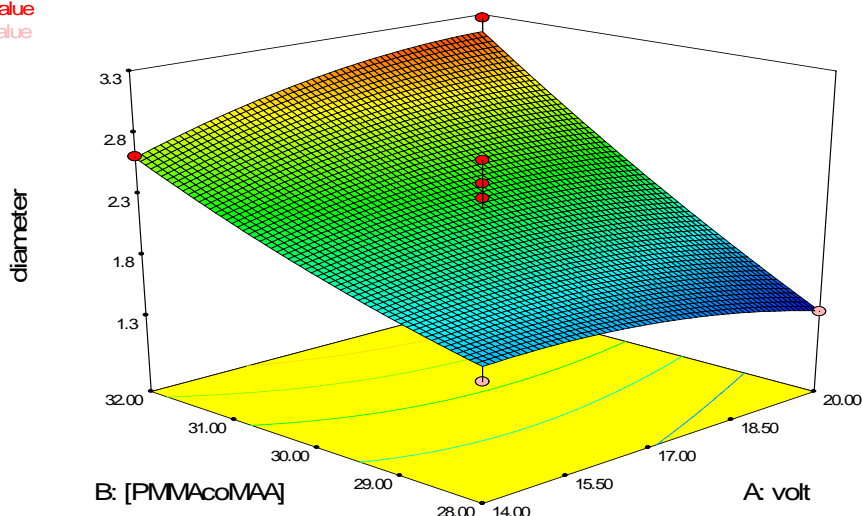


Figure 70 3D surface plot for Voltage-[PMMAcoMAA] interaction, actual variables.

Design-Expert® Software

diameter

● Design Points

X1 = A: volt

X2 = B: [PMMAcoMAA]

Coded Factors

C: Flow rate = 0.000

D: Distance = 0.000

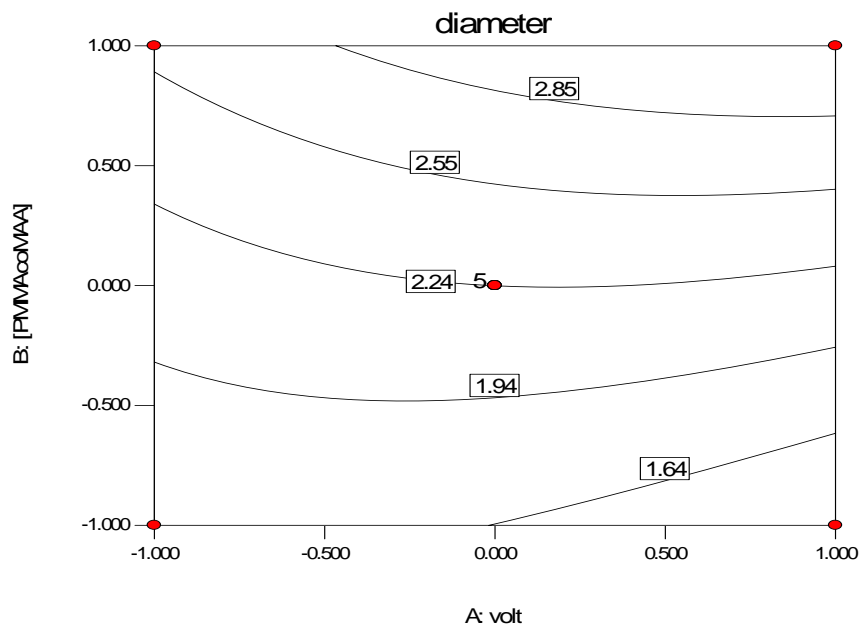


Figure 71 Contour plot for Voltage-[PMMAcoMAA] interaction

Response surface analysis of the polymer-solvent system revealed a mean fibers diameter ranging in the microscale. Other interesting information gathered from this methodology regards the significance of the factors. The distance between the tip of the needle and the collector seems not affecting the response, or to be more exact, the range of distance we dealt with is not wide enough for sensing a difference on the response. Because of this, in the next section this parameter will be left out while Voltage effect will stay among the factors due to his possible interactions.

6.3 Case study: Polymer/solvent/salt system

6.3.1 Screening experiments for the system polymer-solvent-salt

According to the response surface analysis performed on the previous system, it has been pointed out that the response, which is the mean fiber diameter, falls into the microscale range. In order to move to the nanoscale we decided to turn the solution properties, in particular surface tension and conductivity. The surface tension has been slightly increased using a solvent ratio DMF: Acetone equal to 2:1, and the conductivity is modified by addition of 0.2%w Lithium Chloride (LiCl). Figure 72 shows SEM micrographs of 30% w electrospun samples, other conditions being equal to Table 6.2 (DMF:Ac =2:1). The fibers are smooth and beads-free, and the mean diameter is fourfold lower than the electrospun sample without salt. This result suggests that for this new system the critical concentration of entanglements is different with respect to the previous case studied and then a new set of screening experiment has been proposed, according to Table 6.12.

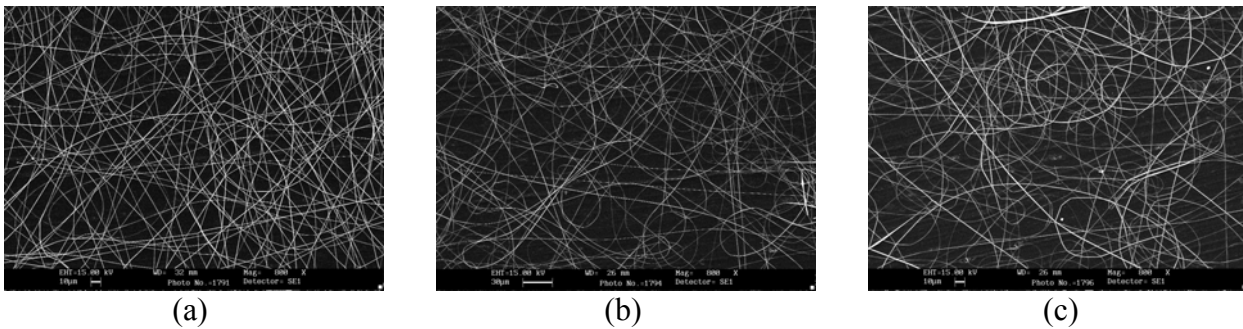


Figure 72 SEM micrographs of electrospun samples at [PMMA-co-MAA] 30%w, DMF:Ac=2:1, (a) 17 kV, 1 ml/hr; (b) 14kV, 1ml/hr; (c) 14kV 3 ml/hr

LiCl [w/w %]	[PMMA-co-MAA] [w/w %]	ID	Flow rate [ml/h]	Applied Voltage [kV]
0,2	27	54	3	14
		55	1	14
		56	1	17
	25	57	3	14
		58	1	14
		59	1	17
	23	60	3	14
		61	1	14
		62	1	17

Table6. 13 Screening experiment data set at [LiCl] =0,2wt%

SEM micrographs of electrospun samples have been processed by an image software analyzer (two representative images for every sample) and the statistical distribution of the diameters is shown in Figure 73-Figure 74. The processed images were branched using a virtual grid, measurements of the mean diameter are counted for every image (roughly100 each).

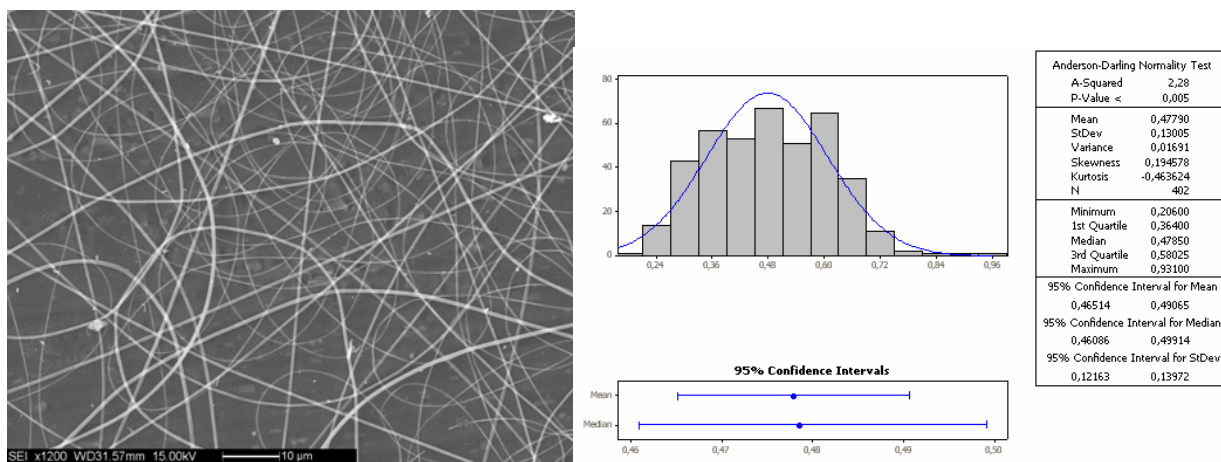


Figure 73 SEM micrograph of sample ID54 (see electrospinning conditions in Table 6.6) and the graphical summary which includes: histogram of data with an overlaid normal curve, 95% confidence intervals for mean, and 95% confidence intervals for the median.

Electrospun samples from 27%w polymer solution have a mean fiber diameter of 0.477 μm (95% confidential interval for mean from 0.425 μm to 0.490 μm) and a mean standard deviation of 0.12 μm , that means a wide spread of the distribution curve.

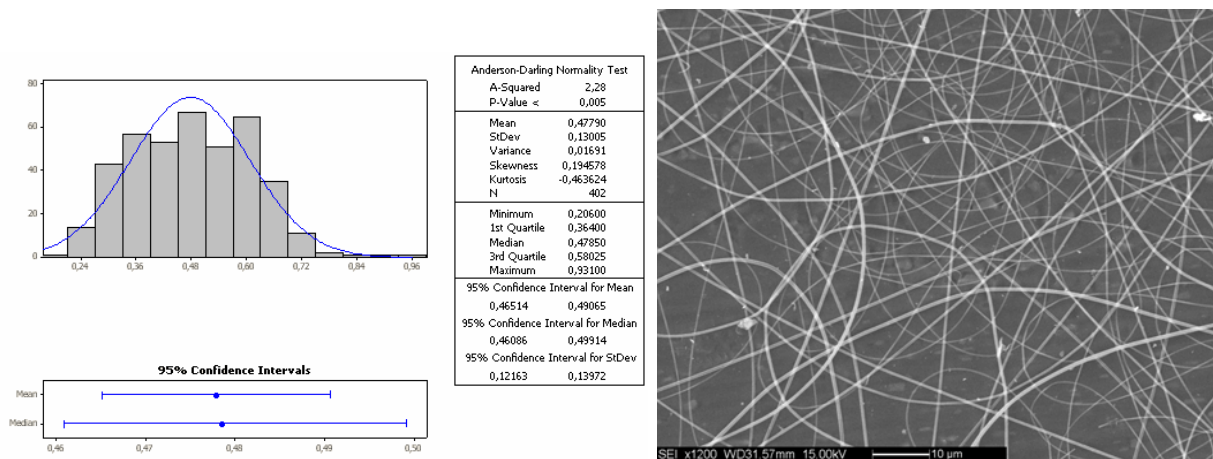


Figure 74 SEM micrograph of sample ID55 (see electrospinning conditions in Table 6.6) and the graphical summary which includes: histogram of data with an overlaid normal curve, 95% confidence intervals for mean, and 95% confidence intervals for the median.

Smooth fibers are electrospun also with polymer concentration of 25%w (see Figure 75) resulting in a lower mean diameter of 0,266 μm and standard deviation (0,05 μm).

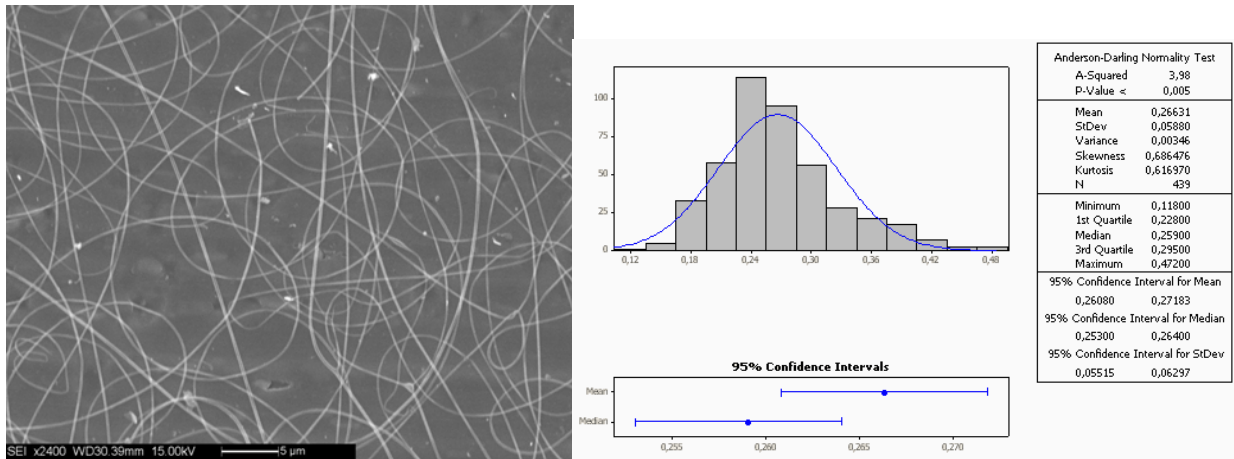


Figure 75 SEM micrograph of sample ID57 (see electrospinning conditions in Table 6.6) and the graphical summary which includes: histogram of data with an overlaid normal curve, 95% confidence intervals for mean, and 95% confidence intervals for the median.

A further decrease in polymer concentration to 23%w reveals the critical entanglement concentration and then a new set of screening experiments (Table 6.13) has been carried out for evaluating the qualitative effect of salt concentration, which affects the conductivity of the solutions. Moving from 0.1%w to 0.3%w, other conditions being equal, (see an example in Figure 76) it can be observed a tangible increase of the mean fiber diameter from a mean value of 0,210 μm to 0,450 μm , contrasting the fundamentals of electrospinning. An effective explanation of this behaviour will be clear with the response surface analysis in the next paragraph.

LiCl [% w/w]	ID	Flowrate[ml/h]	Applied Voltage [KV]
0,1	63	3	14
	64	1	17
	65	1	14
0,3	66	3	14
	67	1	17
	68	1	14

Table6. 14 Screening experiments data set ad different [LiCl]

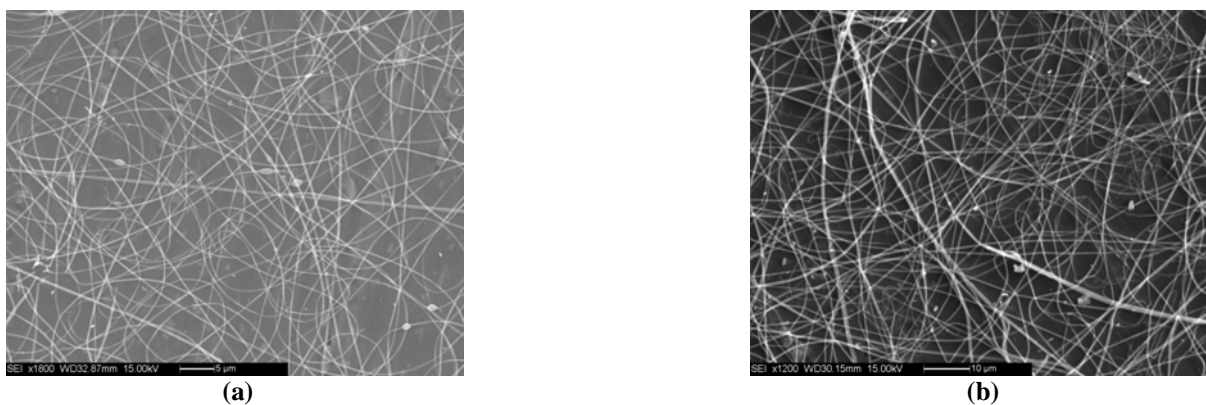


Figure 76 SEM micrographs of electrospun sample ID63 (a) and ID66 (b): (a)[LiCl]=0.1%w; (b) [LiCl]=0.3%w, other conditions being equal.

6.3.2 RSM for the system polymer-solvent-salt

6.3.2.1 Design Summary

According to the screening experiments, from a Box-Behnken design we moved to a D-optimal design for the study of the response as a function of process parameters. The Design Summary is shown in Table 6.14 and the whole design plan can be seen in Appendix C.

Design Summary									
Study Type	Response Surface	Runs	43						
Initial Design	D-optimal	Point Exchange	Blocks	No Blocks					
Design Model	Quadratic								
Factor	Name	Units	Type	Low Actual	High Actual	Low Coded	High Coded	Mean	Std. Dev.
A	Volt	kV	Numeric	14.00	20.00	-1.000	1.000	17.070	2.28
B	[PMMAco MAA]	%w/w	Numeric	23.00	27.00.00	-1.000	1.000	25.047	1.52
C	[LiCl]	%w/w	Numeric	0.10	0.30	-1.000	1.000	0,130	0.075
D	flow_rate	ml/hr	Numeric	1.00	3.00	-1.000	1.000	1.977	0,529

Table 6. 15 Design Summary

Before doing the analysis, it is interesting to take a look at some simple plots. In the scatter plot showed in Figure 77 the factor A:Volt. is on the X-axis (three factor levels) and the response, Diameter, on the Y-axis. It will be much more productive to see the impact of the control factors on response surface graphics to be produced later. For now it is useful to find out if there is any correlation of the single factors (varying their level) to the response. At this regard is it evident that the factors A:Volt and D:FlowRate show a slight correlation (0.098 and 0.154, respectively, see Figure 77 Figure 80) to response, while factor B: Pol.Conc. and factor C:SaltConc. have an higher correlation (0.721 and 0.311, respectively, see Figure 78 Figure 79). In particular for factor B it is possible to detect an ever-growing trend with the increase of level from 23%w to 27%w.

Design-Expert® Software

Correlation: 0.098

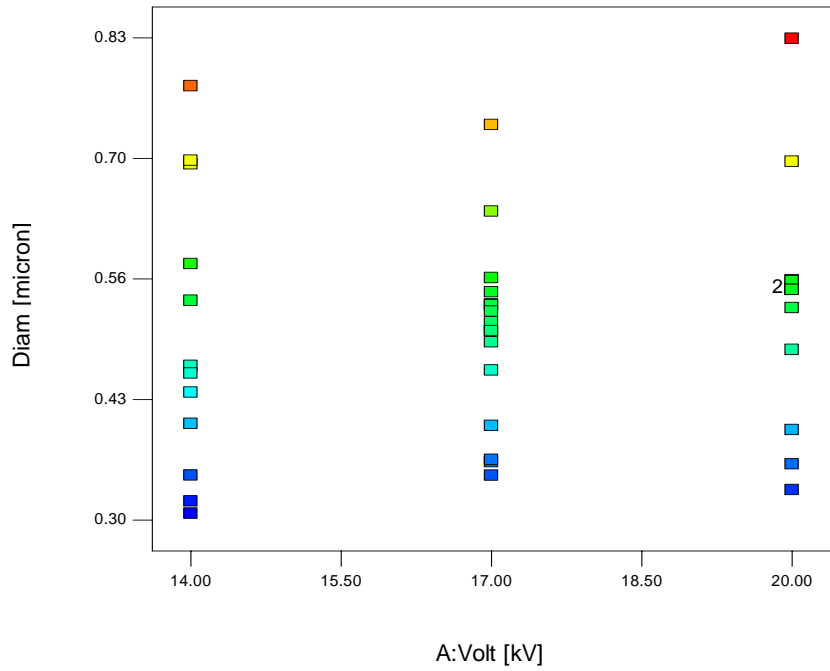


Figure 77 Main effect graph for Volt

Design-Expert® Software

Correlation: 0.721

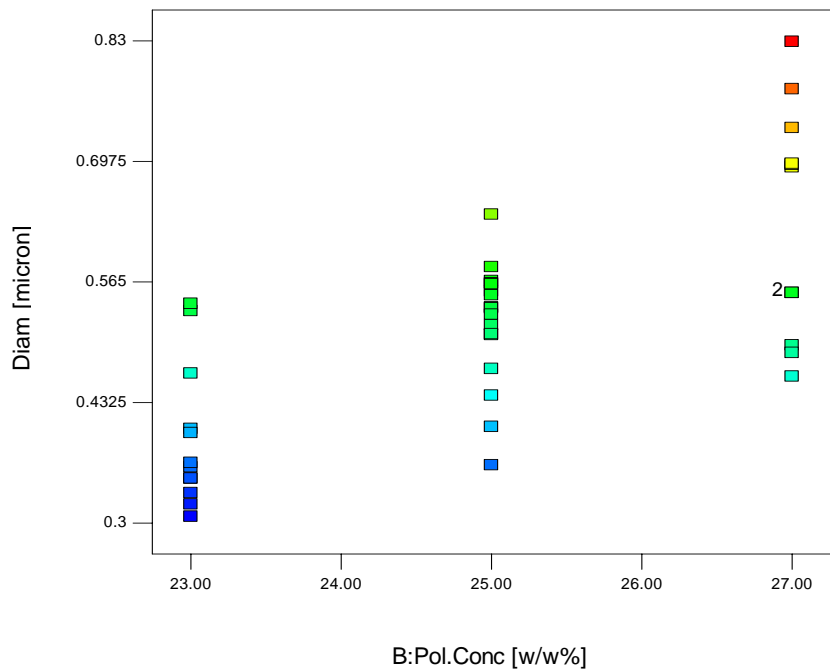


Figure 78 Main effect graph for Polymer concentration

Design-Expert® Software

Correlation: 0.311

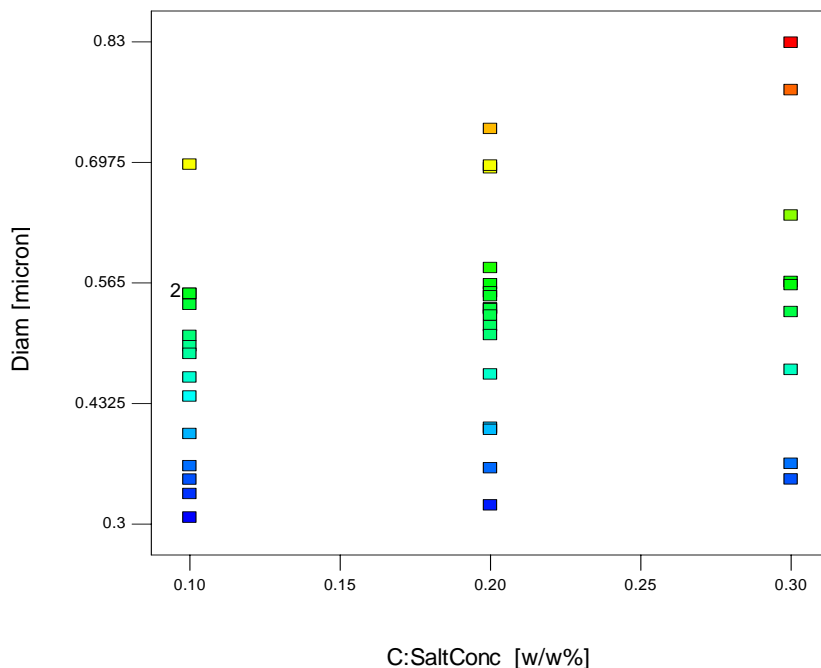


Figure 79 Main effect graph for Salt concentration

Design-Expert® Software

Correlation: -0.154

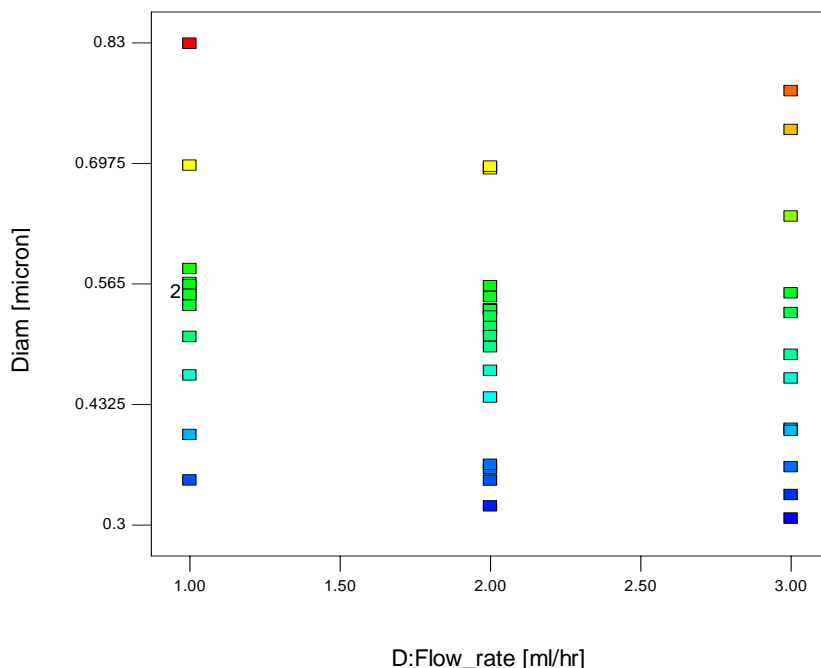


Figure 80 Main effect graph for Flow rate

In order to evaluate which polynomial fits the response, the procedure of Sequential Model Sum of Squares (Table 6.15) shows how terms of increasing complexity contribute to the total model hierarchy. The Quadratic model results the appropriate one for representing this system.

Sequential Model Sum of Squares [Type I]						
Source	Sum of Squares	df	Mean Square	F Value	p-value	
Mean vs Total	10,53	1	10,5338			
Linear vs Mean	0,44	4	0,1109	20,159	< 0.0001	
2FI vs Linear	0,15	6	0,0249	16,707	< 0.0001	
Quadratic vs 2FI	0,03	4	0,0076	14,727	< 0.0001	Suggested
Cubic vs Quadratic	0,01	16	0,0005	1,158	0.4258	Aliased
Residual	0,00	9	0,0005			
Total	11,17	40	0,2792			

Table 6.16 Sequential Model Sum of Squares results

6.3.2.2 Model adequacy checking

Precision-based metrics, provided via fraction of design space (FDS) statistics, have been chosen for evaluating the design adequacy. Design Matrix Evaluation for Response Surface Quadratic Model shows no aliasing and from Figure 81 it can be observed that the quadratic model has enough information for fitting the design space (FDS=0.80).

Design-Expert® Software

Min StdErr Mean: 0.310
 Max StdErr Mean: 1.135
 Cuboidal
 radius = 1
 Points = 50000
 $t(0.05/2,25) = 2.05954$
FDS = 0.80
 StdErr Mean = 0.510

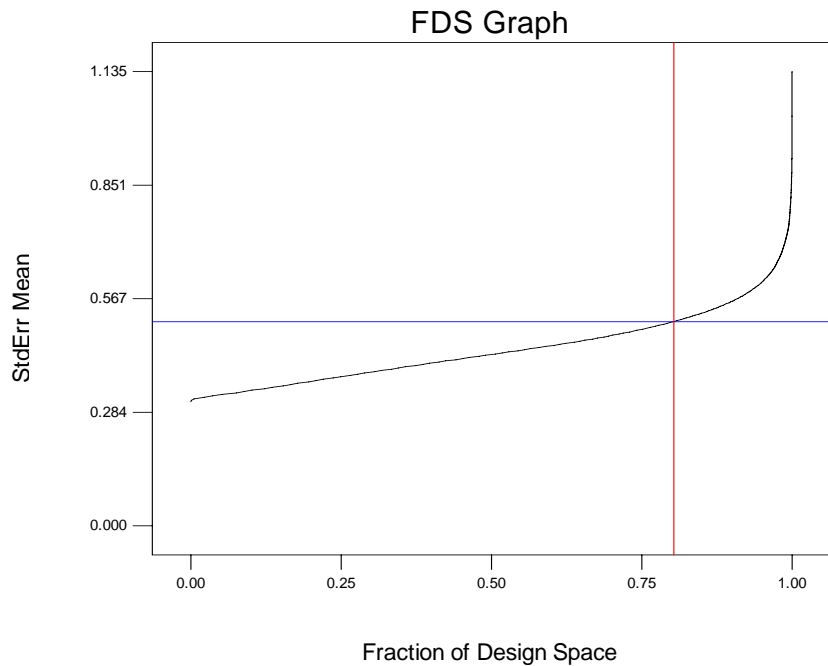


Figure 81 FDS analysis

Model adequacy has been checked performing the Lack of Fit Test, which is necessary since the design contains replicates (multiple runs at identical, but distinct combinations of factor settings). The error term can be partitioned into two parts - pure error (error within replicates) and lack-of-fit error, which represents degrees of freedom that are not in the model (e.g., higher-order interaction terms). The “Lack of Fit Tests” table (Table 6.16) compares the residual error to the “Pure Error” from replicated design points. If there is significant lack of fit, as shown by a low probability value (“Prob>F”), then be careful about using the model as a response predictor. In this case, the linear

model definitely can be ruled out, because its Prob > F falls below 0.05. The quadratic model, identified earlier as the likely model, does not show significant lack of fit.

Lack of Fit Tests						
Source	Sum of		Mean	F	p-value	
	Squares	df			Square	Value
Linear	0,191	29	0,007	34,239	0.0001	
2FI	0,042	23	0,002	9,484	0.0050	
Quadratic	0,012	19	0,001	3,199	0.0775	Suggested
Cubic	0,003	3	0,001	5,276	0.0405	Aliased
Pure Error	0,001	6	0,000			

Table6. 17 Lack of Fit Tests

The quadratic model comes out best: It exhibits low standard deviation (“Std. Dev.”), high “R-Squared” values and a low “PRESS.” (Table 6.17). The terms of quadratic model are evaluated by Stepwise Regression with Alpha to Enter = 0.100, Alpha to Exit = 0.100. (Table 6.18)

Model Summary Statistics						
Source	Std. Dev.	R-Squared	Adjusted R-Squared	Predicted R-Squared	PRESS	
Linear	0,074	0,6973	0,6627	0,5693	0,2738	
2FI	0,039	0,9321	0,9087	0,8730	0,0807	
Quadratic	0,023	0,9798	0,9684	0,9516	0,0308	Suggested
Cubic	0,022	0,9934	0,9713		+	Aliased
+ Case(s) with leverage of 1.0000: PRESS statistic not defined						

Table6. 18 Model Summary Statistics

The model suggested here is the results of an iterative method which first allowed us to identify outliers (three points, runs 5,22,30), that have been consequently ignored for this analysis.

The analysis of variance for the selected model is show in Table 6.19. The Model F-value of 106.81 implies the model is significant. As regards the model terms, values of "Prob > F" less than 0.0500 indicate model terms are significant. In this case A, B, C, D, AC, AD, BC, CD, A², B², C², D² are significant model terms although further observations will explain their effective importance.

Stepwise regression					
Forced Terms	Intercept				
	Coefficient	t for H0			
Added	Estimate	Coeff=0	Prob > t	R-Squared	MSE
B-Pol.Conc	0,12	6,42	<0.0001	0,520	0,008
C-SaltConc	0,06	4,00	0,0003	0,665	0,006
BC	0,06	3,33	0,002	0,744	0,005
CD	0,06	4,18	0,0002	0,829	0,003

AD	0,04	3,37	0,0019	0,872	0,002
AC	0,03	3,12	0,0038	0,901	0,002
D ²	0,04	2,81	0,0085	0,921	0,002
D-Flow_rate	-0,02	-3,14	0,0037	0,940	0,001
C ²	-0,03	-2,61	0,0139	0,951	0,001
B ²	0,03	3,06	0,0047	0,963	0,001
A-Volt	0,02	2,93	0,0067	0,972	0,001
A ²	-0,03	-3,19	0,0036	0,979	0,000

Table6. 19 Stepwise regression

ANOVA for Response Surface Reduced Quadratic Model						
Analysis of variance table [Partial sum of squares - Type III]						
Source	Sum of Squares	df	Mean Square	F Value	p-value	Prob > F
Model	0,623	12	0,052	106,81	< 0.0001	significant
A-Volt	0,005	1	0,005	10,79	0.0028	
B-Pol.Conc	0,437	1	0,437	899,11	< 0.0001	
C-SaltConc	0,116	1	0,116	237,89	< 0.0001	
D-Flow_rate	0,015	1	0,015	30,43	< 0.0001	
AC	0,029	1	0,029	60,11	< 0.0001	
AD	0,029	1	0,029	58,96	< 0.0001	
BC	0,075	1	0,075	153,93	< 0.0001	
CD	0,044	1	0,044	90,89	< 0.0001	
A²	0,005	1	0,005	10,18	0.0036	
B²	0,010	1	0,010	20,77	< 0.0001	
C²	0,008	1	0,008	17,25	0.0003	
D²	0,016	1	0,016	33,95	< 0.0001	
Residual	0,013	27	0,000			
Lack of Fit	0,012	21	0,001	2,96	0.0912	not significant
Pure Error	0,001	6	0,000			
Cor Total	0,636	39				

Table6. 20ANOVA for Response Surface Reduced Quadratic Model

Looking at the statistics to augment the ANOVA (Table 6.20), it can be observed the “Pred R-Squared” of 0.9557 which is in reasonable agreement with the “Adj R-Squared” of 0.9702. “Adeq Precision” measures the signal to noise ratio and the value of 43.561 indicates an adequate signal. Then the model can be used to navigate the design space. In order to detect multicollinearity or correlation among predictors, the variance inflation factor (VIF) measures how much the variance of an estimated regression coefficient increases if predictors are correlated. VIF = 1 indicates no relation among predictors; VIF > 1 indicates that the predictors are correlated; VIF > 5 - 10 indicates that the regression coefficients are poorly estimated. Results showed in Table 6.21 reveal that the coefficients are well estimated and it is possible to go ahead with further analysis.

Statistics summary for ANOVA			
Std. Dev.	0,022	R-Squared	0,9793
Mean	0,513	Adj R-Squared	0,9702
C.V. %	4,29	Pred R-Squared	0,9557
PRESS	0,028	Adeq Precision	43,56

Table6. 21 Statistic summary for ANOVA

Factor	Coefficient		Standard Error	95% CI		VIF
	Estimate	df		Low	High	
Intercept	0,516	1	0,007	0,501	0,530	
A-Volt	0,015	1	0,005	0,006	0,025	1,055
B-Pol.Conc	0,158	1	0,005	0,147	0,169	1,311
C-SaltConc	0,075	1	0,005	0,065	0,085	1,081
D-Flow_rate	-0,026	1	0,005	-0,035	-0,016	1,086
AC	0,044	1	0,006	0,032	0,056	1,065
AD	0,045	1	0,006	0,033	0,057	1,189
BC	0,077	1	0,006	0,064	0,090	1,264
CD	0,053	1	0,006	0,042	0,064	1,076
A^2	-0,025	1	0,008	-0,041	-0,009	1,225
B^2	0,036	1	0,008	0,020	0,053	1,275
C^2	-0,032	1	0,008	-0,048	-0,016	1,214
D^2	0,046	1	0,008	0,030	0,062	1,209

Table6. 22 Variance inflation factor (VIF) of the estimated regression coefficients

The predictive models in terms of coded versus actual factors are shown side-by-side in Table 6.22.

Final Equation in Terms of Coded Factors:	Final Equation in Terms of Actual Factors:
Diam = 0,52 0,02 * A 0,16 * B 0,07 * C -0,03 * D 0,04 * A * C 0,04 * A * D 0,08 * B * C 0,05 * C * D -0,03 * A^2 0,04 * B^2 -0,03 * C^2 0,05 * D^2	Diam = 6,42 0,04 * Volt -0,45 * Pol.Conc -11,16 * SaltConc -0,57 * Flow_rate 0,15 * Volt * SaltConc 0,01 * Volt * Flow_rate 0,39 * Pol.Conc * SaltConc 0,53 * SaltConc * Flow_rate 0,01 * Pol.Conc^2 -3,23 * SaltConc^2 0,05 * Flow_rate^2

Table6. 23 Final equation of the predictive model

6.3.2.3 Diagnose the Statistical Properties of the Model

Diagnostic details are considered for detecting any statistical problem. Just to cite some examples of the used tools, the residual analysis doesn't show any particular trend (Figure 82) and the most important diagnostic, the normal probability plot of the residuals (Figure 83), shows the data points have approximately linear pattern, which means normality in the error term and this justify the choice of no-trasformation of the data.

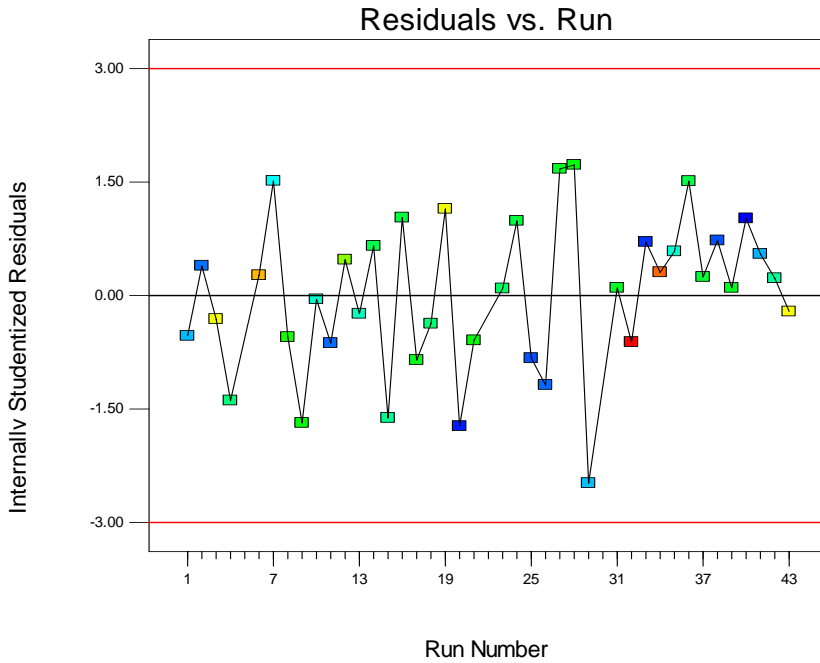


Figure 82 Residual vs Run plot

Design-Expert® Software
Diam

Color points by value of
Diam :

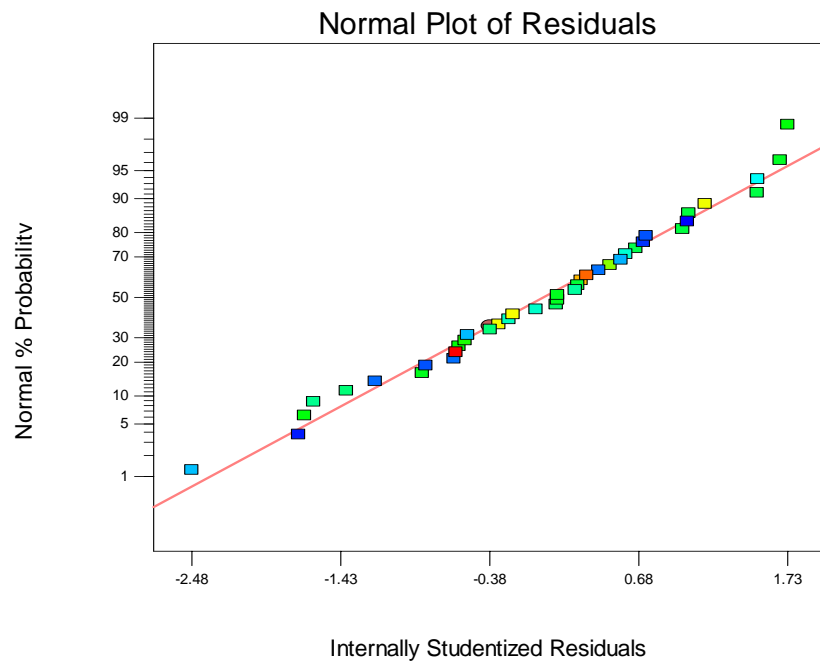


Figure 83 Normal Plot of Residual

Plotting the predicted values versus actual values (Figure 84) we can view the good predictivity of the proposed model.

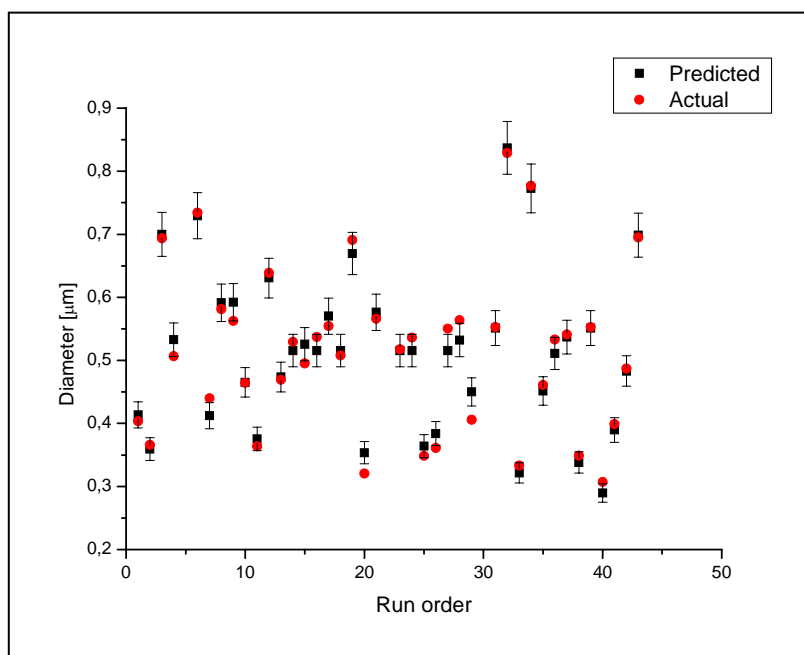


Figure 84 Predicted and actual values for response

6.3.2.4 Contour plot analysis

The analysis of Contour plots has been revealed to be a valid tool to determine the effects of the factors and the interaction terms on the response. In the following pages the effect of the interactions among parameters will be exploited.

Voltage-Flow rate interaction

As suggested from the literature, an increase of applied voltage generally results in a reduction of the mean fiber diameter of electrospun nanofibers while the increase of flow rate has the opposite effect. Looking at Figure 85 it can be observed that for low applied voltage, an increase of flow rate results on the smaller fiber diameter and this behaviour is inverted after the saddle point on the response surface. This can be explained if we consider that for every applied voltage there is a fixed dragging rate which moves the forming-fiber toward the collector. When the feed rate of polymer solution is higher, an excess of electrostatic charges will be cumulated in the solution at the tip of the needle resulting on whipping motion and jet splaying and consequently these instabilities enhance diameter reduction.

Moving up or down the level of factor B [PMMA-co-MAA] the response surface has the same shape with saddle point. On the contrary, if we play on the factor C: salt concentration, other conditions being equal, the response surface of Voltage-Flowrate interaction changes and for high values of [LiCl], there is a threshold value of voltage over which the higher is the flow rate, the higher is the response.

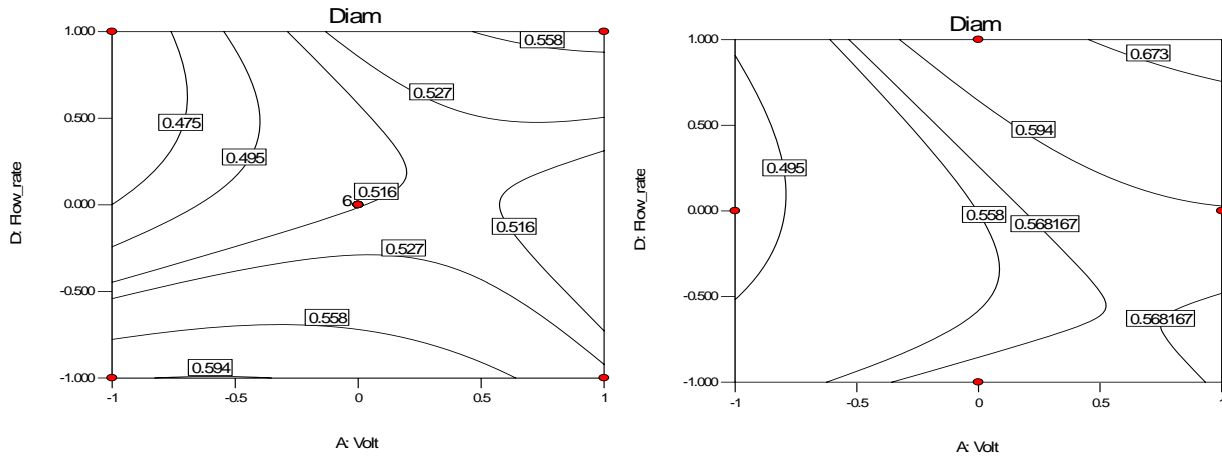


Figure 85 Voltage-Flow rate interaction (a) other factors at middle level (b) [LiCl] set +1

Voltage- salt concentration interaction

As regards [LiCl]-applied voltage interaction (other controllable variables being equal in the mean level), the contour plot in Figure 86 shows how an increase of voltage, at a fixed salt concentration, affects the mean diameter. If the salt concentration is below 0.2wt%, as the applied voltage increases, the smaller fiber diameter is obtained (especially at low level of [LiCl]). Above 0.2%w the trend changes and the higher is [LiCl], the higher is the fibers diameter obtained by raising the applied voltage. This trend could be explained if we consider that out of a specific range, elastic forces arising from solution viscoelasticity or solvent evaporation may intervene under certain operating conditions to arrest the jet prematurely with larger diameter.

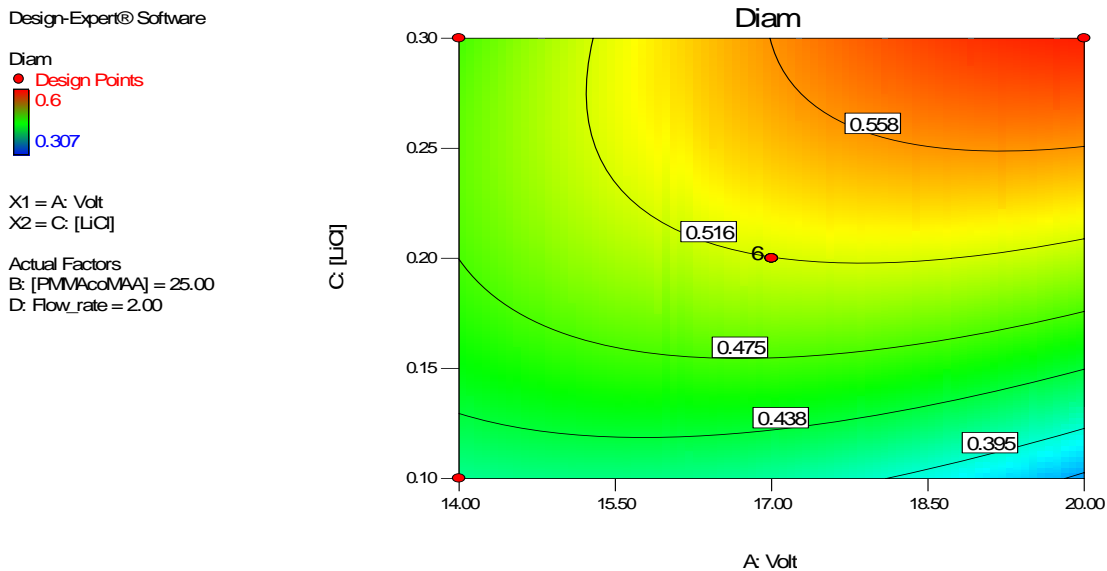


Figure 86 Volt-[LiCl] interaction contour plot

Polymer concentration-Salt concentration interaction

As suggested from the screening experiments, polymer concentration, strictly connected to the elastic forces arising from solution viscoelasticity, plays a fundamental role in electrospinning process and it often hides the interactions among other factors. In polymer concentration seems to

be independent from salt concentration and then it represents the main factor affecting the nanofiber diameter (Figure 87).

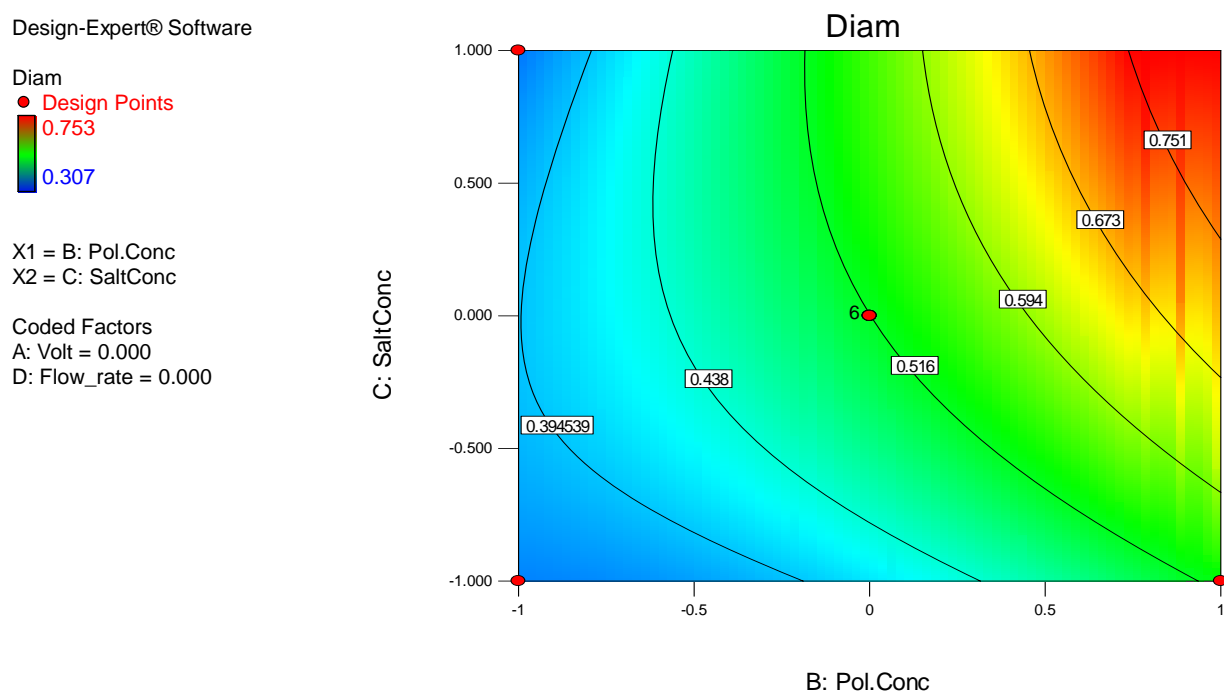


Figure 87 Pol.Conc-SaltConc interaction contour plot

Salt concentration-Flow rate interaction

Salt concentration mainly affects the conductivity of the polymer solution. Figure 88 shows once again that salt concentration of 0.2%w represents a sort of limit beyond which no more effects can be detected on the response. If we work below this threshold value, an increase of flow rate probably induces the rapid growth of the whipping instability during electrospinning, which is responsible for massive stretching of the fluid jet and concurrent decrease in the jet diameter. This reduction in diameter implies both reduced diffusion length and increased contact with the surrounding fluid (air), and provides greater opportunity for solvent evaporation and jet solidification in the whipping regime.

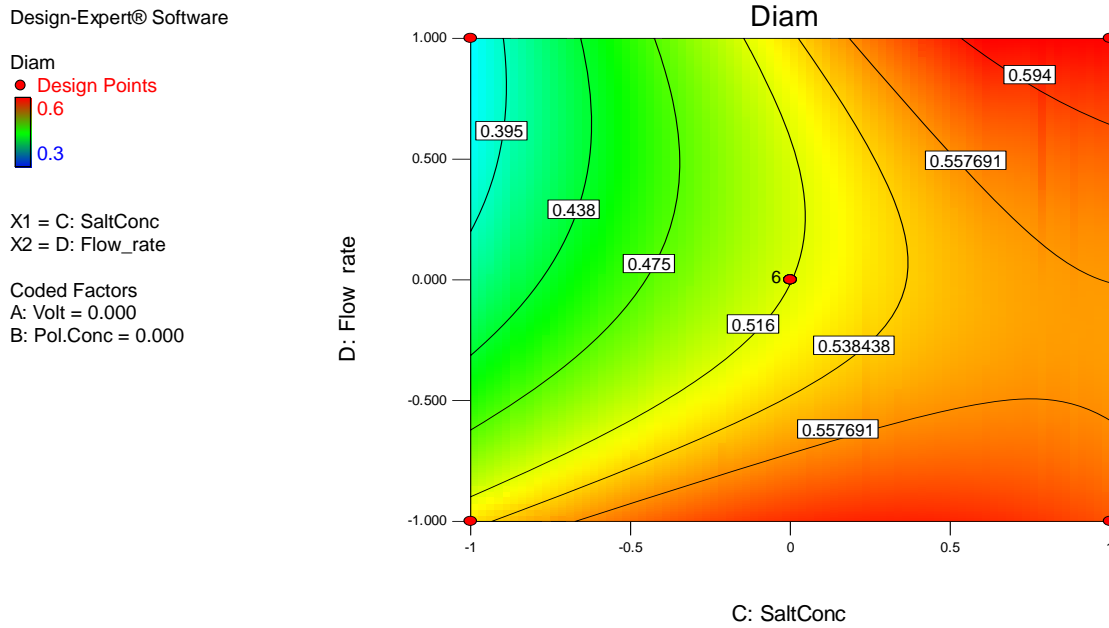


Figure 88 Salt concentration-Flow rate interaction contour plot

6.3.2.5 Propagation of Error (POE)

Thanks to propagation of error (POE) plots it is possible to show how that error is transmitted to the response. The purpose is looking for conditions that minimize the transmitted variation, thus creating a process that is robust to the factor settings. The lower the POE the better the process is, because less of the error in control factors will be transmitted to the selected response, which results in a more robust process. An example of POE on response is reported in Figure 89, where the standard deviation of the transmitted variability in the response is reported as a function of the controllable variables. These graphs are considered in terms of response surface where POE is minimized. Looking at contours plot for different significant interactions, it has been pointed out the higher propagation of error in the region closer to high factors level. This trend could have two different implications: the modelled design space needs more runs for having a better description of the fraction space, or there are parameter ranges out of which the process is not reproducible and this instability is reflected on the response error.

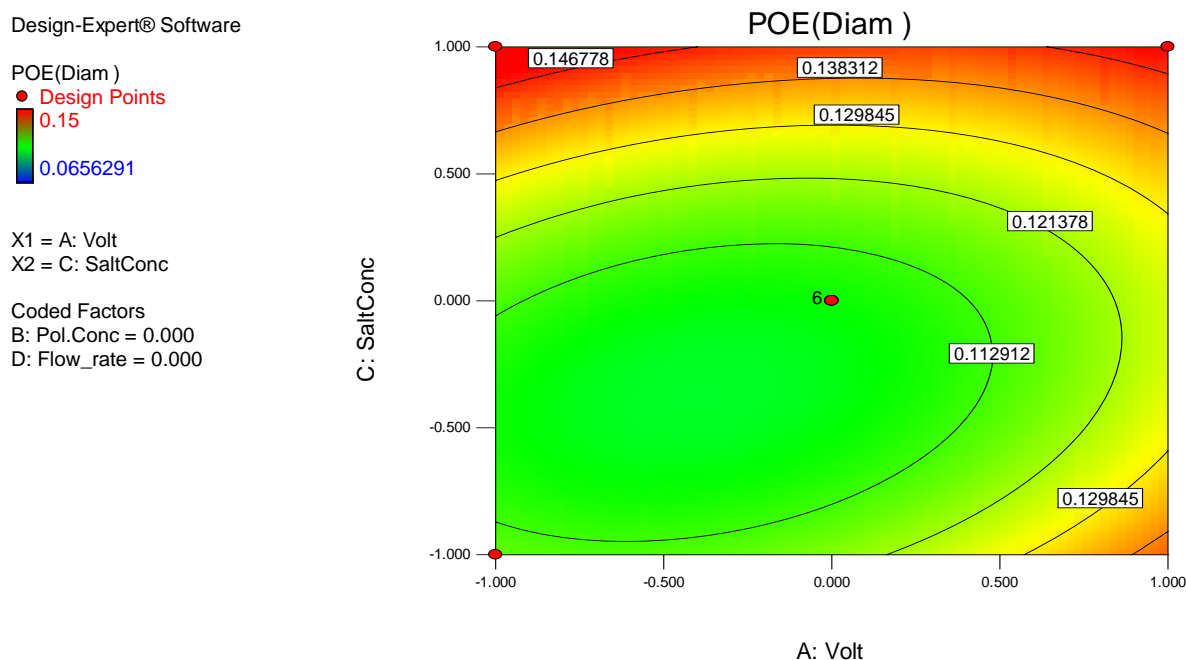


Figure 89 Contour Plot for POE (Diam) for Voltage-Salt concentration factors (coded variables).

6.3.2.6 Finding Solutions of Optimum

This case study needs process optimization in term of minimization of the response. Thresholds for the response are provided to get the desirability equation to work properly. The assignment of optimization parameters has been done in order to minimize every controllable variable, except the flow rate which is set to be maximized. Constraints used for numerical optimization are listed in Table6.23.. Weight of the upper bounds of the response has been emphasized, in order to give more emphasis to the goal, as well as the importance of the response, that is the relative priorities for achieving the goals, has been decided to be higher.

Constraints						
		Lower	Upper	Lower	Upper	
Name	Goal	Limit	Limit	Weight	Weight	Importance
Volt	minimize	-1	1	1	1	3
[PMMacoMAA]	minimize	-1	1	1	1	3
[LiCl]	minimize	-1	1	1	1	3
Flow_rate	maximize	-1	1	1	1	3
Diam	minimize	0.300	0.370	1	4	5
POE(Diam)	minimize	0.066	0.23	1	1	3

Table6. 24Constraints for optimization

Desirabilities range from zero to one for any given response. The program combines the individual desirabilities into a single number and then searches for the greatest overall desirability. A value of one represents the ideal case. A zero indicates that one or more responses fall outside desirable limits. In this case the goal is a fiber diameter ranging from 300 to 370 nm, and the solutions of

numerical optimization are shown in Figure 90 where we can see there is a ridge where desirability can be maintained at a high level over a range of polymer concentration level. In other words the solution is relatively robust to factor B.

Design-Expert® Software

Desirability

X1 = A: Volt
X2 = B: [PMMAcoMAA]

Coded Factors
C: [LiCl] = -1.000
D: Flow_rate = 0.996

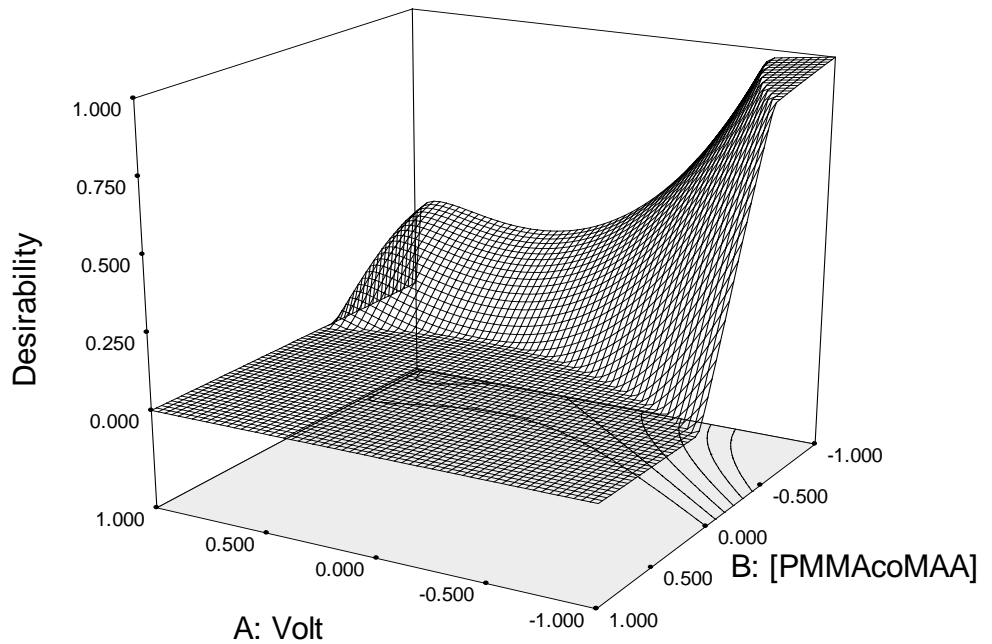


Figure 90 Optimum solution for response minimization

The optimum solution that it has been chosen to minimize the response has the following set of parameters (Table 6.24):

Factor	Operating Condition
Voltage [kV]	14
[LiCl] [w/w%]	0.1
Flow_rate [ml/hr]	4
[PMMAcoMAA] [w/w%]	23

Table 6. 25 Operating Conditions of the Optimized response

Model validation has been carried out processing an electrospun sample at those operating conditions. SEM images have been recorded and results of the descriptive statistics are shown in Figure 91. The mean diameter is consistent with the predicted value

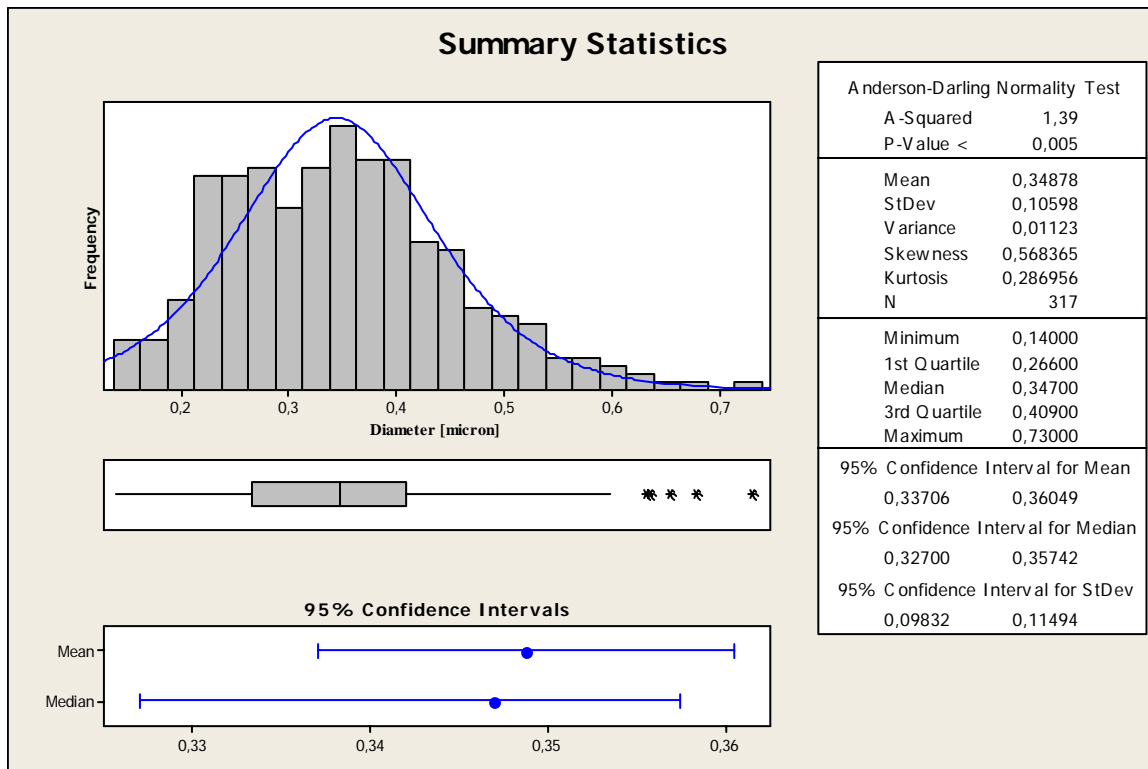


Figure 91 Graphical summary of descriptive statistic for the RSM optimized solution

CHAPTER 7 Fabrication of nanostructured membranes

7.1 Introduction

According to the schematic approach presented before, nanofibers based membranes functionalized with nanoparticles can be useful for catalytic application and in order to make the nanoparticles more accessible to the reagents, a different process has been tested.

This part of the project has been carried out in the framework of the National University of Singapore (NUS)-University of Padova cooperation program in particular at the Nanoscience and Nanotechnology Initiative Laboratories.

In the scientific outlook, this chapter deals with nanostructures development exploiting two powerful techniques, electrospinning and electrospraying, that have been rediscovered a couple of decades ago as a simple, economic and useful tools.

The aim of this part of the project is to create multilayers nanomaterials combining electrospinning and electrospraying techniques in order to obtain a multifunctional membrane as a good candidate in a wide range of application such as for protective clothing, respirators as well as air purifiers.

The implemented method has the objective to deposit inorganic nanoparticles and optimize their distribution over polymeric nanofibers. The following technological objectives summarize the approach that has been assumed:

1. to study electrospraying of inorganic nanoparticles to have a better understanding of the process and suspension parameters effect on the nanoclusters distribution and uniformity.
2. to design a proper process equipment for coupling electrospinning and electrospraying sets up and to optimize them for controllable and reproducible processing.
3. to characterize the manufactured membranes in terms of morphology and filtration property (pressure drop).

According to the technological objectives previously mentioned, an important part of this research work focused on electrospray of inorganic nanoparticles. Basic fundamentals on electrohydrodynamic atomization processes have been extensively covered in Section I. It has been pointed out that electrospraying is not the common route for nanoparticles processing (usually produced by sol-gel process, aerogel process [298-300]) because of the nanoparticles aggregation that always occurs driven by the interparticle forces. Then, the main question incident to the dispersion and the uniform distribution of nanoparticles has been solved studying the electrospraying conditions as well as the suspensions properties. As regards electrospraying

optimization, the effect of the process/suspension parameters has been evaluated and different configurations of the spinning set up were tested.

7.2 Electro spraying optimization

Electro spraying of TiO₂ suspensions was performed and a brief review on the effect of different parameters is presented in this section in term of:

- Sonication time effect;
- Feed rate effect;
- Applied voltage effect;
- Nanoparticle concentration effect;

Moreover nanoparticles dispersion studies have been performed because the ability to have a uniform deposition of nanoparticles will play a key role on the membrane properties.

Details about the processed nanoparticles have been previously mentioned in Section II.

7.2.1 Sonication time effect

In order to promote the nanoparticle disaggregation, it has been chosen to sonicate the suspension before electro spraying by probe ultrasonic mixer. Different sonication times (5, 10, 15, 20 and 40min) were tested and then all the suspension were sprayed.

The electro spraying condition, the same for all the sprayed samples, are summarized in Table7.1.

Electro spraying conditions	
TiO ₂ concentration (% v/v)	1.25
Applied voltage (kV)	15
Feed rate (ml/h)	12
Distance needle-collector (cm)	8
Drum speed (rpm)	860
Needle	18G
Temperature (°C)	29
Humidity (%)	<35

Table7. 1 Electro spraying conditions

As shown in Figure 92 an increase in sonication time results in a decrease of big clusters formation and because of this further experiments were carried out assuming a sonication time of 40 min.

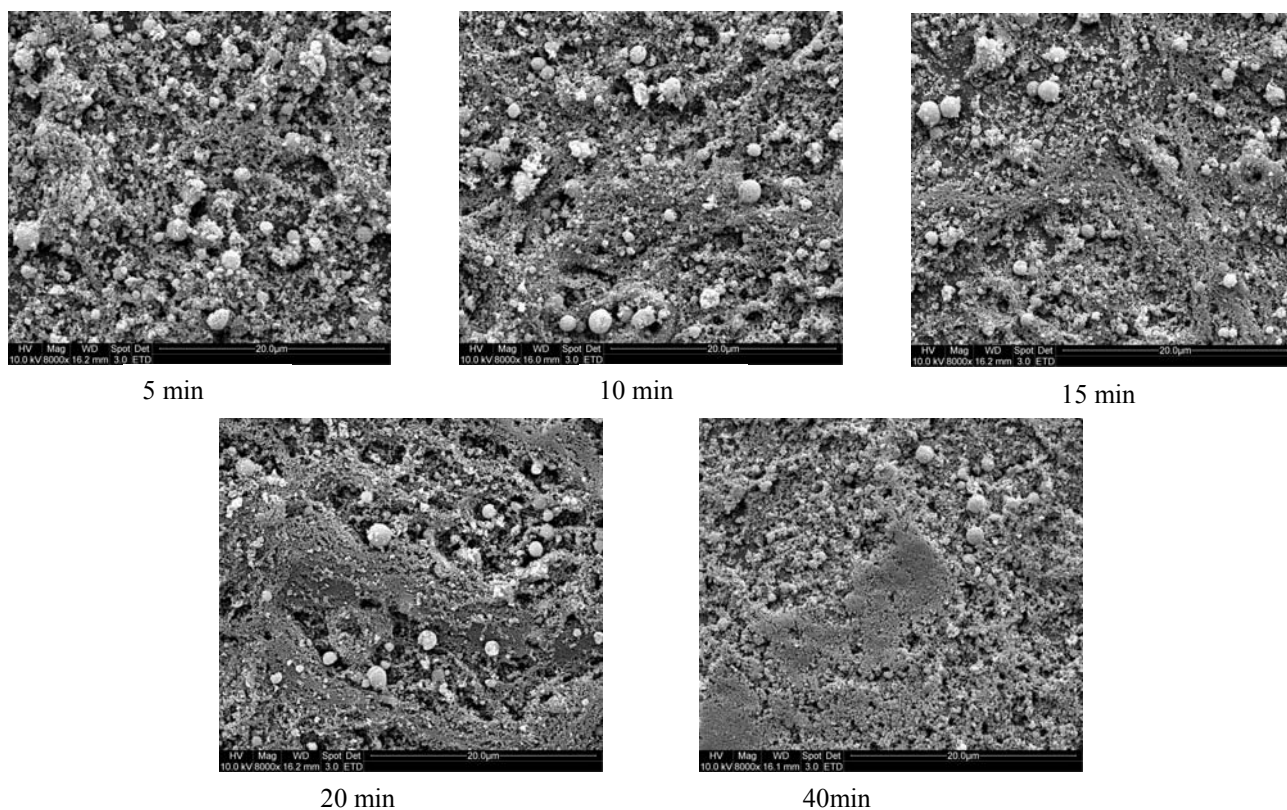


Figure 92. Effect of different sonication time on nanoparticles morphology and distribution

7.2.2 Feed rate effect

Three different feed rate values (8 ml/hr, 12ml/hr and 16 ml/hr) have been considered for the electrohydrodynamic deposition of mechanical mixed suspensions, other conditions being equal. Of course an increased flow rate means a larger amount of suspension available at the end of the electrified needle and then the deposition on the collector rises up. However a relevant effect on the nanoparticles distribution is not easily appreciated as shown in Figure 93.

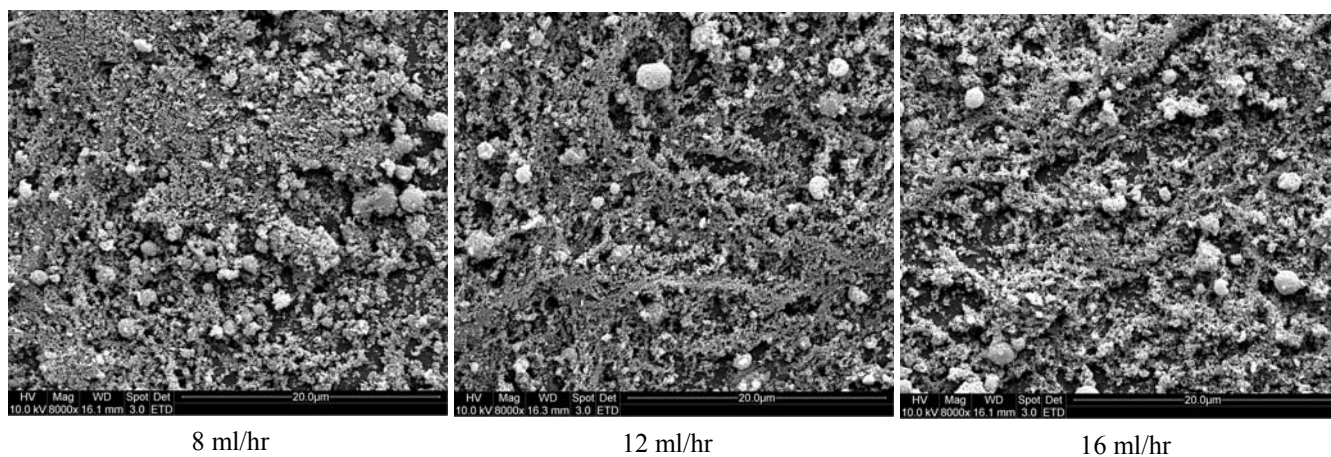


Figure 93. Effect of different flow rate on nanoparticles spraying

Then, electrospraying was performed feeding a suspension previously sonicated 40 mins, according to the optimum sonication time previously tested. In this case varying the flow rate from 8ml/hr to 12 ml/hr, the effect on the distribution is more evident and it results in a reduction of the spherical shape clusters density as shown in Figure 94.

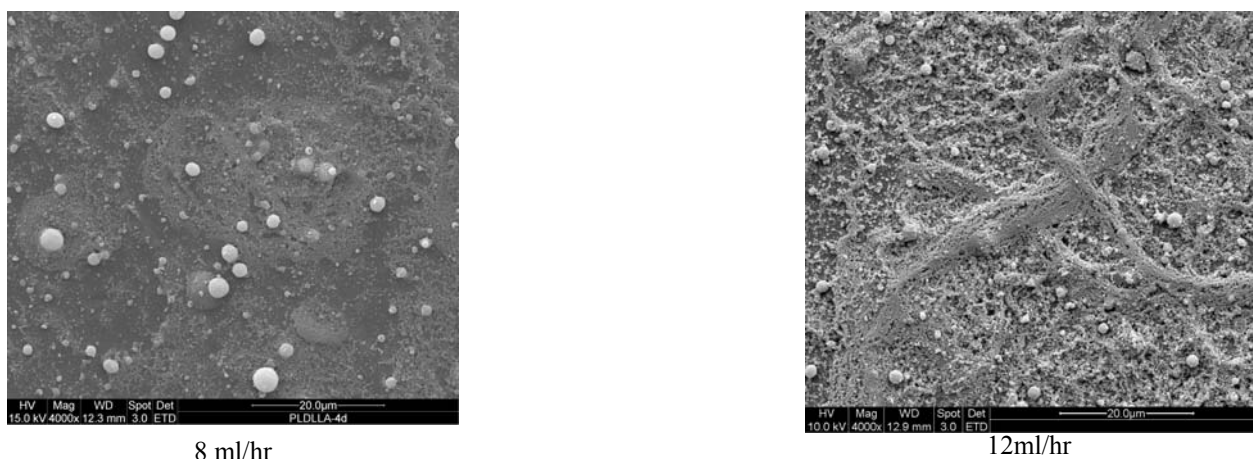


Figure 94. SEM images of sprayed samples (according to conditions in Table1) at two different flow rate

7.2.3 Applied voltage

In Figure 95 SEM micrographs show the effect of applied voltage on the nanoparticles distribution. As expected, an increase from 9 kV to 12kV results on switching from cone-jet mode to multi-jet mode. It means higher covered surface but more jet instability. However it has been noted that the dimensions of spherical clusters tend to decrease as well as the nanoparticle distribution is more uniform.

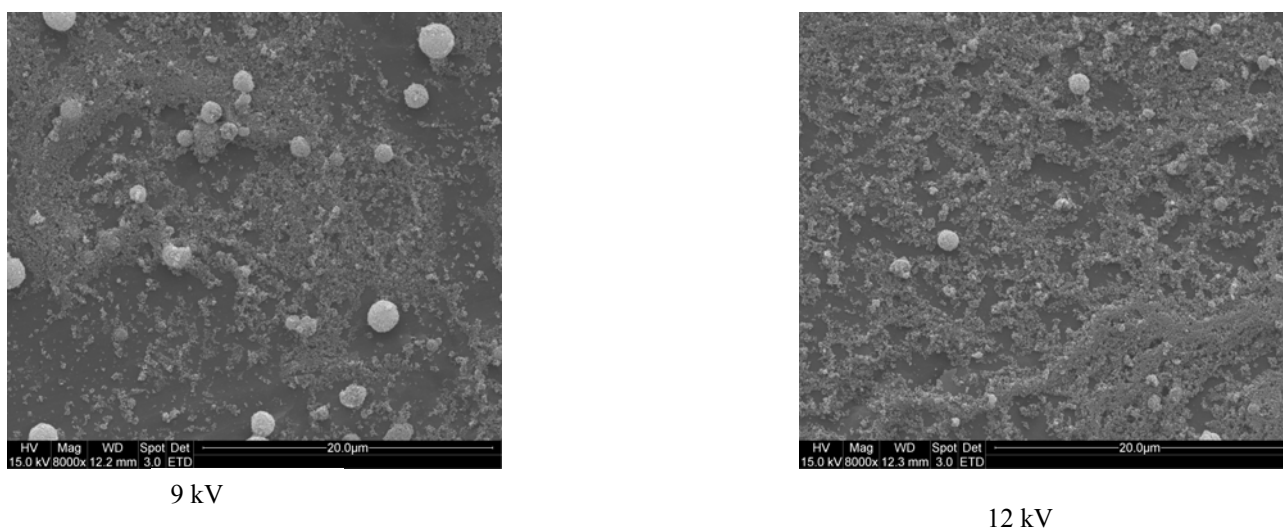


Figure 95. SEM images of sprayed samples at different applied potential, all the conditions being equal (Table 7.1)

7.2.4 Nanoparticles concentrations

Different concentrations in nanoparticles (TiO_2) were tested: 0.5%(w/v), 1.25% (w/v), 2% (w/v); as shown below (Figure 96) increasing the nanoparticles concentration the number of cluster with spherical shape increases but at the same time the distribution is more uniform in term of covered surface.

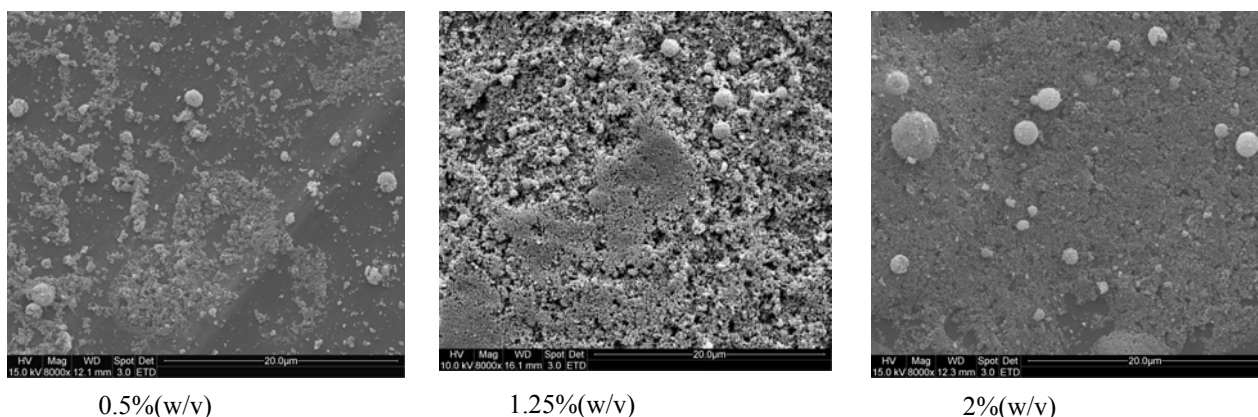


Figure 96. SEM images of sprayed sample at different concentration in TiO_2 , all the conditions being equal

In order to improve the dispersion, a proper amount diethylene glycol [299] (equal to the nanoparticles concentration) was added in two suspensions of TiO_2 (0.5%w/v and 2%w/v) and these samples were sprayed at the same conditions after 40 min of sonication.

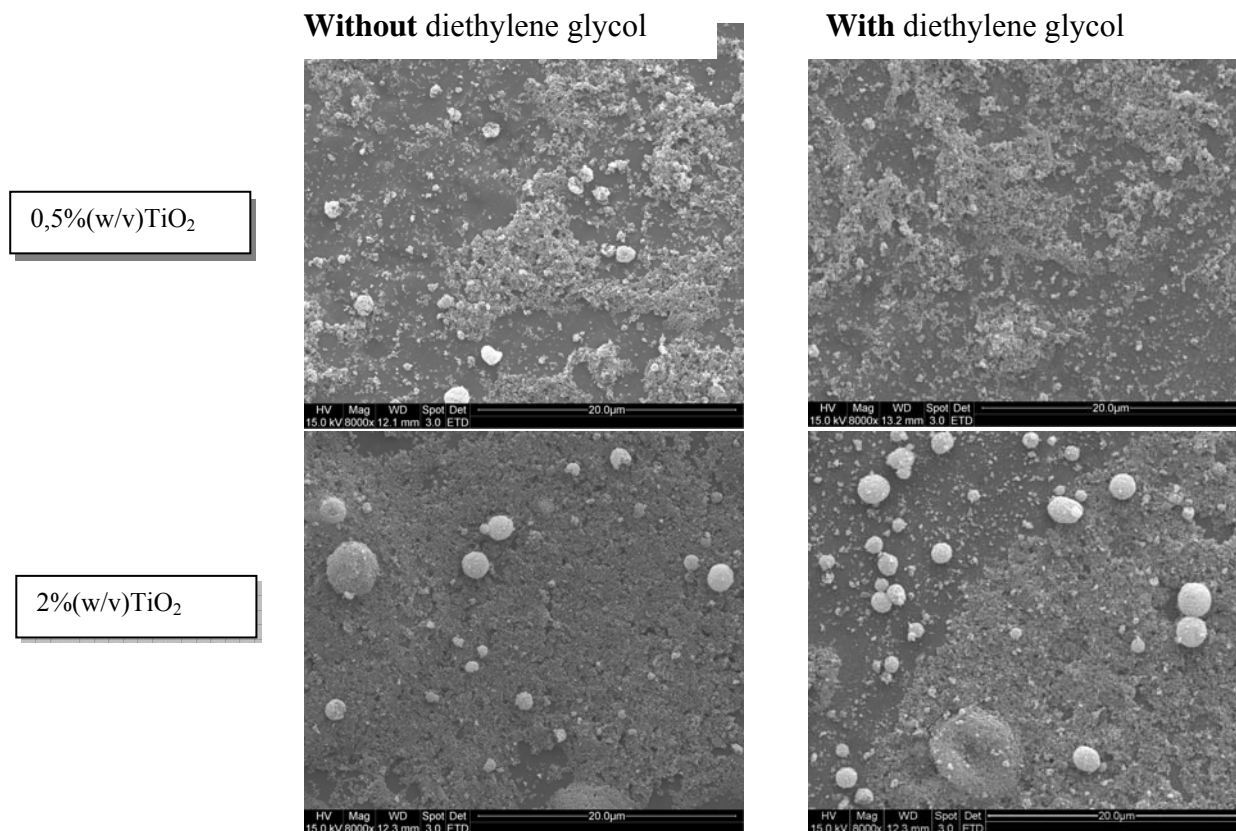
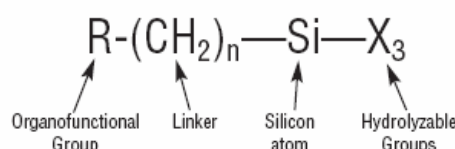


Figure 97. SEM images of sprayed samples at two different concentration in nanoparticles and with or without diethylene glycol (all the other conditions being equal)

In spite of expectations, diethylene glycol didn't have a good result in term of improved dispersion even if its –OH groups are supposed to promote particle disaggregation, as shown in Figure 97.

7.2.5 Nanoparticles dispersion studies

In order to improve the nanoparticles distribution on the collector first and subsequently on the nanofibers substrate, our aim was to stabilize the suspension before electro spraying to avoid the nanoparticles aggregation that always occurs after a while from sonication. Another technical reason to achieve this goal is for processing more than once the suspensions daily prepared. The surfactant chosen was silane MEMO, that is 3(trimethoxysilyl) propyl methacrylate.



Silane coupling agents have already been used widely in industry for many applications. They basically contain two functional parts in one molecule see Figure 98. One is a hydrolysable group, which can hydrolyze when there is water and forms a silanol groups. Usually, inorganic particles like TiO₂ will have hydroxyl groups on surface when exposed Figure 98. Silane structure to atmosphere. The silanol groups on organosilane condense with hydroxyl groups on particle surface and form siloxane linkages. The other part in an organosilane is a non-hydrolyzable organic tail that may possess a functionality that imparts desired characteristics, for example, affinity or chemical bonding with monomer or polymer.

Figure 99 shows the schematic activity of a silane as well as one example of different distributions of silane-modified particles rather than unmodified particles [300].

The calculation of silane dosage was obtained according to the literature [301] as follows:

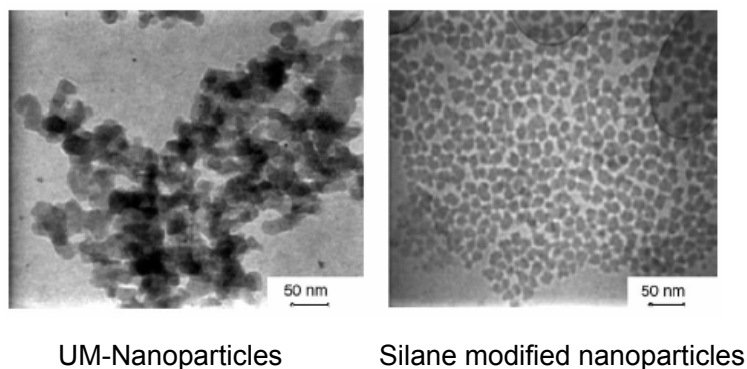
$$m_f = \frac{M_f m_s A_{sp}}{A_f} \quad (\text{Eq. 7.1})$$

with m_s = mass of TiO₂ nanoparticles = 1.25% w/v, 2% w/v, 5% w/v, respectively; A_{sp} = specific surface area of TiO₂ = 50000 m²/kg; M_f = molar mass of silane MEMO = 248.4 g mol⁻¹; A_f = molar area coverage of MEMO = 105 m²mol⁻¹. This equation gives the dosage of silane that is necessary to create a theoretical monomolecular layer around the nanoparticles, but a general guideline suggests to use the proper for having 4 monolayers.

Table 7.2 summarizes the dosage calculation obtained in different samples:

Silane MEMO dosage		
Nanoparticles concentration	Monolayer dose (see Eq.(1))	4-layers dose
1,25%w/v = 0.375g TiO ₂ in 30ml methanol	0.04661 g	0.1864 g
2% w/v = 0.4g TiO ₂ in 20 ml methanol	0.04968 g	0.1987g
5% w/v = 1g TiO ₂ in 20 ml methanol	0.1242 g	0.4960g

Table7. 2 Dosage calculation for different samples



UM-Nanoparticles

Silane modified nanoparticles

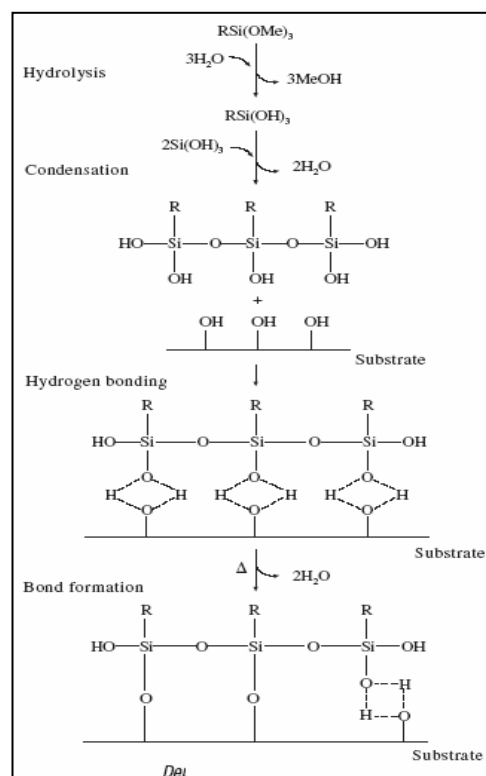


Figure 99. Example of silane modified nanoparticle [300]; on the right a schematic diagram of the silane activity

In order to have information about the dispersion of the colloidal suspensions and the effectiveness of sonication and surfactant actions, the size distribution of TiO₂ (1.25%w/v)-methanol system have been monitored by dynamic light scattering after ultrasonic mixing and results for different sonication times (20 mins and 45 mins) were recorded and compared to the mechanical mixing. Four scattering analysis have been performed for every sample with a time interval of 20, 25, 43 mins after the first scattering run.

The first expected conclusion, concerns the polydispersity of the samples which is related to the width of the distribution and it is calculated according to the literature [302]. The polydispersity index tends to decrease from the mean values usually observed by mechanical mixed suspensions from 0.230-0.360 to a mean value of 0.160 in a strong ultrasonic mixing. Although the

polydispersity of the latter is still in the mid-range (0.08-0.7), it confirms the ultrasonication is an effective tool to disturb efficiently the cluster formation. Results recorded for the mechanical mixing sample showed that the effective diameter of nanoparticles increases from 34.5 ± 0.5 nm to 772.6 ± 41.4 nm within 20 mins, after which it is not possible to run a scattering analysis anymore because of the mean count rate out of range that means the aggregation occurs and the suspension is not stable. Moreover, a bimodal size distribution is revealed with a second peak of mean diameter at $1.4 \mu\text{m}$.

The same trend has been noticed for the colloidal suspension of 20 mins sonicated sample, wherein the effective diameter of nanoparticles grows up to 271.4 ± 2.5 nm after 20 mins (second run). Then this result reveals the sonication acts on a reduction of clusters size, but this effect vanishes, as expected, so rapidly after a while and, in particular, after 20 mins the nanoparticles cluster size is far away from the initial value of ≈ 25 nm nominal diameter. The results obtained for the 45 mins-sonicated suspension indicates that the effective diameter after the fourth scattering run is still very close to the nominal diameter revealing a partial stability of the sample. As regards the effect of dispersant agent, it has been showed that the suspension of TiO_2 (1.25%w/v) in methanol, with the proper amount of silane, has a mean effective diameter of nanoparticles equal to 20.7 ± 1.2 nm after overnight storage and this result represents the optimal condition for going ahead with multistructured membrane processing.

7.2.6 Electro spraying modified set up

Since the nanoparticles distribution in term of uniform deposition on the collector was not completely achieved using the common set up, the electro spraying apparatus was modified adding an individual ring induction electrode. Two different configurations were tested, grounding the ring (applied voltage to the needle, collector grounded), Configuration 1, or applying the voltage to the ring (needle and collector grounded), Configuration 2. A schematic representation of them is shown in Figure 100. It must be emphasized that close beneath the ring, the horizontal component of the electric field vector is higher than the vertical ones, and this component drives the droplets outside and then the spray plume is wider in this kind of system. The only drawback of these configurations is the aerosol loss due to the high electric charge of the droplets that are easily bent to other grounded elements located nearby, including induction electrode.

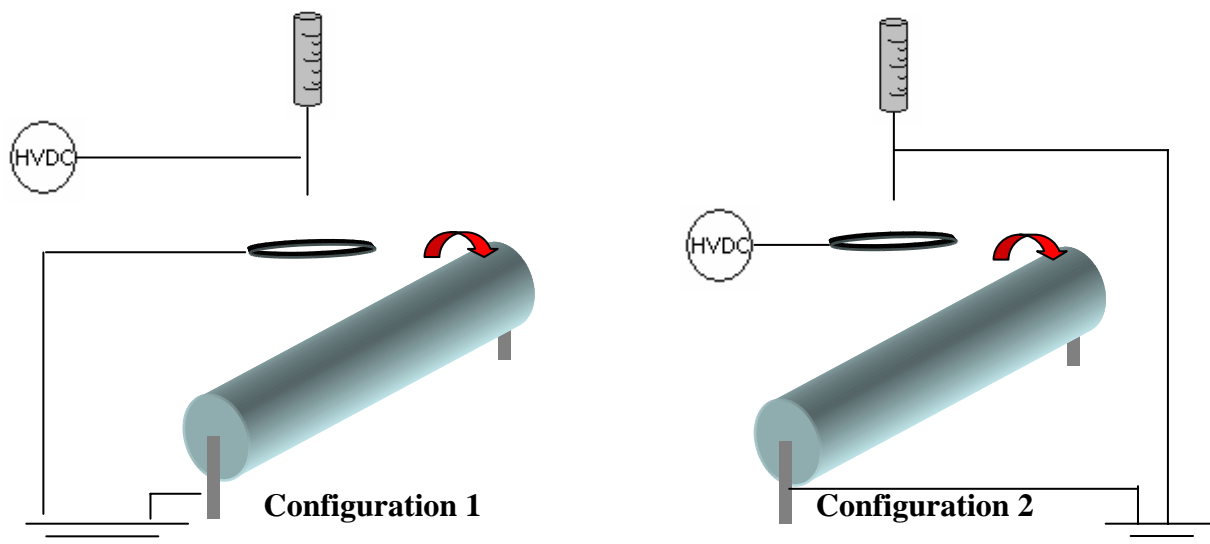
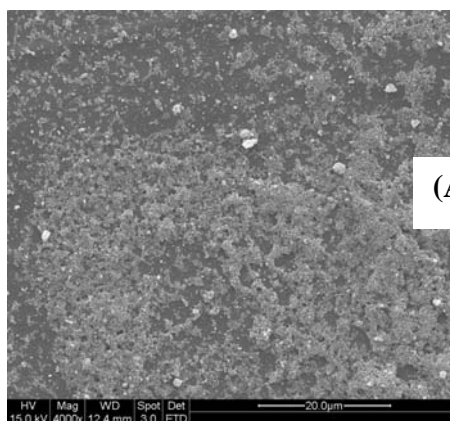
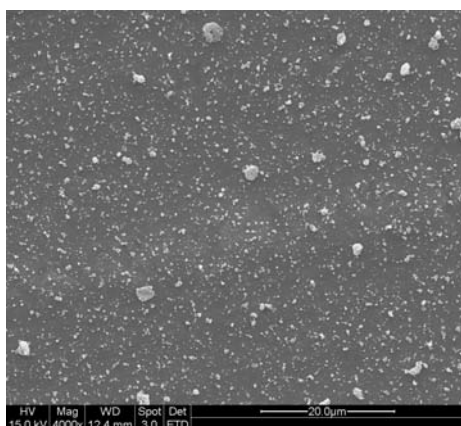
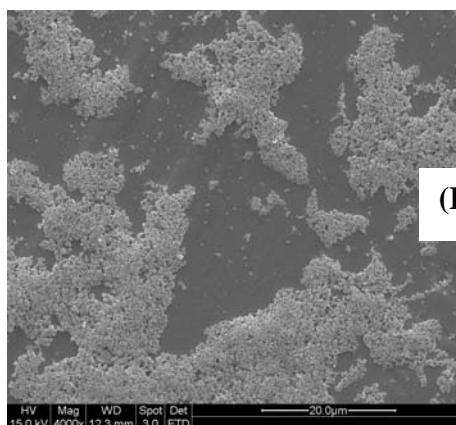
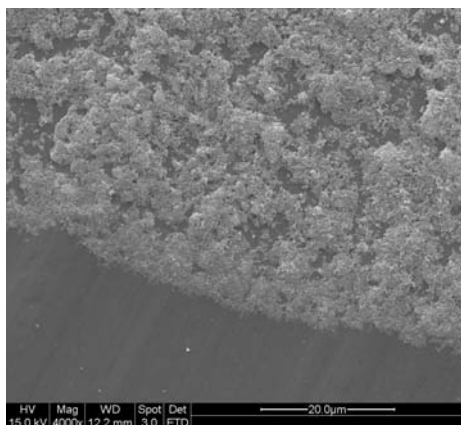


Figure 100. Electrospaying different configurations

In Figure 101 SEM micrographs of sprayed samples of TiO₂ 1,25%w/v performed in Configuration 1 and Configuration 2 are reported and Table 5 summarizes the electrospaying conditions.



(A) Configuration 1



(B) Configuration 2

Figure 101. (A) SEM images obtained spraying in Configuration 1 and in Configuration 2 (B)

Electrospraying conditions (both configurations)	
Applied Voltage (kV)	15
Feed rate (ml/hr)	12
Nanoparticles concentration (w/v)	1,25%
Distance needle-ring (cm)	3,5
Distance ring-collector (cm)	7
Needle	18G
Drum speed (rpm)	860
Temperature °C	30°C
Humidity %	< 35%

Table7. 3. Electrospaying conditions

It has been noted that a uniform distribution is achieved using Configuration 1 because with Configuration 2 there are non-covered areas on the collector. Further optimization on Configuration 1 was carried out working on the flow rate (8 ml/hr) and then Figure 102 shows the final uniform distribution obtained at the same conditions in Table7.3.

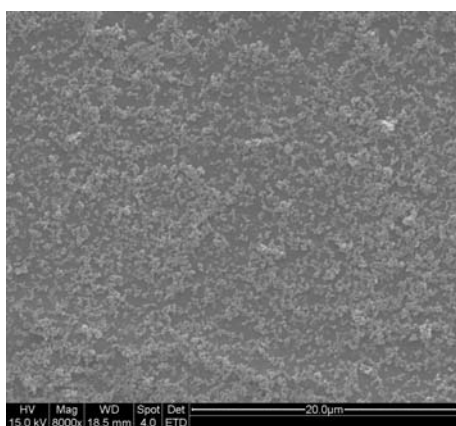


Figure 102. SEM image of TiO₂ sprayed sample according the conditions in Table5. Only the flow rate has been changed from 12 ml/hr to 8 ml/hr.

7.3 Membranes processing and characterization

7.3.1 Multistructured membranes production PSU-TiO₂/MgO

Multilayers membrane processing was obtained performing alternatively electrospinning of poly sulphone (PSU) (20%w/w in DMF) and electrospaying of TiO₂ or MgO at three different concentrations (1,25%w/v, 2%w/v, 5%w/v), working with the apparatus shown in Figure 103. Table 6 reports the spinning assumed conditions.

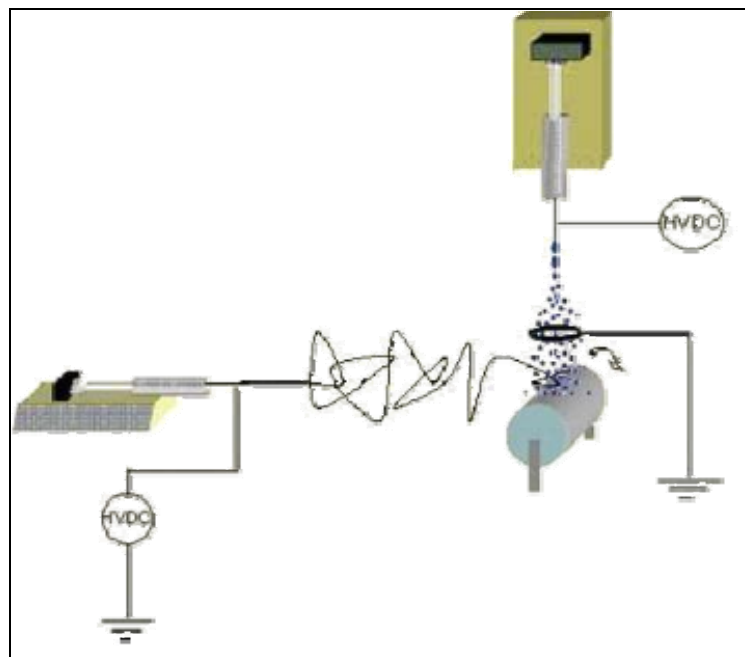


Figure 103. Electrospinning-Electrospraying set up

	Electrospinning conditions	Electrospraying conditions
Applied Voltage (kV)	13.5	15
Feed rate (ml/hr)	3	12
Polymer conc. %(w/w)	20	
Nanoparticles conc. % (w/v)		1.25 or 2 or 5
Distance needle-ring (cm)	/	3.5
Distance ring-collector (cm)	/	7
Distance needle-collector (cm)	13	/
Needle	27G1/2	18G
Drum speed (rpm)	860	860
Temperature °C	30	30
Humidity %	<35	< 35

Table7. 4 E.spinning-E.spraying conditions in membrane processing

Membranes based on 5 layers (ES-EHDA-ES-EHDA-ES), or 7 layers, or 5 layers with the sprayed ones at different nanoparticles concentration, were then obtained and in Figure 104 SEM images of some of them are reported.

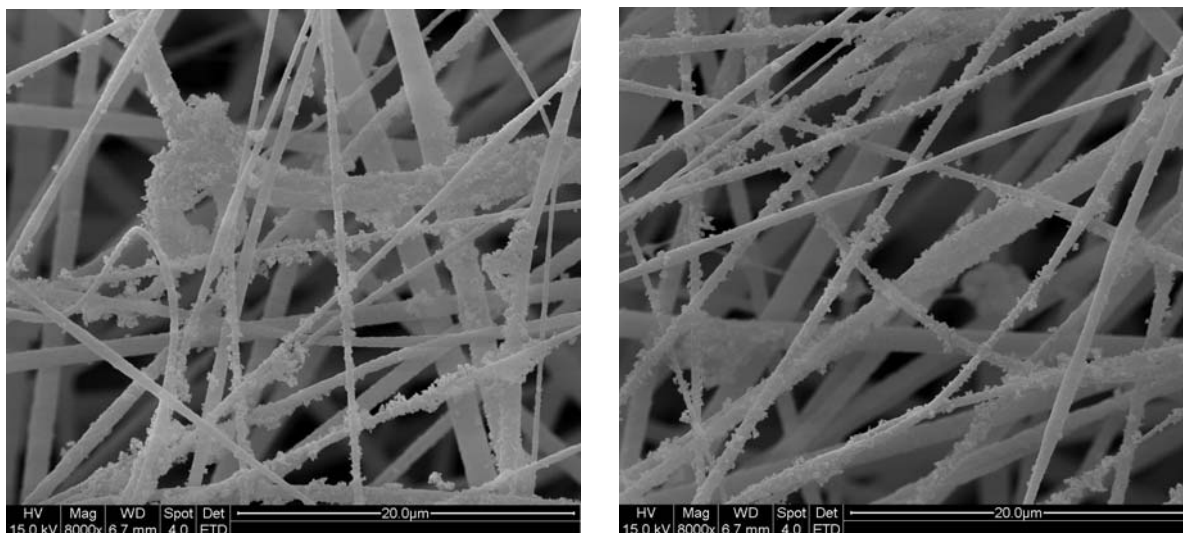


Figure 104. SEM images of membrane based on TiO₂ nanoparticles (1,25%w/v) sprayed over electrospun polysulphone nanofibers according the conditions in Table6

It can be pointed out that the nanoparticles are uniformly distributed over the electrospun nanofibers forming small dendritic structure as well as the interfibers pores are not clogged.

7.3.1.1 Pressure drop analysis

As previously mentioned this new kind of multifunctional membranes could be a good candidate as filter media for respirators and for protective clothing because small fibers in the submicron range, in comparison with larger ones, are well known to provide better filter efficiency at the same pressure drop in the interception and inertial impaction regimes.

Pressure drop analysis was carried out thanks to a device built up at the NUS NNI laboratories that allowed to measure the pressure drop across the membrane as a function of the gas (nitrogen) flow rate according to the scheme reported in Figure 105.

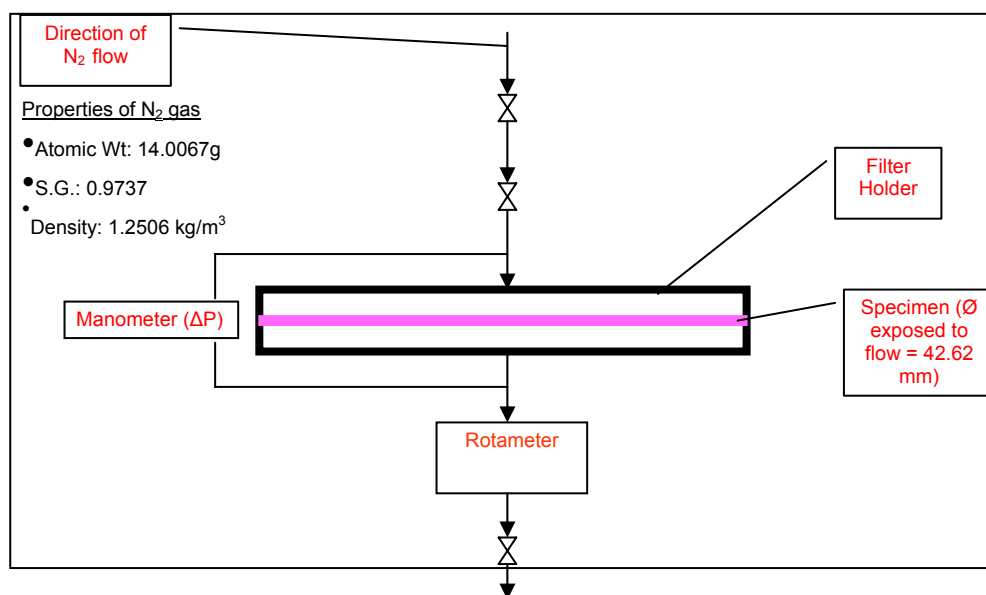


Figure 105 Schematic apparatus for pressure drop analysis

The control was a Polysulphone membrane (red line); the membranes tested were the following:

Memb13%: membrane based on 5 layers: electrospun PSU-electrosprayed TiO_2 1.25%w/v-electrospun PSU-electrosprayed TiO_2 2%w/v; final content of nanoparticle 13wt%;

Memb17%: membrane based on 5 layers spraying TiO_2 2%w/v; final content of nanoparticles 17wt%;

Memb. Nanocomp11%: membrane based on ESspinning and electrodynamical deposition of TiO_2 (1.25%) performed simultaneously; final content in nanoparticle 11wt%;

Memb11%: membrane based on 5 layers spraying TiO_2 1.25%w/v; final content of nanoparticles 11wt%

Memb32%: membrane based on 5 layers spraying TiO_2 5%w/v; final content of nanoparticles 32wt%

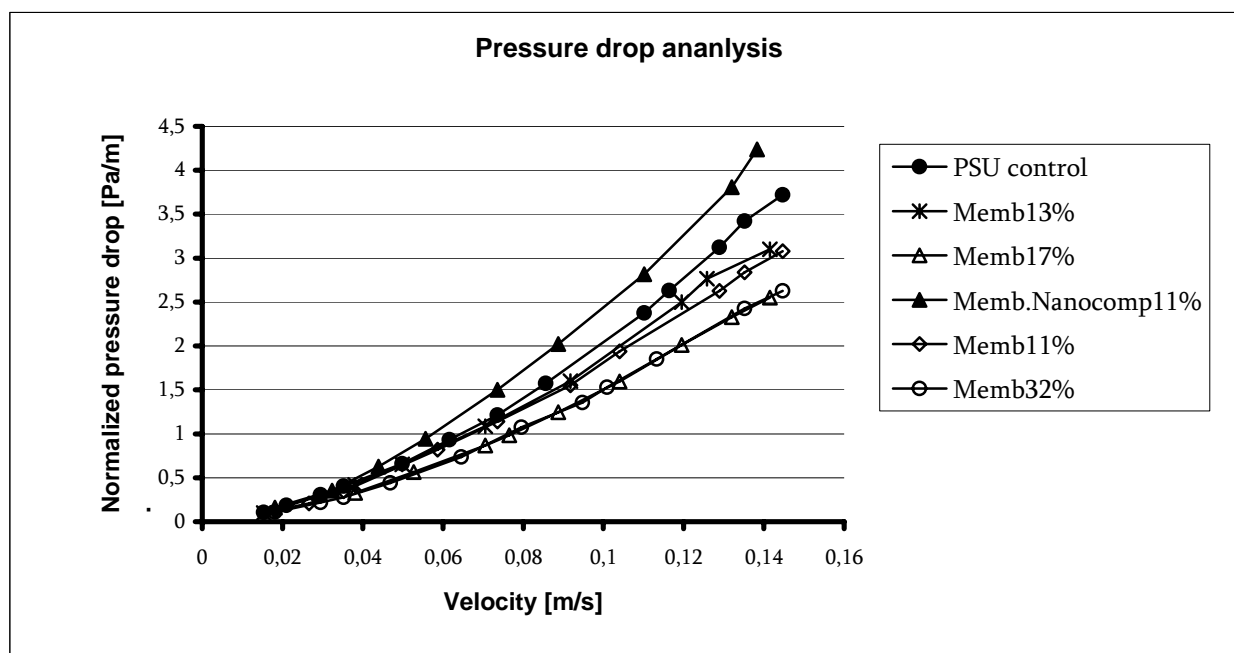


Figure 106. Pressure drop curves for different membranes tested.

As shown in Figure, the membrane produced performing simultaneously the spinning processes reveals an increase in pressure drop throughout it, if compared to the PSU control membrane, that is a ΔP increase of 17% in the range $0.08 < v < 0.14$ m/s. This result well explains the reason over which it has been chosen to produce multilayers membranes rather than nanocomposite membranes.

Table 7.5 summarizes the results in term of pressure drop decrease with respect to control membrane for the main membranes in the velocity range $0.08 < v < 0.13$ m/s.

Range $0.08 < v < 0.14$ m/s	ΔP decrease %
Memb32%	27 ± 0.2
Memb17%	27 ± 1.07
Memb11%	13 ± 0.13

Table 7. 5 Pressure drop decrease for different samples.

An unexpected result concerns an higher decrease of pressure drops through the membrane increasing the nanoparticles concentration. It has been speculated that nanoparticles small clusters act improving the interfibers distance between two electrospun nanofibers layers. This results in more “free” space within the membrane for gas flowing and then the pressure drop, which is a measure of the membrane drag to the air/gas flow, is affected by an effective decrease.

As regards the membrane based on MgO sprayed nanoparticles results are shown in Figure 107 for MgO concentrations of 2% and 5% respectively. In contrast to the expectations, the pressure drop for MgO_5% is higher than the PSU control, and further investigation are necessary to understand

this behaviour. Probably this is due to the nanoparticles which tend to aggregate and clog the interfiber pores because the surfactant used is not the best one for this kind of nanoparticles.

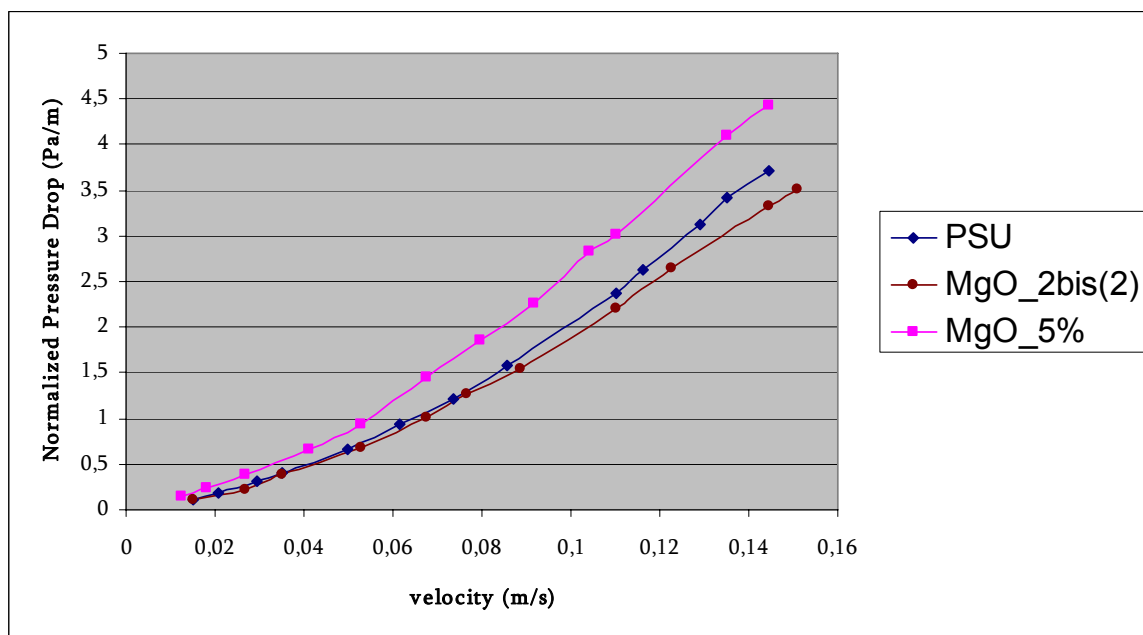


Figure 107. Pressure drop curves for MgO-PSU based membrane at the concentrations indicated.

7.3.2 Multistructured membranes production PMMAcO_{MMA}/PANcoVAc/TiO₂

According to the schematic apparatus for coupling electrohydrodynamic techniques showed in Figure 103 and thanks to the results of response surface analysis proposed on Chapter x, the fabrication of multistructured membranes based on PMMAcO_{MMA}, PANcoVAc, and TiO₂ have been optimized in order to have a nanostructured catalytic media for testing VOC degradation.

PMMAcO_{MMA} has been chosen due to its chemical structure, which presents pending carboxylic groups which are able to interact with the hydroxylic groups exposed on the TiO₂ surface. The purpose here is the optimization of a multifunctional nanostructured membrane where electrospun nanofibers represent the scaffold of the media and photocatalytic nanoparticles are spread over their surface. The resulting multilayer structure is then a good candidate for working as a filter media coupling the mechanical filtration of the web-micropores to the chemical action of the nanoparticles against VOCs.

The multilayer membrane was then obtained performing alternatively electrospinning of PMMAcO_{MMA} solution in DMF:Ac=2:1 (according to RSM, 23% by weight, [LiCl] 0,1%w) and electrohydrodynamic atomization of TiO₂ (1.25%w) suspensions in methanol. The optimized conditions for TiO₂ electrodeposition have been previously showed in Table7.4 as well as the operating parameters for processing polymer solution.

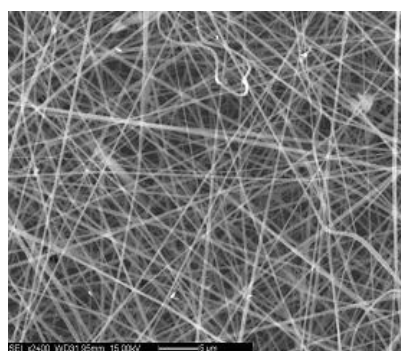
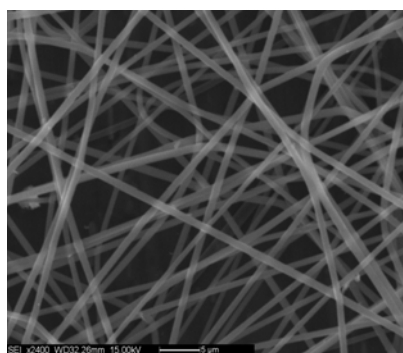
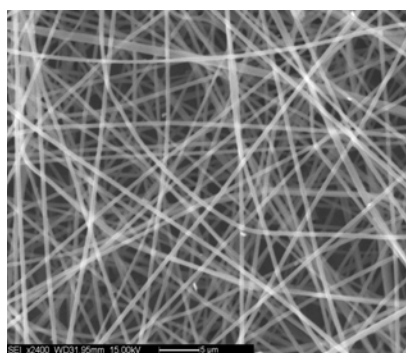
The obtained membrane however presented some drawbacks concerning its mechanical properties as well as it was not so easy to handle. In order to overcome those aspects, a different polymer has been chosen for the first layer of the membrane and design of experiments has been carried out for evaluating the proper conditions of electrospinning. Three different system were studied, that is:

- Polyacrylonitrile (PAN) in N,N Dimethylformamide (DMF),
- Polyacrylonitrile in N,N Dimethylacetamide (DMA),
- Polyacrylonitrile -co-Vinyl acetate in N,N Dimethylformamide (DMF).

Secondary electron (SE) based micrographs, by SEM analysis, of these samples are shown in Figure 108 and it can be observed the electrospun fibers of Polyacrylonitrile -co-Vinyl acetate results on smaller mean diameter. A further aspect was concerning the peeling of the membrane from the aluminium foil: as shown in Figure 108, the membrane based on PANcoVAc as first layer, does not oppose any peeling-resistance. Thanks to its properties this copolymer was then chosen, and the optimized operating conditions are summarized in Table7.6. According to the optimized conditions, a batch of 17 membranes has been produced and characterized. Herein the main results of membranes features have been reported.

Layer	Material	Process	Operating conditions
1°	PANcoVAc	ESspinning	1 ml/hr, 15kV, 27 cm
2°	TiO ₂	EHDA	8 ml/hr, 15 kV, distance4-7 cm
3°	PMMAcoMAA	ESspinning	1.5 ml/hr, 17kV, distance15cm
4°	TiO ₂	EHDA	8 ml/hr, 15 kV, distance4-7 cm
5°	PMMAcoMAA	ESspinning	1.5 ml/hr, 17kV, distance15cm

Table7. 6Structure of the multilayers membrane baseb on PMMAcoMAA/PANcoVAc/TiO₂



(a)

(b)

(c)

Figure 108 SE micrographs of electrospun fibers of: a) PAN/DMF; b) PAN/DMA; c) PAN-co-acetato di vinile/DMF



Figure 108 Peeling of the membrane from the alluminium foil (a) membrane based on electrospun PMMAcoMAA; (b) membrane based on electrospun PANcoVAc

7.3.2.1 Multistructured membranes characterization

The processed multistructured membranes have been characterized in term of morphology, inorganic content (by means of thermogravimetical analisys TGA), Pressure drop and Water vapour permeability. Basic fundamentals of these methodologies have been reported in Chapter 4.

Morphology and structure

The morphology of the obtained membranes has been studied by Scanning Electron Microscopy. SE-Micrographs of the first layer on the bottom (PANcoVAc) and on the top (PMMAcoMAA) are reported in Figure 109 and in Figure 110, respectively. Both the images were processed by image software analyzer for evaluating the diameter distribution and graphical summaries of descriptive statistics show a mean diameter of 360 ± 0.1 nm for the first layer and 400 ± 0.09 nm for the layer on the top. Moreover from the confidence intervals it can be pointed out the coefficient of variation is roughly 25 nm, in agreement with the experimental error of the measurement. The electrospun web is beads-free and the fibers surface appears smooth; the whole membrane thickness ranges from 320 μ m to 360 μ m, according to Figure 111 (this value for thickness comes from a mean measurement performed over 17 processed membranes).

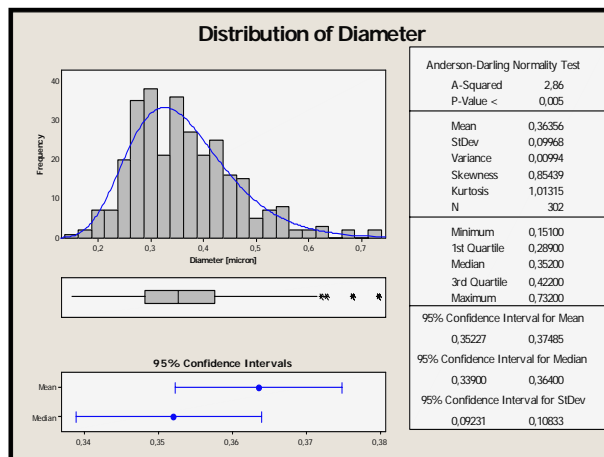
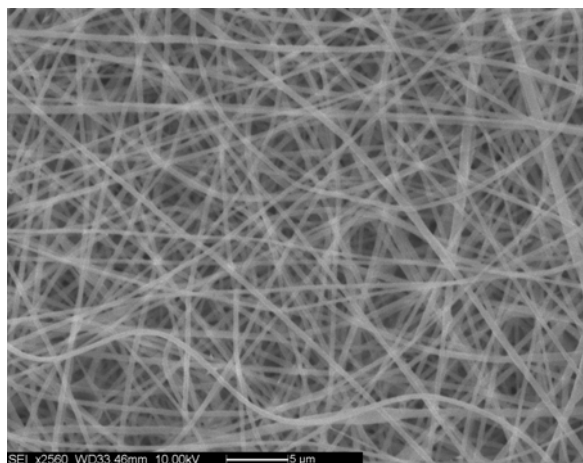


Figure 109 (a)SE micrograph of PANcoVAc layer; (b) Graphical summary statistic

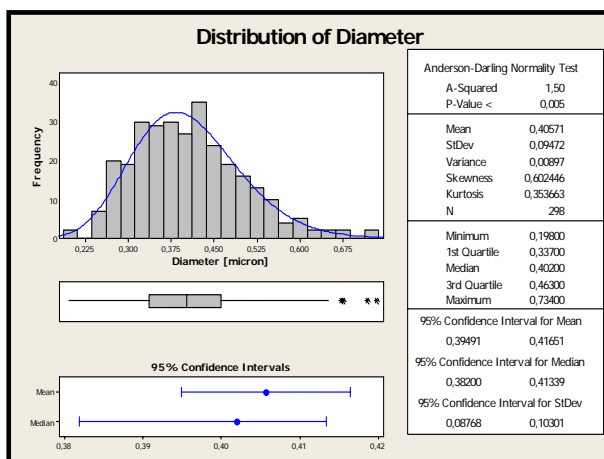
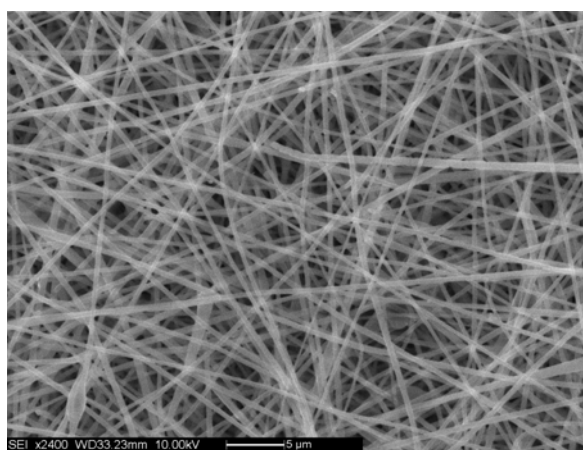


Figure 110 (a)SE micrograph of PMMAcoMAA layer (b) Graphical summary statistic

As regards the intermediate layers where TiO₂ nanoparticles are sprayed over electrospun nanofibers, it was important to avoid the inter-fiber pore clogging and at the same time to achieve their uniform deposition. This for a double reason: if the pores are clogged the pressure drop across the membrane tends to increase and the photocatalytic activity is strongly related to the specific surface area. Figure 112 shows how the TiO₂ nanoparticles look like after electrohydrodynamic deposition and the detail of membrane section support the evidence that nanoparticles tend to hook

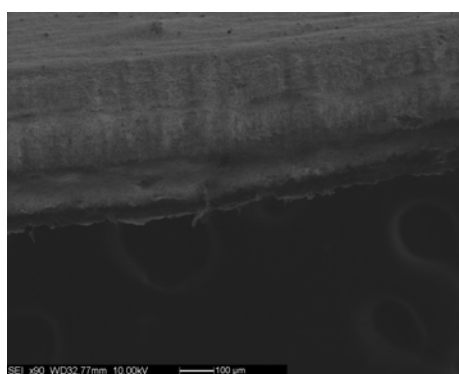


Figure 111 SE micrograph of membrane section

into the web structure thanks to the porosity. Nanoparticles form small dendritic structures and pore clogging is skipped out.

Back scattering micrographs as well as EDAX microanalysis of the samples were used for supporting the evidence of qualitative presence of TiO₂ nanoparticles. Both punctual and widespread analysis were carried out as shown in Figure 113 Figure 114. From microanalysis of a

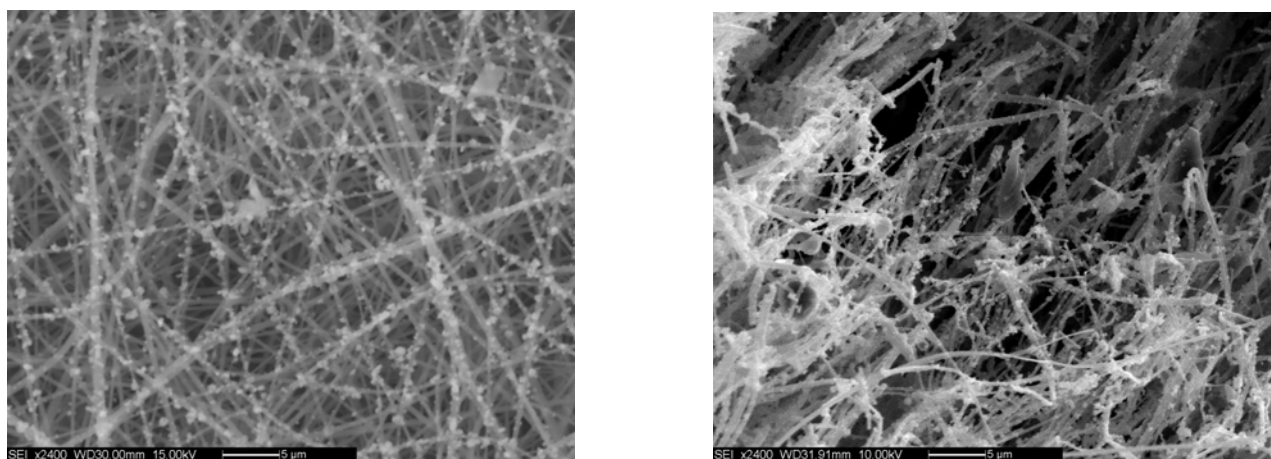


Figure 112 (a) SE micrograph of TiO₂ nanoparticles spread over nanofibers surface; (b) Section of multilayer membrane with detail of nanoparticles

mean surface area of the sample a small amount of other metal oxides was detected, coming from the processing, that is ZnO and Cu₂O, and it has been verify they do not affect the photocatalytic performances of the TiO₂ or better Cu²⁺ behaves as electron scavenger ($\text{Cu}^{2+} + \text{e}^- \rightarrow \text{Cu}^+$), preventing the recombination of electron–hole pairs, thus increasing the chances of the formation of OH on the TiO₂ surface. This is favourable for the photocatalytic reactions while Zn²⁺ metal ions have no obvious effect on the photocatalytic efficiency as suggested from the literature [303].

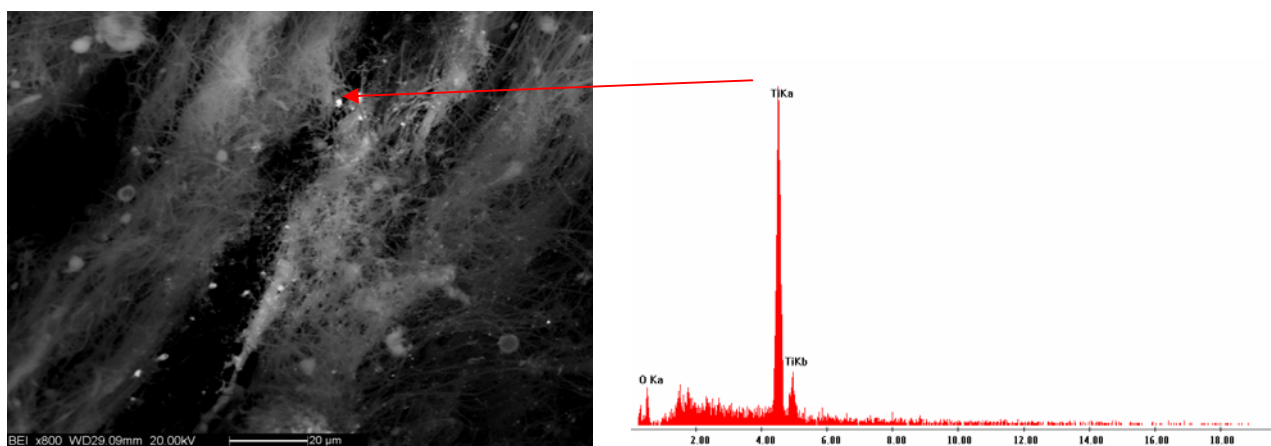


Figure 113 (a) BEI micrographs on multistructured membrane; (b) Punctual EDAX microanalysis of the sample

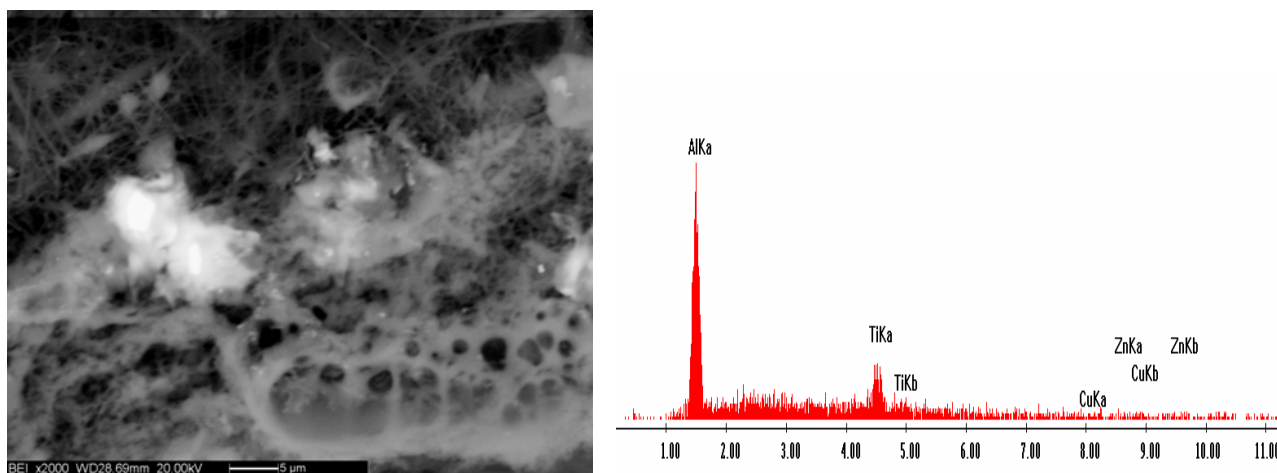


Figure 114 (a) BEI micrographs on multistructured membrane;(b) Widespread EDAX microanalysis of the sample (light grey area)

Still concerning the morphology, SEM image at higher magnification allows distinguishing different layers within the membrane section and these facts bear out the exposed theory according to which the nanoparticles are able to increase the interlayer distance among electrospun layers.

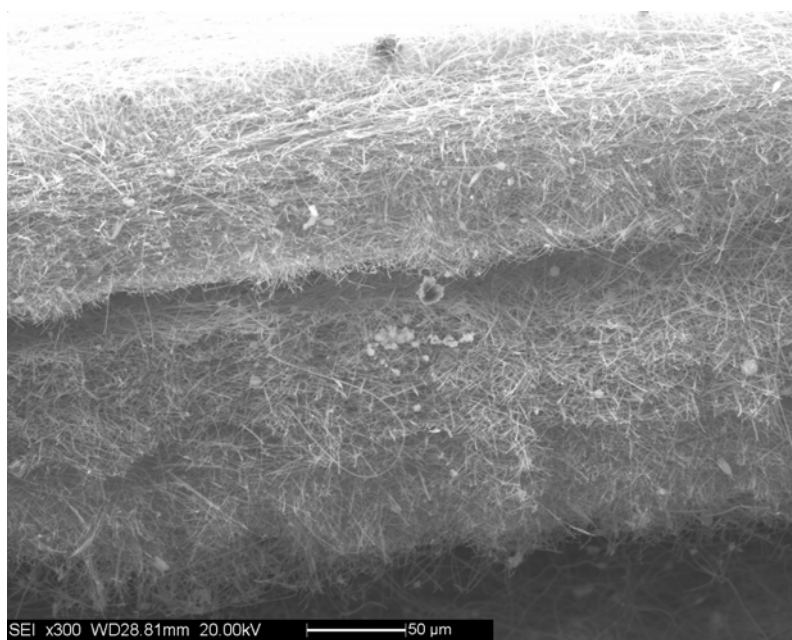
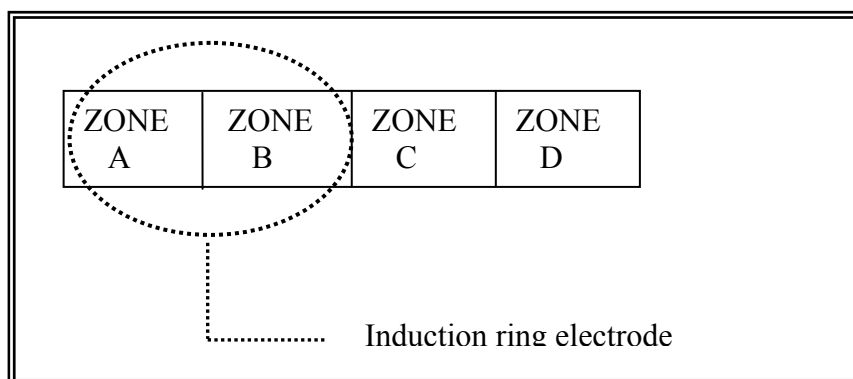


Figure 115 SE micrograph of a membrane section

Thermogravimetric analysis (TGA)

Thermogravimetric analysis was used to have a quantitative analysis about the amount of TiO_2 in the multistructured processed membrane. In order to have representative samples, a stripe (1cm width, 15 cm length) has been cut into four partitions and TGA curve was recorded for everything. The partition of the membrane was carried out according to Scheme 1, which also represents the position of the ring induction electrode.



Scheme 1 Membrane partitioning for TGA

Results were obtained performing dual sample analysis in a dry air atmosphere at heating rates of 20°C/min raising the temperature from 30°C to 800°C and the final content in TiO₂ is summarized in Table 7.7. The final content was calculated taking in account the weight loss due to the TiO₂ itself (its residual weight from TGA analysis is 98% at 800 °C)

Membrane ID	ZONE A	ZONE B	ZONE C	ZONE D
ID4	6.53%	9.70%	4.29%	6.84%
ID6	5.40 %	9.49%	4.90%	2.76%
ID5	6.32 %	12.25%	2.55%	1.43%

Table7. 7TiO₂ content within partitioned zone of multistructured membranes

From the results shown in TableXX it is evident that the concentration of nanoparticles is strongly related to the ring electrode position. The surface area perpendicular to the ring has a higher content in nanoparticles and this can be explained because of the induction of a more stable electric field close beneath the electrode which involves a more uniform deposition on the collector. Examples of TGA curves are reported in Figure 116 Figure 117 for the outer side of the sample and for the inner one, respectively. Figure 118 shows the final content in nanoparticles in ZONE B and ZONE D on a different tested membrane and confirms the observed trend.

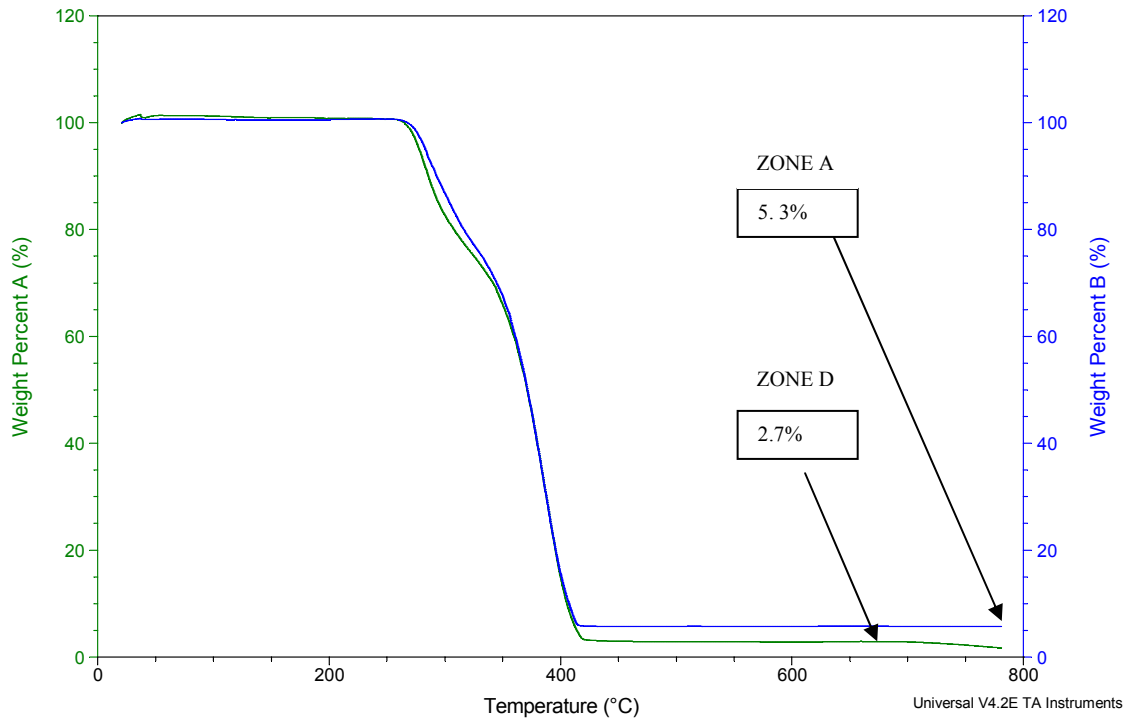


Figure 116 Thermogram of ID6 ZONE A and ZONE D

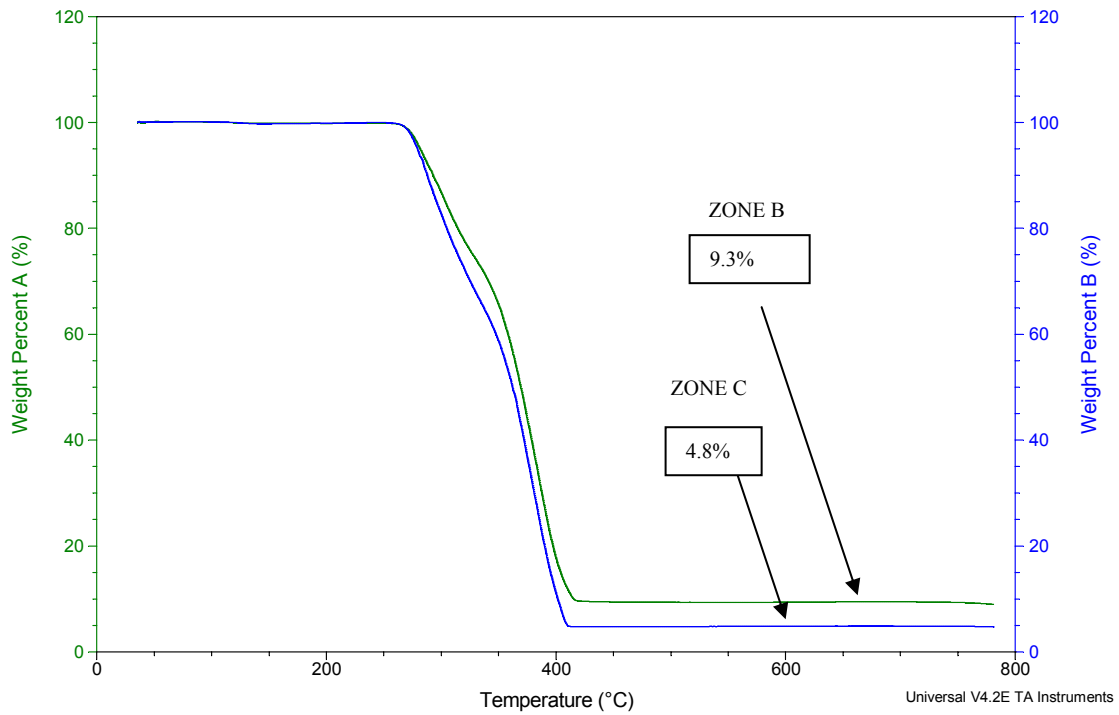


Figure 117 Thermogram of ID6 ZONE B and ZONE C

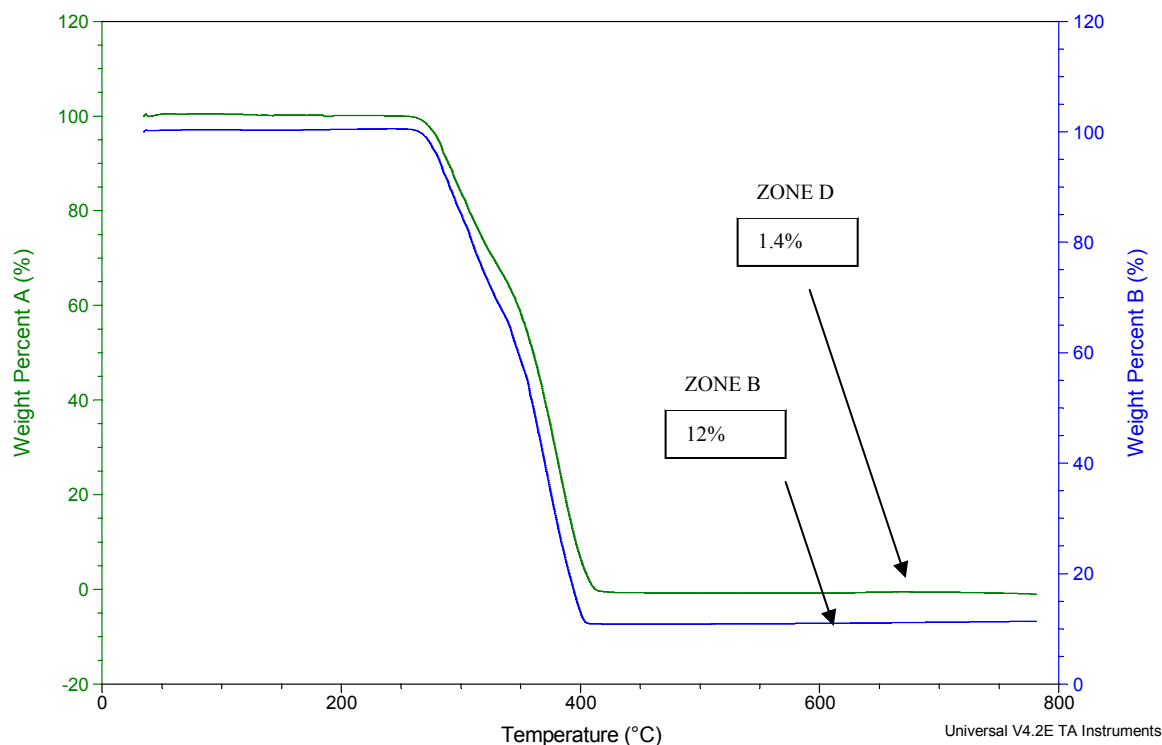


Figure 118 Thermogram of ID5 ZONE B and ZONE D

Water vapour permeability

Water vapour permeability test has been carried out in order to evaluate the performance of the processed membrane in comparison with other commercial membranes, which have a different purpose of application but they are characterized from high water vapour permeability. This test has been performed according to the Cup test method (JIS I 1099) and the measures were recorded in parallel for two samples of each membrane. Results of the permeability are reported in Table 7.8.

IDMembrane21					
	time	sample a	sample b	Permeability a	Permeability b
	[min]	[gr]	[gr]	[gr/m ² hr]	[gr/m ² hr]
	0	134.9748	128.192		
pretest	15	136.1243	129.2921	1867.77	1787.50
test	30	137.2012	130.3478	1749.80	1715.36
	45	138.2365	131.3588	1682.21	1642.73
ID Membrane22					
	time	sample a	sample b	Permeability a	Permeability b
	[min]	[gr]	[gr]	[gr/m ² hr]	[gr/m ² hr]
	0	123.7202	124.0009		
pretest	15	124.857	125.0927	1847.13	1774.01
test	30	125.972	126.0726	1811.71	1592.19
	45	127.123	127.22	1870.20	1864.36

Table 7. 8 Permeability results for two different membranes

The pretest time is necessary for membrane conditioning and then the results show a linear increase of the weight with the time and the mean water permeability has a mean value of 1800 gr/m²hr.

Results concerning two commercial membranes based on Polytetrafluoroethylene/Polyurethane and Polyester/Polyether, are summarized in Table 7.9.

	time [min]	PTFE/PU [gr]	Memb Polyester/Polyether [gr]	Perm PTFE/PU [gr/m ² hr]	Perm Polyester/Polyether [gr/m ² hr]
	0	124.2788	124.0189		
pretest	15	125.9906	128.7854	2781.42	7744.86
test	30	127.6635	133.5432	2718.22	7730.73
	45	129.3269	138.2452	2702.78	7640.06

Table7. 9 Permeability results for two commercial membranes

From the results normalized in the thickness, it has been shown the higher permeability of the multilayers membranes if compared to the commercial ones (Table 7.10). This behaviour is related to the porous structure of the multistructured membrane and this evidence represents a good property of the fabric especially because of the application it will be used for. The photocatalytic activity of TiO₂ is strongly affected from the presence of water vapour and then it is necessary to ensure the contact of the vapour to the catalyst in order to promote desorption of chemicals from the active sites.

	Polyester/polyether	PTFE/PU	Membrane
Mean thickness, μm	10	50	300
Permeabilità, gr/m ² hr	7710	2710	1800
Normalized Permeability (50 μm thickness)	1542	2710	10800

Table7. 10 Comparison of permeability of the processed membrane with two commercial membranes

7.4 Conclusion

Multilayers membranes were produced by spinning technologies. In order to achieve this purpose, it has been necessary to carry out a preliminary study on electrospinning of nanoparticles. The process has been optimized in order to get the best dispersion and uniform distribution of nanoparticles over polymeric nanofibers. Thanks to a suitable sonication time and stabilization of the nanoparticles dispersion before electrospinning we are able to deposit uniformly nanoparticles avoiding the clogging of the interfibers pores. Then the membranes produced performing alternatively electrospinning and electrospinning were studied in term of pressure drop analysis and catalytic tests. It has been revealed they are a good candidate as a filter media for air purification and protective clothes application. Further investigation are in progress to process the obtained results of pressure drop in order to compare experimental values with theoretical values and provide more information about their potential in filtration and catalysis. In fact the modelling of pressure drop

according to the Davies equation needs to be modified in order to evaluate the slip effect aforementioned, related to the fiber size ranging in the nanoscale.

CHAPTER 8 Photocatalytic activity of multistructured membranes

8.1 Introduction

Heterogeneous photocatalytic degradation of various kinds of organic pollutants using semiconductor powders as photocatalysts has been extensively studied since the increasing environmental pollution create a pressing need for new advanced solutions. Since under room temperature and air pressure, the organic pollutants could be completely degraded into CO₂, H₂O and other mineral acids by the photocatalysis method, some scholars predicted that in the near future the photocatalysis method will become one of the most effective means in dealing with various kinds of industrial wastewater as well as air purification. The principle, extensively reviewed in Chapter 3, is based on the generation of photoholes by ultraviolet irradiation and the subsequent generation of OH radicals, caused by reactions with hydroxyl groups adsorbed to the hydrophilic titania surface. These OH radicals play a key role in the oxidation of organic compounds.

Within this outline, here we focus on photocatalytic performances of multistructured membranes based on electrospun fibers and electrosprayed nanoparticles carried out in liquid phase and in gas phase. These case studies involved different problems, different experimental set up and different behaviours and they required the tweak of methods for testing the effectiveness of the multilayers membranes for this purpose, which has not been found yet in the literature. A review of the main obtained results will be presented in this section.

8.2 Liquid phase Photocatalytic activity

8.2.1 PSU/TiO₂/MgO membranes

The membrane based on electrospun PSU and TiO₂ or MgO nanoparticles, can be considered as a multifunctional system because the nanoparticles are useful not only for improving the interfibers distance but also they could be seen as a catalyst for adsorbing and detoxification of harmful airborne contaminants. At this regards, the detoxification activity of multilayers membranes (based on electrospun PSU nanofibers and TiO₂ or MgO sprayed nanoparticles) on a mustard stimulant agent (2-chloroethyl phenyl sulfide (CEPS)) was monitored by UV analysis within 60 mins (every 10 mins) at simulant concentration constant ([CEPS]=10⁻⁶ v/v in heptane).

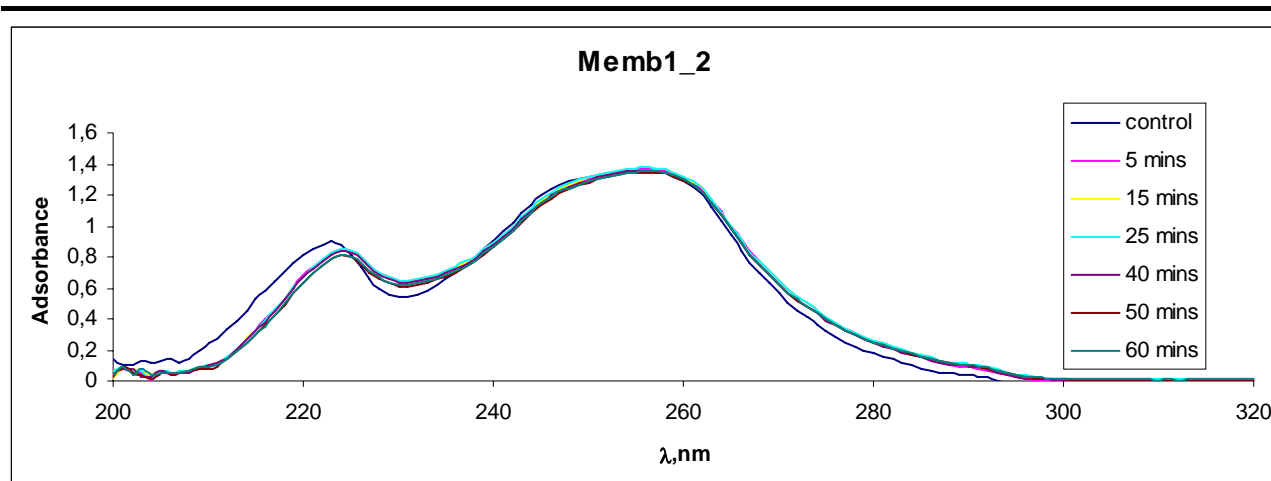


Figure 1 UV spectra of multistructured membrane with nanoparticle content of 13.1 wt %

The % CEPS decomposed has been calculated looking at the first peak at 220 +/-5 nm of UV spectra which is characteristic of CEPS (see an example in Figure 1) and the comprehensive results are presented in Figure 2. The experimental set up was based on a Petri flask where the testing membrane was dipped into a fixed amount of simulant. The UV light source was located 12 cm in front of the membrane and it was turned on, the reaction was followed within 60 mins. The standard operating conditions are summarized in Table 8.1 and before starting the experiments it has been verified that the degradation effect of the light source on the tested chemical was negligible.

Experimental variable	Standard nominal value
Initial CEPS concentration (v/v)	10^{-6}
Reaction Volume (ml)	25
Reaction Temperature (°C)	25± 0.3
Incident light intensity(mW/cm ²)	2.34± 0.23
UVsource/primary wavelenght	3×Black light fluorescent/365 nm, 8W
Solvent	Heptane

Table8. 1Summary of operating conditions for CEPS photocatalysis

As expected, the. TiO₂ nanoparticles as well as MgO nanoparticles act as a catalyst for chemical agent detoxification and this property make these multilayers membranes very attractive for this purpose. From Figure 2 it is also evident that the neat membrane adsorbs itself a non-negligible amount of CEPS and then these membranes play a double action as adsorbent and photocatalyst. Moreover tests performed on membranes based on TiO₂ nanoparticle rather than MgO nanoparticles, don't show a substantial difference with respect to the photocatalytic action on this specific chemical.

Since this analysis was performed in liquid state and in batch reactor the detoxification activity is a function of the nanoparticles content, other conditions being equal. It means, as higher the nanoparticles concentration as higher will be the % of CEPS detoxified. These promising results need further investigations in order to improve the efficiency of degradation as well as a better understanding of the detoxification mechanism.

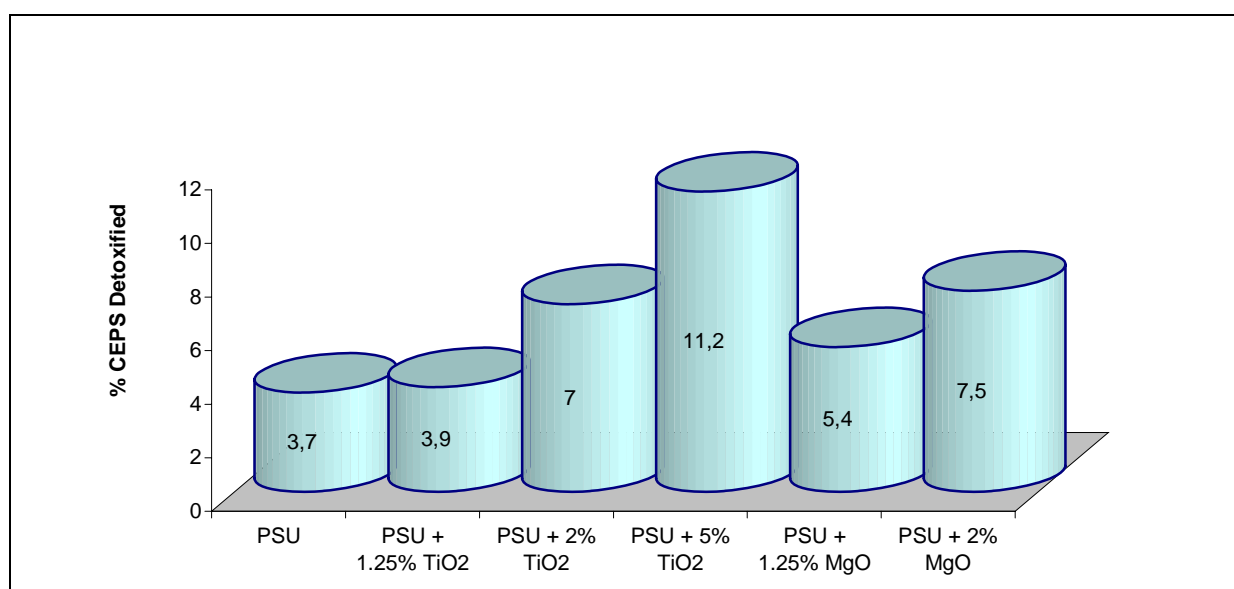


Figure 2 Percentage of CEPS detoxified

8.2.2 PANcoVAc/PMMAcoMAA/TiO₂ Membranes

PANcoVAc/PMMAcoMAA/TiO₂ based membranes were investigated as regards their ability of degradation of phenol, as the model pollutant of water, under UV illumination. The reactions were carried out in batch reactors. The operating conditions are summarized in Table 8.2 and the photocatalytic runs were analyzed using HPLC set with a two-channel UV-vis light absorption detector set at 270 nm absorbance for phenol detection. A Novapack 150 mm x 39 mm ID C18 column was used, and the applied mobile phase was 1 mL min⁻¹ of gradient chromatography grade acetonitril (Merck) and deionized water (0.055 mS) at a ratio of 70:30.

Experimental variable	Standard nominal value
Initial Phenol concentration (mg/l)	37 (4x10 ⁻⁴ M)
Reaction Volume (ml)	25
Reaction Temperature (°C)	25± 0.3
Incident light intensity(mW/cm ²)	2.34± 0.23
UVsource/primary wavelenght	3×Black light fluorescent/365 nm, 8W
Solvent	water

Table8. 2 Summary of operating conditions for phenol photocatalysis

Before starting the analysis it has been verified the negligible effect of UV light on phenol conversion and then the reaction was monitored within a time frame of 13 hours, sampling the liquid from the batch reactor every three hours. The conditioning was necessary for allowing the adsorption of the chemical on the catalyst surface and the results of the performed experiments are shown in Figure 3. The experimental data were well fitted with an exponential decay and they are very interesting if compared to the results obtained performing the same experiment on TiO₂ based paints. From the normalized results it can be observed that the conversion efficiency of the multistructured membranes is much higher of the paint conversion. This can be explained looking at the fabrication techniques used for membrane processing that allow nanoparticles uniform distribution and deposition over the electrospun nanofibers. The resulting nanoscale sizing improves the catalytic activity and makes these membranes a good candidate for environmental applications.

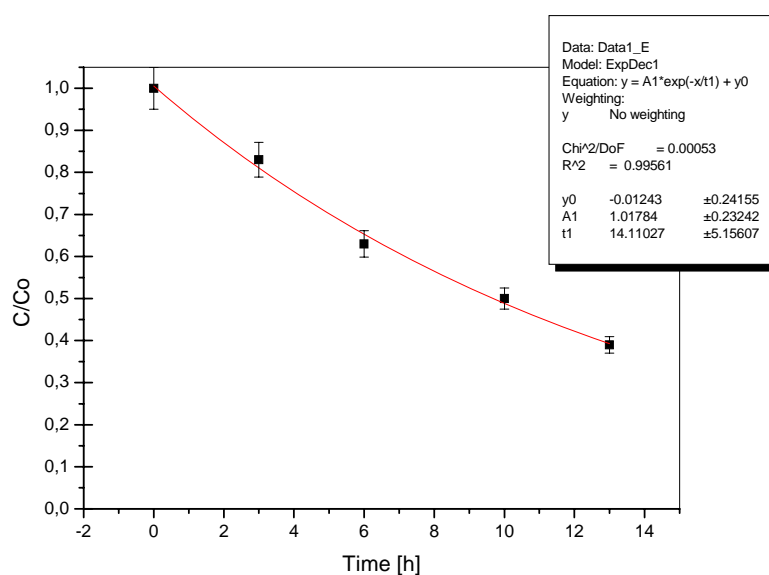


Figure 3 The scenario of phenol degradation under photocatalysis on TiO₂ based multilayers membranes

However, as it has been observed before, in liquid phase the geometry of the membrane doesn't play a fundamental role on the catalytic performances since they are dipped into the polluted solution. Moreover the structure of the membranes we deal with, supposes the flow throughout this fabric of a fluid stream, in particular a gas stream and because of this we moved to the gas phase heterogeneous photocatalysis.

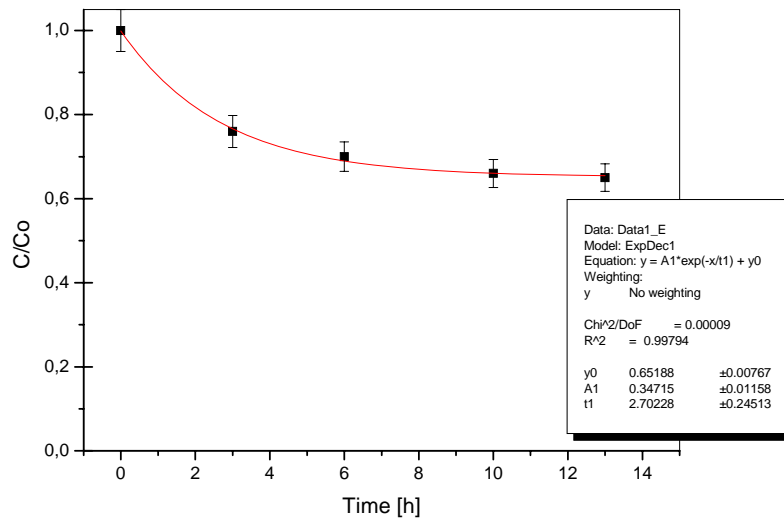


Figure 4 The scenario of phenol degradation under photocatalysis on TiO₂ based paint

8.3 Gas phase Photocatalytic activity

Heterogeneous photocatalysis represent an effective potential application of the processed multistructured membranes since the increasing interest on technology for the purification, decontamination and deodorization of waste gas streams and indoor air [315]. Particularly, photocatalytic degradation of volatile organic compounds (VOCs) is gaining more and more interest, since the emission of these compounds contribute to environmental problems, such as tropospheric ozone formation, stratospheric ozone layer depletion and global warming [316]. Moreover, many VOCs are toxic and/or carcinogenic and can cause serious odour nuisance [317]. In order to exploit the photocatalytic performances of the membranes it has been necessary to develop a proper set up for ensure reproducible operating conditions and to monitor the degradation reactions.

8.3.1 Experimental apparatus

The experimental set-up built up is shown in Figure 5 and it consists of the gas and vapour feed delivery module, the reactor and the analytical unit. The gas vapour feed rate was dependent on his vapour partial pressure at fixed temperature (monitored and kept constant thanks to a thermostatic bath). A controlled flow of Argon lapped the VOC gas vapour dispenser and then it was mixed with dry or wet air before entering the photoreactor where the membrane is positioned. The wet air was obtained bubbling the air gas through a saturator containing distilled water and the mix flows into the reactor and it is forced to pass throughout the membrane. The reactor is made of two coaxial cylinders (glass Pyrex) and the gas feed enters from the bottom, flows up throughout the membrane on the top of the inner cylinder, and then it moves along the annular region toward the reactor exit where the exhausts were discharged or sampled for chromatographic analysis.

Before starting the reaction, regardless of tested VOCs, one/two hour conditioning of the system was necessary in order to promote the adsorption of the chemicals over the active sites of the catalysts and to ensure the stationary regime. This condition has been ensure with a contaminated air stream through the reactor in the absence of UV irradiation until gas–solid adsorption–desorption equilibrium was established (typically within 1 h), i.e. until the pollutant in- and outlet concentrations were not significantly different from each other (t-test, significance level $\alpha \geq 0.05$). During conditioning, polluted gas stream flows continuously and then all the valves were closed and the UV light source, placed 5 cm over the top of the cylinder, was switched on. The outlet gas mixture was collected every 15 mins and it was separated using a PH5 capillary column (0.32mm i.d x 30 m); its composition determined by a HP G1800C GCD series II GC/MS. The recorded data were compared to the set condition at stationary regime.

After the test time of 60 mins, wet air has been allowed to flow 2/3 hours in order to promote desorption of degradation compounds, reactivate and regenerate the catalyst.

As regards the gas carrier, Argon has been chosen so as to an internal standard which not interact with the degradation reaction and at the same time a revealable compound from the GC/MS analyzer. This solution related with a gas sampling 6-port valve and sample loop make an accurate injection possible, since the experimental error of the manual injection can be avoided and it has been useful for performing quantitative analysis of pollutant concentration.

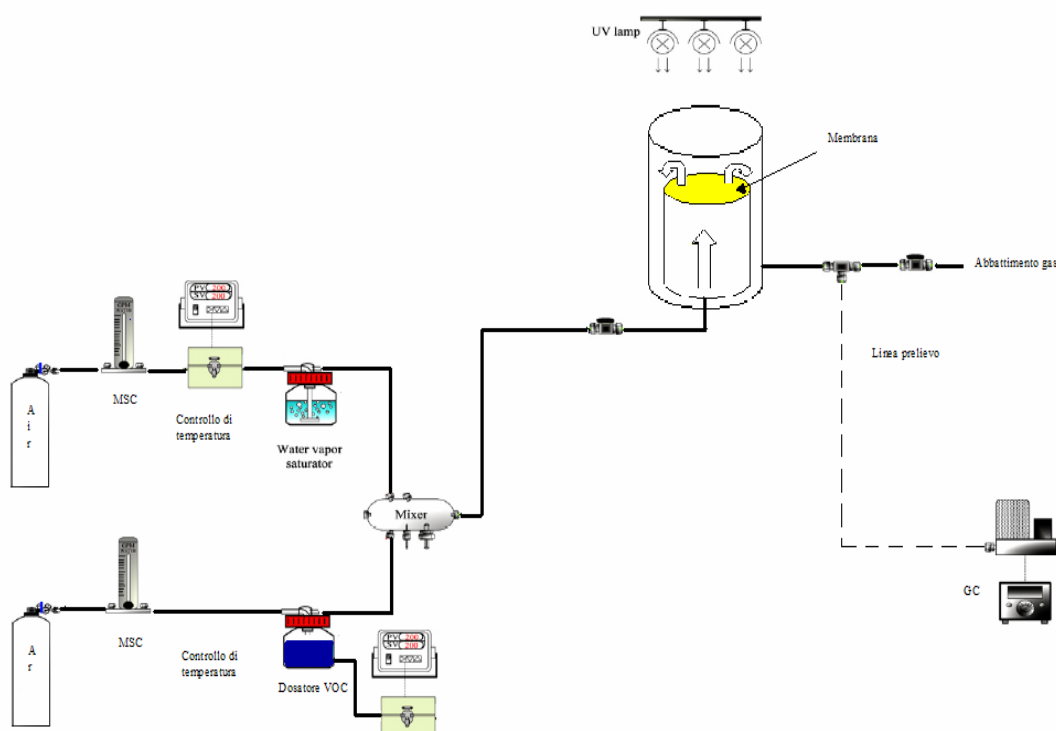


Figure 5 Photocatalytic apparatus setup

8.4 Results and discussion

8.4.1 Case study: Trichloroethylene (TCE) photo-degradation in gas phase

TCE has been widely used in industry and is commonly found in emissions from chemical processing, landfills, hazardous waste disposal, groundwater remediation sites, and even in indoor air [318]. Various treatment technologies such as absorption, adsorption, condensation, biofiltration and incineration are under investigation and/or operation to remove TCE from waste gases. However, all these traditional technologies show several drawbacks and limitations: (1) absorption and adsorption methods do not really degrade pollutants but only transfer them into a secondary liquid and solid waste stream, respectively; (2) the efficiency of condensation and biofiltration is

limited for volatile and hardly biodegradable compounds like TCE; and (3) incineration of Cl-containing compounds can result in hazardous by-products formation, e.g. dioxins [319]. Therefore, the development of advanced oxidation processes like heterogeneous photocatalysis is required to bring forward new and efficient end-of-pipe technologies. At this regard the potential application of the multilayers membranes for indoor and outdoor pollution removal, is the main reason that explains the choice of this chemical for photocatalytic test.

In order to have a complete understanding of the TCE initial concentration, it has been necessary to specify some operating conditions:

Reactor volume, V : 770cm^3 ;

Flow rate of Argon: 40 ml/min ;

Air flow: 80 ml/min ;

TCE dispenser Temperature, T : 0°C

Pressure, P_{TOT} : 1 atm

The vapor pressure of TCE as a function of the temperature can be found out from the vapour pressure chart in Figure 6 where it can be seen the Vapor Pressure of TCE, $P_i^0(T)$, is 20mmHg at 0°C , that is 0.26 atm .

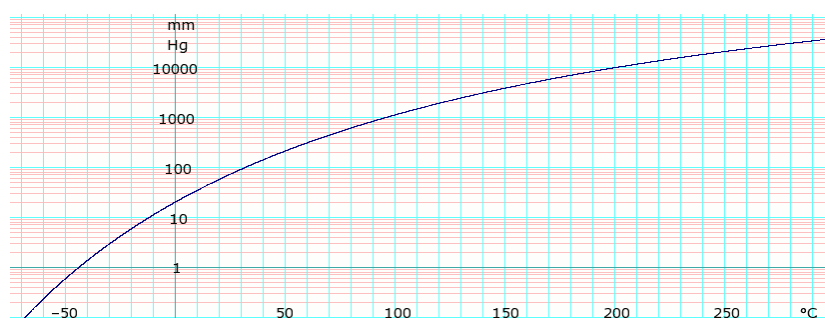


Figure 6 Vapor pressare chart for TCE

The vapor fraction y_i according to the Raoult-Dalton law is:

$$y_i * P_{\text{TOT}} = \gamma_i * x_i * P_i^0(T) \quad \text{Eq. 1}$$

where P_{TOT} is the pressure of the system, γ_i is the coefficient of activity and x_i the liquid fraction of TCE. Since the solution of TCE is pure, the coefficient of activity can be rounded to 1 and then the initial concentration of TCE in gas phase y_i is equal to 0.026, or 260 ppmv. Ppmv can be easily converted to ppm resulting 851 ppm of TCE in the Argon flow. Then, consequently to the mix with the air flow, the concentration goes down approximately to 283.8 ppm. In this paragraph the results about TCE photocatalytic degradation will be reported and discussed.

Every single membrane was subjected to a multiple photodegradation test because the purpose was to identify how many regenerating cycles are tolerated before compromising irreversibly the catalyst performances. The followed steps have been continuously monitored:

Conditioning cycle	STEP 1
Degradation cycle I	STEP 2
Regenerating/Conditioning cycleI	STEP 3
Degradation cycleII	STEP 4
Regenerating/Conditioning cycleII	STEP 5
Degradation cycleIII	STEP 6

Moreover, before performing photocatalysis tests, it has been verify that TCE oxidization was not due to the effect of UV light degradation. Figure 7 shows the recorded data within a frame time of 80 mins and it has been proved that the mean variation of TCE concentration falls into the experimental error of the analytic instrument.

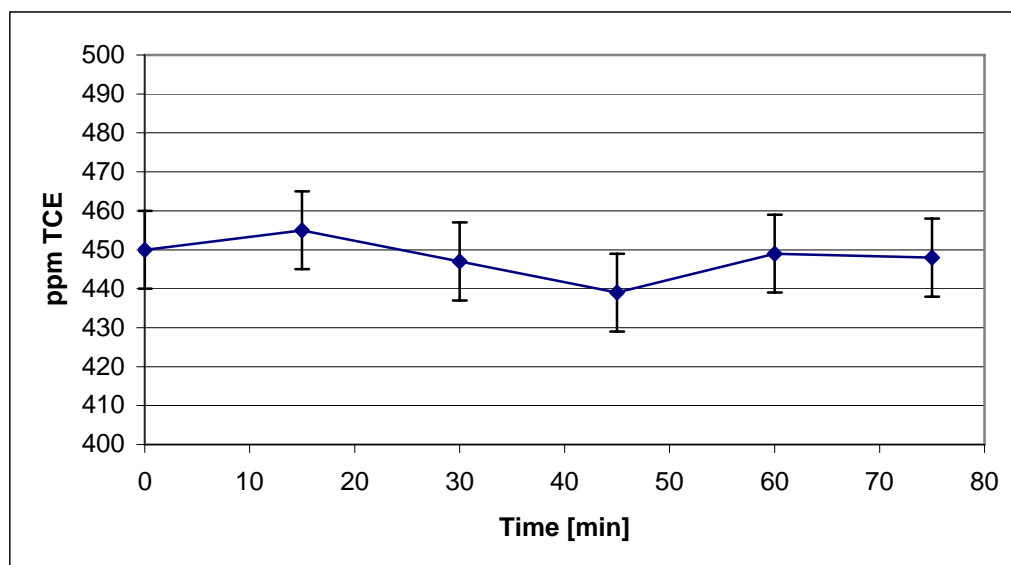


Figure 7 TCE concentration trend upon the effect of UV light

STEP1-STEP 2

The conditioning time was 2 hours, then for the first degradation test, the membrane characteristics are summarized in Table 8.3:

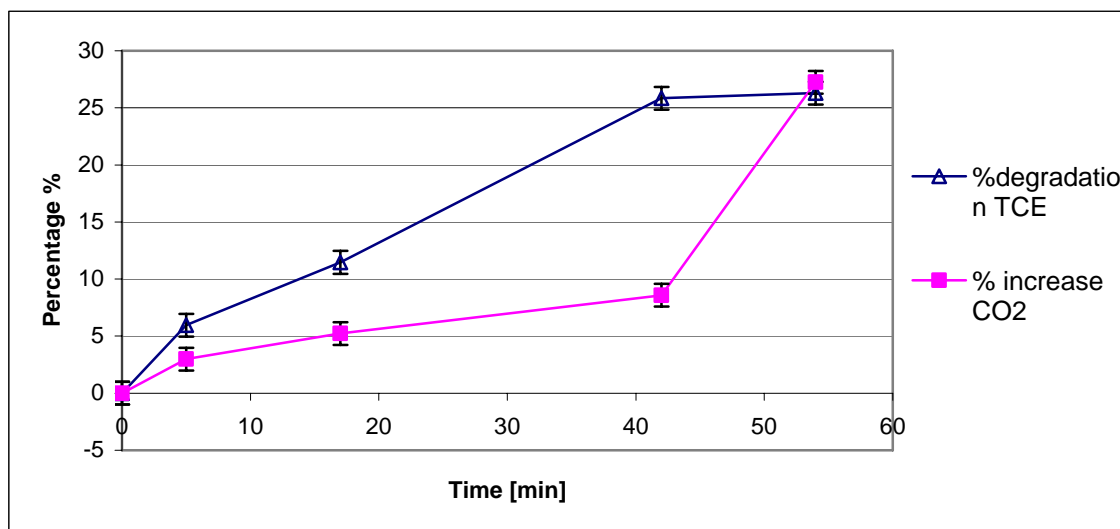
Characteristic	Value
Membrane area [cm ²]	95.7
TiO ₂ content [g]	0.22

Ratio catalyst/membrane area 0.0023
[g/cm²]

Table8. 3 Membrane features

Data obtained from degradation test are reported (Table 8.4) as the ratio of the intensity of GC peak to the internal standard intensity (Ar) measured at their characteristic mass to charge ratio (m/z). The graphical trend of degradation is shown in Figure 8

	time [min]	Ar/TCE	% degradation	Ar/CO2	%generation
Riferiment UV-off	0	890	0	268	0
UV-on	5	943	5.96	260	2.98
UV-on	17	992	11.46	254	5.22
UV-on	42	1120	25.84	245	8.58
UV-on	54	1124	26.29	195	27.24

Table8. 4 Data of TCE degradation test STEP2**Figure 8 The scenario of TCE, CO₂ under 1st cycle of photocatalysis**

With respect to the initial concentration of TCE (283.7 ppm), it has been observed a decrease of 26% that means 335.65 ppm of TCE oxidized per gram of catalyst.

STEP 3-STEP 4

The same membrane previously tested was then regenerated (12h time) and put before conditioning of 1 h. At stationary regime the light source was switched on and the photocatalysis monitored in the time frame of 60 mins. Results of the percentage of removed TCE and the increase of CO₂ are shown in Table 8.5

	Time [min]	Ar/TCE	%degradation	Ar/CO ₂	%generation
Riferiment					
UV-off	0	355	0	242	0
UV-on	18	396	11.55	231	4.54
UV-on	26	434	22.25	219	9.50
UV-on	56	421	18.59	196	19.01
UV-on	94	426	20	162	33.06

Table8. 5 Data of TCE degradation test STEP4

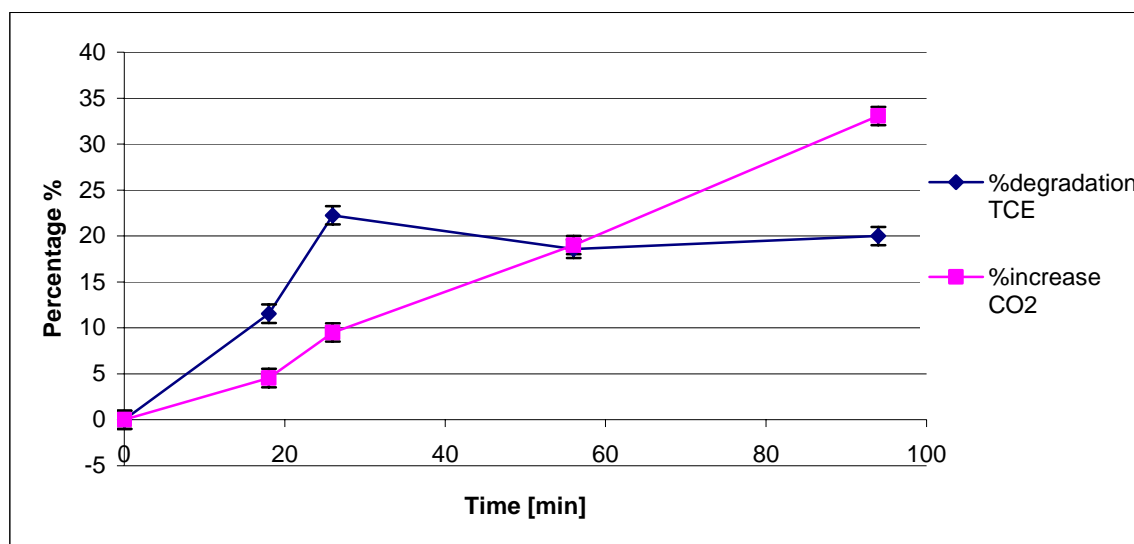


Figure 9 The scenario of TCE, CO₂ under 2nd cycle of photocatalysis

TCE initial concentration (283.7) has been brought down of 22% and representing the photocatalytic activity per gram of catalyst, it is equivalent to 287.3 ppm/gr TiO₂. The worst catalytic performance are consequently related to the poisoning of the catalyst because the regeneration is not able to recondition at all the active sites.

Once the effectiveness of the membranes has been verified, we move in detail towards the identification of oxidization intermediate as suggest from the literature [320]. Dichloroacetyl chloride (DCAC) and phosgene have been shown to be the main organic intermediates while CO₂, CO, HCl and Cl₂ are some other inorganic products of complete TCE oxidization. DCAC and phosgene were detected by mass spectrometry looking at their characteristic mass to charge ratio (m/z), respectively.

According to the following membrane features (surface area = 90.44 cm², TiO₂ grams = 0.0558 gr, density of catalyst = 0.000617 gr/ cm²) photocatalytic tests were carried out and results of the first cycle (STEP 1- STEP 2) are reported in Table 8.6.

	Time [min]	Ar/TCE	%degradation	Ar/phosgene	%increase phosgene	Ar/DCAC	%increase DCAC
Riferiment UV off	0	571	0	471	0	548	0
UV on	4	574	0.525	469	0.424	543	0.912
UV on	15	595	4.203	470	0.212	530	3.284
UV on	30	600	5.079	471	0	522	4.744
UV on	45	605	5.954	470	0.212	540	1.459

Table8. 6 Data of TCE degradation test STEP2

The scenario of TCE, DCAC and phosgene degradation/formation is summarized in Figure 10. TCE initial concentration was decreased of 6% corresponding to $0.235 \text{ cm}^3/\text{gr TiO}_2$, i.e. 305 ppm/gr TiO_2 .

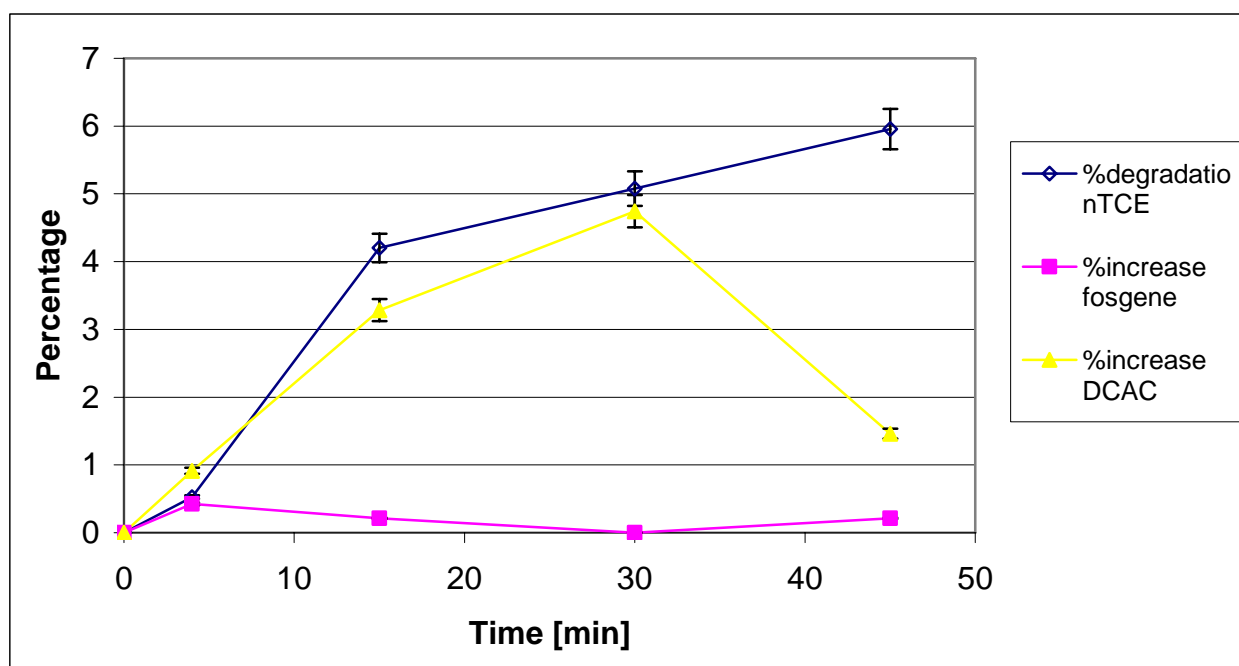


Figure 10 The scenario of TCE, DCAC and phosgene under photocatalysis

Further photocatalytic tests were carried out for evaluating the regeneration effects on the catalyst and, as expected, the catalytic efficiency decreased of 23% since the results showed a degradation of 62 ppmTCE/gr TiO_2 .

In conclusion the maximum amount of TCE photooxidized with the multistructured membranes in the aforementioned conditions has been found to be 305 ppm/gr TiO_2 .

All the obtained data were then normalized with respect to 1 gr of catalyst, electrospayed with a final density $0.0023 - 0.0037 \text{ gr}/\text{cm}^2$, a TCE initial concentration of 450 ppm in the volume reactor of 770 cm^3 . A representative scenario of TCE, DCAC, phosgene and CO_2 under photocatalysis is shown in Figure 11. The reaction pathway of TCE coupled with DCAC can be described as the following channel, $\text{TCE} \rightarrow \text{DCAC} \rightarrow \text{Products (phosgene and } \text{CO}_2)$ in which the formation of DCAC is followed by the degradation of TCE. As regards phosgene, the more oxygen content, the

decreasing yields of phosgene appear while TCE is used as the starting material. This indicates that the formation of phosgene is likely relevant to the DCAC destruction rather than that of TCE [320]. TCE degradation mechanism is proposed in Figure 12 and it involves chain reactions initiated by the Cl atoms instead of OH radicals. Afterward, the Cl atoms is expected to react with $\text{CHClCCl}_2\bullet$ to form $\text{CHCl}_2\text{CCl}_2\bullet$ [321]. $\text{CHCl}_2\text{CCl}_2\bullet$ then combines with the charged radical-ions ($\text{O}^{2-\bullet}$) to form

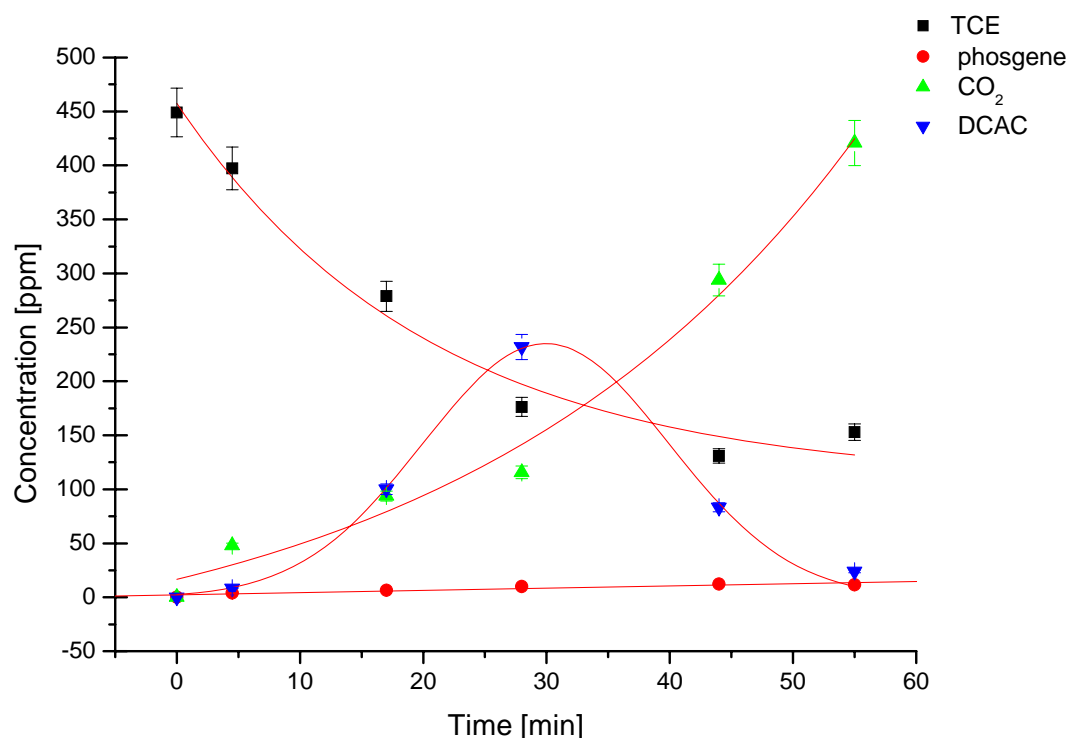


Figure 11 The scenario of TCE, DCAC, phosgene and CO₂ under photocatalysis

$\text{CHCl}_2\text{CCl}_2\text{OO}\bullet$ which was followed by the well-known Russel mechanism [322], causing the generation of the Oatom- centered radicals ($\text{CHCl}_2\text{CCl}_2\text{O}\bullet$). The Cl-elimination of resulting $\text{CHCl}_2\text{CCl}_2\text{O}\bullet$ leads to the formation of CHCl_2COCl (DCAC) while the C–C bond can rupture to formed phosgene (COCl_2) and dichloromethyl radicals ($\text{CHCl}_2\bullet$) in which the reaction pathway are channel (7) and channel (8a), respectively [321,323,324]. Sanhueza et al. [321] also suggested that channel (7) is more favourable and chlorine radical initiated destruction of TCE. As concerns CO₂, the final stoichiometric concentration for a complete oxidation of TCE should be 560 ppm, according to the proposed mechanism. From experimental evidence $[\text{CO}_2]=425$ ppm and this value is significant if we consider that the theoretical one requires a complete degradation of the intermediates, such as DCAC and phosgene. An interesting result regards the concentration trend for DCAC: the fitting curve has a maximum, after 30 mins from the beginning of the reaction and

then its concentration falls down, meaning that there is a threshold value over which the channel (9) is more favourable and this involves an increase of $[\text{CO}_2]$.

The regeneration effect has been evaluated performing three regenerating/conditioning cycles on the membranes alternatively to degradation test. Results of the conversion of TCE in those cycles is shown in Figure 13 and it has been pointed out that after three cycles the conversion falls down of 50% and then it is advisable to change testing membrane after the second study. This behaviour is related to the incomplete removal of the intermediates from the active sites of the catalyst that result non available for any further bond and it means that some intermediate has a poisoning effect on the surface catalyst.. A solution to this problem could be the choice of more efficient catalyst, different from the commercial one, in order to improve its durability and efficiency of degradation.

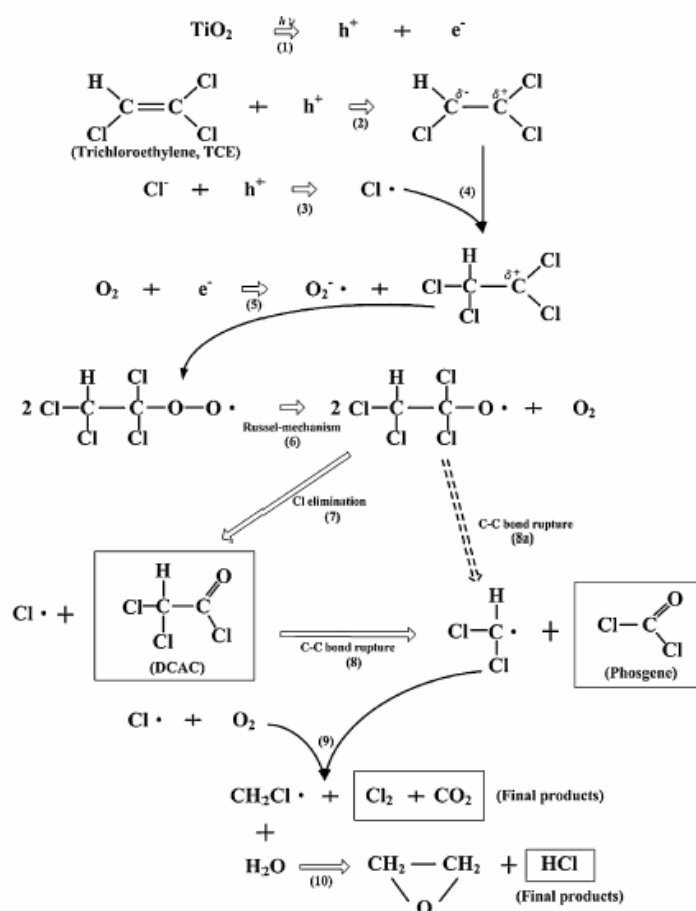


Figure 12 TCE photoxidation mechanism proposed according to the literature.

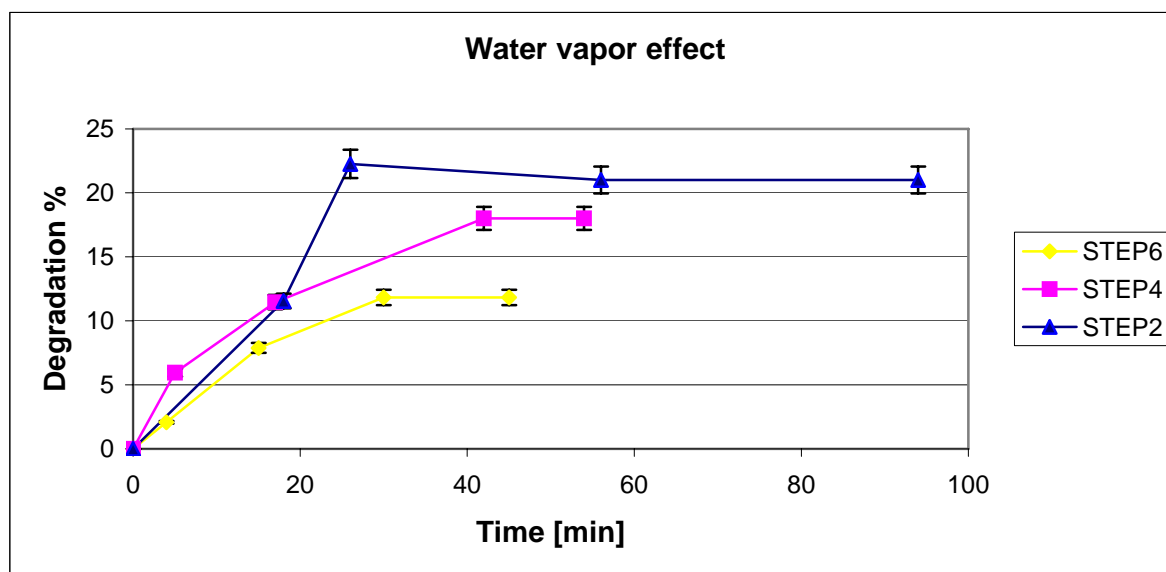


Figure 13 Regenerating effect on the degradation % of TCE

8.4.2 Case study: Acetone photo-oxidation in gas phase

From natural pollution sources, acetone is mainly produced via oxidation of humic substances and it occurs naturally as a metabolic by-product of plants and animals while from artificial pollution sources acetone is widely used as solvent for fats, oils, waxes, resins, rubbers, plastics and pharmaceuticals. Indoor air, the presence of acetone is due to the use of domestic materials and products as paints and cleaning products. Moreover, since the photocatalytic activity of semiconducting nanomaterials, such as TiO_2 nanoparticle, is strongly related to the chemical structure of the tested pollutants, in this work we studied the catalytic performances of the multilayers membranes based on electrospun nanofibers and electrospayed nanoparticles against this common air pollutant.

The experimental tests were performed according to the aforementioned conditions in batch reactor, as shown in Figure 5. the operating conditions were:

Reactor volume, V : 770cm^3 ;

Flow rate of Argon: 40 ml/min;

Air flow: 80 ml/min;

Acetone dispenser Temperature, T : 0°C ;

Pressure, P_{TOT} : 1 atm.

The initial concentration in vapour phase of acetone was calculated according the thermodynamic, thanks to the Raoult-Dalton law and to the Antoine equation:

$$\log_{10} P_i^0(T) = A - [B / (T + C)]$$

with $P_1^0(0^\circ\text{C}) = 9.3$ KPa, $A = 6.25478$ KPa, $B = 1216.69$ KPa, $C = 230.275$ KPa. The resultant initial concentration of acetone in the Argon stream is $y_{\text{Ac}} = 930$ ppmv or 1348.5 ppm. The final y_{Ac} in the gas stream results $y_{\text{Ac}} = 449.5$ ppm.

Whenever from the literature [325] it has been reported a negative effect of water vapour on the catalytic performances, it has been chosen to carry out the same steps conditioning/regenerating cycles in order to have comparable results.

The membrane features are summarized as follows:

Characteristic	Value
Membrane area [cm^2]	78.8
TiO ₂ content [g]	0.2898
catalyst density [g/cm^2]	0.00371

The analytes were detected in the same way previously exposed and Figure 15 reports the characteristic mass to charge ratio (m/z) detected by mass spectrometry [326].

Before performing photocatalysis tests, it has been verified that Acetone oxidization was not due to the effect of UV light degradation. Figure 14 shows the recorded data within a frame time of 80 mins and it has been proved that the mean variation of Acetone concentration falls into the experimental error of the analytic instrument.

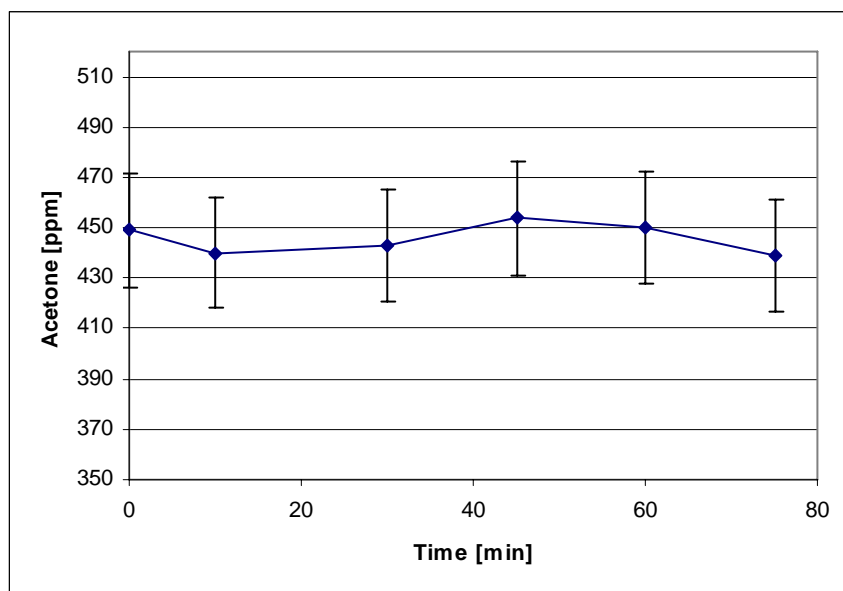


Figure 14 Acetone concentration trend upon the effect of UV light

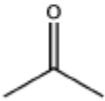
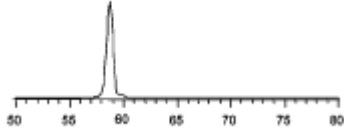
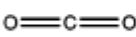
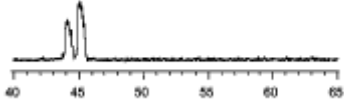
Molecule	Formula	Structure	Protonated Parent Ion [m/z]	Proton Affinity [kJ mol ⁻¹]	CIMS Spectra
Acetone	C ₃ H ₆ O		59	812	
Carbon dioxide	CO ₂		45	540.5	

Figure 15 Analytes detailed properties.

All the tests were performed on three membranes samples and the followed steps have been continuously monitored:

Conditioning cycle	STEP 1
Degradation cycle I	STEP 2
Regenerating/Conditioning cycleI	STEP 3
Degradation cycleII	STEP 4
Regenerating/Conditioning cycleII	STEP 5
Degradation cycleIII	STEP 6

STEP 1-STEP 2

The conditioning time was 2 hours and the results of the first degradation test are reported in Table 8.7 as the ratio of GC peak intensity of the internal standard to the analytes, as well as the percentage of degradation/formation of Acetone and CO₂, respectively.

First degradation cycle analysis					
	Time [min]	Ar/Ac	%degradation Ac	Ar/CO ₂	%increaseCO ₂
Riferiment	0	632	0	503	0
Riferiment	0	645	0	511	0
Riferiment	0	626	0	487	0
UV on	4	673	6.825	510	1.1
UV on	16	677	7.460	492	1.6
UV on	36	672	6.666	414	17.2
UV on	60	684	8.571	366	26.8
UV on	74	680	7.936	312	37.6
UV on	93	679	7.777	286	42.8
UV on	120	650	3.174	214	57.2
UV on	140	643	2.063	204	59.2
UV on	210	640	1.587	164	67.2

Table8. 7 Data of acetone degradation test STEP2

The graphical trend of degradation is shown in Figure 16.

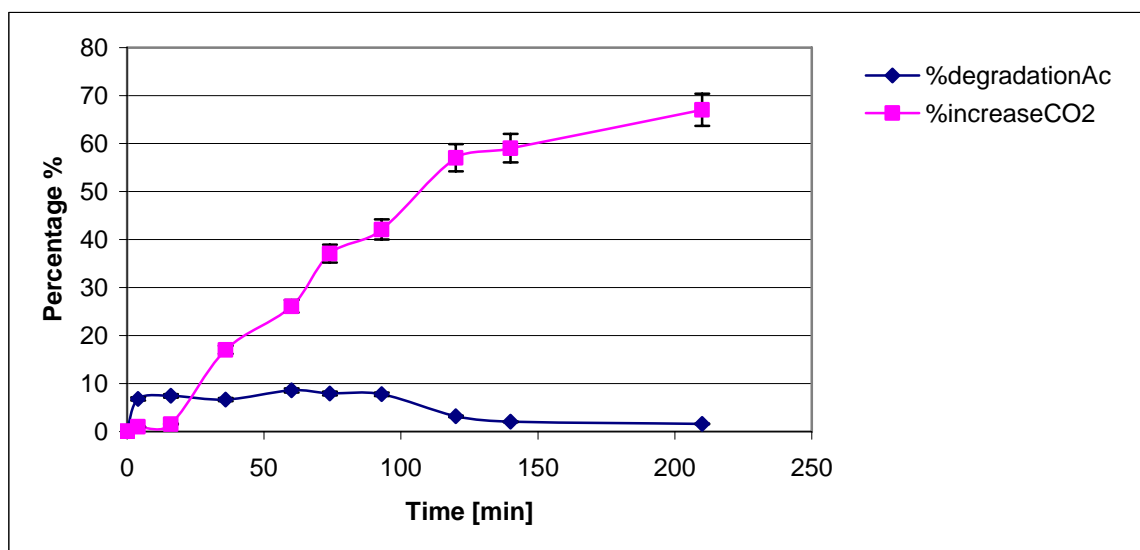


Figure 16 The scenario of Acetone, CO₂ under 1st cycle of photocatalysis

With respect to the initial concentration of Acetone, it has been observed a decrease of [Acetone] lower than 10% while the CO₂ grows up 60% from the initial content.

STEP 3-STEP 4

The same membrane previously tested was then regenerated (12h time) and put before conditioning of 1h. At stationary regime the light source was switched on and the photocatalysis monitored in the time frame of 60 mins. Results of the percentage of removed Acetone and the increase of CO₂ are shown in Table 8.8.

Second degradation cycle analysis					
	Time [min]	Ar/Ac	%degradation Ac	Ar/CO ₂	%increase CO ₂
Riferiment	0	589	0.00	464	0.00
UV on	10	652	10.70	480	3.45
UV on	17	664	12.73	419	9.70
UV on	30	668	13.41	378	18.53
UV on	60	643	9.17	298	35.78
UV on	75	651	10.53	259	44.18
UV on	90	650	10.36	204	56.03

Table8. 8Data of acetone degradation test STEP4

From this second degradation cycle, the percentage of degradation increase up to 13% and then after 60 mis it tends to stabilize itself at 10% of conversion, as suggest in Figure 17. If the result is

compared to the previous one, an effective increase of the conversion has been noticed and a third degradation cycle has been necessary before gaining conclusions.

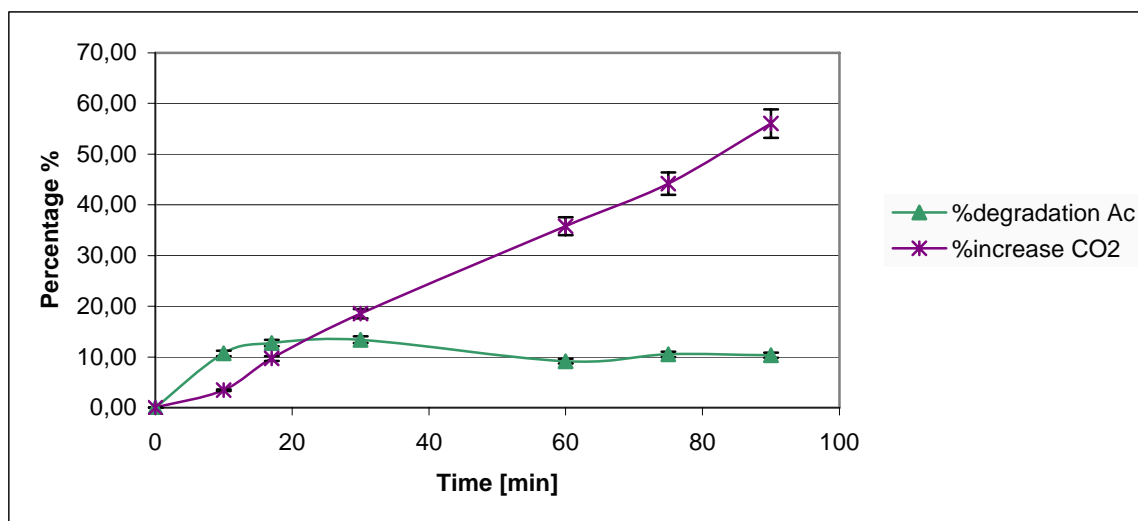


Figure 17 The scenario of Acetone, CO₂ under 2nd cycle of photocatalysis

STEP 5- STEP 6

Recorded data from the third degradation cycle are summarized in Table 8.9. It has been pointed out a maximum conversion of acetone equal to 14% and then it stabilized at 12%. In this case the maximum concentration has been reached later than the previous cycles, but it was slightly increased as we can see in Figure 18 where the time trend shows a shift in the maximum conversion time to 100 min rather than the second or first cycle where it was found to be within 60 mins.

Third degradation cycle					
	Time [min]	Ar/Ac	%degradation Ac	Ar/CO ₂	%increase CO ₂
Riferiment	0	579	0	432	0
UV on	4	612	5.7	427	1.15
UV on	10	615	6.21	395	8.56
UV on	20	608	5.00	297	31.25
UV on	45	623	7.59	258	40.27
UV on	60	635	9.67	246	43.05
UV on	82	654	12.95	213	50.69
UV on	100	661	14.16	206	52.31
UV on	122	651	12.43	178	58.79

Table8. 9 Data of acetone degradation test STEP6

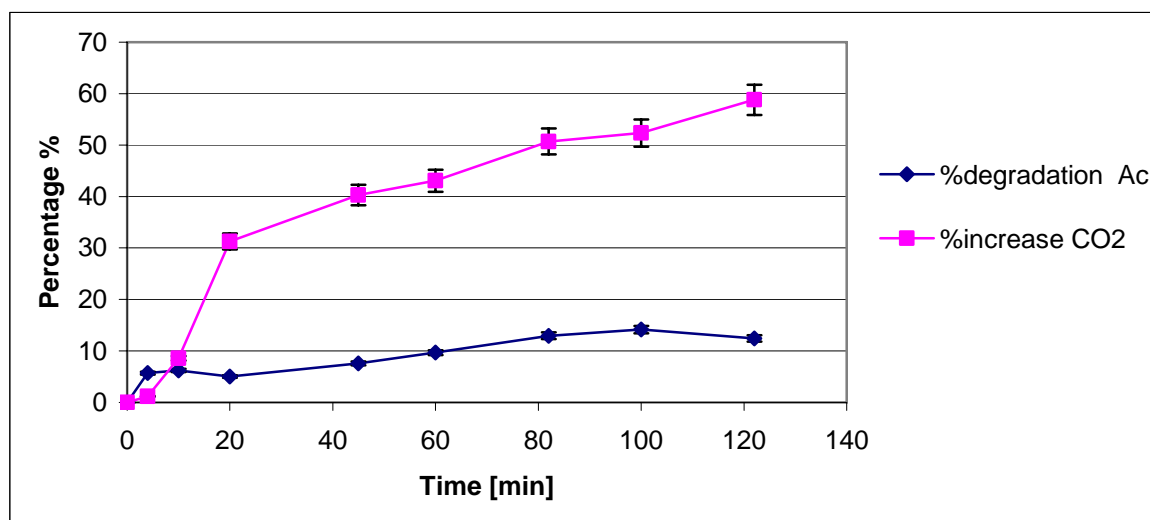


Figure 18 The scenario of Acetone, CO₂ under 3rd cycle of photocatalysis

All the recorded data were normalized with respect to 1 gr of catalyst and it has been found to be 0,131 cm³ of oxidized acetone per gram of TiO₂ catalyst, i.e. 171 ppm Ac./gr TiO₂. This results is the evidence that the photocatalysis performed in the aforementioned conditions is more efficient for TCE, even if its mechanism of degradation is multi-step and its chemical structure is definitely more complex than acetone. The scenario of acetone and CO₂ under photocatalysis is plotted in Figure 19. Looking at acetone concentration, it has been observed an exponential decay till a pseudo constant value has reached. As regards CO₂, a change on the line slope can be seen from data at 30 mins and this trend needs further investigation in order to explain the phenomena. However it should be emphasized that the acetone conversion is not followed by an instant formation of CO₂ and this result means the CO₂ increase has a delay in analyte detection. In order to explain this behaviour it is necessary to take a look at the heterogeneous catalysis steps and in particular at the rate-limiting step, which could be the degradation reaction as well as the desorption rate of the analytes. The temperature dependence of these steps could be useful to understand which is the rate limiting step. The degradation reaction depends on the temperature according to the Arrhenius equation while the desorption rate has a temperature dependence in the form $T^{3/2}$ [327]. Experiments performed at different temperatures will help for a complete explanation of the kinetics of reaction. However in this case the desorption should be promoted from the wet air stream during the regenerating step, but further experiments will make it clear.

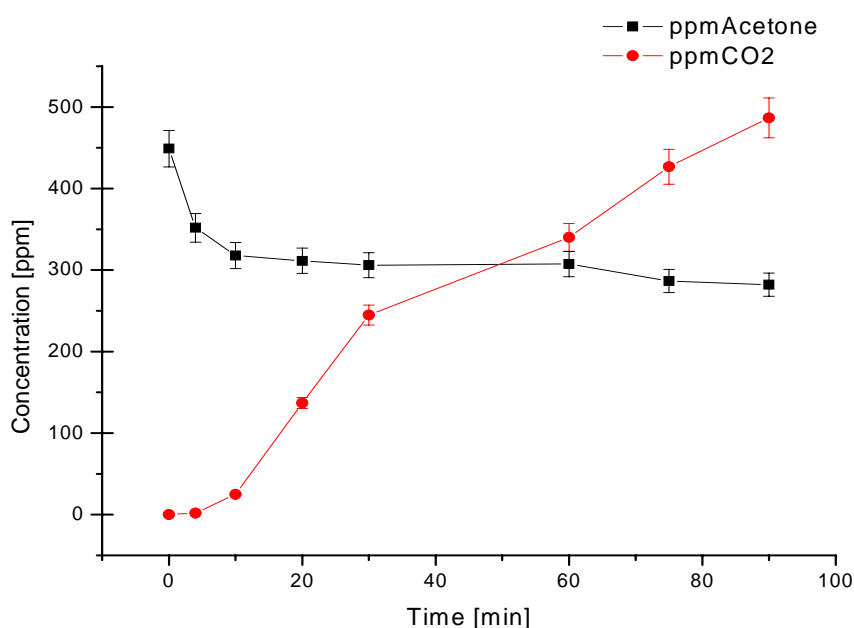
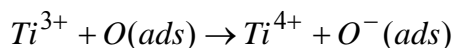
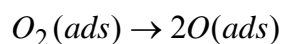
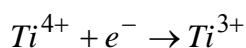
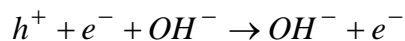
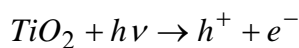


Figure 19 Trend of concentrations during acetone photooxidation

The absence of intermediates during the degradation suggested the simple mechanism of complete mineralization of acetone to CO₂ and water according to the scheme proposed in literature [328]:

1. TiO₂ Photoactivation:



2. Photocatalytic reaction between the reactive species O⁻(ads) and the adsorbed Acetone



Table 8.10 summarizes the theoretical-stoichiometric content that should be formed from a complete degradation of acetone. It can be observed that at 90 min of reaction there is a good agreement between theoretical and experimental data, but looking at the previous ones the experimental data show a delay in detection of CO₂, as suggested before.

CO ₂ experimental [ppm]	CO ₂ theoretical 1Ac=3CO ₂ [ppm]	time [min]
0	0	0
1.93	291.40	4
24.71	393.51	10
137.03	412.79	20
244.80	429.31	30
340.19	425.17	60
426.65	487.29	75
486.79	500.94	90

Table 8. 10 Experimental vs. theoretical CO₂ detection during acetone photooxidation

As regards the water vapor effect, water is thought to affect photo-oxidation reactions on TiO₂ in two primary ways: it enhances reactivity by supplying OH groups for radical-initiated chemistry and it poisons reactivity by blocking key active sites. In particular the competitive interaction between acetone and water for surface sites on TiO₂ should result in a negative effect of acetone photo-oxidation rates since it is inhibited when water is present in the reactant mixture [325]. However from experimental evidence it has been observed the opposite behaviour as shown in Figure 20, that is the higher conversion of acetone as the higher number or regenerating cycles which allow the removal of the analytes as well as the supply of OH groups.

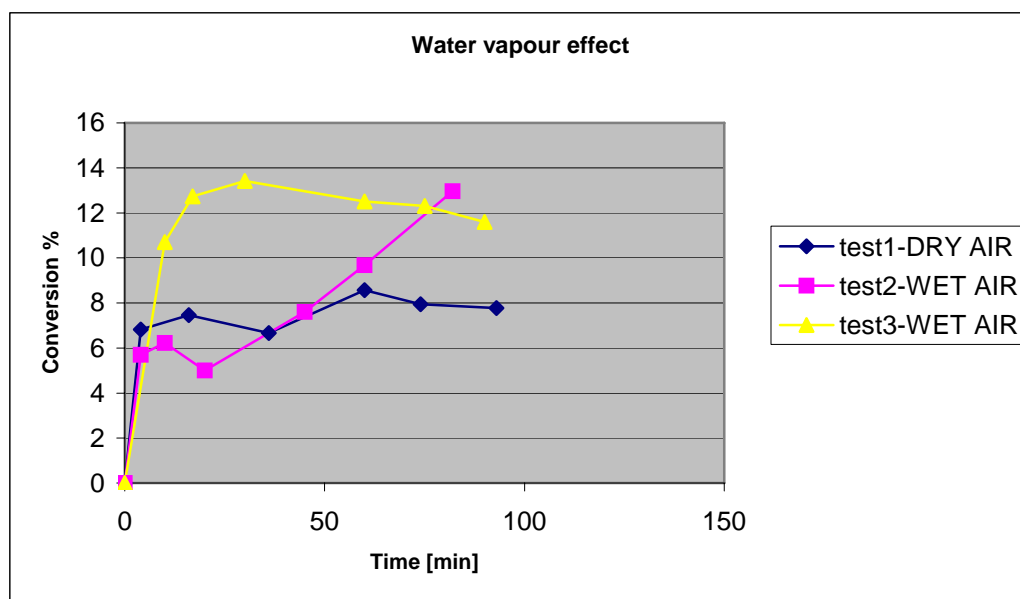


Figure 20 Water vapour effect on acetone photooxidation

Comparing the catalytic performances of the TiO₂ on the tested chemicals, it can be gathered that the photo-oxidation efficiency is strongly related to the chemical structure of the chemicals and in Figure 21 results of the analyzed compounds have been reported. The TCE degradation is double the degradation of acetone and this could be related to the poisoning of the catalyst and especially to the different affinity to the catalyst.

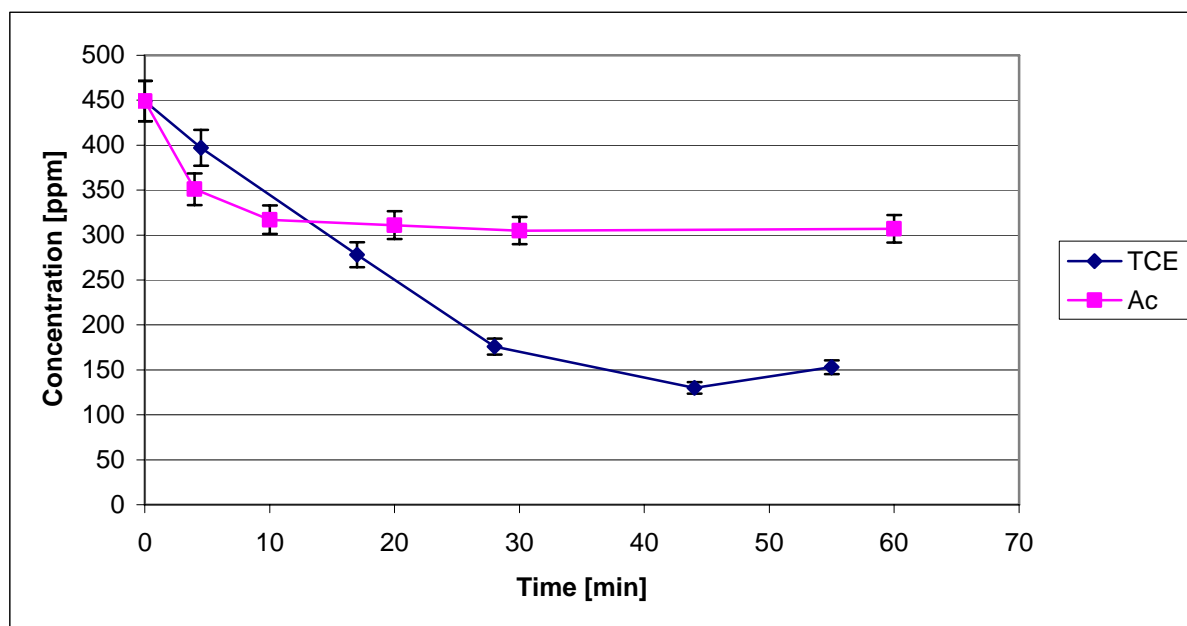


Figure 21 Comparison of photooxidation of TCE and acetone, all the conditions being equal.

Conclusions

This work explored the fabrication and characterization of multilayer membranes based on EHD technologies for multipurpose filtering applications. The main goal of this project was the implementation of reproducible method for combining conveniently nanofibers and nanoparticles on the same media. The first have enabled new levels of filtration and environmental clean up performances in a broad range of applications since they have proven to be a good candidate for promoting a significant increase in filter efficiency and more contaminate holding capacity. On the other hand nanoparticles of semiconducting materials (TiO_2) present photocatalytic properties and they may involve VOCs degradation at room temperature.

RSM has been shown to be a valid tool for performing the optimization of electrospinning process. Two systems were analyzed, Polymer/solvent system and Polymer/solvent/salt system and the latter gave information about the parameters effect and interaction of factors on the response.

According to the response surface analysis performed on the Polymer/solvent system, it has been pointed out that the response, which is the mean fiber diameter, falls into the microscale range. In order to move to the nanoscale we decided to turn the solution properties, in particular surface tension and conductivity. Because of this the Polymer/solvent/salt system has been studied and the effect of 4 factors (A:Voltage, B:[PMMACoMAA], C: [LiCl], D:flow rate) and their interactions effect on the response (mean fiber diameter) have been evaluated.

According to the screening experiments, from a Box-Behnken design we moved to a D-optimal design for the study of the response as a function of process parameters. The Quadratic model results appropriate for representing this system. The significant model terms include the single factors and interaction AC, AD, BC, CD.

As suggest from the literature, an increase of applied voltage generally results in a reduction of the mean fiber diameter of electrospun nanofibers while the increase of flow rate has the opposite effect. For low applied voltage, an increase of flow rate (AD interaction) results on the smaller fiber diameter and this behaviour is inverted after the saddle point on the response surface. This can be explained if we consider that for every applied voltage there is a fixed dragging rate which moves the forming-fiber toward the collector. When the feed rate of polymer solution is higher, an excess of electrostatic charges will be cumulated in the solution at the tip of the needle resulting on whipping motion and jet splaying and consequently these instabilities enhance diameter reduction.

As regards [LiCl]-applied voltage interaction (AC) (other controllable variables being equal in the mean level), the contour plot in shows how an increase of voltage, at a fixed salt concentration, affects the mean diameter. If the salt concentration is below 0.2% by weight, as the applied voltage increase, the smaller fiber diameter is obtained (especially at low level of [LiCl]). Above 0.2%w the

trend changes and the higher is [LiCl], the higher is the fibers diameter obtained by raising the applied voltage. This trend could be explained if we consider that out of a specific range, elastic forces arising from solution viscoelasticity or solvent evaporation may intervene under certain operating conditions to arrest the jet prematurely with larger diameter.

As suggested from the screening experiments, polymer concentration, strictly connected to the elastic forces arising from solution viscoelasticity, play a fundamental role in electrospinning process and it often hides the interactions among other factors. Polymer concentration seems to be independent from salt concentration (BC interaction) and then it represents the main factor affecting the nanofiber diameter.

Salt concentration mainly affects the conductivity of the polymer solution. Results about salt concentration- flow rate (CD) interaction it has been shown once again that salt concentration of 0.2%w represents a sort of limit beyond which no more effects can be detected on the response. If we work below this threshold value, an increase of flow rate probably induces the rapid growth of the whipping instability during electrospinning, which is responsible for massive stretching of the fluid jet and concurrent decrease in the jet diameter. This reduction in diameter implies both reduced diffusion length and increased contact area with the surrounding fluid (air), and provides greater opportunity for solvent evaporation and jet solidification in the whipping regime.

This case study needs process optimization in terms of minimization of the response. Thresholds for the response are provided to get the desirability equation to work properly. The assignment of optimization parameters has been done in order to minimize every controllable variable, except the flow rate which is set to be maximized. The optimum solution has been chosen for obtaining a fiber diameter size ranging from 300nm to 370 nm and this parameters configuration will be used for moving to the fabrication of multistructured membranes.

The obtained and characterized membranes have been shown to have a photocatalytic action both in liquid phase and in gas phase. Results in liquid phase suggested that the geometry of the catalytic system does not affect the percentage of detoxification that is a function just of the nanoparticles amount. Gas phase experiment were carried out choosing Trichloroethylene (TCE) and Acetone as pollutants. It has been performed the degradation analysis exploring the membranes regenerating effect and the affinity of the catalyst to the chemicals. TCE oxidation proceeds throughout a complex mechanism with intermediate formation and the maximum conversion has been found to be about 23% and it increases with the regenerating cycles. As regards acetone, its degradation follows a simple mechanism of mineralization to CO₂ and H₂O and the oxidation is roughly 14%. The effect of regenerating cycles has been performed, even if the literature suggested a poisoning effect of the water vapour molecule by blocking the active sites. Experimental evidences showed

that prevail the positive effect of water vapour which enhances reactivity by supplying OH groups for radical-initiated chemistry.

Since preliminary results presented here showed the potential of these membranes, further experiments are necessary to improve and complete the present work. A future perspective work will see the photocatalytic optimization, varying the catalyst especially with doped-TiO₂ which is activated by UV visible light, as well as the design of a proper reactor for improving the residence time of the gas stream over the tested membranes. Moreover this kind of multistructured membranes will be tailored for higher temperature catalysis in order to have a broader range of applications in the industrial field.

References

1. A Jaworek A. Krupa J. Aerosol Sci., **30**, 873 (1999).
2. S. Ramakrishna, K. Fujihara, *An Introduction to Electrospinning and Nanofibers*. World Scientific Publishing Co. Pte. Ltd. (2005)
3. D. Li, Y. Xia, Adv. Mater. **16**, 1151 (2004)
4. T. Ondarcuhu, C. Joachim, Europhys. Lett. **42**, 215 (1998)
5. C. Martin, Chem. Mater. **8**, 1739 (1996)
6. J. D. Klein, R. D. Herrick, D. Palmer, M. J. Sailor, Chem. Mater. **5**, 902 (1993)
7. P.X. Ma, R. Zhang, J. Biomed. Mater. Res. **46**, 60 (1999)
8. G. M. Whitesides, Grzybowski B, Science. **295**, 2418(2002)
9. G. M. Bose, Recherches sur la cause et sur la veritable teorie de l'Electricite: Wittenberg 1745
10. Lord Rayleigh, Phil. Mag. **14**, 184 (1882)
11. Lord Rayleigh, in *Theory of sound*. (1896)Vol.2, 2nd edition, p.374.
12. G. Taylor, Proc. R. Soc. London, Ser. A, **280**, 383 (1964)
13. J. F. Cooley 1902 US Pat. 692,631
14. W. J. Morton 1902 US Pat. 705,691
15. J. Zeleny, J. Proc. Camb. Phil. Soc. **18**, 71 (1915)
16. J. Zeleny, J. Phys. Rev. **10**, 1 (1917)
17. J. Zeleny, J. J. Franklin Inst. **219**, 659 (1935)
18. C. T. R. Wilson, G. I. Taylor, Proc. Camb. Phil. Soc. **22**, 728 (1925).
19. W. A. Macky, 1931 Proc. Roy. Soc. A. **133**, 565(1931)
20. J. J. Nolan, Proc. Roy. Irish Acad. **37**, 28 (1926)
21. A. Formhals US Pat. 2,109,333 (1938)
22. A. Formhals US Pat. 2,187,306 (1940)
23. B. Vonnegut, R. Neubauer, J. Colloid Sci. **7**, 616 (1952)
24. V. G. Drozin, J. Colloid Sci. **10**, 158 (1955)
25. H. L. Simons US Pat. 3,280,229
26. P. K. Baumgarten, J. Colloid Interface Sci. **36**, 71 (1971)
27. G. E. Martin, I. D. Cockshott, US Pat. 4,043,331; US Pat. 4,044,404, (1977)
28. W. L. Simm, G. O. Claus, R.B. Bonart, V. F. Bela, US Pat. 4,069,026, (1978)
29. J. Fine, S. A. De Tora, US Pat. 4,223,101(1980)
30. C. Guignard US Pat. 4,230,650(1980)
31. L. Larrondo, R.S. Manley a) J. Polym. Sci., Part B: Polym. Phys. **19**, 909 (1981); b) J. Polym. Sci., Part B: Polym. Phys. **19**, 921 (1981); c) J. Polym. Sci., Part B: Polym. Phys. **19**, 933 (1981)
32. S. Torza, R. G. Cox, S. G. Mason, Phil. Trans. R. Soc. Lond. A. **269**, 295 (1971)
33. A. Bornat, US Pat. (1982), 4,323,525; Bornat A, US Pat. (1987), 4,689,186
34. T.V. How, US Pat. 4,552,707
35. I. Hayati, A. I. Bailey, T. F. Tadros: a) J. Colloid Interface Sci. **117**, 205 (1987); b) J. Colloid Interface Sci. **117**, 222 (1987)
36. Doshi J. Reneker D.H. J. Electrostat. **35**, 151 (1995)
37. P. H. M. Bottger, Z. Bi, D. Adolph, K.A Dick, L. S Karlsson, M.N A Karlsson, B.A Wacaser, K. Deppert Nanotechnology **18**, 105304 (2007)
38. J. M. Grace, J.C.M. Marijnissen J. Aerosol. Sci. **25**, 1005 (1994)
39. I. W. Lenggoro, B Xia, K Okuyama, J.F. de la Mora Langmuir **18**, 4584 (2002)
40. F. Schulz, S. Franzk, G. Schmid Adv. Funct. Mater. **12**, 532 (2002)

41. J. Suh, B. Han, K. Okuyama, M. Choi J. Colloid Interface Sci. **287** 135(2005)
42. S. N. Jayasinghe Physica E **31** 17 (2006)
43. S. L. Kaufman J. Aerosol. Sci. **29** 537 (1998)
44. S. L. Kaufman Anal. Chim. Acta **406**, 3 (2000)
45. A. Henglein Topics in Current Chemistry **143**, 113 (1988)
46. M. L. Steigerwald, L.E. Brus Ann. Rev. Mat. Sci. **19**, 471 (1989).
47. Y Wang, N. Herron J. Phys. Chem. **95**, 525 (1991)
48. J. N. Fendler Chem. Rev. **87**, 877 (1987)
49. H. Weller Angewandte Chemie **32**, 41 (1993)
50. A. L. Efros Fiz. Tekn. Poluprovodn. **16**, 1209 (1982)
51. Y. Arakawa, H. Sakaki Appl. Phys. Lett. **24**, 195 (1982)
52. S. Schmitt-Rink, D. A. B Miller, D.S. Chemla Phys. Rev. B. **35**, 8113 (1987)
53. K.J. Vahala IEEE J. Quantum Electron. **24**, 523 (1988)
54. Y. Wang, N. Herron J. Phys. Chem. **91**, 257 (1987)
55. A. Jaworek, M. Lackowski, A. T. Krupa, Czech Experiments in Fluids **40**, 568 (2006)
56. S. R. Snarski, P. F Dunn Exp Fluids **11**, 268 (1991)
57. A. J. Rulison, R. C. Flagan Rev Sci Instrum **64**, 683 (1993)
58. J. D. Regele, M. J. Papac, M. J. A Rickard, D. Dunn-Rankin J Aerosol Sci **32**, 1471 (2002)
59. A. N. Hubacz, J. C. M. Marijnissen J Aerosol Sci **34**, S1269 (2003)
60. Y. M. Shin, M. M. Hohman, M. P. Brenner, G. C. Rutledge, Appl. Phys. Lett. **78**(8), 1149 (2001)
61. D. H. Reneker, A. L. Yarin, H. Fong H; S. J. Koombhongse, Appl. Phys. **87**, 4531 (2000)
62. J. Feng, J. Physics of Fluids. **14**, 3912 (2002)
63. G. Taylor, Proc. R. Soc. London, Ser. A. **313**, 453 (1969)
64. J. R. Melcher, G. I. Taylor, Annu. Rev. Fluid Mech. **1**, 111 (1969)
65. D. A. Seville, Annu. Rev. Fluid Mech. **29**, 27 (1997)
66. S. Koombhongse, D. H. Reneker, A. L. Yarin, J. Appl. Phys. **90**, 4836 (2001)
67. F. Spivak, Y. A. Dzenis, Appl. Phys. Lett. **73**, 3067 (1998); A. F. Spivak, Y. A. Dzenis, D. H. Reneker, Mech. Res. Comm. **27**, 37 (2000)
68. M. M. Hohman, M. Shin, G. Rutledge, M. P. Brenner, Phys. Fluids. **13**, 2201 (2001)
69. Y. Q. Wan, Q. Guo, N. Pan, Int. J. Nonlinear Sci. Numer. Simul. **5**, 5 (2004)
70. Y. M. Shin, M.M. Hohman, M. P. Brenner, G. C. Rutledge, Polymer. **42**, 9955 (2001)
71. J. H. He, Y. Wu, W. W. Zuo, Polymer. **46**, 12637 (2005)
72. C. P. Painter, M. M. Coleman, *Fundamentals of polymer science: an introductory text.* Technomic Publishing Co. (1997)
73. A. Buer, S. C. Ugbohue, S. B. Warner, Textile Research Journal. **71**, 323 (2001)
74. A. L. Yarin S., Koombhongse, D. H. Reneker, J. Appl. Phys. **89**(5), 3018 (2001)
75. J. H. He, Y. Q. Wan, J. Y. Yu, Polymer. **46**, 2799 (2005)
76. J. H. He, H. M. Liu, Nonlinear Analysis. **63**, 919 (2005)
77. J. H. He, Y. Q. Wan, J.Y. Yu, Int. J. Nonlinear Sci. Numer. Simul. **5**, 243 (2004)
78. J. H. He, Y. Q. Wan, Polymer. **45**, 6731 (2004)
79. D. Michelson, *Electrostatic atomization.* Hilger, New York p. 135 (1990)
80. C. J. Buchko, L. C. Chen, Y. Shen, D. C. Martin. Polymer. **40**, 7397 (1999)
81. X. Zong, K. Kim, D. Fang, S. Ran, B. S. Hsiao, B. Chu, Polymer. **43**, 4403 (2002)
82. Z. Jun, H. Hou, A. Schaper, J. H. Wendorff, A. Greiner, e-Polymers. 009 (2003)
83. P. Gupta, C. Elkins, T. E. Long, G. L. Wilkes. Polymer. **46**, 4799 (2005)
84. X. Geng, O. H. Kwon, J. Jang, Biomaterials. **26**, 5427 (2005)
85. K. Kim, M. Yu, X. Zong, J. Chiu, D. Fang, Y.S. Seo, B. S. Hsiao, B. Chu, M. Hadjiargyrou, Biomaterials. **24**, 4977 (2003)
86. S-H. Tan, R. Inai, M. Kotaki, S. Ramakrishna, Polymer. **46**, 6128 (2005)
87. K. W. Kim, K. H. Lee, M. S. Khil, Y. S. Ho, H. Y. Kim, Fibers and Polymers. **5**, 122 (2004)

88. S. L. Shenoy, W. D. Bates, G. Wnek, *Polymer*. **46**, 8990 (2005)
89. H. Fong, I. Chun, D.H. Reneker, *Polymer*. **40**, 4585 (1999)
90. J. M. Deitzel, J. Kleinmeyer, D. Harris, N.C. Beck Tan, *Polymer*. **42**, 261 (2001)
91. M. M. Demir, I. Yilgor, E. Yilgor, B. Erman, *Polymer*. **43**, 3303 (2002)
92. J. N. Doshi. PhD Dissertation, Akron, Ohio: University of Akron, 1994.
93. R. H. Colby, M. Rubinstein, M. Daoud, *J. de Phys II* **4**(8), 1299 (1994)
94. M. G. McKee, G. L. Wilkes, R. H. Colby, T. E. Long, *Macromolecules*. **37**(5),1760 (2004)
95. R. H. Magarvey, L.E. Outhouse. *J. Fluid. Mech.* **13**,151(1962)
96. T. Jarusuwannapoom, W. Hongrojjanawiwat, S. Jitjaicham, L. Wannatong, M. Nithitanakul, C. Pattamaprom, P. Koombhongse, R. Rangkupan, P. Supapho, *Eur. Polym. J.* **41**, 409 (2005)
97. C. Proteasa, *Electrospinning di Polimer Biodegradabili: analisi teorica e sperimentale*, Master degree thesis (2006), Chemical Process Engineering Department, University of Padova, Italy
98. T. Lin, H. Wang, H. Wang, X. Wang, *Nanotechnology*. **15**, 1375 (2004)
99. J. S. Choi, S. W. Lee, L. Jeong, S. H. Bae, B. C. Min, J. H. Youk, W. H. Park, *Int. J. Biol. Macromol.* **34**, 249 (2004)
100. W. K. Son, J. H. Youk, T. S. Lee, W. H. Park, *Polymer*. **45**, 2959 (2004)
101. W. K. Son, J. H. Youk, T. S. Lee, W. H. Park, *J. Polym. Sci. Pt.B-Polym. Phys.* **42**, 5 (2004)
102. K. H. Lee, H.Y. Kim, M.S. Khil, Y.M. Ra, D.R. Lee, *Polymer*. **44**, 1287 (2003)
103. T. Subbiah, G. S. Bhat, R. W. Tock, S. Parameswaran, S. S. Ramkumar, *J. Appl. Polym. Sci.* **96**, 557 (2005)
104. R. Jeager, M. M. Bergshoef, S. Holger, G. Vansco, *J. Macromol. Symp.* **127**, 142 (1998)
105. M. Deitzel, J. Kleinmeyer, D. Harris, N.C. Beck Tan, *Polymer*. **42**, 8163 (2001)
106. S. Megelski, J. S. Stephens, D. B. Chase, J. F. Rabolt, *Macromolecules*. **35**, 8456 (2002)
107. R. Kessick, J. Fenn, G. Tepper, *Polymer*. **45**, 2981 (2004)
108. S. L. Zhao, X. Wu, L. G. Wang, Y. Huang, *J. Appl. Polym. Sci.* **91**, 242 (2004)
109. J. S. Lee, K. H. Choi, H. D. Ghim, S. S. Kim, D. H. Chun, H. Y. Kim, W. S. Lyoo, *J. Appl. Polym. Sci.* **93**, 1638 (2004)
110. C. Mit-uppatham, M. Nithitanakul, P. Suphapol, *Macromol. Chem. Physic.* **205**, 2327 (2004)
111. M. Bognitzki, W. Czado, T. Frese, A. Schaper, M. Hellwig, M. Steinhart, A. Greiner, J. H. Wendorff, *Adv. Mater.* **13**, 70 (2001)
112. C. L. Casper, J. S. Stephens, N. G. Tassi, D. Bruce Chase, J. F. Rabolt, *Macromolecules* **37**, 573 (2004)
113. D. Li, Y. Xia, *Nano. Lett.* **4**, 933 (2004)
114. D. Li, G. Ouyang, J. McCann, Y. Xia, *Nano. Lett.* ASAP article
115. S. Piperno, L. Lozzi, R. Rastelli, M. Passacantando, S. Santucci, *Appl. Surf. Sci.* **252**, 5583 (2006)
116. S. Koombhongse, W. Liu., D. H. Reneker, *J. Polym. Sci. Pt B: Polym. Phys.* **39**, 2598 (2001)
117. H. Fong, W. Liu, C. S. Wang, R. A. Vaia, *Polymer*. **43**, 775 (2002)
118. A. Koski, K. Yim, S. Shivkumar, *Mater. Lett.* **58**, 493 (2004)
119. K. Nagapudi, W. T. Brinkman, J. E. Leisen, L. Huang, R. A. McMillan, R. P. Apkarian, V. P. Conticello, E. L. Chaikof, *Macromolecules*. **35**, 1730 (2002)
120. L. Huang, R. A. McMillan, R. P. Apkarian, B. Pourdeyhimi, V. P. Conticello, E. L. Chaikof *Macromolecules*. **33**, 2989 (2000)
121. R. Kessick, G. Tepper, *Appl. Phys. Lett.* **84**, 4807(2004)

122. M. Bognitzki, T. Frese, M. Steinhart, A. Greiner, J.H. Wendorff, A. Schaper, M. Hellwig, *Polym. Eng. Sci.* **41**, 982 (2004)
123. M. Srinivasarao, D. Collings, A. Philips, S. Patel, *Science* **292**, 79 (2001)
124. H. Matsuyama, M. Teramoto, R. Nakatani, T. Maki, *J. Appl. Polym. Sci.*, **74**, 171 (1999)
125. J. G. Wijmans, C. A. Smolders, in *Synthetic Membranes: Science, Engineering and Applications* edited P. M. Bungay, H. K. Lonsdale, M. N. De Pinho, Ridel Publishing Co., Dordrecht, The Netherlands (1986), p. 39.
126. H. C. Park, Y. P. Kim, Kim, H. Y.; Kang, Y. S. *J. Membr. Sci.* **156**, 169 (1999)
127. H. Matsuyama, T. Maki, M. Teramoto, K. Asano, *J. Membr. Sci.* **204**, 323 (2002)
128. H. Strathmann, in *Synthetic Membranes: Science, Engineering and Applications* edited P. M. Bungay, H. K. Lonsdale, M. N. De Pinho, Ridel Publishing Co., Dordrecht, The Netherlands (1986), p.1
129. P. Van de Witte, P. J. Dijkstra, J. W. A. Van den Berg, J. Feijen, *J. Membr. Sci.* **117**, 1 (1996)
130. S. O. Han, W. K. Son, J. H. Youk, T. S. Lee, W. H. Park, *Mater. Lett.* **59**, 2998 (2005)
131. A. V. Limaye, R. D. Narhe, A. M. Dhote, S. B. Ogale, *Phys. Rev. Lett.* **76**, 3762 (1996)
132. G. Loscertales, A. Barrero, M. Marquez, R. Spretz, R. Velarde-Ortiz, G. Larsen, *J. Am. Chem. Soc.* **126**, 5376 (2004)
133. H. Q. Hou, Z. Jun, A. Reuning, A. Schaper, J. H. Wendorff, A. Greiner, *Macromolecules.* **35**, 2429 (2002)
134. J. H. Yu, S. V. Fridrikh, G. C. Rutledge, *Adv. Mater.* **16**, 1562 (2004)
135. M. Wei, J. Mead, C. Sung, *Polym. Prep. (Am. Chem. Soc., Div Polym. Chem.* **44**, 79 (2003)
136. Z. Sun, E. Zussman, A. L. Yarin, J. H. Wendorff, A. Greiner, *Adv. Mater.* **15**, 1929 (2003)
137. Y. Zhang, Z. M. Huang, X. Xu, C. T. Lim, S. Ramakrishna, *Chem. Mater.* **16**, 3406 (2004)
138. J. Kim, D. S. Lee, *Polymer Journal.* **32**, 616 (2000)
139. S. Cuenot, S. Demoustier-Champagne, B. Nysten, *Phys. Rev. Lett.* **85**, 1690 (2000)
140. J. L. Duvail, P. Retho, C. Godon, C. Marhic, G. Louarn, O. Chauvet, *Synth. Met.* **135**, 329 (2003)
141. W. Xu, P. J. Mulhern, B. L. Blackford, M. H. Jericho, I. Templeton, *Scan. Microscopy.* **8**, 499 (1994)
142. E. P. S. Tan, C. T. Lim *Appl. Phys. Lett.* **84**, 1603 (2004)
143. E. P. S. Tan, C. T. Lim, *Compos. Sci. Tech.* **66**, 1102 (2006)
144. E. P. S. Tan, S. Y. Ng, C. T. Lim, *Biomaterials.* **26**, 1453 (2005)
145. J. S. Kim, D. H. Reneker, *Polym. Compos.* **20**, 124 (1999)
146. W. E. Teo, S. Ramakrishna, *Nanotechnology* **17**, R89 (2006)
147. J. A. Matthews, G. E. Wnek, D. G. Simpson, G. L. Bowlin, *Biomacromolecules.* **3**, 232 (2002)
148. J. Kameoka, H. G. Craighead, *Appl. Phys. Lett.* **83**, 371 (2003)
149. E. Zussman, D. Rittel, A. L. Yarin, *Appl. Phys. Lett.* **82**, 3958 (2003)
150. P. Katta, M. Alessandro, R. D. Ramsier, G. G. Chase, *Nano Lett.* **4**, 2215 (2004)
151. S. Kidoaki, I. K. Kwon, T. Matsuda, *Biomaterials* **26**, 37 (2005)
152. J. Stitzel, J. Liu, S. J. Lee, M. Komura, J. Berry, S. Soker, G. Lim, M. Van Dyke, R. Czerw, J. J. Yoo, A. Atala, *Biomaterials* **27**, 1088 (2006)
153. D. Li, Y. Wang, Y. Xia, *Nano Lett.* **3**, 555 (2003)
154. D. Li, Y. Wang, Y. Xia, *Adv. Mater.* **16**, 361 (2004)
155. W. E. Teo, S. Ramakrishna, *Nanotechnology.* **16**, 1878 (2005)
156. P. D. Dalton, D. Klee, M. Moller, *Polymer* **46**, 611 (2005)
157. W. E. Teo, M. Kotaki, X. M. Mo, S. Ramakrishna, *Nanotechnology.* **16**, 918 (2005)
158. A. Theron, E. Zussman, A. L. Yarin, *Nanotechnology.* **12**, 384 (2001)

159. B. Sundaray, V. Subramanian, T. S. Natarajan, R. Z. Xiang, C. C. Chang, W. S. Fann, *Appl. Phys. Lett.* **84**, 1222 (2004)
160. B. Ding, E. Kimura, T. Sato, S. Fujita, S. Stiratori, *Polymer.* **45**, 1895 (2004)
161. S. A. Theron, A. L. Yarin, E. Zussman, E. Kroll, *Polymer.* **46**, 2889 (2005)
162. W. Tomaszewski, M. Szadkowski, *Fibres & Textiles in Eastern Europe.* **13**, 22 (2005)
163. G. H. Kim, Y. S. Cho, W. D. Kim, *Eur. Polym. J.* **42** 2031 (2006)
164. O. O. Dosunmu, G. G. Chase, W. Kataphinan, D. H. Reneker, *Nanotechnology.* **17**, 1123 (2006)
165. T. H. Grafe, K. M. Graham, Donaldson Company Inc., Nonwovens in Filtration Fifth International Conference, Stuttgart, Germany, March 2003.
166. D. Groitzsch, E. Fahrback, US Pat. 4,618,524 (1986)
167. D. Emig, A. Klimmek, E. Raabe, US Patent 6,395,046 B1 (2002)
168. R. C. Brown, *Air Filtration*, Pergamon Press, Oxford, (1993)
169. [http:// www.donaldson.com/en/filtermedia](http://www.donaldson.com/en/filtermedia)
170. P. P. Tsai, H. S. Gibson, P. Gibson, *J. Electrostatics.* **54**, 333 (2002)
171. M. G. Hajra, K. Mehta, G.G. Chase, *Sep. Purif. Technol.* **30**, 79 (2003)
172. L. Li, M. W. Frey, T. B. Green, *J. Engineer. Fib. Fabr.* **1**, (2006)
173. R. S. Barhate, C. K. Loong, S. Ramakrishna, *J. Mem. Sci.* **283**, 209 (2006)
174. R. Gopal, S. Kaur, Z. Ma, C. Chan, S. Ramakrishna, T. Matsuura, *J. Mem. Sci.* **281**, 581 (2006)
175. M. Schlossberger, M. Rafailovich, p.40 in http://polymer.matscieng.sunysb.edu/abstracts_2005.pdf
176. R.C. Brown *Air Filtration*, Pergamon Press, Oxford, 1993.
177. I. B. Stechkina, A. A. Kirsch, N. A. Fuchs, *Ann. Occup. Hug.* **12**, 1 (1969)
178. J. Pich *Filtration - Principles and Practices*, edited by M.J. Matteson and C. Orr, Chapter 1, 1-132, 1987.
179. K. Yoon, K. Kim, X. Wang, D. Fang, B. S. Hsiao, B. Chu, *Polymer.* **47**, 2434 (2006)
180. S. Madhugiri, W. Zhou, J. P. Ferraris, K. J. Balkus Jr., *Microporous Mesoporous Mater.* **63**, 75 (2003)
181. A. Suthar, G. Chase, *Chem. Eng.* 726, **26** (2001)
182. D. Smith, DH. Reneker. PCT/US00/27737. (2001)
183. P. W Gibson, H. L. Schreuder-Gibson, D. Riven, *AIChE J.* **45**, 190 (1999)
184. P. W Gibson, H. L. Schreuder-Gibson, C. Pentheny, *J. Coated Fabrics* **28**, 63 (1998)
185. P. W. Gibson, H. L. Schreuder-Gibson, D. Riven, *Colloids Surf., A.* **187**, 469 (2001)
186. K. Graham, M. Gogins, H. Schreuder-Gibson, *Int. Nonwovens J. Summer* **21** (2004)
187. C. H. Bamford, K.G. Al-Lamee, M. D. Purbrick, T.J. Wear, *J. Chromatogr.* **606**, 19(1992)
188. Z. Ma, M. Kotaki, S. Ramakrishna, *J. Membr. Sci.* **265**, 115 (2005)
189. H. Lia, G. Zhu, B. Vugrinovich, W. Kataphinan, D. H. Reneker, P. Wang, *Biotechnol. Prog.* **18**, 1027 (2002)
190. M. M. Demir, M. A. Gulgun, Y. Z. Menciloglu, B. Erman, S. S. Abramchuk, E. E. Makhaeva, A. R. Khokhlov, V. G. Matveeva, M. G. Sulman, *Macromolecules.* **37**, 1787 (2004)
191. Q. B. Yang, D.M. Li, Y. L. Hong, Z. Y. Li, C. Wang, S. L. Qiu, Y. Wei , *Synth. Met.* **137**, 973 (2003)
192. H. K. Lee, E. H. Jeong, C. K. Baek, J. H. Youk, *Mater. Lett.* **59**, 2977 (2005)
193. Y. Wang, Q. Yang, G. Shan, C. Wang, J. Du, S. Wang, Y. Li, X. Chen, X. Jing, Y. Wie, *Mater. Lett.* **59**, 3046 (2005)
194. D. Li, J. T. McCann, M. Gratt, Y. Xia, *Chem. Phys. Lett.* **394**, 387 (2004)
195. G. M. Kim, A. Wutzler, H. J. Radusch, G. H. Michler, P. Simon, R. A. Sperling, W. J. Parak, *Chem. Mater.* **17**, 4949 (2005)
196. N. M. Rodriguez, M. S. Kim, R. Terry, K. Baker, *J. Phys. Chem.* **98**, 13108 (1994)

197. X. Yang, C. Shao, Y. Liu, R. Mu, H. Guan, *Thin Solid Films*. **478**, 228 (2005)
198. S. Madhugiri, B. Sun, Panagiotis G. Smirniotis, J. P. Ferrarsi, K. J. Balkus Jr., *Microporous Mesoporous Mater.* **69**, 77 (2004)
199. C. H. He, J. Gong, *Polym. Degrad. Stab.* **81**, 117 (2003)
200. H. Jia, G. Zhu, B. Vugrinovich, W. Kataphinan, D. H. Reneker, P. Wang, *Biotechnol. Prog.* **18**, 1027 (2002)
201. B. Ding, M. Yamazaki, S. Shiratori, *Sens. Actuators, B.* **106**, 477 (2005)
202. B. Ding, J. Kima, Y. Miyazaki, S. Shiratori, *Sens. Actuators, B.* **101**, 373 (2004)
203. H. Liu, J. Kameoka, D. A. Czaplewski, H. G. Craighead, *Nano Lett.* **4**, 671 (2004)
204. D. Aussawasathien, J. H. Dong, L. Dai, *Synth. Met.* **154**, 37 (2005)
205. S. J. Kwoun, R. M. Lec, B. Han, F. K. Ko, *Int. Frequency Control Symp. Exh.* **52**, (2000)
206. K. Sawicka, P. Gouma, S. Simon, *Sens. Actuators, B.* **108**, 585 (2005)
207. N. Lala, M. Sastry, *Phys. Chem. Chem. Phys.* **2**, 2461 (2000)
208. X. Wang, Y. G. Kim, C. Drew, B. C. Ku, J. Kumar, L. A. Samuelson, *Nano Lett.* **4**, 331 (2004)
209. S. H. Lee, B. C. Ku, X. Wang, L. A. Samuelson, J. Kumar, *Mater. Res. Soc. Symp. Proc.* 708 BB10.45.1 (2002)
210. X. Wang, C. Drew, S. H. Lee, K. J. Senecal, J. Kumar, L. A. Samuelson, *Nano Lett.* **2**, 1273 (2002)
211. J. R. Kim, S. W. Choi, S. M. Jo, W. S. Lee, B. C. Kim, *Electrochim. Acta* **50**, 69 (2004)
212. S. S. Choi, Y. S. Lee, C. W. Joo, S. G. Lee, J. K. Park, K. S. Han, *Electrochim. Acta* **50**, 339 (2004)
213. R. Gonzalez, N. J. Pinto, *Synth. Met.* **151**, 275 (2005)
214. K. J. Pawlowski, H. L. Belvin, D. L. Raney, J. Su, J. S. Harrison, E. J. Siochi, *Polymer.* **44**, 1309 (2003)
215. C. Kim, S. H. Park, W. J. Lee, K. S. Yang, *Electrochim. Acta* **50**, 877 (2004)
216. H. Guan, C. Shao, Y. Liu, N. Yu, X. Yang, *Solid State Comm.* **131**, 107 (2004)
217. Y. A. Dzenis, D. H. Reneker, *Mar. Res. Soc. Symp Proc.* 702 U5.4.1 (2001)
218. M. M. Bergshoef, G. J. Vancso, *Adv. Mater.* **11**, 1362 (1999)
219. H. Fong, *Polymer.* **45**, 2427 (2004)
220. G. Mathew, J. P. Hong, J. M. Rhee, H. S. Lee, C. Nah, *Polym. Test.* **24**, 712 (2005)
221. F. K. Ko, S. Khan, A. Ali, Y. Gogotsi, N. Naguib, G. Yang, C. Li, P. Willis, *Adv. Mater.* **15**, 1161 (2003)
222. J. J. Mack, L. M. Viculis, A. Ali, R. Luoh, G. Yang, H. T. Hahn, F. K. Ko, R. B. Kaner, *Adv. Mater.* **17**, 77 (2005)
223. F. K. Ko, M. Gandhi, C. Karatzas, *Proc. 19th Am. Soc. Comp. Annual Technical Conference, Atlanta, GA*, (2004)
224. R. Sen, B. Zhao, D. Perea, M. E. Itkis, H. Hu, J. Love, E. Bekyarova, R. C. Haddon, *Nano Lett.* **4**, 459 (2004)
225. I. S. Chronakis, *J. Mater. Process. Technol.* **167**, 283 (2005)
226. R. Langer, J.P. Vacanti, *Science* **260**, 920 (1993)
227. <http://www.ncbi.nlm.nih.gov/books/bv.fcgi?rid=eurekah.section.2752>
228. D. W. Hutmacher, *Biomaterials.* **21**, 2529 (2000)
229. S. R. Bhattarai, N. Bhattarai, H. K. Yi, P. H. Hwang, D. I. Chad, H. Y. Kim, *Biomaterials.* **25**, 2595 (2004)
230. N. Bhattarai, D. Edmondson, O. Veiseh, F. A. Matsen, M. Zhang, *Biomaterials.* **26**, 6176 (2005)
231. F. H. Martini, R. B. Tallitsch, M. J. Timmons, *Human Anatomy*. Benjamin Cummings Publishing (2003)
232. C. M. Vaz, S. Van Tuijl, C. V. C. Bouten, F. P. T. Baaijens, *Acta Biomater.* **1**, 575 (2005)
233. Z. Ma, M. Kotaki, T. Yong, W. He, S. Ramakrishna, *Biomaterials.* **26**, 2527 (2005)

234. W. J. Li, R. Tuli, X. Huang, P. Laquerriere, R. S. Tuan, *Biomaterials*. **26**, 5158 (2005)
235. W. J. Li, R. Tuli, C. Okafor, A. Derfoul, K. G. Danielson, D. J. Halla, R. S. Tuan, *Biomaterials*. **26**, 599 (2005)
236. H. Yoshimoto, Y. M. Shin, H. Terai, J. P. Vacanti, *Biomaterials*. **24**, 2077 (2003)
237. M. Shin, H. Yoshimoto, J. P. Vacanti, *Tissue Eng.* **10**, 33 (2004)
238. C. H. Lee, H. J. Shin, I. H. Cho, Y. M. Kang, I. A. Kim, K. D. Park, J. W. Shin, *Biomaterials*. **26**, 1261 (2005)
239. X. Zong, H. Bien, C. Y. Chung, L. Yin, D. Fang, B. S. Hsiao, B. Chua, E. Entcheva, *Biomaterials*. **26**, 5330 (2005)
240. J. J. Stankus, J. Guan, K. Fujimoto, W. R. Wagner, *Biomaterials*. **27**, 735 (2006)
241. T. Nicholson, S. N. Jayasinghe, *Biomacromolecules*. **7**, 3364 (2006)
242. Y. Z. Zhang, J. Venugopal, Z. M. Huang, T. Lim, S. Ramakrishna, *Biomacromolecules*. **6**, 2583 (2005)
243. Y. You, S. W. Lee, J. H. Youk, B. M. Min, S. J. Lee, W. H. Park, *Polym. Degrad. Stab.* **90**, 441 (2005)
244. Y. You, J. H. Youk, S. W. Lee, B. M. Min, S. J. Lee, W. H. Park, *Mater. Lett.* **60**, 757 (2006)
245. T. A. Telemeco, C. Ayres, G. L. Bowlin, G. E. Wnek, E. D. Boland, N. Cohen, C. M. Baumgarten, J. Mathews, D. G. Simpson, *Acta Biomater.* **1**, 377 (2005)
246. M. S. Khil, D. I. Cha, H.Y. Kim, I. S. Kim, N. Bhattarai, *J. Biomed. Mater. Res., Part B*. **67**, 675 (2003)
247. K. S. Rho, L. Jeong, G. Lee, B.M. Seo, Y. J. Park, S. D. Hong, S. Roh, J. J. Cho, W.H. Park, B.M. Min, *Biomaterials* **27**, 1452 (2006)
248. H. K. Noh, S. W. Lee, J. M. Kim, J. E. Oh, K. H. Kim, C. P. Chung, S. C. Choi, W. H. Park, B. M. Min, *Biomaterials*. **27**, 3934 (2006)
249. B. M. Min, S. W. Lee, J. N. Lim, Y. You, T. S. Lee, P. H. Kang, W. H. Park, *Polymer*. **45**, 7137 (2004)
250. W. H. Park, L. Jeong, D. I. Yoo, S. Hudson, *Polymer*. **45**, 7151 (2004)
251. C. P. Barnes, M. J. Smith, G. L. Bowlin, S. A. Sell, T. Tang, J. A. Matthews, D. G. Simpson, *J. Engineer. Fib. Fab.* **1**, (2006)
252. G. E. Wnek, M.E. Carr, D. Simpson, G.L. Bowlin, *Nano Lett.* **3**, 213 (2003)
253. A. S. Grewal, T. Mackey, p.42 http://polymer.matscieng.sunysb.edu/abstracts_2005.pdf
254. I. C. Um, D. Fang, B.S. Hsiao, A. Okamoto, B. Chu, *Biomacromolecules*. **5**, 1428 (2004)
255. X. Wang, I. C. Um, D. Fang, A. Okamoto, B.S. Hsiao, B. Chu, *Polymer*. **46**, 4853 (2005)
256. H. Jiang, Y. Hu, Y. Li, P. Zhao, K. Zhu, W. Chen, *J. Controlled Release*. **108**, 237 (2005)
257. G. Verreck, I. Chun, J. Rosenblatt, J. Peeters, A. Van Dijck, J. Mensch, M. Noppea, M. E. Brewster, *J. Controlled Release* **92**, 349 (2003)
258. X. Xu, L. Yang, X. Xu, X. Wang, X. Chen, Q. Liang, J. Zeng, X. Jing, *J. Controlled Release*. **108**, 33 (2005)
259. J. Zeng, X. Xu, X. Chen, Q. Liang, X. Bian, L. Yang, X. Jing, *J. Controlled Release*. **92**, 227 (2003)
260. J. Zeng, L. Yang, Q. Liang, X. Zhang, H. Guan, X. Xu, X. Chen, X. Jing, *J. Controlled Release*. **105**, 43 (2005)
261. K. Kim, Y. K. Luu, C. Chang, D. Fang, B. S. Hsiao, B. Chua, M. Hadjiargyrou, *J. of Controlled Release*. **98**, 47 (2004)
262. E. R. Kenawy, G. L. Bowlin, K. Mansfield, J. Layman, D. G. Simpson, E. H. Sanders, G. E. Wnek, *J. Controlled Release*. **81**, 57 (2002)
263. J. Zeng, A. Aigner, F. Czubyko, T. Kissel, J. H. Wendorff, A. Greiner, *Biomacromolecules*. **6**, 1484 (2005)
264. Y. K. Luu, K. Kim, B. S. Hsiao, B. Chu, M. Hadjiargyrou, *J. Controlled Release*. **89**, 341 (2003)

265. D. Liang, Y. K. Luu, K. Kim, B. S. Hsiao, M. Hadjiargyrou, *Nucleic Acids Res.* **33**, e170 (2005)
266. H. Myers Raymond, D.C. Montgomery "Response Surface Methodology: process and product optimization using designed experiment,." A Wiley-Interscience Publication (2002.)
267. G. Taguchi "Introduction to Quality Engineering," Asian Productivity Organization, UNIPUB, White Plains, NY. (1986)
268. G. Taguchi "System of Experimental Design: Engineering Methods to Optimize Quality and Minimize Cost," UNIPUB/Kraus International, White Plains, NY. (1987)
269. G. E. P. Box, N.R. Draper "Empirical Model-Building and Response Surfaces", Jon Wiley & Sons, New York. (1987).
270. A. I. Khuri, J.A. Cornell, "Response Surfaces," 2nd edition, Marcel Dekker. NY (1996).
271. D. M. Allen *Technometrics*, **13**, 469 (1971)
272. D. M., Allen *Technometrics* **16**, 125 (1974)
273. D. C. Montgomery, E. A. Peck, G. G. Vining "Introduction to Linear Regression Analysis," 3rd edition, John Wiley & Sons, NY (2001)
274. R. H. Myers "Classical and Modern Regression with Applications," 2nd edition, Duxbury Press, Boston. (1990)
275. M. Carley Kathleen D. Fridsma, E. Casman, N. Altman, J. Chang, B. Kaminsky, D. Nave, A. Yahia, "BioWar: Scalable Multi-Agent Social and Epidemiological Simulation of Bioterrorism Events", NAACSOS conference proceedings, Pittsburgh, PA (2003)
276. S. Joshi., H.D. Sherali, J.D. Tew, *Computers and Operations Research* **25**, 531 (1998)
277. X. Chen, S. S. Mao, *Chem. Rev.* **107**, 2891 (2007)
278. M. Miyauchi, A. Nakajima, T. Watanabe, K. Hashimoto, *Chem. Mat.* **14**, 2812 (2002)
279. B. Neppolian, H. C. Choi, S. Sakthivel, B. Arabindoo, V. Murugesan *J. Hazardous Mat.* **89**, 303 (2002)
280. R. Comparelli, E. Fanizza, M. L. Curri, P. D. Cozzi, G. Mascolo, A. Agostiano, *Appl. Cat. B* **60**, 1 (2005)
281. N. Serpone, P. Maruthamuthu, P. Pichat, E. Pelizzetti, H. Hidaka, *J. Photochem. Photobio. A* **85**, 247 (1995)
282. C. H. Wu, G. P Chang-Chien, W. S. Lee, *J. Hazardous Mat.* **114**, 191 (2004)
283. S. Rajagopalan, O. Koper, S. Decker, K. J. Klabunde *Chem. Eur. J.* **8**, 2602 (2002)
284. R. M Morris, K. J. Klabunde *Inorg. Chem.* **22**,682 (1983)
285. G. W. Wagner, P. W, Bartram, O. Koper, K. J. Klabunde *J. Phys.Chem. B.* **103**, 3225 (1999)
286. T. L. Vigo, *Polym. Adv. Tech.* **7**, 17 (1995)
287. T. L. Vigo, D. V. Parikh, G. F. Danna *Int. Nonwoven J.* **10**, 48 (2001)
288. S. Wang, H.M. Ang, Moses O. Tade *Env. Int.* **33**, 694 (2007)
289. A. Fujishima, T. N. Rao, D. A. Tryk *J. Photochemi Photobio C.* **1**, 1 (2000)
290. C. S. Turchi, D. F. Ollis, *J. Catalysis* **122**, 178 (1990)
291. A. Mills, A. Lepre, N. Elliott, S. Bhopal, I. P. Parkin, S. A. O'Neill, *J. Photochem. Photobio. A* **160**, 213 (2003)
292. R. Wang, K. Hashimoto, A. Fujishima, M. Chikuni, E. Kojima, A. Kitamura, M. Shimohigoshi, T. Watanabe, *Nature* **388**,431 (1997)
293. T. Zubkov, D. Stahl, T. L. Thompson, D. Panayotov, O. Diwald, J. T. Yates *J. Phys. Chem B* **109**, 15454 (2005)
294. M. Cheng, S. K. Brown. *Proce. National Clean Air Conference* 23–7 Newcastle, Nov. (2003)
295. J. Namiesnik, T .Gorecki, B. Kozdronzabiegala, J. Lukasiak.. *Build Environ* **27**,339 (1992).
296. X. Chen S. S. Mao *Chem. Rev.***107**, 2891 (2007)
297. X. Li, Z. Cao *Appl. Surf. Sci.* **252**, 7856 (2006)

298. T. Sugimoto *J. Colloid Int. Sci.* **259**, 43(2003)
299. A. Jaworek, A.T. Sobczyk, *J. Electrostatics* **66**, 197 (2008)
300. X. Li, Z. Cao *Appl. Surf. Sci.* **252**, 7856 (2006)
301. V. Yong *Nanotechnology* **15**, 1338(2004)
302. B. J Frisken *Appl. Opt.* **40**, 4087 (2001)
303. S. Chen, Y.Liu *Chemosphere* **67**, 1010 (2007)
304. Berry, G.C. and P.M. Cotts, Static and dynamic light scattering, in *Experimental methods in polymer characterization*, R.A. Pethrick and J.V. Dawkins, Editors. 1999, John Wiley & Sons Ltd.: Sussex, UK. p. 81-108.
305. J. Goldstein *Scanning electron microscopy and x-ray microanalysis*. Kluwer Academic/Plenum Publishers, 689 p. (2003)
306. L. Reimer *Scanning electron microscopy : physics of image formation and microanalysis*. Springer, 527 p. (1998)
307. R. F. Egerton *Physical principles of electron microscopy : an introduction to TEM, SEM, and AEM*. Springer, 202 (2005)
308. A. R. Clarke *Microscopy techniques for materials science*. CRC Press (electronic resource) (2002)
309. Sadtler *Handbook of UV spectra*, Heyden, London (1979).
310. K. Hirayama *Handbook of UV & visible absorption spectra of organic compounds*, Plenum Press. (1967)
311. *British Pharmacopoeia Appendix IIB*, A88-A89, HMSO, London (1993).
312. R.P.W. Scott, *Techniques and Practices of Chromatography*, Marcel Dekker (1995).
313. K. Blau, J. Halket, *Handbook of Derivatives for Chromatography*, John Wiley and Sons, (1993).
314. <http://www.chromatography-online.org/index.html>
315. K. Demeestere, A. De Visscher, J. Dewulf, M. Van Leeuwen, H. Van Langenhove, *Appl. Catalysis B* **54**, 261(2004)
316. R.M. Alberici, W.F. Jardim, *Appl. Catal. B* **14** 55 (1997)
317. R.A. Larson, E.J. Weber, *Reaction Mechanisms in Environmental Organic Chemistry*, Lewis Publishers, Boca Raton, 1994.
318. T.K. Lim, S.D. Kim, *Chemosphere* **54**, 305 (2004)
319. K.-H. Wang, H.-H. Tsai, Y.-H. Hsieh, *Chemosphere* **36**, 2763(1998)
320. H. H. Ou, S. L.Lo, *J. Haz. Mat.* **146**, 302(2007)
321. E. Sanhueza, I.C. Hisatsune, J. Hecklen, *Chem. Rev.* **76**, 801(1976)
322. M. Hedegus, A. Dombi, *Appl. Catal. A* 271 (2004) 177–184.
323. M. Mohseni, *Chemosphere* **59**, 335(2005)
324. P.B. Amama, K. Itoh, M. Murabayashi, *Appl. Catal. B* **37**, 321(2002)
325. M. A. Henderson, *Langmuir* **21**, 3443 (2005)
326. C. M. Schmidt, A. M. Buchbinder, E. Weitz, F. M. Geiger, *J. Phys. Chem. A* **111**, 13023 (2007)
327. B. viswanathan, S. Sivasanker, A. V. Ramaswamy, *Catalysis Principles and Applications*, Published by Narosa Publishing House, Delhi 110040 (India)
328. M. Zhou, J. Yu, B. Cheng, H. Yu, *Materials Chemistry and Physics* **93**, 159(2005)